

BIOENERGETIC MODELING OF HOMEOTHERMIC ANIMALS

A Dissertation

Presented to the Faculty of the Graduate School

of Cornell University

In Partial Fulfillment of the Requirements for the Degree of

Doctor of Philosophy

by

Hugo Fernando Maia Milan

December 2019

© 2019 Hugo Fernando Maia Milan

## BIOENERGETIC MODELING OF HOMEOTHERMIC ANIMALS

Hugo Fernando Maia Milan, Ph. D.

Cornell University 2019

### ABSTRACT

Methods to predict bioenergetic responses of homeothermic animals were developed. The methods can predict temperatures (e.g., internal, skin surface, and hair-coat surface), heat fluxes (e.g., internal, skin surface, hair-coat surface, convection, and radiation), metabolic heat flux, respiratory variables (respiration rate, tidal volume, expired air temperature), respiratory heat transfer (evaporation and convection), sweating rate, and cutaneous evaporation. The bioenergetic methods were applied to predict bioenergetic responses of livestock. The two main motivations for predicting bioenergetic responses of livestock are 1) the need to sustainably increase food production by 25-70% up to 2050 and 2) to develop systems to ameliorate the negative effects of heat stress on livestock, which costs more than \$3 billion to American farmers every year. Bioenergetic models provide insights about animal thermal stress status and comfort, which can be used for timely interventions and/or to design heat reduction systems for animals. Limitations of existing bioenergetic models are a) lack of providing uncertainty measures for the predictions and b) assumption of steady-state. In this study, the first limitation was addressed by developing an integrated bioenergetic model, which integrates fundamental models (analytical and numerical), machine learning models, bioheat transfer, Monte Carlo optimization method, ensemble learning techniques, energy conservation of biological objects, and bootstrapping. The integrated model was applied to predict bioenergetic responses of piglets. The predicted skin and hair-coat surface temperatures (prediction errors of

3.04% and 2.09%, respectively) are the second most accurate predictions published in the literature. The second limitation was addressed through developing the transmission-line modeling (TLM) method to predict dynamic bioenergetic responses. The TLM formulation was shown to predict temperatures with errors within 2% and 1,550 times faster than analytical solutions (based on the truncation of an infinite series solution). The TLM bioenergetic model was applied to predict dynamic bioenergetic responses of dairy-cows and the predictions of skin surface, and hair-coat surface temperatures were within 5% of the measured values. The strength of the methods developed herein are on proving accurate dynamic predictions of bioenergetic responses as well as on providing uncertainty measures of the predictions.

Keywords: Bio-heat transfer, bioenergetics, precision livestock farming, transmission-line modeling method.

## BIOGRAPHICAL SKETCH

Hugo Fernando Maia Milan was born in 1991 in Ariquemes (state of Rondônia), Brazil, a city in the inner state of the Amazon Rainforest region. He was always passionate about physics and mathematics, a passion encouraged by his parents, a math teacher and a special education teacher. His passion led him to move to Porto Velho city (capital of the state of Rondônia) in 2008 to pursue a degree in Electrical Engineering at the University of Rondônia. Encouraged by his family, Hugo moved to Campinas city (state of São Paulo) in 2012 to pursue an M.S. degree in Electrical Engineering, minoring Biomedical Engineering, at the University of Campinas, the best Brazilian Electrical Engineering University. In 2015, Hugo moved to Ithaca to pursue a Ph. D. degree in Biological Engineering, minoring Electrical and Biomedical Engineering, at Cornell University. During his academic journey, Hugo was awarded by prestigious scientific societies, including the Brazilian Society of Biophysics, the Brazilian Society of Biomedical Engineering, and the Brazilian Society of Biometerology.

To my son, *Carlos*.

## ACKNOWLEDGEMENTS

I am thankful for all support I received from my family during this long journey (12 years since when I started college). My especial thanks go to my parents, Suelene Soares Maia and Geninho Rodrigues Milan, and my uncle, Alex Sandro Campos Maia.

I am thankful for the collaborations with the Innovation in Biometeorology and Animal Welfare Research Group (INO BIO-MANERA), especially for sharing their animal expertise and helping with data collection.

I am thankful to my advisor, Prof. Kifle G. Gebremedhin, for his wise instructions and guidance.

Funding: Brazilian National Council of Technological and Scientific Development (CNPq, Proc. 203312/2014-7).

## TABLE OF CONTENTS

|  |       |
|--|-------|
| ABSTRACT .....   | iii   |
| BIOGRAPHICAL SKETCH.....   | v     |
| DEDICATION .....   | vi    |
| ACKNOWLEDGEMENTS .....   | vii   |
| LIST OF FIGURES .....  | xviii |
| LIST OF TABLES .....   | xxxvi |
| LIST OF ABBREVIATIONS .....  | xli   |
| LIST OF SYMBOLS.....   | xliv  |
| PREFACE.....   | 1     |
| Organization of the dissertation.....  | 4     |
| Conclusion .....   | 9     |
| Future studies.....  | 10    |
| REFERENCES .....   | 11    |
| CHAPTER 1: TRIANGULAR NODE FOR TRANSMISSION-LINE MODELING<br>(TLM) APPLIED TO BIO-HEAT TRANSFER..... | 17    |
| Abstract.....  | 17    |
| Keywords.....  | 18    |
| Highlights .....   | 18    |

|   |    |
|---|----|
| 1. INTRODUCTION .....   | 19 |
| 2. PROCEDURE .....  | 19 |
| 2.1 Isomorphism .....   | 20 |
| 2.2. Connection, Scattering and Matrix equations .....  | 24 |
| 2.3. Calculating temperature and heat flux.....   | 27 |
| 2.4. Boundary conditions.....   | 29 |
| 2.5. Initial Conditions.....  | 31 |
| 2.6. Convergence .....  | 32 |
| 2.7. Summary.....   | 33 |
| 2.8. Validation .....   | 33 |
| 2.9. Mesh-independent test.....   | 37 |
| 3. RESULTS AND DISCUSSION.....  | 39 |
| 4. CONCLUSIONS .....  | 42 |
| Acknowledgment.....   | 42 |
| REFERENCES .....  | 43 |
| CHAPTER 2: TETRAHEDRAL NODE FOR TRANSMISSION-LINE MODELING<br>(TLM) APPLIED TO BIO-HEAT TRANSFER..... | 47 |
| Abstract.....   | 47 |
| Keywords.....   | 48 |
| Highlights .....  | 48 |

|   |    |
|---|----|
| 1. INTRODUCTION .....   | 49 |
| 2. PROCEDURE .....  | 50 |
| 2.1. Isomorphism .....  | 51 |
| 2.2. Connection, scattering and matrix equations.....               | 54 |
| 2.3. Calculating temperature and heat flux.....                     | 56 |
| 2.4. Boundary conditions.....                                       | 57 |
| 2.5. Initial conditions .....                                       | 57 |
| 2.6. Convergence .....  | 57 |
| 2.7. Validation .....   | 58 |
| 2.8. Effect of breast tumor on breast skin-surface temperature..... | 62 |
| 2.9. Mesh-independent test.....                                     | 64 |
| 3. RESULTS AND DISCUSSION.....                                      | 65 |
| 4. CONCLUSIONS .....  | 71 |
| Acknowledgment.....   | 72 |
| REFERENCES .....  | 73 |
| CHAPTER 3: GENERAL NODE FOR TRANSMISSION-LINE MODELING (TLM)        |    |
| METHOD APPLIED TO BIO-HEAT TRANSFER.....                            | 76 |
| Abstract.....   | 76 |
| Keywords.....   | 77 |
| 1. INTRODUCTION .....   | 78 |

|   |         |
|---|---------|
| 2. PROCEDURE .....  | 79      |
| 2.1. Isomorphism .....  | 80      |
| 2.2. Scattering, connection, boundary conditions, initial conditions, temperature<br>calculation, and heat flux calculation ..... | 86      |
| 2.3. Validation .....   | 87      |
| 3. RESULTS AND DISCUSSION.....  | 94      |
| 4. CONCLUSION .....   | 102     |
| Acknowledgment.....   | 103     |
| REFERENCES.....   | 104     |
| <br>CHAPTER 4: PREDICTION OF OPTIMUM SUPPLEMENTAL HEAT FOR<br>PIGLETS .....   | <br>110 |
| Abstract.....   | 110     |
| Keywords.....   | 111     |
| 1. INTRODUCTION.....  | 112     |
| 2. MATERIALS AND METHODS .....  | 113     |
| 2.1. Experimental measurements.....   | 113     |
| 2.2. Data preprocessing .....   | 115     |
| 2.3. Mathematical modeling framework .....  | 116     |
| 2.4. Machine learning models to predict input temperatures .....  | 117     |
| 2.5. Mechanistic model of bio-heat transfer.....  | 119     |

|   |     |
|---|-----|
| 2.6. Monte Carlo optimization of system parameters.....                           | 122 |
| 2.7. Ensemble learning .....  | 128 |
| 2.8. Energy balance .....   | 133 |
| 3. RESULTS AND DISCUSSION.....  | 136 |
| 3.1. Environmental data.....  | 136 |
| 3.2. Machine learning models to predict input temperatures .....                  | 137 |
| 3.3. Monte Carlo optimization and ensemble learning.....                          | 140 |
| 3.4. Energy balance .....   | 144 |
| 3.5. Limitations of the model .....   | 152 |
| 4. CONCLUSION .....   | 154 |
| Acknowledgment.....   | 155 |
| APPENDIX A: SOLUTION PROCEDURE FOR THE MECHANISTIC MODEL                          |     |
| .....   | 156 |
| A1. Solution procedure for mechanistic model .....                                | 156 |
| A2. Analytical solution of the bio-heat equation.....                             | 157 |
| A3. Numerical solution of the absorbing-emitting radiation fibrous layer equation |     |
| .....   | 157 |
| A4. Coupled solution of bio-heat equation and absorbing-emitting radiation        |     |
| fibrous layer equation .....  | 162 |
| A5. Equations to calculate convection heat transfer and mean radiant temperature  |     |

|   |     |
|---|-----|
| .....   | 163 |
| A6. Mesh-size independent study.....  | 166 |
| APPENDIX B: PHYSICAL VARIABLES AND IRRADIANCE DATA .....  | 168 |
| APPENDIX C: MACHINE LEARNING ALGORITHMS .....   | 169 |
| C1. Ordinary linear regression with backwards selection .....   | 169 |
| C2. Generalization study .....  | 170 |
| APPENDIX D: LINEAR REGRESSION APPROXIMATIONS.....   | 173 |
| APPENDIX E: COMPUTATIONAL TIMES .....   | 175 |
| REFERENCES .....  | 178 |
| CHAPTER 5: PREDICTION OF BIOENERGETIC RESPONSES OF DAIRY-<br>COWS USING THE TRANSMISSION-LINE MODELING (TLM) METHOD ..... | 189 |
| Abstract.....   | 189 |
| Keywords.....   | 190 |
| Highlights .....  | 190 |
| 1. INTRODUCTION .....   | 196 |
| 2. MATERIALS AND METHODS .....  | 198 |
| 2.1. Model description.....   | 201 |
| 2.2. Experimental data processing.....  | 203 |
| 2.3. Model optimization .....   | 204 |
| 3. RESULTS AND DISCUSSION.....  | 205 |

|  |     |
|--|-----|
| 4. CONCLUSION .....  | 206 |
| Acknowledgement.....   | 207 |
| APPENDIX A: MODEL PARAMETERS.....  | 207 |
| APPENDIX B: MESH VALIDATION.....   | 227 |
| REFERENCES .....   | 232 |
| <br>   |     |
| CHAPTER 6: TECHNICAL NOTE: DEVICE FOR MEASURING RESPIRATION<br>RATE OF CATTLE UNDER FIELD CONDITIONS.....    | 243 |
| Abstract.....  | 243 |
| Keywords.....  | 244 |
| 1. INTRODUCTION.....   | 245 |
| 2. MATERIALS AND METHODS .....   | 246 |
| 3. RESULTS AND DISCUSSION.....   | 249 |
| 4. CONCLUSIONS .....   | 252 |
| REFERENCES .....   | 257 |
| <br>   |     |
| CHAPTER 7: MACHINE LEARNING ALGORITHMS TO PREDICT CORE, SKIN,<br>AND HAIR-COAT TEMPERATURES OF PIGLETS ..... | 260 |
| Abstract.....  | 260 |
| Keywords.....  | 261 |
| Highlights .....   | 261 |
| 1. INTRODUCTION .....  | 262 |

|  |     |
|--|-----|
| 2. MATERIALS AND METHODS .....   | 264 |
| 2.1. Experimental Measurements .....   | 264 |
| 2.2. Model Development .....   | 265 |
| 2.2.1. Data Processing .....   | 265 |
| 2.2.2. Overview of Machine Learning models .....   | 266 |
| 2.2.3. Training and Testing Machine Learning Models .....                                | 270 |
| 3. RESULTS AND DISCUSSION.....   | 272 |
| 3.1. Environmental data.....   | 272 |
| 3.2. Performance of machine learning models .....  | 276 |
| 3.3. Test of robustness and generalization of the best machine learning models.<br>..... | 281 |
| 3.4. Limitations and potential applications of machine learning models .....             | 286 |
| 4. CONCLUSIONS .....   | 287 |
| Acknowledgment.....  | 288 |
| REFERENCES .....   | 289 |
| CHAPTER 8: PHOTOVOLTAIC PANELS AS SHADING RESOURCES FOR<br>LIVESTOCK.....                | 296 |
| Abstract.....  | 296 |
| Keywords.....  | 297 |
| Highlights .....   | 297 |

|  |     |
|--|-----|
| 1. INTRODUCTION .....  | 299 |
| 2. MATERIALS AND METHODS .....   | 303 |
| 2.1. Animals and experimental design .....                               | 303 |
| 2.2. Behavioral observations .....                                       | 304 |
| 2.3. Meteorological data .....   | 306 |
| 2.4. Electricity generation and CO <sub>2</sub> savings estimation ..... | 306 |
| 2.5. Statistical analyses.....   | 307 |
| 3. RESULTS AND DISCUSSION.....   | 311 |
| 4. CONCLUSION .....  | 322 |
| Acknowledgment.....  | 323 |
| REFERENCES .....   | 324 |
| CHAPTER 9: PRECISION LIVESTOCK FARMING BIG DATA: PLFBD.....              | 334 |
| Abstract.....  | 334 |
| Keywords.....  | 335 |
| Highlights .....   | 335 |
| 1. INTRODUCTION .....  | 336 |
| 2. MATERIALS AND METHODS .....   | 338 |
| 2.1. Experimental procedure using dairy cows .....                       | 338 |
| 2.2. Experimental procedure using piglets .....                          | 343 |
| 2.3. Computer vision benchmark task: mesh registration .....             | 346 |

|  |     |
|--|-----|
| 2.4. Machine learning benchmark task: supervised learning .....            | 349 |
| 3. RESULTS AND DISCUSSION.....   | 353 |
| 3.1. Mesh registration performance.....                                    | 353 |
| 3.2. Challenges and future directions in mesh registration .....           | 354 |
| 3.3. Machine learning performance.....                                     | 361 |
| 3.4. Machine learning interpretability and generalization assessment ..... | 363 |
| 3.5. Challenges and future directions in machine learning .....            | 367 |
| 3.6. Algorithm selection .....   | 369 |
| 3.7. Other applications of PLFBD .....                                     | 371 |
| 4. CONCLUSION .....  | 372 |
| Acknowledgment.....  | 373 |
| REFERENCES .....   | 374 |

## LIST OF FIGURES

Figure 1. Nomenclature for (a) triangle and space discretization, and (b) unitary vectors (note that the lengths of the vectors are exaggerated). The thick dot represents the center of the triangle, which is connected through transmission lines to the midpoint in each triangular face. The connection point between adjacent triangles is called port. The length of the transmission line is  $\Delta\ell$ . The length of the triangular face is  $L$ . The unitary vectors  $LT$ ,  $\ell_1$ ,  $\ell_2$  always point toward the center of the node. .... 20

Figure 2. (a) TLM node for a triangle, and (b) detail of the electrical circuit between the center of the node and port  $n$ .  $V_c$  is voltage in the center of the node,  $V_{pn}$  is voltage in port  $n$ ,  $I_n$  is current flowing from port  $n$  to the center of the node.  $C_{dn}$  and  $L_{dn}$  are, respectively, the capacitance and inductance per unit length of transmission line  $n$ .  $R_n$  is resistance connected in series with transmission line  $n$ . .... 22

Figure 3. Equivalent electrical circuit (a) of the center of the node, which represents the scattering process, and (b) of the port (between two nodes), which represents the connection process. .... 25

Figure 4. Equivalent electrical circuit for *Connection* and the circuits for different types of boundary conditions. .... 30

Figure 5. The analytical problem used to validate the TLM is shown by the 1<sup>st</sup> rectangle. To solve this problem analytically, the temperature is firstly shifted by  $T_c$  and then separated into 4 linear related problems. The solutions to these 4 problems define the solution to the 1<sup>st</sup> rectangular problem. .... 34

Figure 6. TLM (a) absolute error in estimating temperature, and (b) absolute difference in estimating heat flux. Bars represent standard error, and SS represents steady state. The mean error and absolute differences for the steady state correspond to the mean and standard deviation for all nodes and ports. For the time evolution problem, mean error and absolute differences for all the simulation time (mean values for each time-step) are shown..... 40

Figure 7. Nomenclature for (a) tetrahedron and space discretization, and (b) unitary vectors (note that the lengths of the vectors are exaggerated for clarity). Black dots represent the center of each tetrahedron. The center of the tetrahedron is connected through transmission lines to the midpoint of each tetrahedron face. The connection point between adjacent tetrahedrons is called port. In (b) two tetrahedrons are shown and the transmission lines that do not connect in the highlighted area (thick lines) were omitted for clarity. The length of the transmission line is  $\Delta\ell$ . The unitary vectors  $A$ ,  $\ell_1$ ,  $\ell_2$  always point toward the center of the node. .... 51

Figure 8. (a) TLM node for a tetrahedron, and (b) detail of the electrical circuit between the center of the node and port  $n$ .  $V_c$  is voltage in the center of the node,  $V_{pn}$  is voltage in port  $n$ ,  $I_n$  is current flowing from port  $n$  to the center of the node.  $C_{dn}$  and  $L_{dn}$  are, respectively, the capacitance and inductance per unit length of transmission line  $n$ .  $R_n$  is resistance connected in series with transmission line  $n$ ..... 53

Figure 9. Equivalent electrical circuit of the center of the tetrahedral node that represents the scattering process. .... 55

Figure 10. Computational domain for the analytical solution.  $H$  = height,  $L$  = length,

and  $T_z =$  thickness. .... 58

Figure 11. Computational domain for the breast with tumor. .... 63

Figure 12. (a) Absolute percentage error in predicting the temperature, and (b) absolute difference in predicting the heat flux using the TLM tetrahedral node. Bars represent standard error, and *SS* represents steady-state condition. The mean error and absolute difference for the steady state correspond to the mean and standard error for all nodes and ports. For the problem solved in time domain, the mean error and absolute error for all the simulation time (mean values for each time step) are shown. .... 67

Figure 13. Maximum skin-surface temperature difference between a breast with tumor and without ( $\Delta T_{\max}$ ).  $(c_b \omega_b)_n$  represent different blood perfusion values (Table 3)..... 71

Figure 14. Example of control volumes for a general TLM node in (a) 1-D, (b) 2-D, and (c) 3-D. The dot represents the center of the geometry and  $\Delta \ell_n$  is the distance between the center and border  $n$ , which is defined as the length of the transmission line  $n$ . Transmission lines are represented by thin lines and control volume boundaries are represented by thick lines. .... 80

Figure 15. General node for the transmission line modeling method applied to a bio-heat transfer problem.  $V_c$  is voltage in the center of the node,  $I_n$  is current flowing through transmission line  $n$ ,  $L_{dn}$  and  $C_{dn}$  are, respectively, inductance and capacitance per unit length of transmission line  $n$ ,  $R_n$  is resistance connected in series with transmission line  $n$ ,  $I_S$  is current source connected to the center of the node, and  $G$  is conductance connected to the center of the node. .... 83

Figure 16. Thévenin's equivalent circuit of the general TLM node circuit (Figure 15).

$V_c$  represents voltage at the center of the node,  $Z_n$  represents impedance of transmission line  $n$ , and  $V_n^i$  represents incident voltage in transmission line  $n$ . ..... 87

Figure 17. Example of meshes with (a) irregular quadrangles, (b) irregular hexahedrons, and (c) pyramids. In (c), pyramids (blue lines) were used to connect boundaries segmented with irregular quadrangles (black lines) with the domain segmented with tetrahedrons (not shown). Lines represent borders of geometry elements..... 89

Figure 18. Problem domain for the analytical solutions in two-dimensions Milan and Gebremedhin, 2016a) (a) and three-dimensions (Milan and Gebremedhin, 2016b) (b). ..... 91

Figure 19. Problem domain for breast with tumor. .... 93

Figure 20. Representation of a quarter of a spherical tumor with diameter of 30 mm using irregular (a) and regular hexahedrons for mesh-size #7 show in Table 8..... 95

Figure 21. Mean and standard deviation of absolute temperature percentage error using the general TLM node vs. the analytical solutions for: (a) regular (□) and irregular (■) quadrangles, (b) regular (□) and irregular (■) hexahedrons, and (c) pyramids. .... 97

Figure 22. Mean and standard deviation of absolute heat-flux difference divided by maximum input heat flux (100,000 W/m<sup>2</sup>) using the general TLM node vs. the analytical solutions for: (a) regular (□) and irregular (■) quadrangles, (b) regular (□) and irregular (■) hexahedrons, and (c) pyramids. .... 98

Figure 23. Maximum difference of skin-surface temperature between a breast without and with tumor of the indicated diameter and for the described blood perfusion values.

..... 101

Figure 24. Flowchart of mathematical framework used to predict optimum supplemental heat ( $H_{opt}$ ), hair-coat temperature ( $T_h$ ), skin temperature ( $T_s$ ), and skin heat-flux ( $q''_s$ ). Boxes represent models. Arrows represent flow of input/output. See text for description..... 118

Figure 25. Control volume and boundary conditions for the mechanistic model. Subscripts  $m, f, s$ , and  $h$  represent muscle, fat, skin, and hair-coat layers, respectively;  $L_i$  represents thickness of layer  $i$ ;  $T_r$  represents rectal temperature used as a boundary condition;  $q''_{conv,i}$  represents convection heat transfer from the surface of layer  $i$ ;  $\omega$  is proportion of  $q''_{conv,h}$ ;  $\phi$  is additional proportion of  $q''_{conv,s}$ ..... 120

Figure 26. Experimental data (mean  $\pm$  standard error of the mean) for air ( $T_a$ ) and black-globe ( $T_g$ ) temperatures and relative humidity (RH) inside the brooder, and air temperature in the pen ( $T_{a,pen}$ ) stratified by measurement time and supplemental heat. .... 137

Figure 27. Performance of the best fit machine learning algorithms to predict air temperature inside the brooder ( $T_a$ ; a), black-globe temperature inside the brooder ( $T_g$ ; b), and rectal temperature ( $T_r$ ; c) given air temperature in the pen and supplemental heat. Mean squared error (MSE) for training, cross-validation (CV), and testing are shown. Selected model was LM for  $T_a, T_g$ , and  $T_r$ . LM: ordinary linear regression with backwards selection; GLM: generalized linear regression model with elastic net

regularization; RF: random forests; GBM: gradient boosted machines; DL: deep learning with ReLU activation function. .... 138

Figure 28. Measured (●) and predicted (■) air ( $T_a$ , a) and black-globe ( $T_g$ , a) temperatures inside the brooder and rectal temperature ( $T_r$ , b) for the mean dataset stratified by measurement time and supplemental heat. Absolute percentage errors of the predicted temperatures (c). Data shown are mean  $\pm$  standard error of the mean. Temperatures were predicted using ordinary linear regression with backwards selection (LM). .... 139

Figure 29. Performance of sets of system parameters (a) and ensembles (b) in predicting skin ( $T_s$ ) and hair-coat ( $T_h$ ) surface temperatures. Ensemble candidates are in the order from low-to-high (left-to-right) log-likelihood. The best performing ensemble candidate was GB. Performance metrics were mean squared error (MSE) evaluated in training, cross-validation (CV), and testing datasets, and mean standard deviation squared ( $\sigma^2$ ) evaluated in the testing dataset (43 samples). CV MSE and  $\sigma^2$  are only defined for ensembles. TM: traditional set of system parameters and measured input data; TP: traditional set of system parameters and expected input data predicted with machine learning algorithms; MC: set of system parameters drawn from Monte Carlo sampling method with minimum training MSE; NB: ensemble obtained with naïve search and bagging; RO: ensemble obtained with random search with optimum weights; NO: ensemble obtained with naïve search and optimum weights; RB: ensemble obtained with random search and bagging; GB: ensemble obtained with greedy search and bagging; GO: ensemble obtained with greedy search and optimum weights. .... 142

Figure 30. Hair-coat ( $T_h$ ; a) and skin ( $T_s$ ; b) surface temperatures, and skin-surface heat flux ( $q''_s$ ; d) predicted using the best performing ensemble (greedy search with bagging) for the mean dataset (stratified by measurement time and supplemental heat), and (c) absolute percentage errors of the predicted temperatures. Measured values and absolute percentage errors are presented as mean  $\pm$  standard error of the mean. Predicted values are presented as mean  $\pm$  standard deviation of the mean. .... 145

Figure 31. Surface plots for the relationship between supplemental heat ( $x$ -axis) and air temperature ( $y$ -axis) with hair-coat surface temperature ( $T_h$ , °C), skin surface temperature ( $T_s$ , °C), and skin surface heat flux ( $q''_s$ , W m<sup>-2</sup>). Plots show (a) lower 95% confidence interval (CI), (b) mean, and (c) upper 95% CI for  $T_h$ ; (d) lower 95% CI, (e) mean, and (f) upper 95% CI for  $T_s$ ; and (g) lower 95% CI, (h) mean, and (i) upper 95% CI for  $q''_s$ .  $T_h$ ,  $T_s$ , and  $q''_s$  are shown using color gradients and contours. Color gradients are the same for each set of plots (a-c, d-f, and g-i). Numbers and lines on the surface plots indicate contours. Dashed rectangles represent range of measured experimental data..... 146

Figure 32. Surface plots for the relationship between animal weight ( $x$ -axis) and air temperature ( $y$ -axis) with optimum supplemental heat ( $H_{opt}$ , W) and energy flux imbalance (W m<sup>-2</sup>). Plots show (a) lower 95% confidence interval (CI), (b) mean, and (c) upper 95% CI for  $H_{opt}$ , and (d) lower 95% CI, (e) mean, and (f) upper 95% CI for energy flux imbalance.  $H_{opt}$  and energy flux imbalance are shown using color gradients and contours. Color gradients are the same for each set of plots (a-c and d-f). Numbers and lines in the surface plots indicate contour plots. Negative values in

energy flux imbalance plots (d-f) represent piglets gaining energy flux. Dashed rectangles represent range of measured data. .... 149

Figure 33. Zone of least thermoregulation of piglets when supplemental heat is not provided. Thinner solid lines represent lower and upper 95% confidence interval for our result. Plots from Harmon and Xin (1995) represent their suggested optimum temperature ranges. Range of measured data is 2.2-6.1 kg and 17.8-33.6 °C. .... 151

Figure 34. Control volume and conditions imposed between sublayers. .... 156

Figure 35. Finite difference discretization space used to solve Eqs. (161) and (170). Temperature at  $0 \leq x < \Delta x/2$  is assumed equal to the skin-surface temperature ( $T_s$ ). Temperatures at  $(2i - 1)\Delta x/2 \leq x < (2i + 1)\Delta x/2$  is assumed equal to  $T(x + i\Delta x)$ . Temperature at  $(L_h - \Delta x/2) \leq x \leq L_h$  is assumed equal to the hair-coat surface temperature ( $T_h$ ). .... 161

Figure 36. Mesh-size independent study.  $T_s$ : skin surface temperature;  $T_h$ : hair-coat surface temperature; min: minimum value for the training dataset; mean: mean value for the training dataset; max: maximum value for the training dataset. .... 167

Figure 37. Dependence plot for predicting air temperature inside the brooder ( $T_a$ ) using (a) deep learning with ReLU activation function, (b) gradient boosted machines, (c) random forests, (d) generalized linear regression with elastic net regularization, and (e) ordinary linear regression with backwards selection. Dashed rectangle represents range of measured experimental data. .... 171

Figure 38. Dependence plot for predicting black-globe temperature inside the brooder ( $T_g$ ) using (a) deep learning with ReLU activation function, (b) gradient boosted

machines, (c) random forests, (d) generalized linear regression with elastic net regularization, and (e) ordinary linear regression with backwards selection. Dashed rectangle represents range of measured experimental data. .... 172

Figure 39. Dependence plot for predicting rectal temperature ( $T_r$ ) using (a) deep learning with ReLU activation function, (b) gradient boosted machines, (c) random forests, and (d) generalized linear regression with elastic net regularization. Predictions using ordinary linear regression with backwards selection were independent of input data:  $T_r = 37.91$  °C. Dashed rectangle represents range of measured experimental data. .... 173

Figure 40. Flowchart of the modeling procedure. The transmission-line modeling (TLM) bioenergetic model predicts several bioenergetics variables, including 1) temperatures at any position in the control volume ( $T$ , °C), 2) heat fluxes at any position in the control volume ( $q''$ ,  $W m^{-2}$ ), 3) metabolic heat generation ( $q''_{met}$ ,  $W m^{-2}$ ), 4) respiratory evaporation and convection heat transfer ( $q''_r$ ,  $W m^{-2}$ ), 5) cutaneous evaporation heat transfer ( $q''_{ce}$ ,  $W m^{-2}$ ), 6) convection heat transfer ( $q''_{conv}$ ,  $W m^{-2}$ ), and 7) radiation heat transfer ( $q''_{rad}$ ,  $W/m^2$ ). The model inputs are the environmental conditions: 1) air temperature ( $T_a$ , °C), 2) relative humidity ( $RH$ , %), 3) air velocity ( $v_a$ ,  $m s^{-1}$ ), and 4) black-globe temperature ( $T_g$ , °C). .... 199

Figure 41. Control volume and boundary conditions of the transmission-line modeling (TLM) bioenergetic model.  $q''_{met}$  ( $W m^{-2}$ ) represents metabolic heat generation,  $q''_r$  ( $W m^{-2}$ ) represents respiratory evaporation and convection heat transfer,  $q''_{ce}$  ( $W m^{-2}$ ) represents cutaneous evaporation heat transfer,  $q''_{conv}$  ( $W m^{-2}$ ) represents convection

heat transfer,  $q''_{rad}$  ( $\text{W}/\text{m}^2$ ) represents radiation heat transfer,  $\square_w$  represents variables for to the model with white hair-coat, and  $\square_b$  represents variables for the model with black hair-coat. .... 200

Figure 42. Mean squared error for the training, cross-validation (CV), and testing datasets using the traditional set of system parameters (TM) and the set of system parameters optimized using the Monte Carlo optimization method (MC)..... 206

Figure 43. Probability of observing valid predictions vs. number of nodes ( $n_N$ )  $\times$  time-step ( $\Delta t$ ). .... 229

Figure 44. Skin surface temperature ( $T_s$ , a and b) and hair-coat surface temperature ( $T_h$ , c and d) for white ( $T_{s,w}$  in a and  $T_{h,w}$  in b) and black ( $T_{s,b}$  in c and  $T_{h,b}$  in d) hair-coat colors..... 230

Figure 45. Observed and predicted (using Eq. (224)) maximum number of nodes, given time-step, that provides precise predictions. .... 231

Figure 46. Schematic of the halter. Electronic device and temperature sensor are contained in the halter. .... 248

Figure 47. Flowchart of the device. The respiration rate is calculated from the number of oscillations of the temperature signal (shown in the inset of Figure 48). Patent of the device is pending. .... 249

Figure 48. Air temperature measurement near the nostrils of the animal. The inset is a zoomed-in image of the temperature reading of one-minute segment. .... 252

Figure 49. Respiration rate measured using the device and by counting the flank

|  |     |
|--|-----|
| movements of Animal 1. ....  | 253 |
| Figure 50. Respiration rate measured using the device and by counting the flank movements of the animals (mean $\pm$ SEM). ....  | 254 |
| Figure 51. Linear regression of respiration rate measured by counting flank movement (RRC) against respiration rate measured by the device (RRD) in respirations per minute (RPM). ....  | 255 |
| Figure 52. Measured environmental variables (mean $\pm$ SEM).....  | 256 |
| Figure 53. Example of a decision tree for predicting hair-coat surface temperature. A decision tree is developed by segmenting the input space into structured outputs. Each decision (e.g., Time < 6) represents a split of the tree. A leaf is the end node of the tree (e.g., the node with the value of 31 for Time $\geq$ 6 and Heat < 30). Random forests are based on creating several decision trees and averaging their output. Gradient boosted machines are based on creating several sequential decision trees, where new trees focus on improving the prediction accuracy of previous trees, and linearly combining the predictions of these trees. Time: time of measurement (hours); Heat: intensity of supplemental heat (W); T <sub>a</sub> : air temperature (°C); T <sub>g</sub> : black globe temperature (°C). .... | 268 |
| Figure 54. Feedforward neural network. Each input variable represents one neuron (I <sub>n</sub> ) that connects to every hidden neuron in the first hidden layer (H <sub>1m</sub> ). Each hidden neuron is a non-linear function (activation function), where the outputs of the hidden neurons in the previous hidden layer are inputs to the hidden neurons in the next hidden layer. The outputs of the last hidden layer are inputs to the output neuron (O), which provides the prediction of the neural network. Time: time of measurement  |     |

(hours); Heat: intensity of supplemental heat (W);  $T_a$ : air temperature ( $^{\circ}\text{C}$ );  $T_g$ : black globe temperature ( $^{\circ}\text{C}$ );  $I_n$ : input neuron  $n$ ;  $H_{nm}$ : hidden neuron  $m$  of hidden layer  $n$ ;  $O$ : output neuron;  $T_r$ : rectal temperature ( $^{\circ}\text{C}$ ). ..... 271

Figure 55. Experimental data (mean +/- standard error of the mean) for air temperature ( $T_a$ ), black-globe temperature ( $T_g$ ), and relative humidity (RH) separated by time of measurement and intensity of supplemental heat. .... 274

Figure 56. Performance of the best machine learning models for predicting rectal ( $T_r$ ; a), skin-surface ( $T_s$ ; b), and hair-coat surface ( $T_h$ ; c) temperatures. GLM: generalized linear regression model with elastic net regularization; RF: random forests; GBM: gradient boosted machines; DNN: deep neural network with ReLU activation function. .... 277

Figure 57. Mean squared error (MSE) on the training (a, c, e) and testing (b, d, f) datasets for predicting rectal ( $T_r$ ; a, b), skin-surface ( $T_s$ ; c, d), and hair-coat surface ( $T_h$ ; e, f) temperatures using the best performing machine learning models..... 280

Figure 58. Measured ( $\bullet$ ) and predicted ( $\blacksquare$ ) rectal ( $T_r$ ), skin-surface ( $T_s$ ), and hair-coat surface ( $T_h$ ) temperatures for the mean dataset stratified by (a) time of measurement and intensity of supplemental heat, and (b) absolute percentage errors of the predicted temperatures. Measured values and absolute percentage errors are presented as mean +/- standard error of the mean. Temperatures were predicted from the best performing machine learning models. RF: random forests; GBM: gradient boosted machines; DNN: deep neural network with ReLU activation function..... 281

Figure 59. Test of robustness and generalization of the best machine learning models

in predicting rectal temperature when changing (a) air temperature, (b) black-globe temperature, (c) time of measurement, or (d) intensity of supplemental heat, while keeping the remaining predictor variables at their mean values. The vertical dashed lines represent the range of the measured predictor variable. The horizontal solid line represents the mean rectal temperature, and the horizontal dashed lines represent the mean rectal temperature  $\pm$  one standard deviation from the mean. .... 282

Figure 60. Test of robustness and generalization of the best machine learning models in predicting skin-surface temperature when changing (a) air temperature, (b) black-globe temperature, (c) time of measurement, or (d) intensity of supplemental heat, while keeping the remaining predictor variables at their mean values. The vertical dashed lines represent the range of the measured predictor variable. The horizontal solid line represents the mean skin-surface temperature, and the horizontal dashed lines represent the mean skin-surface temperature  $\pm$  one standard deviation from the mean. .... 283

Figure 61. Test of robustness and generalization of the best machine learning models in predicting hair-coat surface temperature when changing (a) air temperature, (b) black-globe temperature, (c) time of measurement, or (d) intensity of supplemental heat, while keeping the remaining predictor variables at their mean values. The vertical dashed lines represent the range of the measured predictor variable. The horizontal solid line represents the mean hair-coat surface temperature, and the horizontal dashed lines represent the mean hair-coat surface temperature  $\pm$  one standard deviation from the mean. .... 284

Figure 62. Test of robustness and generalization of the best machine learning models in predicting rectal ( $T_r$ ), skin-surface ( $T_s$ ), and hair-coat surface ( $T_h$ ) temperatures when randomly changing air temperature, black-globe temperature, time of measurement, and intensity of supplemental heat. Points represent mean  $\pm$  one standard deviation of the mean (10,000 samples). Horizontal solid lines represent mean temperatures, and horizontal dashed lines represent mean  $\pm$  one standard deviation of the mean. ....285

Figure 63. Photo showing sheep under the shade from photovoltaic panels..... 304

Figure 64. Flowchart of animal behavior recording. .... 305

Figure 65. Means ( $\pm$ SEM) of air temperature ( $T_A$ , °C), relative air humidity ( $R_H$ , %), solar radiation ( $R_s$ ,  $W\ m^{-2}$ , spectral range = 0.3-3.6  $\mu m$ ), ultraviolet solar irradiance ( $U_V$ ,  $W\ m^{-2}$ , spectral range = 0.28-0.4  $\mu m$ ), and wind speed ( $W_s$ ,  $m\ s^{-1}$ )..... 312

Figure 66. Least square means ( $\pm$ SEM) of the time animals spent in the shade or under the sun (%) for different levels of solar radiation..... 314

Figure 67. Least square mean ( $\pm$ SEM) of air temperature ( $T_A$ , °C), solar radiation ( $R_s$ ,  $W\ m^{-2}$ ; spectral range = 0.3-3.6  $\mu m$ ) and time lambs and ewes spent in the photovoltaic panel shade (%) by lambs and ewe..... 315

Figure 68. Least square means ( $\pm$ SEM) of time of animal activities (%). .... 316

Figure 69. Estimated probabilities for lambs (a) and ewes (b) under the shade from cloth (Cloth) or solar panels (Panel) or exposed to the sun (Sun). Continuous lines represent expected values. Broken lines represent simultaneous 95% Bayesian credible

|  |     |
|--|-----|
| intervals. ....  | 317 |
| Figure 70. Observed probabilities for lambs (a) and ewes (b) under the shade from cloth (Cloth) or solar panels (Panel) or exposed to the sun (Sun). N represents number of samples for each range of solar radiation. The ranges for solar radiation were inclusive for the lower bound and exclusive for the upper bound. ....   | 319 |
| Figure 71. Radiant heat load measured in the shade projected underneath the shade structure (a) or outside (b). Difference between radiant heat load in the shade projected by photovoltaic panels and cloth (c), and between underneath and outside (d). Broken lines represent simultaneous 95% Bayesian credible intervals. ....  | 320 |
| Figure 72. Power output vs. intensity of solar radiation (a). Monthly energy generated by the photovoltaic panels (bars) and amount of CO <sub>2</sub> (points) not emitted to the atmosphere (b). Broken lines represent simultaneous 95% Bayesian credible intervals. ....   | 321 |
| Figure 73. Examples of pairs of meshes (target and source) with little (a), moderate (c), and considerable overlap (e). Pseudo-colors (b, d, f) represent the Hausdorff distance between the meshes pairs (Cignoni, Rocchini, Scopigno, 1998), from near (red) to far (blue). Color bars show the color scale for the Huasdorff distance. ....   | 348 |
| Figure 74. Euclidean distances evaluated on the sets of close points (ground truth corresponding points that should be in the same position if the meshes were perfectly aligned; a) and far points (pair of points that should be distant if the meshes were perfectly aligned; b). Boxplots sorted from high-to-low mean Euclidean distance (top-to-bottom). Performance metrics for EDSM and MRF are not shown because they |     |

involved sampling procedures, which prevented manually tracking the position of correspondence points in pre-processed and registered meshes. ICP: iterative closest point algorithm; ARAP: as-rigid-as-possible; NICP: non-rigid ICP; ID: isometric deformations; SHOT: isometric deformations with SHOT descriptors; NDS: non-rigid depth scans. EDSM: embedded deformation for shape manipulation; MRF: Markov random fields. .... 355

Figure 75. Initial (a) and final (b) correspondences obtained with SHOT on two partial meshes with moderate overlap (pair of meshes shown in Figure 73cd). Alignment performed with SHOT distorted one of these partial meshes to a spherical-like geometry (c; inside the orange circle). Overlap between these two meshes occurs on the left side of the cow. Initial correspondences were found between parts of the partial meshes that did not relate to ground truth, such as correspondences between the thorax and head. Final correspondences were mostly found between legs in one mesh and other body parts in the other mesh. Correspondences are indicated as purple lines connecting point clouds of the two meshes. .... 356

Figure 76. Hausdorff distance between mesh pairs with little (a, b; Figure 73ab) and considerable (c, d; Fig. Figure 73ef) overlap when registered with non-rigid iterative closest point algorithm (NICP). Pseudo-colors represent near (red) to far (blue) Hausdorff distances. Gray color (b, d) represents the target mesh. Color bars show the color scale for the Hausdorff distance. .... 357

Figure 77. Hausdorff distance between mesh pairs with little (a, b; Figure 73ab) and considerable (c, d; Figure 73ef) overlap when registered with non-rigid depth scans

(NDS). Pseudo-colors represent near (red) to far (blue) Hausdorff distances. Gray color (b, d) represents the target mesh. Color bars show the color scale for the Hausdorff distance..... 358

Figure 78. Hausdorff distance between mesh pairs with little (a, b; Figure 73ab) and considerable (c, d; Figure 73ef) overlap when registered with the Markov random fields algorithm (MRF). Pseudo-colors represent near (red) to far (blue) Hausdorff distances. Gray color (b, d) represents the target mesh. Color bars show the color scale for the Hausdorff distance. .... 359

Figure 79. Performance of the best machine learning models developed to predict respiration rate of piglets from environmental variables. Data shown in order from high-to-low (top-to-bottom) testing mean squared error (MSE). Error bars represent standard error of the mean (SEM) for CV (5-folds) MSE. RPM: number of respirations per minute; CV: cross-validation; GAM: generalized additive model; SVM: support vector machine with radial basis function kernel; DL: deep learning with ReLU activation function; GBM: gradient boosted machine; OLS: ordinary least squares regression; RF: random forests; GP: Gaussian processes with radial basis function kernel; GLM: generalized linear regression model with elastic net regularization..... 362

Figure 80. Measured and predicted respiration rate using generalized additive model (a) and ordinary least squares regression (b).  $T_{\text{gnl},-100}$ : black-globe temperature, not exposed to the infrared lamp, measured 100 min. before recording respiration rate;  $T_{\text{gl},-180}$ : black-globe temperature, exposed to the infrared lamp, measured 180 min. before

recording respiration rate. 95% CI: predicted 95% confidence interval for the mean.  
.....364

Figure 81. Partial dependence plots for respiration rate predicted using support vector machines (SVM; a), deep learning (DL; b), gradient boosted machine (GBM; c), random forests (RF; d), Gaussian processes (GP; e), and generalized linear regression (GLM; f). These figures show a surface plot for the effects of changing time of measurement (x axis) and air temperature (y axis) in respiration rate (shown with color gradients and contours). The other predictors were changed accordingly to values predicted from time of measurement and air temperature using generalized additive models as described in Sec. 2.4. Numbers and lines in the surface plots indicate contour plots. Number and lines in (f) were constrained to the range [-100, 100] for clarity. White circles represent the location of measured training data points.....367

## LIST OF TABLES

|   |    |
|---|----|
| Table 1. Boundary and initial conditions for the problem in Figure 5. ....  | 37 |
| Table 2. Boundary and initial conditions for the problem geometry given in Figure 10.<br>.....  | 60 |
| Table 3. Blood perfusions values (Amri et al., 2011; Ng and Sudharsan, 2001) used in<br>the simulation to solve the breast tumor model (Figure 11).....   | 64 |
| Table 4. Number of nodes, results of minimum, average and maximum temperature,<br>computing time and memory space used in the mesh-independent test for the breast<br>tumor model.....  | 69 |
| Table 5. Definition of $L1$ and $L2, n$ for 1-D, 2-D, and 3-D. $L1$ is a measure of node<br>dimension and $L2, n$ is a measure of boundary $n$ dimension. ....  | 82 |
| Table 6. Definition of meshes for regular and irregular quadrangles and regular<br>hexahedrons. The meshes are defined in terms of number of nodes ( $\#N$ ), number of<br>ports ( $\#P$ ), and the angle ( $\theta$ ) between vectors $L2, n$ and $\ell n$ . ....  | 90 |
| Table 7. Definition of meshes for irregular hexahedrons and pyramids. The meshes are<br>defined in terms of number of nodes ( $\#N$ ), number of ports ( $\#P$ ), and the angle ( $\theta$ )<br>between vectors $L2, n$ and $\ell n$ . ....   | 92 |
| Table 8. Mesh independent test for the breast with tumor model. The data shown for<br>each mesh size is number of nodes, computing time and peak RAM memory use, and<br>minimum, average, and maximum temperature difference for the models without vs.<br>with $D = 30$ mm tumor when using regular and irregular hexahedrons as well as the |    |

|   |     |
|---|-----|
| angle ( $\theta$ ) between vectors $L2, n$ and $\ell n$ computed for irregular hexahedrons. ....  | 99  |
| Table 9. Traditional system parameters and distributions used to solve the mechanistic model. ....  | 123 |
| Table 10. Equations used to compute energy terms in Eq. (156). ....   | 135 |
| Table 11. Mean predicted optimum supplemental heat ( $H_{opt}$ , W) for piglets given air temperature ( $T_a$ , rows) and animal weight ( $w$ , columns). ....  | 148 |
| Table 12. Physical measurements of piglets. Values expressed in mean $\pm$ standard deviation (number of samples). ....   | 168 |
| Table 13. Irradiance of the supplemental heat. ....   | 169 |
| Table 14. Quantile of the residues obtained using linear regression approximation for Eqs. (211)-(208). ....  | 175 |
| Table 15. Computational times (in seconds) for training, evaluating performance, and obtaining predictions using machine learning algorithms. ....              | 176 |
| Table 16. Computational times (in seconds) to train and obtain predictions using ensemble learning algorithms. ....   | 177 |
| Table 17. Nomenclature table. ....  | 191 |
| Table 18. Traditional values and distributions for parameters related to the transmission-line modeling configuration, animal, blood, and the environment. .... | 207 |
| Table 19. Traditional values and distributions for parameters for muscle, skin, and fat layers. ....  | 210 |

|   |     |
|---|-----|
| Table 20. Traditional values and distributions for parameters for black and white hair-coat colors.....   | 213 |
| Table 21. Animal surface area model. Both hair-coat colors have the same model. Brody (1945) model was used for the set with traditional parameters (see Berman, 2005).....                         | 215 |
| Table 22. Respiratory system waveform multiplication factor. Both hair-coat colors have the same model. The constant waveform was used for the set with traditional parameters.....                 | 216 |
| Table 23. Respiration rate models. Both hair-coat colors have the same model. Maia et al. (2005a) model was used for the set with traditional parameters. ....                                      | 217 |
| Table 24. Tidal volume models. Both hair-coat colors have the same model. Maia et al. (2005a) model was used for the set with traditional parameters. ....  | 218 |
| Table 25. Expired air temperature models. Both hair-coat colors have the same model. Maia et al. (2005a) model was used for the set with traditional parameters. ....                               | 219 |
| Table 26. Respiratory system convection heat transfer models. Both hair-coat colors have the same model. Maia et al. (2008) model was used for the set with traditional parameters.....             | 219 |
| Table 27. Respiratory system evaporation heat transfer models. Both hair-coat colors have the same model. The first Maia et al. (2008) model was used for the set with traditional parameters. .... | 220 |
| Table 28. Models for the effect of the environment on the metabolic heat. Both hair-  |     |

|   |     |
|---|-----|
| coat colors have the same model. Pedersen and Sällvik (2002) model was used for the set with traditional parameters.....  | 221 |
| Table 29. Basal metabolic heat models. Both hair-coat colors have the same model. Pedersen and Sällvik (2002) model was used for the set with traditional parameters. ....  | 222 |
| Table 30. Milk production metabolic heat model. Both hair-coat colors have the same model. Pedersen and Sällvik (2002) model was used for the set with traditional parameters.....  | 223 |
| Table 31. Pregnancy metabolic heat model. Both hair-coat colors have the same model. Pedersen and Sällvik (2002) model was used for the set with traditional parameters.....  | 224 |
| Table 32. Sweating rate models. Each hair-coat color may have a different model. Collier et al. (2008) model was used for the set with traditional parameters. ....   | 225 |
| Table 33. Comparison between respiration rates measured using the device and counting the flank movement of the animals. ....   | 251 |
| Table 34. Hyperparameter space used to sample hyperparameters for training the machine learning algorithms. ....  | 273 |
| Table 35. Correlation coefficients, mean and standard error of the mean, and number of univariate outliers of the measured data. The number of outliers is displayed on the rightmost column, the mean and standard error of each data variable is displayed on the main diagonal of the table, and the correlation coefficients are displayed on the |     |

|  |     |
|--|-----|
| remaining entries of the table. No outliers were removed from training and testing datasets. ....  | 275 |
| Table 36. Hyperparameters of the best machine learning models.....   | 278 |
| Table 37. Confusion matrices and performance metrics (sensitivity, specificity, precision, and accuracy) of the statistical model developed to predict shade preference. Results shown for lambs, ewes, and both animals. .... | 318 |
| Table 38. Measured variables, sampling rates, and number of samples for the dataset obtained from the experiment performed with dairy-cows. ....   | 339 |
| Table 39. Experimental times that dairy cows were moved to the tie-stall barn and the time the pumps were turned on to circulate water through the waterbeds. Waterbeds were removed from the tie-stall barn after Day 6.....  | 340 |
| Table 40. Measured variables, sampling rates, and number of samples for the dataset obtained using piglets. ....   | 344 |

## LIST OF ABBREVIATIONS

|                |  |
|----------------|--|
| iid            | independent and identically distributed  |
| AIC            | Akaike information criterion   |
| ANOVA          | analysis of variance   |
| ARAP           | as-rigid-as-possible   |
| BIC            | Bayesian information criterion   |
| CI             | confidence interval; credible interval   |
| CNPq           | Brazilian National Council of Technological and Scientific Development   |
| CV             | cross-validation   |
| DL             | deep learning with ReLU activation function  |
| DNN            | deep neural networks (feedforward neural networks) with the ReLU activation function   |
| EDSM           | embedded deformation for shape manipulation  |
| EPE            | Brazilian governmental company for research on energy  |
| FAPESP         | São Paulo State Research Foundation  |
| FCAV/UNESP     | Faculty of Agricultural and Veterinary Sciences, State University of São Paulo   |
| FDM            | finite difference method   |
| FEM            | finite element method  |
| FFT            | fast Fourier transform   |
| FVM            | finite volume method   |
| GAM            | generalized additive models  |
| GB             | greedy search and bagging  |
| GBM            | gradient boosted machines  |
| GLM            | generalized linear regression model with elastic net regularization  |
| GO             | greedy search and optimum weights  |
| GP             | Gaussian processes   |
| HFAC           | Humane Farm Animal Care organization   |
| HFMM           | Hugo Fernando Maia Milan   |
| ICP            | iterative closest point algorithm  |
| ID             | isometric deformations   |
| INO BIO-MANERA | Innovation in Animal Biometeorology and Welfare Research Group   |
| LM             | ordinary linear regression model   |
| L.P.A.         | animal behavior, where L represents location (S: under the sun; P: under the shade from photovoltaic panels; C: under the shade from cloths), P represents posture (L: lying; S: standing), and A represents |

|                 |  |
|-----------------|--|
|                 | activity (G: grazing; R: ruminating; I: idling)  |
| MC              | set of system parameters drawn from Monte Carlo sampling method with minimum training MSE  |
| MCTIC           | Ministry of Science, Technology, Innovation and Communication of Brazil                    |
| MNOL            | minimum number of observations in a leaf   |
| MRF             | Markov random fields   |
| MSE             | mean squared error   |
| #N              | number of nodes  |
| NASA            | National Aeronautics and Space Administration  |
| NB              | naïve search and bagging   |
| NDS             | non-rigid depth scans  |
| NICP            | non-rigid ICP  |
| NO              | naïve search and optimum weights   |
| #N <sub>p</sub> | number of pyramidal nodes  |
| NSF             | National Science Foundation  |
| #N <sub>T</sub> | number of tetrahedral nodes  |
| NVS             | number of variables used in each split   |
| OLS             | ordinary least squares regression  |
| #P              | number of ports  |
| PLFBD           | precision livestock farming big data   |
| PROC GLM        | generalized least squares with the general linear model procedure of SAS                   |
| Proc.           | process  |
| RAM             | random access memory   |
| RB              | random search and bagging  |
| ReLU            | rectified linear unit function   |
| RF              | random forests   |
| RHL             | radiant heat load  |
| RO              | random search and optimum weights  |
| RPM             | respirations per minute  |
| RR              | respiration rate   |
| RRC             | respiration rate measured by counting flank movement                                       |
| RRD             | respiration rate measured by the developed device  |
| SAS             | Statistical Analysis System  |
| SEM             | standard error of the mean   |
| SHOT            | isometric deformations using the Signature of Histograms of Orientations (SHOT) descriptor |
| SS              | steady state   |

|      |  |
|------|--|
| SVM  | support vector machines  |
| THP  | total heat production  |
| TLM  | Transmission Line Modeling   |
| TM   | set with traditional parameter values and measured input data  |
| TP   | set with traditional parameters and expected input data predicted<br>using machine learning algorithms |
| UFAW | Universities Federation of Animal Welfare  |
| USDA | United States Department of Agriculture  |

## LIST OF SYMBOLS

|                    |  |
|--------------------|--|
| $a$                | intercept of the statistical model; absorption coefficient   |
| $a:b:c$            | series of values from $a$ to $c$ with step $b$   |
| $b_1$              | linear regression coefficient for air temperature  |
| $b_2$              | linear regression coefficient for relative humidity  |
| $b_3$              | linear regression coefficient for solar radiation  |
| $c$                | specific heat; gland specific heat; tumor specific heat  |
| $c_a$              | air specific heat  |
| $c_b$              | blood specific heat  |
| $(c_b \omega_b)_n$ | blood perfusion condition $n$  |
| $c_f$              | subcutaneous fat specific heat   |
| $d$                | diameter   |
| $d_g$              | black-globe diameter   |
| $d_p$              | days in pregnancy  |
| $e_{ijk}$          | residual term  |
| $e_{ijkLm}$        | residual term  |
| $f$                | user selected activation function  |
| $f_w$              | proportion of white hair-coat surface are  |
| $g$                | gravity  |
| $h$                | convective transfer coefficient; convective heat transfer coefficient  |
| $h_{panel}$        | link function for predicting probability of animals under the shade of solar panels                                  |
| $h_{sun}$          | link function for predicting probability of animals exposed to the sun   |
| $k$                | thermal conductivity; gland thermal conductivity; tumor thermal conductivity; number of $\Delta t$ in the simulation |
| $k_a$              | air thermal conductivity   |
| $k_{eff}$          | effective thermal conductivity of the hair-coat layer  |
| $k_f$              | fat thermal conductivity   |
| $k_{x'}$           | thermal conductivity in the direction perpendicular to the skin  |
| $k_{y'}$           | thermal conductivity in the direction parallel to the skin   |
| $\ell$             | log-likelihood function  |
| $\bar{\ell}_n$     | unit vector of the transmission-line $n$ point inwards the transmission-line node                                    |
| $n$                | number of samples; number of iterations; number of nodes   |
| $n_N$              | number of nodes  |
| $n_{SM}$           | fractional number of iterations (total equals to $n_{SM} \times n_N$ ) to solve the scattering multiplication matrix |
| $n_{SS}$           | number of iterations to solve the steady-state inversion matrix  |
| xliv               |  |

|              |   |
|--------------|---|
|              | equation  |
| $obj$        | objective function  |
| $p$          | Probability of the null hypothesis of a statistical test  |
| $p_{cloth}$  | probability of animals at the shade from cloth  |
| $p_{panel}$  | probability of animals at the shade from solar panels   |
| $p_{sun}$    | probability of animals exposed to the sun   |
| $q''$        | heat flux   |
| $q''_s$      | skin heat flux  |
| $q''_x$      | heat flux in the direction of the $x$ axis  |
| $q''_z$      | heat flux in the direction of the $z$ axis  |
| $q''_{An}$   | heat flux in the direction of the vector $\bar{A}_n$  |
| $kq''_{An}$  | heat flux in the direction of the vector $\bar{A}_n$ at time-step $k\Delta t$   |
| $kq''_{Ln}$  | heat flux at face $n$ in the direction of the vector $\bar{L}$ at time-step $k\Delta t$   |
| $q''_{LTn}$  | heat flux at face $n$ in the direction of the vector $\bar{L}_T$  |
| $kq''_{LTn}$ | heat flux at face $n$ in the direction of the vector $\bar{L}_T$ at time-step $k\Delta t$   |
| $tq''_n$     | heat flux in the direction of the transmission line $n$ at time $t$   |
| $q''_o$      | heat flux offset  |
| $q'''$       | Volumetric heat source; metabolic heat generation   |
| $q'''_{ext}$ | external heat generation  |
| $q'''_f$     | subcutaneous fat metabolic heat generation  |
| $q'''_g$     | gland metabolic heat generation   |
| $q'''_{met}$ | metabolic heat generation   |
| $t$          | time  |
| $u_a$        | is air velocity inside the brooder  |
| $w$          | weight of a piglet  |
| $x$          | position direction  |
| $x$          | vector of predictor variables   |
| $x_i$        | vector of predictor variables for sample $i$  |
| $y_i$        | predicted variable for sample $i$   |
| $z$          | elevation   |
| $A$          | animal surface area   |
| $\bar{A}$    | unit vector of an area  |
| $A_j(C_i)$   | random effect of the $j^{\text{th}}$ animal within the $i^{\text{th}}$ age group (if $i = \text{lamb}$ s, then $j = 1, \dots, 5$ ; if $i = \text{ewes}$ , then $j = 6, \dots, 11$ ) |
| $A_n$        | area of triangle $n$  |
| $\bar{A}_n$  | unit vector of area $n$   |
| $A_s$        | animal surface area   |
| $A_F/A_T$    | is cross-sectional area of hairs per unit area  |
| $A_T$        | triangular area   |

|                  |   |
|------------------|---|
| $C_d$            | capacitance per unit length   |
| $C_{dn}$         | capacitance per unit length of transmission-line $n$  |
| $C_i$            | fixed effect of the $i^{\text{th}}$ age group ( $i = \text{lamb or ewe}$ )  |
| $D$              | tumor diameter; diameter of a piglet; diffusivity   |
| $D_a$            | air thermal diffusivity   |
| $D_k$            | random effect of the $k^{\text{th}}$ day of observation ( $k = 1, \dots, 5$ )   |
| $D_k A_j(C_i)$   | interaction between the random effect of the $k^{\text{th}}$ day of observation within the random effect of the $j^{\text{th}}$ animal within the $i^{\text{th}}$ age group |
| $E_n$            | exponential integral of order $n$   |
| $E_F$            | energy from feed  |
| $E_G$            | energy available for growth   |
| $E_L$            | latent heat production  |
| $E_{Mai}$        | energy required for maintenance   |
| $E_{Met}$        | energy from metabolism  |
| $E_P$            | energy available for production   |
| $E_R$            | energy available for reproduction purposes  |
| $E_S$            | sensible heat production  |
| $G$              | conductance connected in parallel with the transmission-line node   |
| $G_r$            | Grashof number  |
| $H$              | height; gland thickness; supplemental heat for piglets  |
| $HD$             | hair density  |
| $H_D$            | hair diameter   |
| Heat             | intensity of supplemental heat  |
| $HL$             | hair length   |
| $H_L$            | hair length   |
| $H_{\text{opt}}$ | optimum supplemental heat for piglets   |
| $H_k$            | fixed effect of the $k^{\text{th}}$ hour class  |
| $H_{nm}$         | hidden neuron $m$ of hidden layer $n$   |
| $H_R$            | relative humidity   |
| $I_B$            | electric current at the boundary node   |
| $I_n$            | input neuron $n$  |
| $I_n$            | current flowing from port $n$ towards the center of the transmission-line node  |
| $I_S$            | current source connected in parallel with the transmission-line node  |
| $J$              | Irradiance inside the brooder   |
| $L$              | number of individual learners   |
| $L$              | length; side lengths  |
| $\bar{L}$        | unit vector of a triangle edge  |
| $L_l$            | measure of node dimension; sum of the magnitude of the linear   |

|                  |   |
|------------------|---|
|                  | coefficients in GLM   |
| $L_2$            | measure of node dimension; sum of the square of the magnitude of the linear coefficients in GLM |
| $L_{2,n}$        | measure of boundary $n$ dimension   |
| $\vec{L}_{2,n}$  | unitary vector perpendicular to $L_{2,n}$   |
| $L_d$            | inductance per unit length  |
| $L_{dn}$         | inductance per unit length of transmission-line $n$   |
| $L_f$            | thickness of fat  |
| $L_h$            | hair-coat thickness   |
| $L_m$            | thickness of muscle   |
| $L_{mean}$       | mean value of $L$   |
| $L_n$            | length of edge $n$ of a triangle  |
| $L_s$            | thickness of skin   |
| $L_t$            | latitude  |
| $\vec{L}_T$      | unit vector perpendicular to a triangle edge, pointing inwards                                  |
| $L_{Tn}$         | unit vector perpendicular to the triangle edge $n$ , pointing inwards                           |
| $M$              | milk production   |
| $M_i$            | fixed effect of the $i^{th}$ method (device or counting)  |
| $(MA)_{ij}$      | interaction of the $i^{th}$ method with the $j^{th}$ animal                                     |
| $(MH)_{ik}$      | interaction between the $i^{th}$ method with the $k^{th}$ hour class                            |
| MSE              | mean squared error  |
| $N$              | number of samples   |
| $N(\mu, \sigma)$ | normal distribution with mean $\mu$ and standard deviation $\sigma$                             |
| $N_h$            | density of hairs  |
| $Nu$             | Nusselt number  |
| $Nu^F$           | Nusselt number for forced convection  |
| $Nu^N$           | Nusselt number for natural convection   |
| $O$              | output neuron   |
| $P$              | power output of the photovoltaic panels   |
| $P_a$            | air pressure  |
| $P_r$            | Prandtl number  |
| $Q$              | heat  |
| $R^2$            | coefficient of determination  |
| $R^2_{adj}$      | adjusted coefficient of determination   |
| $R_c$            | resistance for convection heat transfer   |
| $R_e$            | Reynolds number   |
| $R_n$            | resistance connected in series with transmission-line $n$                                       |
| RH               | relative humidity inside the brooder  |
| $R_L$            | fixed effect of the $L^{th}$ class of solar radiation ( $<200$ ; $200 \leq R_s < 300$ ;         |

$300 \leq R_s < 400$ ;  $400 \leq R_s < 500$ ;  $500 \leq R_s < 600$ ;  $600 \leq R_s < 700$ ;  $700 \leq R_s < 800$  and  $R_s \geq 800$  W m<sup>-2</sup>)

|               |  |
|---------------|--|
| $RR$          | respiration rate   |
| $R_s$         | solar radiation  |
| $S(a)$        | step function, defined as 1 when $a$ is positive and 0 otherwise                     |
| $SR$          | sweating rate  |
| $T$           | temperature  |
| $T$           | temperature  |
| $T_a$         | air temperature inside the brooder   |
| $T_{a,eq}$    | equivalent air temperature, defined as $q''_s(T_{a,eq}, 0) = q''_s(T_a, H)$          |
| $T_{a,in}$    | air temperature including the effect of supplemental heat                            |
| $T_{a,pen}$   | air temperature inside the pen   |
| $T_{avg}$     | average temperature  |
| $T_b$         | blood temperature  |
| $T_c$         | core temperature   |
| ${}_k T_c$    | temperature in the center of the transmission-line node at time-step $k\Delta t$     |
| ${}_k T_{cn}$ | temperature in the center of the transmission-line node $n$ at time-step $k\Delta t$ |
| $T_{exp}$     | expired air temperature  |
| $T_{fat}$     | subcutaneous fat thickness   |
| $T_g$         | black-globe temperature inside the brooder   |
| $T_h$         | hair-coat surface temperature  |
| Time          | time of measurement at surface $j$ for data point $i$                                |
| $T_{j,e,i}$   | ensemble temperature prediction  |
| $T_{j,l}$     | temperature at surface $j$ estimated by learner $l$                                  |
| $T_{max}$     | maximum temperature  |
| $T_{min}$     | minimum temperature  |
| $T_o$         | temperature offset   |
| ${}_k T_p$    | temperature in the transmission-line port at time-step $k\Delta t$                   |
| ${}_k T_{pn}$ | temperature in the transmission-line port $n$ at time-step $k\Delta t$               |
| $T_r$         | rectal temperature   |
| $T_s$         | skin surface temperature   |
| $T_z$         | thickness  |
| $T_A$         | air temperature  |
| $T_B$         | temperature at the boundary node; convective boundary temperature                    |
| $T_F$         | thickness of subcutaneous fat  |
| $T_G$         | black-globe temperature  |
| $T_{MR}$      | mean radiant temperature   |

|                       |   |
|-----------------------|---|
| $T_{\infty}$          | boundary temperature for an analytical problem  |
| $U(a, b)$             | Uniform real distribution from $a$ to $b$   |
| $\mathcal{U}(a, b)$   | uniform random distribution from $a$ to $b$   |
| $\mathcal{U}_d(a, b)$ | uniform discrete random distribution from $a$ to $b$  |
| $U_I(a, b)$           | Uniform integer distribution from $a$ to $b$  |
| $U_R(a, b)$           | Uniform real distribution from $a$ to $b$   |
| $U_V$                 | ultraviolet solar radiation (spectral range = 0.28 – 0.4 $\mu\text{m}$ )  |
| $V$                   | voltage   |
| $V_c$                 | voltage in the center of the transmission-line node   |
| ${}_k V_c$            | voltage in the center of the transmission-line node at time-step $k\Delta t$  |
| $V_{cn}$              | voltage in the center of the transmission-line node $n$   |
| ${}_k V_p$            | voltage in the transmission-line port at time-step $k\Delta t$  |
| $V_{pn}$              | voltage in port $n$ of the transmission-line node   |
| $V_n^i$               | voltage incident on transmission-line $n$   |
| ${}_k V_n^i$          | voltage incident on transmission-line $n$ at time-step $k\Delta t$  |
| $V_n^r$               | voltage reflected from transmission-line $n$  |
| ${}_k V_n^r$          | voltage reflected from transmission-line $n$ at time-step $k\Delta t$   |
| $V_t$                 | tidal volume  |
| $V_B$                 | voltage at the boundary node  |
| $V_T$                 | volume of tetrahedron   |
| $W$                   | matrix of weights; animal weight  |
| $Weibull(a, b)$       | Weibull distribution (a long tail distribution), with shape parameter $a$ and scale parameter $b$   |
| $W_S$                 | wind speed  |
| $X_n^2$               | Chi-squared distribution with $n$ degrees   |
| $Y_{ijk}$             | respiration rate observed in the hour class $k^{th}$ , in animal $j^{th}$ , and by method $i^{th}$  |
| $Y_{ijkLm}$           | $m^{th}$ observation of the behavioral activity (expressed in percentage, with a logarithmic transformation) in the age group $i^{th}$ (lambs or ewes), in animal $j^{th}$ , day $k^{th}$ , and $L^{th}$ level of solar radiation |
| $Z_n$                 | impedance of transmission-line $n$  |
| $\alpha$              | distributes penalty between $L_1$ and $L_2$ norms of the regression coefficients; intercept   |
| $\alpha_{i,j}$        | intercept for location $i$ (underneath or outside the structure) and structure $j$ (panel or cloth)   |
| $\alpha_{lamb}$       | additive effects for lambs  |
| $\beta$               | vector of regression coefficients; intercept  |
| $\beta_0$             | intercept coefficient   |
| $\beta_{lamb}$        | additive effects for lambs  |

|                      |   |
|----------------------|---|
| $\gamma$             | hyperparameter of the SVM model   |
| $\gamma_{ewe}$       | standard deviation of the random effect of the ewes   |
| $\gamma_{lamb}$      | standard deviation of the random effect of the lambs  |
| $\delta$             | Laminar boundary thickness  |
| $\varepsilon$        | hyperparameter of the ADADELTA optimization framework; residue  |
| $\eta_l$             | weight of learner l   |
| $\eta_n$             | convergence parameter for the TLM applied to transmission-line n  |
| $\theta$             | vector of offsets   |
| $\theta_n$           | angle between $\bar{\ell}_n$ and $\bar{L}_T$ ; angle between $\bar{\ell}_n$ and $\bar{A}$ ; angle between $\vec{\ell}_n$ and $\vec{L}_{2,n}$        |
| $\theta_p$           | angle $\theta$ for pyramidal nodes  |
| $\theta_T$           | angle $\theta$ for tetrahedral nodes  |
| $\lambda$            | wavelength; severity of elastic net penalty applied on GLM; tradeoff between minimizing MSE and maximizing $\ell$ ; hyperparameter of the SVM model |
| $\lambda(T)$         | Latent heat of vaporization at temperature $T$ : 2,500.7879 - 2.3737T   |
| $\mu$                | overall mean  |
| $\nu_a$              | air kinematic viscosity   |
| $\xi_n$              | convergence parameter for the TLM applied to transmission-line n  |
| $\rho$               | hyperparameter of the ADADELTA optimization framework   |
| $\rho$               | density; gland density; tumor density   |
| $\rho_a$             | air density   |
| $\rho_b$             | blood density   |
| $\rho_f$             | subcutaneous fat density  |
| $\rho_{\alpha\beta}$ | reflection coefficient from port $\alpha$ to port $\beta$   |
| $\sigma$             | Stefan-Boltzmann constant; standard deviation; standard deviation of the residues   |
| $\sigma_d$           | standard deviation of the random effect of the day $d$  |
| $\sigma_{day}$       | standard deviation of the random effect of the day  |
| $\sigma_{ewe}$       | standard deviation of the random effect of the ewes   |
| $\sigma_{i,j,d}$     | standard deviation of the random effect of the location $i$ within the structure $j$ within the day $d$   |
| $\sigma_{j,e,i}^2$   | variance of the ensemble temperature prediction at surface $j$ for data point $i$   |
| $\sigma_{lamb}$      | standard deviation of the random effect of the lambs  |
| $\tau$               | average hairs spacing   |
| $\tau_{\alpha\beta}$ | transmission coefficient from port $\alpha$ to port $\beta$   |
| $\varphi$            | additional proportion of convection heat flux at the surface of the skin; correlation coefficient for temporal correlation                          |

|                  |  |
|------------------|--|
| $\omega$         | proportion of convection heat transfer at the surface of the hair-coat |
| $\omega_b$       | blood perfusion  |
| $\omega_{blood}$ | Blood perfusion  |
| $\Delta \ell_n$  | length of transmission-line $n$  |
| $\Delta t$       | temporal discretization  |
| $\Psi(T)$        | Saturated vapor density at temperature T                               |

### Subscripts

|                   |   |
|-------------------|---|
| $\square_a$       | Denotes a variable of the air                             |
| $\square_A$       | Denotes a variable for the animal                         |
| $\square_b$       | Denotes a variable for the black hair-coat                |
| $\square_{blood}$ | Denotes a variable for the blood                          |
| $\square_c$       | Denotes a variable for the core of the animal             |
| $\square_{ce}$    | Denotes a variable for cutaneous evaporation              |
| $\square_{evap}$  | Denotes a variable for evaporation                        |
| $\square_{conv}$  | Denotes a variable for convection                         |
| $\square_{end}$   | Denotes a variable at a specific end time                 |
| $\square_f$       | Denotes a variable for the fat                            |
| $\square_h$       | Denotes a variable for the surface of the hair-coat       |
| $\square_{ht}$    | Denotes a variable for heat transfer                      |
| $\square_i$       | Denotes a variable at the internal boundary of the model  |
| $\square_{ini}$   | Denotes a variable at a specific initial time             |
| $\square_{itm}$   | Denotes a variable for the internal tissue metabolic heat |
| $\square_m$       | Denotes a variable for the muscle                         |
| $\square_{mes}$   | Denotes the measured value of a variable                  |
| $\square_{met}$   | Denotes a variable for the metabolism                     |
| $\square_p$       | Denotes the predicted value of a variable                 |
| $\square_r$       | Denotes a variable for the respiratory system             |
| $\square_s$       | Denotes a variable at the surface of the skin             |
| $\square_{sk}$    | Denotes a variable for the skin                           |
| $\square_v$       | Denotes a variable for vapor mass transfer                |
| $\square_w$       | Denotes a variable for the white hair-coat                |

## PREFACE

The objective of this dissertation was to develop methods to predict bioenergetic responses of homoeothermic animals. The two main motivations for predicting bioenergetic responses of livestock are 1) the need to sustainably increase food production by 25-70% up to 2050 (Hunter et al., 2017) and 2) to develop systems to ameliorate the negative effects of heat stress on livestock, which costs more than \$3 billion to American farmers every year (Ferreira et al., 2016; St-Pierre et al., 2003).

Global population will reach nearly 10 billion in 2050 (United Nations, 2019). This surge of about 3 billion people, in conjunction with the increased global wealth (driving up the per-capita consumption of animal products; Alexandratos and Bruinsma, 2012; Milford et al., 2019), calls for a sustainable growth of food production by 25-70% (Hunter et al., 2017). Of special importance are current livestock farming practices, which possess a high environmental cost (McAlpine et al., 2009) through emission of greenhouse gases (Tilman and Clark, 2014) and high demands on land, water, energy, and other natural resources (Pelletier and Tyedmers, 2010).

To reduce the high environmental costs of livestock farming practices, new technology to precisely manage livestock are being developed. These new approaches of precision livestock farming (or digital agriculture) can be characterized as paradigm shifts, focused on developing technologies to monitor and farm each animal

individually, assisting in performing timely interventions based on the demands and health status of animals. These new technologies demand fast bioenergetic methods that can provide accurate predictions of the health status and thermal comfort of animals and, using these predictions, assist in optimizing their environment.

The huge \$3 billion cost of heat stress comes from its negative effects (Bernabucci et al., 2014; Kadzere et al., 2002), which include decreased production (West, 2003) and welfare (Polsky and von Keyserlingk, 2017; Silanikove, 2000) as well as increased health risks (Bernabucci et al., 2010) and production costs (Ferreira et al., 2016; St-Pierre et al., 2003). Animals exposed to heat-stressful environments cannot dissipate their internal energy (Collier and Gebremedhin, 2015). To allow animals to dissipate their internal energy and to mitigate the negative effects of heat-stress, farmers provide heat reduction systems, such as shades (Maia et al., 2020; Schütz et al., 2010), ventilation (Turner et al., 1992), sprinklers (Chen et al., 2015; Turner et al., 1992), and conductive cooling (Ortiz et al., 2015; Perano et al., 2015). The most challenging decision for farmers is to determine which of these systems is more appropriate for the animals, given their productive performance and the environmental conditions of the region of the farm. Bioenergetic models provide insights that can help farmers decide which heat reduction system to use.

The main limitations of existing bioenergetic models are 1) lack of providing uncertainty measures for the predictions and 2) the assumption of steady-state, although experimental data suggests a strong time-dependence of bioenergetic

responses on previous environmental conditions (Gaughan et al., 2000). The limitation with providing uncertainty measure is likely because bioenergetic models are based on fundamentals. Fundamental models are designed to provide precise predictions, not uncertainty measures, given model parameters and environmental conditions. The main issue with providing dynamic predictions of bioenergetic responses are likely the high computational costs (computational time and RAM memory requirements) of numerical methods classically used in our field. These methods (e.g., finite element method, FEM, finite difference method, FDM, and finite volume method, FVM) are based on matrix inversion computations, which possess high computational costs. To the best of our knowledge, only one study has included time-dependence effects on predictions of bioenergetic responses of beef cattle (Turner et al., 1987ab).

To solve the limitations of existing bioenergetic models, we developed integrated models and the transmission-line modeling (TLM) computational method to predict bioenergetic responses of livestock. Our integrated model (Milan et al., 2019) combined fundamental models (analytical and numerical), machine learning models, bioheat transfer, Monte Carlo optimization method, ensemble learning techniques, energy conservation of biological objects, and bootstrapping. The combination of these techniques allowed the development of models that predict bioenergetic responses as well as their uncertainties. The TLM is a numerical method that solves partial differential equations in the time and space domains. Differently from other numerical methods, the advance in time is modelled implicitly with the TLM, leading

to highly sparse matrix computations (instead of time-consuming matrix inversions). Hence, TLM bioenergetic models are capable of providing fast dynamic predictions of bioenergetic responses of homoeothermic animals.

### **Organization of the dissertation**

This dissertation consists of 9 chapters (or papers; first author in 7 papers). The first 5 chapters involve the development of bioenergetic models. The last 4 chapters are complimentary research related to this study.

#### CHAPTER 1: TRIANGULAR NODE FOR TRANSMISSION-LINE MODELING (TLM) APPLIED TO BIO-HEAT TRANSFER

Our study with the TLM started in 2014 (Milan et al., 2014), when we improved the theory of the TLM to solve for graded meshes in 1-D, 2-D, and 3-D. The limitation with this formulation was that it did not allow for irregular elements in 2-D or 3-D. In this paper, we improved the TLM theory to allow for triangular representations in 2-D (Milan and Gebremedhin, 2016a), which allowed to better represent complex geometries in 2-D. The accuracy of this new formulation was better than 1%.

#### CHAPTER 2: TETRAHEDRAL NODE FOR TRANSMISSION-LINE MODELING (TLM) APPLIED TO BIO-HEAT TRANSFER

The TLM formulation was expanded for tetrahedral representations in 3-D (Milan and Gebremedhin, 2016b), which allowed for a better representation of complex

geometries in 3-D. We showed that TLM computations were 1,550 faster than analytical solutions of time-domain bioheat propagations (based on the truncation of an infinite series solution) while maintaining an accuracy better than 2%.

### CHAPTER 3: GENERAL NODE FOR TRANSMISSION-LINE MODELING (TLM) METHOD APPLIED TO BIO-HEAT TRANSFER

Our previous three formulations (Milan et al., 2014; Milan and Gebremedhin, 2016ab) were disconnected. In this study (Milan and Gebremedhin, 2018), we developed a general TLM theory that combined not only our previous 3 formulations but also other 6 formulations proposed by other studies in one general theory for the TLM method applied to bio-heat transfer. This new formulation allows for representing complex geometries in any dimension (Milan and Gebremedhin, 2018).

### CHAPTER 4: PREDICTION OF OPTIMUM SUPPLEMENTAL HEAT FOR PIGLETS

In this paper, we developed the first interconnected bioenergetic model (Milan et al., 2019). The main limitation with fundamental models (e.g., the TLM) is their inability of providing uncertainty measures, which can be obtained using machine learning techniques. The main limitation with using machine learning models to predict bioenergetics is that, for regions outside the training data, their predictions might violate conservation equations (e.g., predicting that animals would be more comfortable in high heat-stressful conditions; Gorczyca et al., 2018). To solve these

limitations, we developed the first integrated model (Milan et al., 2019), integrating fundamental models (analytical and numerical), machine learning models, bioheat transfer, Monte Carlo optimization method, ensemble learning techniques, energy conservation of biological objects, and bootstrapping. The integration of these techniques resulted in the second most accurate bioenergetic model reported in the literature, with prediction errors within 3.04% and 2.09% for skin and hair-coat surface temperatures, respectively. Most importantly, the prediction did not violate conservation equations and allowed for prediction of the optimum supplemental heat for piglets given their age and environmental conditions.

## CHAPTER 5: PREDICTION OF BIOENERGETIC RESPONSES OF DAIRY-COWS USING THE TRANSMISSION-LINE MODELING (TLM) METHOD

In this paper, we developed the first dynamic model to predict bioenergetic responses of dairy-cows (Milan and Gebremedhin, 2020). The model predicts temperatures (e.g., internal, skin surface, and hair-coat surface), heat fluxes (e.g., internal, skin surface, hair-coat surface, convection, and radiation), metabolic heat flux, respiratory variables (respiration rate, tidal volume, expired air temperature), respiratory heat transfer (evaporation and convection), sweating rate, and cutaneous evaporation. The TLM was used to model two 1-D mediums composed of muscle, fat, skin, and hair-coat layers. The main difference between the two mediums is the color of the hair-coat (black vs. white). The model incorporates heat exchange through metabolism,

respiratory ventilation, sweating, convection, and radiation. The parameters of the model were optimized using Monte Carlo optimization method to improve the accuracy in predicting skin and hair-coat surfaces temperatures, which resulted in prediction accuracy better than 5%.

## CHAPTER 6: TECHNICAL NOTE: DEVICE FOR MEASURING RESPIRATION RATE OF CATTLE UNDER FIELD CONDITIONS

The respiration rate is the first visible response to heat stress (Gaughan et al., 2000) and is commonly used by farmers to assess the thermal comfort of their animals. Previously to our device (Milan et al., 2016), the only practical way of measuring the respiration rate was through a highly trained observer near the animal, which is time-consuming, labor-intensive, and not-scalable. Our patented device (Maia and Milan, 2015, 2016) addresses these issues and can provide real-time information of the health status of the livestock (Milan et al., 2016).

## CHAPTER 7: MACHINE LEARNING ALGORITHMS TO PREDICT CORE, SKIN, AND HAIR-COAT TEMPERATURES OF PIGLETS

In this paper, we were the first to develop machine learning models to predict physiological temperatures of livestock (Gorczyca et al., 2018). The machine learning models developed to predict physiological temperatures of piglets are the most accurate models described in the literature, with errors of 0.36% for rectal temperature, 0.62% for skin surface temperature, and 1.35% for hair-coat surface

temperature.

## CHAPTER 8: PHOTOVOLTAIC PANELS AS SHADING RESOURCES FOR LIVESTOCK

Intense solar irradiation (da Silva and Maia, 2013), such as those observed in tropical regions, heat stresses livestock. For this environmental condition, one simple strategy farmers adopt to increase animal welfare and comfort is to provide shades. However, shading structures can be expensive. Hence, I designed shading structures for livestock using photovoltaic panels (Milan, 2015), which have the potential to generate electricity for the farm and increase the profit of farming. We observed that livestock unconditionally preferred shade from photovoltaic panels over the traditional 80%-blockage cloth, likely because photovoltaic panels block 100% of solar irradiation (Maia et al., 2020). In addition, the installation cost of the shading structures is paid off in approximately 8 of their expected 25 years of operation.

## CHAPTER 9: PRECISION LIVESTOCK FARMING BIG DATA: PLFBD

We are providing the first publicly available big data for precision livestock farming (Milan et al., 2020). The field of precision livestock farming is advancing quickly through recent advances in machine learning and computer vision algorithms. One issue with applying machine learning and computer vision algorithms to problems in digital agriculture is that they can produce counterintuitive predictions (which might violate conservation laws and established research findings) when the dataset is small

or has few predictor variables (Gorczyca et al., 2018; Milan et al., 2019). This issue may be resolved by using big data.

In precision livestock farming, researchers have demonstrated the capability to collect big data (e.g., EU-PLF, Guarino et al., 2017), but this process is challenging, time-consuming, expensive, and labor intensive. Sharing big data for precision livestock farming can reduce the need for many researchers to collect data as well as facilitate data aggregation from diverse sources. For example, data sharing has driven advances in other fields (Huffman et al., 1997) and data sharing supports the development of sophisticated models with strong predictive performance (Hastie et al., 2008). With these motivations, we are providing the first publicly available big data for precision livestock farming (Milan et al., 2020).

## **Conclusion**

The following conclusions can be drawn from this dissertation:

- Integrated models to predict bioenergetic responses of livestock were developed.
- Integrated models allow for providing uncertainty measures of the predictions with high accuracy (prediction errors within 3.04% and 2.09% for skin and hair-coat surface temperatures).
- The TLM method was developed to predict bioenergetic responses.

- The TLM bioenergetic method allows for providing accurate (within 5% for skin and hair-coat surface temperatures) dynamic predictions of bioenergetic responses.

### **Future studies**

The bioenergetic models developed herein were in 1-D. This reduction in complexity was necessary to allow for reasonable computational times of the models (which lasted for weeks in some cases). Future work could develop models in 2-D and 3-D, better capturing the complexity of the geometry of livestock, but they will likely require the development of faster methods to allow for practical computational times.

Farmers need specific data (nutritional, thermal stress level, health status, reproduction status, etc.) of each cow to make individual cow decisions and intervene as appropriate before major negative effects occur. However, all bioenergetic models reported in the literature are population models, providing predictions for a population of livestock (or for an “average animal”). To address this limitation, individual bioenergetic models could be developed in the future. This new class of models would allow for providing predictions specific for each and every animal in a farm.

## REFERENCES

- Alexandratos N, Bruinsma J. *World Agriculture Towards 2030/2050: the 2012 Revision*. Food and Agriculture Organization of the United Nations. ESA Working Paper no. 12-03. United Nations, New York, NY, 2012.
- Bernabucci U, Biffani S, Buggiotti L, Vitali A, Lacetera N, Nardone A. The effects of heat stress in Italian Holstein dairy cattle. *J Dairy Sci* 97:471-486, 2014.
- Bernabucci U, Lacetera N, Baumgard LH, Rhoads RP, Ronchi B, Nardone A. Metabolic and hormonal acclimation to heat stress in domesticated ruminants. *Animal* 4:1167-1183, 2010.
- Chen JM, Schütz KE, Tucker CB. Cooling cows efficiently with sprinklers: physiological responses to water spray. *J Dairy Sci* 98:6925-6938, 2015.
- Collier RJ, Gebremedhin KG. Thermal biology of domestic animals. *Ann Rev Anim Biosci* 3:513-532, 2015.
- da Silva RG, Maia ASC. *Principles of animal biometeorology*. Springer, New York, 2013.
- Ferreira FD, Gennari RS, Dahl GE, De Vries A. Economic feasibility of cooling dry cows across the United States. *J Dairy Sci* 99:9931-9941, 2016.
- Gaughan JB, Holt SM, Hahn GL, Mader TL, Eigenberg R. Respiration rate – is it a

good measure of heat stress in cattle? *Asian-Aus J Anim Sci* 13(C):329-332, 2000.

Guarino M, Norton T, Berckmans D, Vranken E, Berckmans D. A blueprint for developing and applying precision livestock farming tools: a key output of the EU-PLF project. *Anim Front* 7(1):12-17, 2017

Gorczyca MT, Milan HFM, Maia ASC, Gebremedhin KG. Machine learning algorithms to predict core, skin, and hair-coat temperatures of piglets. *Comput Electron Agric* 151:286-294, 2018.

Hastie T, Tibshirani R, Friedman J. *The Elements of Statistical Learning: Data Mining, Inference, and Prediction* (2nd ed.). New York: Springer, 2008.

Huffman GJ, Adler RF, Arkin P, Chang A, Ferraro R, Gruber A, Janowiak J, McNab A, Rudolf B, Schneider U. *The Global Precipitation Climatology Project (GPCP) Combined Precipitation Dataset*. Bulletin of the American Meteorological Society, 78(1), 5-20, 1997.

Hunter MC, Smith RG, Schipanski ME, Atwood LW, Mortense DA. Agriculture in 2050: recalibrating targets for sustainable intensification. *BioScience* 67(4):386-391, 2017.

Kadzere CT, Murphy MR, Silanikove N, Maltz E. Heat stress in lactating dairy cows: a review. *Lives Prod Sci* 77:59-91, 2002.

Maia ASC, Milan HFM. RR *Respiratory rate – respiration rate of large animals in*  
12

*field conditions [Portuguese]*. Patent number BR512016000418-5, 2015.

Maia ASC, Milan HFM. *System and method to indirect measure the respiration rate of animals [Portuguese]*. Patent number BR1020160118794, 2016.

Maia ASC, Culhari EA, Fonsêca VFC, Milan HFM, Gebremedhin KG. Photovoltaic panels as shading resources for livestock. *In Preparation*, 2020.

McAlpine CA, Etter A, Fearnside PM, Seabrook L, Laurance WF. Increasing world consumption of beef as a driver of regional and global change: a call for policy action based on evidence from Queensland (Australia), Colombia and Brazil. *Global Environ Chang* 19:21-33, 2009.

Milan HFM. *Design of shading structures for livestock using photovoltaic panels [Portuguese]*. Engineering Council of São Paulo State, Brazil. Project number 92221220150819429, 2015.

Milan HFM, Carvalho Jr CAT, Maia ASC, Gebremedhin KG. Graded meshes in bio-thermal problems with transmission-line modeling method. *J Therm Biol* 45:43-53, 2014.

Milan HFM, Maia ASC, Gebremedhin KG. Technical note: Device for measuring respiration rate of cattle under field conditions. *J Anim Sci* 94(12):5434-5438, 2016.

Milan HFM, Gebremedhin KG. Triangular node for Transmission-Line Modeling (TLM) applied to bio-heat transfer. *J Therm Biol* 62:116-122, 2016a.

Milan HFM, Gebremedhin KG. Tetrahedral node for Transmission-Line Modeling (TLM) applied to Bio-heat Transfer. *Comp Biol Med* 79:243-249, 2016b.

Milan HFM, Gebremedhin KG. General node for transmission-line modeling (TLM) method applied to bio-heat transfer. *Int J Numer Model* 31:e2455, 2018.

Milan HFM, Maia ASC, Costa CCM, Perano KM, Gorczyca MT, Moura GAB, Castro PA, Fonsêca VFC, Hariharan B, Chiquitelli Neto M, Gebremedhin KG. Precision livestock farming big data: PLFBD. *In Preparation*, 2020.

Milan HFM, Gebremedhin KG. Prediction of bioenergetics of dairy-cows using the transmission-line modeling method. *In Preparation*, 2020.

Milford AB, Le Mouël C, Bodirsky BL, Rolinski S. Drivers of meat consumption. *Appetite* 141:10431, 2019.

Ortiz XA, Smith JF, Rojano F, Choi CY, Bruer J, Steele T, Schuring N, Allen J, Collier RJ. Evaluation of conductive cooling of lactating dairy cows under controlled environmental conditions. *J Dairy Sci* 98:1759-1771, 2015.

St-Pierre NR, Cobanov B, Schnitkey G. Economic losses from heat stress by US livestock industries. *J Dairy Sci* 86:E52-E77, 2003.

Pelletier N, Tyedmers P. Forecasting potential global environmental costs of livestock production 2000-2050. *PNAS* 107:18371-18374, 2010.

Perano KM, Usack JG, Angenent LT, Gebremedhin KG. Production and physiological responses of heat-stressed lactating dairy cattle to conductive cooling. *J Dairy Sci* 98:5252-5261, 2015.

Polsky L, von Keyserlingk MAG. Invited review: effects of heat stress on dairy cattle welfare. *J Dairy Sci* 100:8645-8657, 2017.

Schütz KE, Rogers AR, Poulouin YA, Cox NR, Tucker CB. The amount of shade influences the behavior and physiology of dairy cattle. *J Dairy Sci* 93:125-133, 2010.

Silanikove N. Effects of heat stress on the welfare of extensively managed domestic ruminants. *Lives Prod Sci* 67:1-18, 2000.

Tilman D, Clark M. Global diets link environmental sustainability and human health. *Nature* 515:518-522, 2014.

Turner LW, Blandford GE, Loewer OJ, Taul KL. Finite element model of heat transfer in the bovine. Part 1: theory. *Trans ASAE* 30(3):768-774, 1987a.

Turner LW, Loewer OJ, Taul KL, Munifering RB, Gay N. Finite element model of heat transfer in the bovine. Part 2: validation. *Trans ASAE* 30(3):775-781, 1987b.

Turner LW, Chastain JP, Hemken RW, Gates RS, Crist WL. Reducing heat stress in dairy cows through sprinklers and fan cooling. *Appl Eng Agric* 8(2):251-256, 1992.

United Nations, Department of Economic and Social Affairs, Population Division.

*World Population Prospects 2019: Ten Key Finds.* United Nations, New York, NY,  
2019.

CHAPTER 1: TRIANGULAR NODE FOR TRANSMISSION-LINE MODELING  
(TLM) APPLIED TO BIO-HEAT TRANSFER

Hugo Fernando Maia Milan, Kifle G. Gebremedhin

Published in *Journal of Thermal Biology*: Milan HFM, Gebremedhin KG. Triangular node for transmission-line modeling (TLM) applied to bio-heat transfer. *J Therm Biol* 62:116-122, 2016.

***Abstract***

Transmission-Line Modeling (TLM) is a numerical method used to solve complex and time-domain bio-heat transfer problems. In TLM, rectangles are used to discretize two-dimensional problems. The drawback in using rectangular shapes is that instead of refining only the domain of interest, a large additional domain will also be refined in the x and y axes, which results in increased computational time and memory space. In this paper, we developed a triangular node for TLM applied to bio-heat transfer that does not have the drawback associated with the rectangular nodes. The model includes heat source, blood perfusion (advection), boundary conditions and initial conditions. The boundary conditions could be adiabatic, temperature, heat flux, or convection. A matrix equation for TLM, which simplifies the solution of time-domain problems or solves steady-state problems, was also developed. The predicted results were compared against results obtained from the solution of a simplified two-dimensional problem, and they agreed within 1% for a mesh length of triangular faces of  $59 \mu\text{m} \pm 9$

$\mu\text{m}$  (mean  $\pm$  standard deviation) and a time step of 1 ms.

**Keywords:** Bio-heat equation, Triangular node, Pennes' equation, Numerical method, Transmission-Line Modeling.

***Highlights***

- Triangular node for TLM that can be used for heat transfer in biological systems.
- Heat source, blood perfusion, and different boundary conditions are considered.
- In the validation, accuracy was within 1% when convergence criteria was met.

## ***1. INTRODUCTION***

Transmission-line modeling (TLM) is a numerical method that has been in use to solve problems of heat transfer in biological systems (Amri et al., 2011, 2016; Bellia et al., 2008ab; Belil and Bennaoum, 2013; Bellil et al., 2013). TLM solutions are intrinsically time-domain. The current TLM approach to solve the bio-heat equation in two-dimensions uses rectangular nodes to discretize the geometry and has been proven to be fast and reliable (Milan et al., 2014). The drawback associated with the TLM rectangular node is, however, the requirement that the space discretization in the  $x$ -axis must be the same in all nodes in a given  $y$  line and vice-versa (Fig. 1b in Milan et al., 2014). Because of this drawback, the mesh needs to be refined not only in the regions of interest but also in a large additional domain. Consequently, the computational time and memory space increases considerably. A TLM triangular node has been proven to overcome this drawback for modeling problems in electromagnetism (Sewell et al., 2004ab). However, no similar approaches have been applied to bio-heat transfer problems.

The objective of this study was to develop and validate a TLM triangular-node model for bio-heat transfer. The model includes heat source, blood perfusion (advection), boundary and initial conditions.

## ***2. PROCEDURE***

Figure 1 shows the nomenclature for a triangular node and space discretization and

unitary vectors. To develop the TLM triangular node, we need to: (1) prove the isomorphism between the thermal equations and parameters with the electrical circuit equations and parameters, (2) describe the connection and scattering process, which ensures the spread of temperature in time and space, (3) express temperature and heat flux using incident voltages, (4) formulate boundary conditions, and (5) establish convergence.

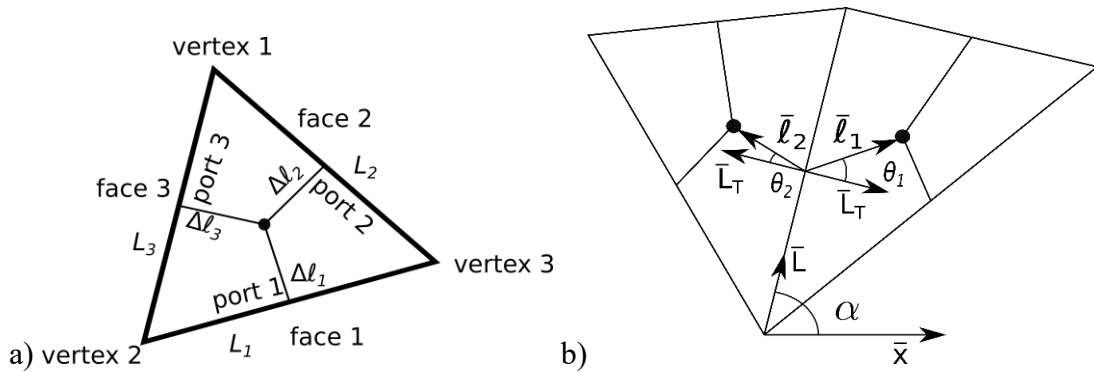


Figure 1. Nomenclature for (a) triangle and space discretization, and (b) unitary vectors (note that the lengths of the vectors are exaggerated). The thick dot represents the center of the triangle, which is connected through transmission lines to the midpoint in each triangular face. The connection point between adjacent triangles is called port. The length of the transmission line is  $\Delta\ell$ . The length of the triangular face is  $L$ . The unitary vectors  $\bar{L}_T, \bar{\ell}_1, \bar{\ell}_2$  always point toward the center of the node.

## 2.1 Isomorphism

For bio-heat transfer, we need to prove the isomorphism between the bioenergy

equation (Pennes, 1948; Minkowycz and Sparrow, 2009; Xu et al., 2011) for a triangle (Eq. (1)), where we have assumed that the heat flux in the direction  $\bar{L}_T$  does not change with  $\bar{L}$ , and the Fourier's conduction law (Eq. (2)), expressed as

$$\rho c \frac{\partial T}{\partial t} A_T = q''_{LT1} L_1 + q''_{LT2} L_2 + q''_{LT3} L_3 + \omega_b \rho_b c_b (T_b - T) A_T + q''' A_T \quad (1)$$

$$-k \frac{\partial T}{\partial L_{Tn}} = q''_{LTn} \quad (2)$$

where,  $\rho$  ( $\text{kg/m}^3$ ) = density,  $c$  ( $\text{J}/(\text{kg } ^\circ\text{C})$ ) = specific heat,  $T$  ( $^\circ\text{C}$ ) = temperature,  $A_T$  ( $\text{m}^2$ ) = triangular area,  $q''_{LTn}$  ( $\text{W}/\text{m}^2$ ) = heat flux at face  $n$  in the direction of  $\bar{L}_T$ ,  $L_n$  ( $\text{m}$ ) = length of face  $n$ ,  $\omega_b$  ( $\text{s}^{-1}$ ) = blood perfusion,  $\rho_b$  ( $\text{kg}/\text{m}^3$ ) = blood density,  $c_b$  ( $\text{J}/(\text{kg } ^\circ\text{C})$ ) = blood specific heat,  $T_b$  ( $^\circ\text{C}$ ) = blood temperature,  $q'''$  ( $\text{W}/\text{m}^3$ ) = heat sources,  $k$  ( $\text{W}/(\text{m } ^\circ\text{C})$ ) = thermal conductivity.

The proposed TLM electrical circuit for a triangular node is shown in Figure 2. Applying Kirchoff's laws (Alexander and Sadiku, 2012) to the circuit of Figure 2(a) and assuming that  $C_{d1} = C_{d2} = C_{d3} = C_d$ , yields

$$(\Delta\ell_1 + \Delta\ell_2 + \Delta\ell_3) C_d \frac{\partial V}{\partial t} = I_1 + I_2 + I_3 - GV + I_S \quad (3)$$

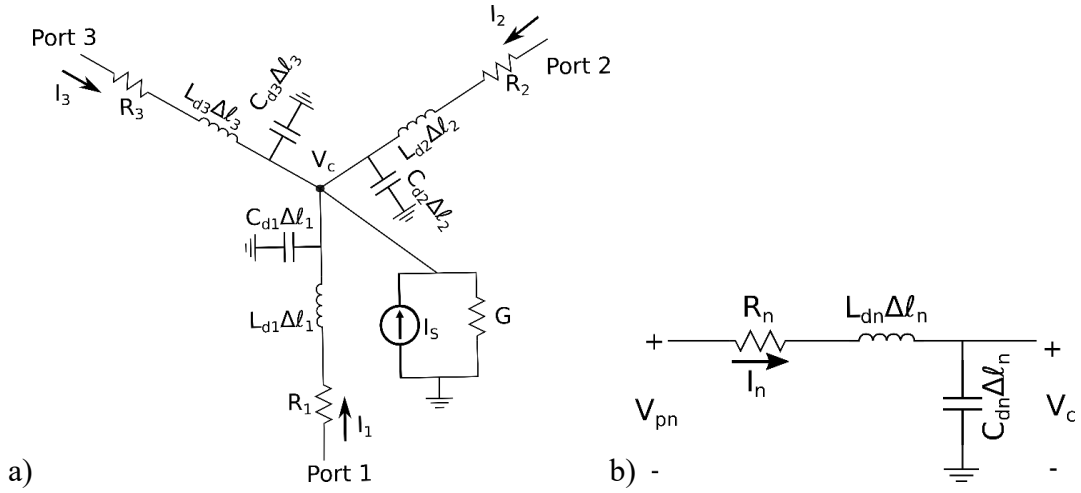


Figure 2. (a) TLM node for a triangle, and (b) detail of the electrical circuit between the center of the node and port  $n$ .  $V_c$  is voltage in the center of the node,  $V_{pn}$  is voltage in port  $n$ ,  $I_n$  is current flowing from port  $n$  to the center of the node.  $C_{dn}$  and  $L_{dn}$  are, respectively, the capacitance and inductance per unit length of transmission line  $n$ .  $R_n$  is resistance connected in series with transmission line  $n$ .

The isomorphism between Eq. (1) and Eq. (3) occurs when

$$V \equiv T \quad (4)$$

$$C_d \equiv \frac{\rho c A_T}{\Delta\ell_1 + \Delta\ell_2 + \Delta\ell_3} \quad (5)$$

$$I_n \equiv q''_{LTn} L_n \quad (6)$$

$$I_s \equiv A_T (q''' + \omega_b \rho_b c_b T_b) \quad (7)$$

$$G \equiv A_T \omega_b \rho_b c_b \quad (8)$$

Applying Kirchhoff's laws to the circuit shown in Figure 2(b) yields

$$I_n + \frac{L_{dn} \Delta \ell_n}{R_n} \frac{\partial I_n}{\partial t} = -\frac{V_c - V_{pn}}{R_n} \quad (9)$$

Assuming

$$|I_n| \gg \left| \frac{L_{dn} \Delta \ell_n}{R_n} \frac{\partial I_n}{\partial t} \right| \quad (10)$$

Eq. (9) can be written as

$$-\frac{V_c - V_{pn}}{R_n} \approx -\frac{\Delta \ell_n}{R_n} \frac{\partial V}{\partial \ell_n} \approx I_n \equiv q''_{LTn} L_n = -k L_n \frac{\partial T}{\partial L_{Tn}} \quad (11)$$

Analyzing Figure 1(b), we can expect  $\theta_1 \approx \theta_2 \approx 0$ , which makes Eq. (12) a reasonable assumption.

$$\frac{\partial T}{\partial \ell_n} \approx \frac{\partial T}{\partial L_{Tn}} \quad (12)$$

The isomorphism between Eq. (2) and Eq. (11) occurs when

$$-\frac{\Delta \ell_n}{R_n} \frac{\partial V}{\partial \ell_n} \equiv -k L_n \frac{\partial T}{\partial \ell_n} \quad (13)$$

$$R_n \equiv \frac{\Delta \ell_n}{k L_n} \quad (14)$$

## 2.2. Connection, Scattering and Matrix equations

To facilitate the mathematical development and interpretation of voltage propagation in a transmission line, the transmission-line theory defines that the voltage in the transmission line is equal to the sum of the incident ( $V_n^i$ ) and reflected ( $V_n^r$ ) voltages.  $V_n^i$  represents the part of the voltage that propagates from the center of the transmission line to its end, while  $V_n^r$  represents the part of the voltage that propagates from the end towards the center. These voltages can assume any value, including negative values, which means that the voltage is propagating in the opposite direction.

In this TLM node, we assumed that  $V_n^i$  is the part of the voltage that travels from port  $n$  to the center of the node, while  $V_n^r$  travels from the center of the node to port  $n$ . The process that  $V_n^i$  at time-step  $k\Delta t$  ( ${}_kV_n^i$ ) are used to calculate  $V_n^r$  at time-step  $k\Delta t$  ( ${}_kV_n^r$ ) is called *Scattering*. The process that  ${}_kV_n^r$  are used to calculate  $V_n^i$  at time-step  $(k+1)\Delta t$  ( ${}_{k+1}V_n^i$ ) is called *Connection*. Figure 3 shows the equivalent circuits used to express the *Connection* and *Scattering* processes.

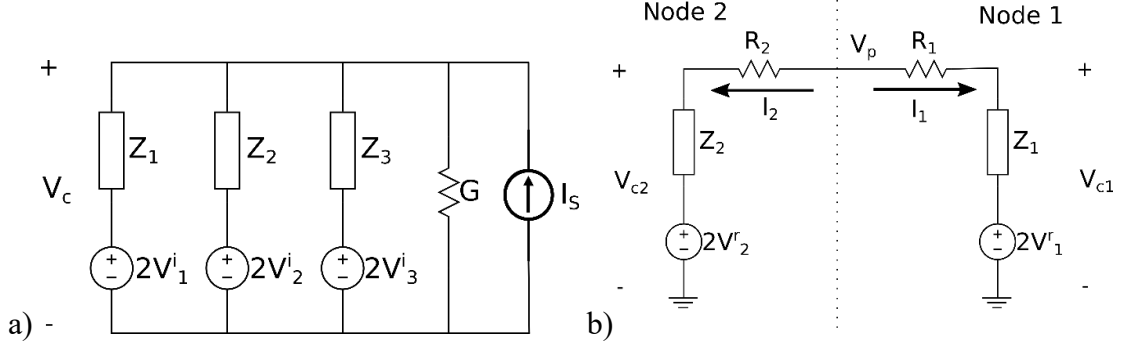


Figure 3. Equivalent electrical circuit (a) of the center of the node, which represents the scattering process, and (b) of the port (between two nodes), which represents the connection process.

Analyzing the resultant voltages in the impedances ( $Z_n$ ) in Figure 3(a), we can express the *Scattering* process as

$$\hat{Z} = \frac{Z_1 Z_2 Z_3}{Z_1 Z_2 + Z_1 Z_3 + Z_2 Z_3 + Z_1 Z_2 Z_3 G} \quad (15)$$

$$\tau_n = 2 \frac{\hat{Z}}{Z_n} \quad (16)$$

$$[{}_k V^r] = [S][{}_k V^i] + \hat{Z} I_S = \begin{bmatrix} {}_k V_1^r \\ {}_k V_2^r \\ {}_k V_3^r \end{bmatrix} = \begin{bmatrix} \tau_1 - 1 & \tau_2 & \tau_3 \\ \tau_1 & \tau_2 - 1 & \tau_3 \\ \tau_1 & \tau_2 & \tau_3 - 1 \end{bmatrix} \begin{bmatrix} {}_k V_1^i \\ {}_k V_2^i \\ {}_k V_3^i \end{bmatrix} + \hat{Z} I_S \quad (17)$$

where,  $[S]$  is the scattering matrix,  $\hat{Z} I_S$  accounts for external heat sources and

$$Z_n = \frac{\Delta t}{2 \Delta \ell_n C_d} \quad (18)$$

The *Connection* process of the TLM triangular node is similar to that of the TLM rectangular node (Milan et al., 2014) except that the reflection and transmission coefficients are expressed as

$$\rho_{\alpha\beta} = \frac{R_\alpha + R_\beta + Z_\beta - Z_\alpha}{R_\alpha + R_\beta + Z_\alpha + Z_\beta} \quad (19)$$

$$\tau_{\alpha\beta} = \frac{2Z_\alpha}{R_\alpha + R_\beta + Z_\alpha + Z_\beta} \quad (20)$$

Then, we can express the *Connection* process as

$$[{}_{k+1}V^i] = [C][{}_kV^r] + [B] \quad (21)$$

where,  $[C]$  is the *Connection* matrix and  $[B]$  accounts for the boundary condition effects (the elements of  $[B]$  are zero for cases without boundary condition. For other cases, see the discussion in Section 2.4). Applying Eq. (17) into Eq. (21) yields

$$[{}_{k+1}V^i] = [M][{}_kV^i] + [E] \quad (22)$$

$$[M] = [C][S] \quad (23)$$

$$[E] = [C][\hat{Z}I_S] + [B] \quad (24)$$

The time evolution of the problem is analyzed using Eq. (22). The steady-state solution can be obtained using

$$[V^i] = ([I] - [M])^{-1}[E] \quad (25)$$

where,  $[I]$  stands for identity matrix.

### 2.3. Calculating temperature and heat flux

Using the TLM procedure, incident and reflected voltages are first solved and then temperature and heat flux are calculated using post-processing. In other words, temperature and heat flux cannot be directly obtained by the TLM procedure. In addition, temperatures and heat fluxes are defined at the center of the node and at the ports—if temperature and heat flux at any other position are desired, they can be obtained by interpolation. For example, for the temperature at the center of the node, we need to analyze  $V_c$  in Figure 3(a), which can be expressed as

$${}_kT_c = {}_kV_c = [\tau][{}_kV^i] + \hat{Z}I_S = [\tau_1 \quad \tau_2 \quad \tau_3] \begin{bmatrix} {}_kV_1^i \\ {}_kV_2^i \\ {}_kV_3^i \end{bmatrix} + \hat{Z}I_S \quad (26)$$

For the temperature at the ports, we need to analyze  $V_p$  in Figure 3(b), which yields

$${}_kT_p = {}_kV_p = [\beta][{}_kV^r] + {}_TB = [\beta_1 \quad \beta_2] \begin{bmatrix} {}_kV_1^r \\ {}_kV_2^r \end{bmatrix} + {}_TB \quad (27)$$

where,  ${}_TB$  represents the effect of boundary conditions (the elements of  $[_TB]$  are zero for the cases without boundary condition. For other cases, see the discussion in Section 2.4) and  $\beta_n$  represents the effect of the reflected voltages. For cases with boundary conditions, see Section 2.4 for calculation of  $\beta_n$ . For cases where there is no

boundary conditions in the port,  $\beta_n$  is calculated as

$$\beta_n = 2 \frac{R_1 + Z_1 + R_2 + Z_2 - (R_n + Z_n)}{R_1 + Z_1 + R_2 + Z_2} \quad (28)$$

The numbers in Eq. (26) refer to voltages and circuit elements within a node, whereas the numbers in Eqs. (27) and (28) refer to voltages and circuit elements within a port (*i.e.*, different nodes).

The matrix equation for temperatures at the center of the node and at the ports can be appended to yield a unified matrix equation for the temperatures in TLM, that is,

$$[{}_kT] = {}_T[M][{}_kV^i] + {}_T[E] \quad (29)$$

$${}_T[M] = [{}_T] + [\beta][S] \quad (30)$$

$${}_T[E] = [\hat{Z}I_S] + ([\beta]{}_T[\hat{Z}I_S] + {}_T[B]) \quad (31)$$

where, the subscript  $T$  was used to differentiate the matrices that contain the same name.

For heat flux, the approximation applied in Eq. (12) yields

$${}_kq''_{LTn} = \frac{{}_kT_{pn} - {}_kT_{cn}}{LR_n} \quad (32)$$

Since heat flux cannot be calculated directly for  $\bar{L}$  ( ${}_kq''_{Ln}$ , perpendicular to  ${}_kq''_{LTn}$ ), then, it is not possible to calculate heat fluxes in  $x$ ,  $y$ , and  $z$  directions using  ${}_kq''_{LTn}$

without making an assumption about  ${}_k q''_{Ln}$  (like  ${}_k q''_{Ln} = 0$ ). One way to overcome this limitation is to interpolate temperature values at triangular vertices and then estimate  ${}_k q''_{Ln}$ . This approach is not shown in this paper.

## 2.4. Boundary conditions

The discussion herein assumes that the calculations for  $B$ ,  ${}_T B$ , and  $\beta_1$  are performed for node 1 (where we use  $\beta_1$ ). The composition of the vectors is done by appending the values of  $B$ ,  ${}_T B$ , and  $\beta_1$  on their respective vectors. For cases without boundary conditions,  $B = {}_T B = 0$  and  $\beta_1$  is calculated using Eq. (28).

Four types of boundary conditions can be considered in the *Connection* process of TLM, and they are: adiabatic, temperature, heat flux, and convection. Figure 4 shows the different circuits that represent these boundary conditions. Effects of adiabatic boundary condition in the *Connection* processes was discussed in Milan et al. (2014) and it makes  $B = 0$ ,  $\beta_1 = 2$ ,  ${}_T B = 0$ . Effects of heat flux boundary condition in the *Connection* process was also discussed in Milan et al. (2014) and it makes  $B = Z_1 I_B$ ,  $\beta_1 = 2$ ,  ${}_T B = (R_1 + Z_1) I_B$ , where,  $I_B$  is the current in the direction of  $\bar{L}_T$ . For temperature as a boundary condition,  $\beta_1 = 0$ ,  ${}_T B = T_B$ ,

$$B = \frac{Z_1}{R_1 + Z_1} T_B \quad (33)$$

and the reflection coefficient is adjusted to (for details of the *Connection* process, refer to Milan et al., 2014)

$$\rho = \frac{R_1 - Z_1}{R_1 + Z_1} \quad (34)$$

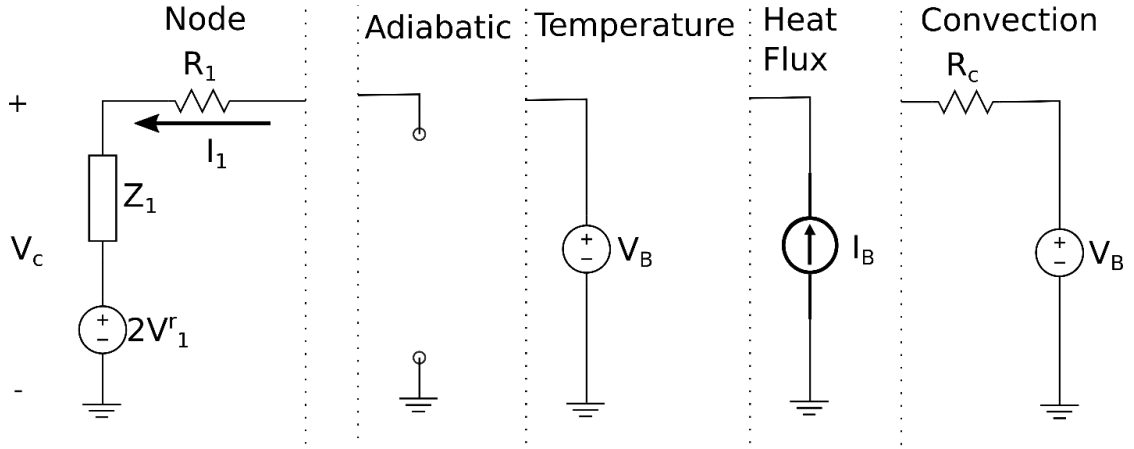


Figure 4. Equivalent electrical circuit for *Connection* and the circuits for different types of boundary conditions.

For convection boundary condition,

$$\rho = \frac{R_1 + R_c - Z_1}{R_1 + R_c + Z_1} \quad (35)$$

$$B = \frac{Z_1}{R_1 + R_c + Z_1} T_B \quad (36)$$

$$\beta_1 = \frac{2R_c}{R_1 + R_c + Z_1} \quad (37)$$

$${}^T B = \frac{R_1 + Z_1}{R_1 + R_c + Z_1} T_B \quad (38)$$

where,

$$R_c = \frac{1}{hL_1} \quad (39)$$

is achieved using the following definition of convection heat transfer

$$q''_{LT} = h(T_B - T_p) \quad (40)$$

where,  $h$  (W/(m<sup>2</sup> °C)) = convective heat transfer coefficient. Similarly, for radiation heat transfer, Eq. (40) can be used by adjusting  $h$  and  $T_B$  (da Silva and Maia, 2013).

In this study, it is important to note that the boundary conditions are considered to be time dependent.

## 2.5. Initial Conditions

Complex initial conditions are still an issue in the application of TLM (Enders and de Cogan, 2001; Enders et al., 2002; Koay et al., 2008; Kennedy and O'Connor, 2008). Four approaches are discussed herein. Two approaches give good approximation for problems that have homogeneous initial conditions throughout the mesh. The first approach (Amri et al., 2011) shifts the temperature at all nodes in such a way that instead of starting the simulation, say at 37 °C, it would start at 0 °C. The second approach (Milan et al., 2014) assumes that  ${}_0V_n^i$  in a node are equal, which results in

$${}_0V_n^i = \frac{{}_0T_c - \hat{Z}I_S}{\tau_1 + \tau_2 + \tau_3} \quad (41)$$

The third approach simulates the steady-state condition (Eq. (25)) for the initial

conditions. The fourth approach solves Eq. (29) for  $V_n^i$ , which requires a matrix inversion or a combination of Eqs. (29) and (32). The simulations in this paper were based on Eq. (41).

## 2.6. Convergence

The TLM method solves the wave equation. Therefore, to model the Fourier's conduction law, we had to make the assumption stated in Eq. (10).

Expressing the relationship between inductance and capacitance as

$$\frac{1}{\sqrt{L_{dn}C_{dn}}} = 2 \frac{\Delta \ell_n}{\Delta t} \quad (42)$$

and defining

$$\eta_n = \frac{L_n}{\Delta \ell_n^2} \frac{k}{\rho c} \frac{\Delta t (\Delta \ell_1 + \Delta \ell_2 + \Delta \ell_3)}{4A_T} \quad (43)$$

the TLM approximation to the Fourier's conduction law is satisfied when

$$1 \gg \eta_n \left| \frac{k-1q_{LTn}''}{kq_{LTn}''} - 1 \right| \quad (44)$$

Knowing how well TLM models the Fourier's conduction law using  $\eta_n$  as a parameter can help in developing automatic changing in time-step algorithms (Gui et al., 1992; Pulko et al., 1990). For example, we were able to satisfactorily run simulations with the right side of Eq. (44)  $\sim 0.05$ . Some spikes ( $\sim 50$ ) did, however, occurred at the

beginning of the simulation. In addition, TLM requires  $\Delta\ell_n/\lambda \leq 0.1$ , where,  $\lambda$  is the wavelength of the heat source (Christopoulos, 1995, 2006).

## 2.7. Summary

The computational procedure can be summarized as follows:

1. Segment the control volume using triangles
2. Calculate the electrical parameters based on the thermal and geometrical parameters (Eqs. (5), (7), (8), and (14))
3. Calculate matrix  $[M]$  and  $[E]$  using (Eqs. (15) - (24))
4. Apply boundary conditions, (Eqs. (33) - (40)), and (a) solve the inverse matrix for steady-state solution (Eq. (25)), calculate temperature and heat flux using (Eqs. (26) - (32)) and end the simulation, or (b) calculate the initial conditions using (Eq. (41))
5. Solve Eq. (22)
6. Verify convergence using Eqs. (43) and (44)
7. Calculate the temperatures and heat flux using (Eqs. (26)-(32)) (optional)
8. Go back to Step 5 and continue with the remaining steps until the simulation reaches the desired end time.

## 2.8. Validation

The problem shown in Figure 5 was used to validate the TLM triangular node. The

purpose of this exercise is to validate the TLM procedure. The validation has no reference to any biological thermal problem, even though one could assume that the heat flux at  $x = L$  represents an input of heat from the environment (or from any other source), the temperatures at  $y = 0$  and  $y = H$  could be measured values, and the adiabatic boundary at  $x = 0$  could be from symmetry in the geometry.

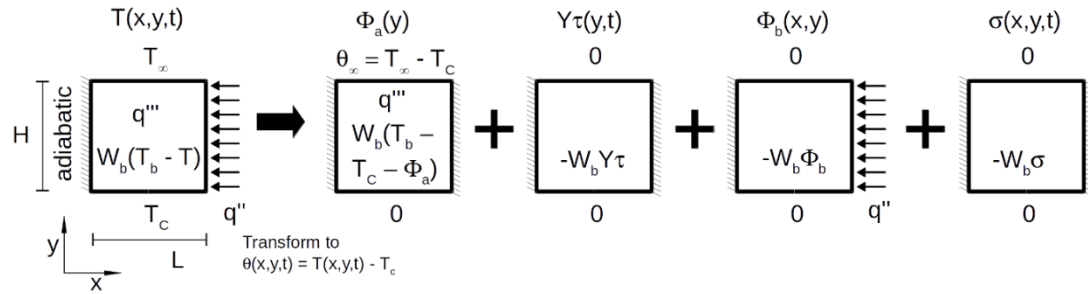


Figure 5. The analytical problem used to validate the TLM is shown by the 1<sup>st</sup> rectangle. To solve this problem analytically, the temperature is firstly shifted by  $T_c$  and then separated into 4 linear related problems. The solutions to these 4 problems define the solution to the 1<sup>st</sup> rectangular problem.

Using the principle of superposition, the problem in Figure 5 can be separated into four linear problems that can be solved using separation of variables. The equation for the temperature profile can be expressed as

$$T(x, y, t) = \Phi_a(y) + Y\tau(y, t) + \Phi_b(x, y) + \sigma(x, y, t) + T_c \quad (45)$$

and the terms in the Eq. (45) are defined as

$$\Phi_a(x) = \frac{Q_T}{W_b} + c_1 \sinh \sqrt{\frac{W_b}{k}} y - \frac{Q_T}{W_b} \cosh \sqrt{\frac{W_b}{k}} y \quad (46)$$

$$Y\tau(y, t) = \sum_{m=1}^{\infty} C_{3m} \sin \lambda_m y \exp \left[ - \left( \lambda_m^2 + \frac{W_b}{k} \right) \alpha t \right] \quad (47)$$

$$\Phi_b(x, y) = \sum_{m=1}^{\infty} C_{4m} \sin \lambda_m y \cosh \gamma x \quad (48)$$

$$\sigma(x, y, t) = \sum_{n=0}^{\infty} \sum_{m=1}^{\infty} C_{5nm} \sin \lambda_m y \cos \eta_n x \exp \left[ - \left( \lambda_m^2 + \eta_n^2 + \frac{W_b}{k} \right) \alpha t \right] \quad (49)$$

Table 1 shows the boundary and initial conditions for each problem (Eqs. (46)-(49)) and the following parameters were kept constant in solving the problem (Eq. (45)):  $L = 1 \text{ mm}$ ,  $H = 1 \text{ mm}$ ,  $\rho = 1200 \text{ kg/m}^3$ ,  $c = 3200 \text{ J/(kg } ^\circ\text{C)}$ ,  $k = 0.3 \text{ W/(m } ^\circ\text{C)}$ ,  $\omega_b = 10^{-4} \text{ s}^{-1}$ ,  $\rho_b = 1052 \text{ kg/m}^3$ ,  $c_b = 3600 \text{ J/(kg } ^\circ\text{C)}$ ,  $T_b = 37 \text{ } ^\circ\text{C}$ ,  $q''' = 500 \text{ W/m}^3$ ,  $T_c = 37 \text{ } ^\circ\text{C}$ ,  $T_\infty = 150 \text{ } ^\circ\text{C}$ , and  $q'' = 100,000 \text{ W/m}^2$ . The values of  $T_\infty$  and  $q''$  were exaggerated in order to show the precision obtained using the TLM triangular node.

The terms in Eqs. (46)-(49) are defined as

$$\alpha = \frac{k}{\rho c_p} \quad (50)$$

$$W_b = \omega_b \rho_b c_b \quad (51)$$

$$\lambda_m = \frac{m\pi}{H} \quad (52)$$

$$\eta_n = \frac{n\pi}{L} \quad (53)$$

$$\gamma = \sqrt{\frac{W_b}{k} + \lambda_m^2} \quad (54)$$

$$Q_T = q''' + W_b(T_b - T_c) \quad (55)$$

$$c_1 = \frac{\theta_\infty + \frac{Q_T}{W_b} \left( \cosh \sqrt{\frac{W_b}{k}} H - 1 \right)}{\sinh \sqrt{\frac{W_b}{k}} H} \quad (56)$$

$$C_{3m1} = \frac{2Q_T}{H\lambda_m W_b} (\cos \lambda_m H - 1) \quad (57)$$

$$C_{3m2} = \frac{2c_1 \cos \lambda_m H \sinh \sqrt{\frac{W_b}{k}} H}{H \left( \lambda_m + \frac{W_b}{k\lambda_m} \right)} \quad (58)$$

$$C_{3m3} = \frac{2Q_T}{HW_b} \frac{1 - \cos \lambda_m H \cosh \sqrt{\frac{W_b}{k}} H}{\lambda_m + \frac{W_b}{k\lambda_m}} \quad (59)$$

$$C_{3m} = \sum_{n=1}^3 C_{3mn} \quad (60)$$

$$C_{4m} = \frac{2q''}{\lambda_m H k \gamma \sinh \gamma L} (1 - \cos \lambda_m H) \quad (61)$$

$$C_{5nm} = \frac{4q'' \cos \eta_n L}{\lambda_m H L k (\gamma^2 + \eta_n^2)} (\cos \lambda_m H - 1) \quad (62)$$

$$C_{5nm} \Big|_{n=0} = C_{50m} = \frac{2q''}{\lambda_m H L k \gamma^2} (\cos \lambda_m H - 1) \quad (63)$$

Heat flux was calculated from Fourier's conduction law.

Table 1. Boundary and initial conditions for the problem in Figure 5.

|         | $T(x, y, t)$                    | $\theta(x, y, t)$                    | $\Phi_a(y)$              | $Y\tau(y, t)$     | $\Phi_b(x, y)$                       | $\sigma(x, y, t)$        |
|---------|---------------------------------|--------------------------------------|--------------------------|-------------------|--------------------------------------|--------------------------|
| $x = 0$ | $\frac{dT}{dx} = 0$             | $\frac{d\theta}{dx} = 0$             | -                        | -                 | $\frac{d\Phi_b}{dx} = 0$             | $\frac{d\sigma}{dx} = 0$ |
| $x = L$ | $\frac{dT}{dx} = \frac{q''}{k}$ | $\frac{d\theta}{dx} = \frac{q''}{k}$ | -                        | -                 | $\frac{d\Phi_b}{dx} = \frac{q''}{k}$ | $\frac{d\sigma}{dx} = 0$ |
| $y = 0$ | $T = T_c$                       | $\theta = 0$                         | $\Phi_a = 0$             | $Y\tau = 0$       | $\Phi_b = 0$                         | $\sigma = 0$             |
| $y = H$ | $T = T_\infty$                  | $\theta = \theta_\infty$             | $\Phi_a = \theta_\infty$ | $Y\tau = 0$       | $\Phi_b = 0$                         | $\sigma = 0$             |
| $t = 0$ | $T = T_c$                       | $\theta = 0$                         | -                        | $Y\tau = -\Phi_a$ | -                                    | $\sigma = -\Phi_b$       |

## 2.9. Mesh-independent test

A numerical solution is sensitive to the number of mesh elements. The smaller the number of elements, the finer the mesh, and the higher the prediction accuracy. A fine

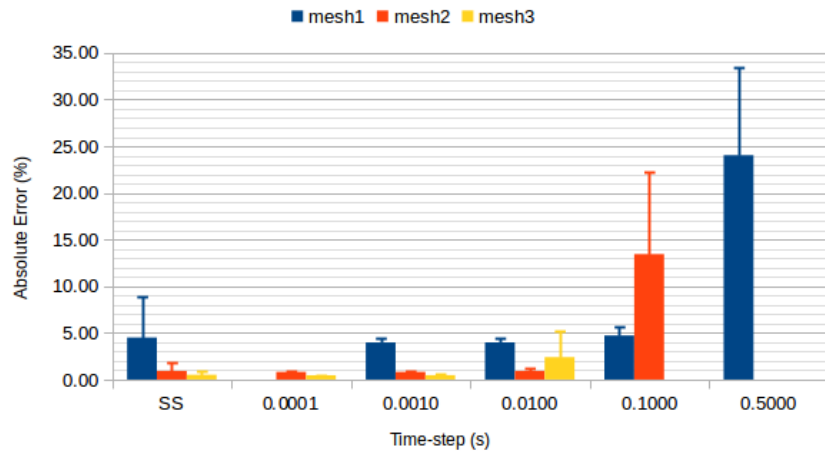
mesh requires a longer computing time to obtain one solution. The principal purpose of mesh-independent test is to reach a compromise between computing time and prediction accuracy. In order to obtain an acceptable number of mesh elements, a mesh-independent test is usually performed by checking various mesh sizes and observing how the solution changes with respect to the mesh size. In this study, the mesh-independent test was conducted simultaneously with model validation.

Effect of mesh size on TLM accuracy was analyzed with the problem stated above (Eq. (45)) using three different mesh sizes: mesh-size 1 consists of 40 nodes and 68 ports (length of triangular face,  $L_{mean} = 251 \mu\text{m} \pm 50 \mu\text{m}$ , mean  $\pm$  standard deviation), mesh-size 2 consists of 682 nodes and 1055 ports ( $L_{mean} = 59 \mu\text{m} \pm 9 \mu\text{m}$ ), and mesh-size 3 consists of 10766 nodes and 16277 ports ( $L_{mean} = 15 \mu\text{m} \pm 2 \mu\text{m}$ ). The meshes were created using Gmsh software (Geuzaine and Remacle, 2009). Effect of time step ( $\Delta t$ ) on TLM precision was also analyzed. TLM accuracy for estimating temperatures was determined by calculating the mean absolute percentage error during 10 seconds of simulation. TLM accuracy for estimating heat flux was determined by calculating the mean absolute difference rather than mean absolute percentage error because heat flux could sometimes become near zero during the 10 seconds of simulation. The accuracy of the model for estimating temperature and heat flux in steady-state condition was also determined using the same procedure.

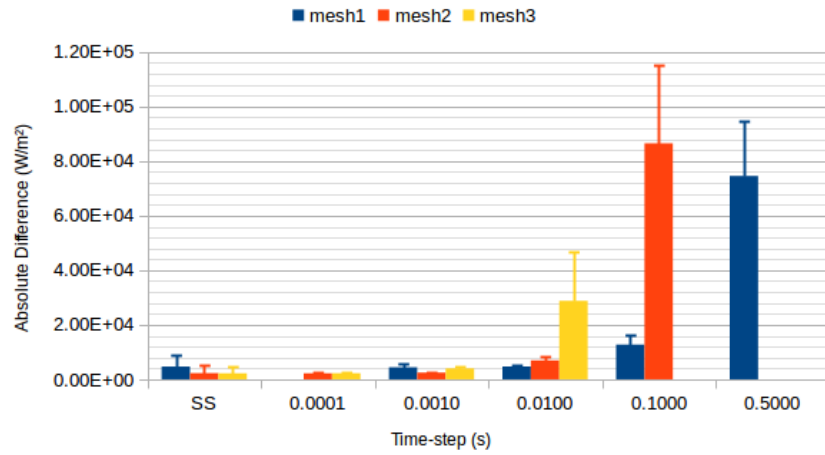
### 3. RESULTS AND DISCUSSION

The disadvantage of the triangular node over the rectangular node (Milan *et al.*, 2014) is that triangular nodes require the approximation associated with Eq. (12). This approximation implies that rectangular nodes would be more appropriate for problems without complex geometries. For problems with complex geometries, the solution using rectangular nodes would require refined mesh to account for the irregularities in the geometry, whereas triangular nodes could be used to fit the complex geometry with low number of nodes, which makes the triangular node advantageous over the rectangular node especially for problems with complex geometries.

Figure 6 shows the accuracy of the model. The accuracy of the model for the steady-state solution was independent of the time step ( $\Delta t$ ) but dependent on the length of the triangular faces ( $L_{mean}$ ), *i.e.*, the accuracy of the model increased when  $L_{mean}$  was decreased. Furthermore, for the time-domain solution, the accuracy was increased when the time step was decreased. The decrease of  $L_{mean}$  lead to a decrease in the length of the transmission-line ( $\Delta \ell_n$ ). The decrease of  $\Delta \ell_n$ , then, lead to an improvement in the approximation applied to Eq. (12). When the time step was decreased,  $\eta_n$  also decreased, which resulted in a better approximation of Eq. (10).



a)



b)

Figure 6. TLM (a) absolute error in estimating temperature, and (b) absolute difference in estimating heat flux. Bars represent standard error, and SS represents steady state. The mean error and absolute differences for the steady state correspond to the mean and standard deviation for all nodes and ports. For the time evolution problem, mean error and absolute differences for all the simulation time (mean values for each time-step) are shown.

As shown in Figure 6, when  $\Delta\ell_n$  decreases, the accuracy of the model might decrease if the time step remains unchanged. This happens because the TLM approximation done on Eq. (10), as predicted by Eq. (44), become worse when only  $\Delta\ell_n$  decreases (mainly because of the term  $\Delta\ell_n^2$ ). Therefore, in order to maintain accuracy, the time step needs to be decreased, which would lead to increased computational time with refined mesh sizes. One alternative to overcome this limitation is to use an effective time-step, that is, based on Eq. (64), expressed as

$$[{}_{k+n}V^i] = [M]^n [{}_kV^i] + \left( [I] + \sum_{m=1}^{n-1} [M]^m \right) [E] \quad (64)$$

where, the effective time step becomes  $n\Delta t$  ( $n$  is a natural number  $> 0$ ). Using this approximation, the heat source term and the boundary conditions remain the same for  $n\Delta t$ . When they change, the matrix  $[E]$  should be updated. Matrix  $[M]$  is updated for convection boundary condition with  $h$  changing over time. Only few terms are involved in the update and could easily be mapped by an algorithm to avoid the need to calculate the entire matrices, *i.e.*,  $[E]$ ,  $[M]^n$  and  $[M]^m$ , every effective time step.

Based on the results shown in Figure 6, it can be concluded that the TLM triangular node has great potential for application in heat transfer in biological systems. This model has several advantages, which includes: (1) using a triangular node as a control volume allows to model complex geometries, and (2) using time dependent heat sources, blood perfusion (advection), and different types of boundary conditions

(adiabatic, temperature, heat flux, convection), allows to model complex time-dependent problems.

#### ***4. CONCLUSIONS***

The following specific conclusions can be drawn from this study:

- (1) A triangular node for the Transmission-Line modeling (TLM) that may have great potential for application in heat transfer in biological systems was developed. The model includes heat source, blood perfusion (advection), boundary conditions (adiabatic, temperature, heat flux or convection) and initial conditions.
- (2) The advantage of the triangular node over a rectangular node includes fitting complex geometries with less number of nodes. The disadvantage of the triangular node is the necessity of an additional approximation (Eq. (12)).
- (3) The predicted results were compared against results obtained from the solution of a simplified two-dimensional problem, and they agreed within 1% for a mesh with length of triangular faces of  $59 \mu\text{m} \pm 9 \mu\text{m}$  (mean  $\pm$  standard deviation) and a time step of 1 ms.

#### ***Acknowledgment***

Brazilian National Council of Technological and Scientific Development (Proc. 203312/2014-7) for scholarship to HFMM.

## REFERENCES

Alexander CK, Sadiku MNO. *Fundamentals of Electric Circuits (5th ed)*. McGraw-Hill: New York, NY, 2012.

Amri A, Pulko SH, Wilkinson AJ. Potentialities of steady-state and transient thermography in breast tumour depth detection: A numerical study. *Comput Methods Programs Biomed* 123:68-80, 2016.

Amri A, Saidane A, Pulko S. Thermal analysis of a three-dimensional breast model with embedded tumour using the transmission line matrix (tlm) method. *Comput Biol Med* 41:76-86, 2011.

Bellia SA, Saidane A, Benzohra M, Saiter JM, Hamou A. Dimensional soft tissue thermal injury analysis using transmission line matrix (tlm) method. *Int J Numer Model* 21:531-549, 2008a.

Bellia SA, Saidane A, Hamou A, Benzohra M, Saiter JM. Transmission line matrix modelling of thermal injuries to skin. *Burns* 34:688-697, 2008b.

Bellil M, Bennaoum S. *Tlm modelling of laser thermal treatment of benign prostate hyperplasia*. International Conference on Control, Engineering & Information Technology, pp. 1-5, 2013.

Bellil M, Saidane A, Bennaoum S. *Transmission line matrix modelling of bioheat transfer in cryogenic therapy applications*. International Conference on Control, 43

Engineering & Information Technology, pp. 1-6, 2013.

Christopoulos C. *The Transmission Line Modeling Method*. IEEE Press: New York, NY, 1995.

Christopoulos C. *The Transmission Line Modeling (TLM) Method in Electromagnetics*. Morgan & Claypool: Williston, VT, 2006.

da Silva RG, Maia ASC. *Principles of Animal Biometeorology*. Springer: Berlin, Germany, 2013.

Enders P, de Cogan D. TLM for diffusion: the artefact of the standard initial conditions and its elimination within an abstract TLM suite. *Int J Numer Model* 14:107-114, 2001.

Enders P, Pulko SH, Stubbs DM. TLM for diffusion: consistent first time step. Two-dimensional case. *Int J Numer Model* 15:251-259, 2002.

Geuzaine C, Remacle JF. A three-dimensional finite element mesh generator with built-in pre- and post-processing facilities. *Int J Numer Meth Eng* 79:1309-1331, 2009.

Gui X, Webb PW, de Cogan D. An error parameter in tlm diffusion modelling. *Int. J Numer Model* 5:129-137, 1992.

Koay AL, Wilkinson AJ, Pulko SH. TLM nodal state estimator: an alternative method of initializing a two-dimensional diffusion model. *Int J Numer Model* 21:351-368,

2008.

Kennedy A, O'Connor WJ. Error analysis and reduction in lossy TLM. *Int J Numer Model* 73:1027-1045, 2008.

Milan HFM, Carvalho Jr CAT, Maia ASC, Gebremedhin KG. Graded meshes in bio-thermal problems with transmission-line modeling method. *J Therm Biol* 45:43-53, 2014.

Minkowycz WJ, Sparrow EM. *Advances in Numerical Heat Transfer (volume 3)*. CRC Press: Boca Raton, FL, 2009.

Pennes HH. Analysis of tissue and arterial blood temperature in the resting human forearm. *J Appl Phys* 1:93-122, 1948.

Pulko SH, Mallik A, Allen R, Johns PB. Automatic time-stepping in tlm routines for the modelling of thermal diffusion processes. *Int J Numer Model* 3:127-136, 1990.

Sewell P, Wykes J, Benson T, Christopoulos C, Thomas DWP, Vukovic A. Transmission-line modeling using unstructured triangular meshes. *IEEE T Microw Theory Tech* 52:1490-1497, 2004a.

Sewell P, Wykes JG, Benson T, Thomas DWP, Vukovic A, Christopoulos C. Transmission line modelling using unstructured meshes. *IEE Proc-Sci Meas Technol* 151:445-448, 2004b.

Xu F, Lu T. *Introduction to skin biothermomechanics and thermal pain*. Springer:  
Berlin, Germany, 2011.

## CHAPTER 2: TETRAHEDRAL NODE FOR TRANSMISSION-LINE MODELING (TLM) APPLIED TO BIO-HEAT TRANSFER

Hugo Fernando Maia Milan, Kifle G. Gebremedhin

Published in *Computers in Biology and Medicine*: Milan HFM, Gebremedhin KG. Tetrahedral node for transmission-line modeling (TLM) applied to bio-heat transfer. *Comput Biol Med* 79:243-249, 2016.

### ***Abstract***

Transmission-Line Modeling (TLM) is a numerical method used to solve complex and time-domain bio-heat transfer problems. In TLM, parallelepipeds are used to discretize three-dimensional problems. The drawback in using parallelepiped shapes is that instead of refining only the domain of interest, a large additional domain would also have to be refined, which results in increased computational time and memory space. In this paper, we developed a tetrahedral node for TLM applied to bio-heat transfer that does not have the drawback associated with the parallelepiped node. The model includes heat source, blood perfusion, boundary conditions and initial conditions. The boundary conditions could be adiabatic, temperature, heat flux, or convection. The predicted temperature and heat flux were compared against results from an analytical solution and the results agreed within 2% for a mesh size of 69,941 nodes and a time step of 5ms. The method was further validated against published results of maximum skin-surface temperature difference in a breast with and without

tumor and the results agreed within 6%. The published results were obtained from a model that used parallelepiped TLM node. An open source software, *TLMBHT*, was written using the theory developed herein and is available for download free-of-charge.

**Keywords:** Bio-heat equation, Numerical method, Pennes' equation, Tetrahedral node, Transmission-Line Modeling, Unstructured mesh.

### ***Highlights***

- TLM tetrahedral node removes the associated drawback with parallelepiped node.
- TLM model can be used in solving heat transfer problems in biological systems.
- Heat source, blood perfusion, and different boundary conditions are considered.
- Validated against analytical solution and results from parallelepiped TLM node.
- TLM computation was 1550x faster than analytical computation.

## ***1. INTRODUCTION***

The transmission-line modeling (TLM) method is used to solve problems of heat transfer in biological systems (Amri et al., 2011, 2016; Bellia et al., 2008ab; Bellil and Bennaoum, 2013; Bellil et al., 2013; Maia et al., 2014). The current TLM approach in three-dimensions uses parallelepiped nodes to discretize the geometry and requires the space discretization in the  $x$ -axis to be the same in all nodes in a given  $y, z$  planes and vice-versa (Milan et al., 2014). Because of this drawback, the mesh needs to be refined not only in the region of interest but also in a large additional domain. Consequently, computational time and memory requirements increase considerably.

The triangular node for the bio-heat equation overcomes this drawback for two-dimensional problems (Milan and Gebremedhin, 2016) but no similar solution has been developed for three-dimensional problems. Sewell et al. (2004, 2005) developed a TLM tetrahedral node applicable for modeling problems in electromagnetism; however, TLM models developed for problems in electromagnetism cannot be directly applied to solve problems in heat transfer (de Cogan, 1998; de Cogan et al., 2006). Moreover, the models reported by Sewell et al. (2004, 2005) are based on a truncated spherical harmonic series of electromagnetic field that imposes some restrictions on the mesh (Sewell et al., 2005).

The objective of this study was to develop and validate a TLM tetrahedral node that is applicable for bio-heat transfer, and that overcomes the limitations imposed by the parallelepiped node. Furthermore, our model is based on the limit of space and time

discretizations going to zero and, thus, does not have the restrictions that are in the models developed by Sewell et al. (2004, 2005). Our model includes heat sources, blood perfusion, boundary and initial conditions. A software, *TLMBHT*, which is written based on the theory developed herein is available free at <https://github.com/hugomilan/tlmbht>.

## **2. PROCEDURE**

Figure 7 shows the nomenclature for a tetrahedral node, space discretization and unitary vectors. To develop the TLM tetrahedral node, we need to: (1) prove the isomorphism between the thermal equations and parameters and the electrical circuit equations and parameters, (2) describe the connection and scattering process, which ensures the spread of temperature in time and space, (3) express temperature and heat flux using incident voltages, (4) formulate boundary conditions, and (5) establish convergence.

Calculations in this paper were performed using the laptop Oryx Pro from System76, with Ubuntu 16.04, 512 GB PCIe M.2 SSD, 64 GB DDR4 RAM memory (2133 MHz), i7-6820HK (3.6 GHz), 8 GB GeForce GTX 980M.

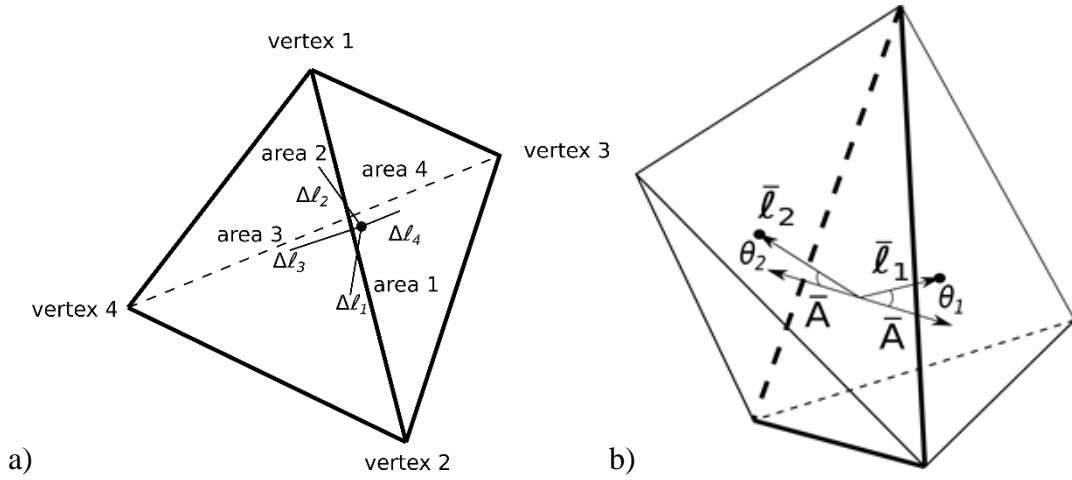


Figure 7. Nomenclature for (a) tetrahedron and space discretization, and (b) unitary vectors (note that the lengths of the vectors are exaggerated for clarity). Black dots represent the center of each tetrahedron. The center of the tetrahedron is connected through transmission lines to the midpoint of each tetrahedron face. The connection point between adjacent tetrahedrons is called port. In (b) two tetrahedrons are shown and the transmission lines that do not connect in the highlighted area (thick lines) were omitted for clarity. The length of the transmission line is  $\Delta\ell$ . The unitary vectors  $\bar{A}$ ,  $\bar{\ell}_1$ ,  $\bar{\ell}_2$  always point toward the center of the node.

## 2.1. Isomorphism

For bio-heat transfer, we need to prove the isomorphism between the bioenergy equation (Minkowycz and Sparrow, 2009; Pennes, 1948; Xu and Fu, 2011) for a tetrahedron (Eq. (65)), where it is assumed that the heat flux in the direction  $\bar{A}$  does not change inside the area, and the Fourier's conduction law (Eq. (66)), expressed as

$$\rho c \frac{\partial T}{\partial t} V_T = q''_{A1} A_1 + q''_{A2} A_2 + q''_{A3} A_3 + q''_{A4} A_4 + \omega_b \rho_b c_b (T_b - T) V_T + q''' V_T \quad (65)$$

$$-k \frac{\partial T}{\partial A_n} = q''_{An} \quad (66)$$

where,  $\rho$  ( $\text{kg/m}^3$ ) = density,  $c$  ( $\text{J}/(\text{kg } ^\circ\text{C})$ ) = specific heat,  $T$  ( $^\circ\text{C}$ ) = temperature,  $V_T$  ( $\text{m}^3$ ) = tetrahedron volume,  $q''_{An}$  ( $\text{W}/\text{m}^2$ ) = heat flux in triangle  $n$  in the direction of the vector area  $n$  ( $\bar{A}_n$ ),  $A_n$  ( $\text{m}$ ) = area of triangle  $n$ ,  $\omega_b$  ( $\text{s}^{-1}$ ) = blood perfusion,  $\rho_b$  ( $\text{kg}/\text{m}^3$ ) = blood density,  $c_b$  ( $\text{J}/(\text{kg } ^\circ\text{C})$ ) = blood specific heat,  $T_b$  ( $^\circ\text{C}$ ) = blood temperature,  $q'''$  ( $\text{W}/\text{m}^3$ ) = heat sources,  $k$  ( $\text{W}/(\text{m } ^\circ\text{C})$ ) = thermal conductivity.

The proposed TLM electrical circuit for the tetrahedral node is shown in Figure 8. Applying Kirchhoff's laws (Alexander and Sadiku, 2012) to the circuit in Figure 8(a) and assuming that  $C_{d1} = C_{d2} = C_{d3} = C_{d4} = C_d$ , yields

$$(\Delta\ell_1 + \Delta\ell_2 + \Delta\ell_3 + \Delta\ell_4) C_d \frac{\partial V}{\partial t} = I_1 + I_2 + I_3 + I_4 - GV + I_S \quad (67)$$

The isomorphism between Eq. (65) and Eq. (67) occurs when

$$V \equiv T \quad (68)$$

$$C_d \equiv \frac{\rho c V_T}{\Delta\ell_1 + \Delta\ell_2 + \Delta\ell_3 + \Delta\ell_4} \quad (69)$$

$$I_n \equiv q''_{An} A_n \quad (70)$$

$$I_S \equiv V_T (q''' + \omega_b \rho_b c_b T_b) \quad (71)$$

$$G \equiv V_T \omega_b \rho_b c_b \quad (72)$$

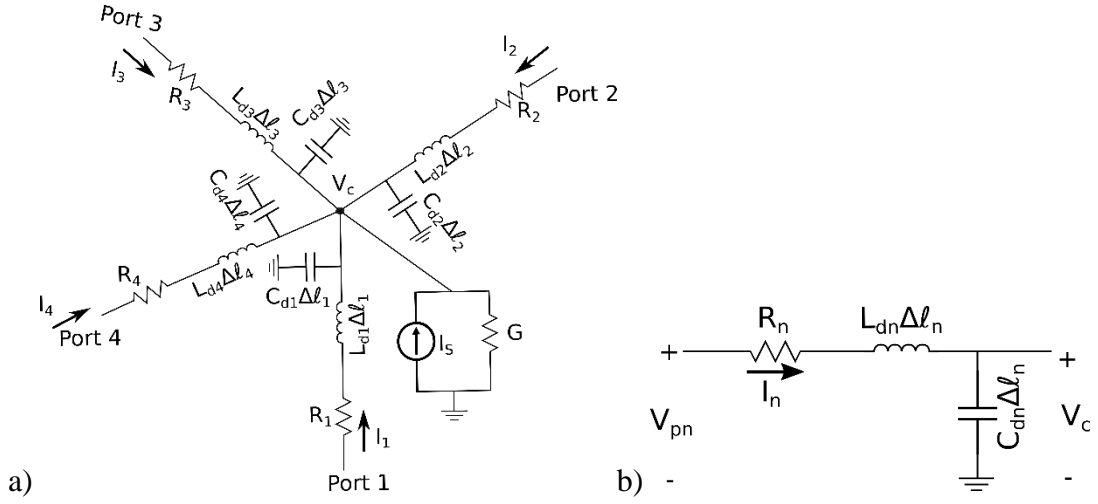


Figure 8. (a) TLM node for a tetrahedron, and (b) detail of the electrical circuit between the center of the node and port  $n$ .  $V_c$  is voltage in the center of the node,  $V_{pn}$  is voltage in port  $n$ ,  $I_n$  is current flowing from port  $n$  to the center of the node.  $C_{dn}$  and  $L_{dn}$  are, respectively, the capacitance and inductance per unit length of transmission line  $n$ .  $R_n$  is resistance connected in series with transmission line  $n$ .

Applying Kirchoff's laws to the circuit shown in Figure 8(b) yields

$$I_n + \frac{L_{dn}\Delta\ell_n}{R_n} \frac{\partial I_n}{\partial t} = -\frac{V_c - V_{pn}}{R_n} \quad (73)$$

Assuming

$$|I_n| \gg \left| \frac{L_{dn}\Delta\ell_n}{R_n} \frac{\partial I_n}{\partial t} \right| \quad (74)$$

Eq. (73) can be written as

$$-\frac{V_c - V_{pn}}{R_n} \approx -\frac{\Delta\ell_n}{R_n} \frac{\partial V}{\partial \ell_n} \approx I_n \equiv q''_{An} A_n = -k A_n \frac{\partial T}{\partial A_n} \quad (75)$$

If the assumption that  $\theta_1 \approx \theta_2 \approx \theta_3 \approx \theta_4 \approx 0$  is satisfied, then

$$\frac{\partial T}{\partial \ell_n} \approx \frac{\partial T}{\partial A_n} \quad (76)$$

and the isomorphism between Eq. (66) and Eq. (75) becomes

$$-\frac{\Delta \ell_n}{R_n} \frac{\partial V}{\partial \ell_n} \equiv -k A_n \frac{\partial T}{\partial \ell_n} \quad (77)$$

$$R_n \equiv \frac{\Delta \ell_n}{k A_n} \quad (78)$$

## 2.2. Connection, scattering and matrix equations

In the transmission-line theory, the voltage propagation is divided into two components: the incident voltage ( $V_n^i$ ), which represents voltage traveling from the center towards its end, and reflected voltage ( $V_n^r$ ), which represents voltage traveling from the end towards its center. This assumption facilitates the mathematical development and interpretation of the solutions. The sum of  $V_n^i$  and  $V_n^r$  is equal to the voltage in the transmission line.

For this TLM node, we assumed that  $V_n^r$  travels from the center of the node to port  $n$ , and  $V_n^i$  travels from port  $n$  to the center of the node. *Scattering* is the process by which incident voltages at time-step  $k\Delta t$  ( ${}_k V_n^i$ ) are used to calculate reflected voltages at time-step  $k\Delta t$  ( ${}_k V_n^r$ ). The equivalent circuit used to express the scattering processes is shown in Figure 9. The resultant voltages in the impedances ( $Z_n$ ) in Figure 9 are expressed as

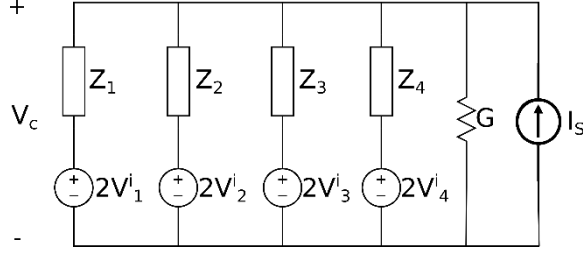


Figure 9. Equivalent electrical circuit of the center of the tetrahedral node that represents the scattering process.

$$\hat{Z} = \frac{Z_1 Z_2 Z_3 Z_4}{Z_1 Z_2 Z_3 + Z_1 Z_2 Z_4 + Z_1 Z_3 Z_4 + Z_2 Z_3 Z_4 + Z_1 Z_2 Z_3 Z_4 G} \quad (79)$$

$$\tau_n = 2 \frac{\hat{Z}}{Z_n} \quad (80)$$

$$[{}_k V^r] = [S][{}_k V^i] + \hat{Z} I_s \quad (81)$$

$$\begin{bmatrix} {}_k V_1^r \\ {}_k V_2^r \\ {}_k V_3^r \\ {}_k V_4^r \end{bmatrix} = \begin{bmatrix} \tau_1 - 1 & \tau_2 & \tau_3 & \tau_4 \\ \tau_1 & \tau_2 - 1 & \tau_3 & \tau_4 \\ \tau_1 & \tau_2 & \tau_3 - 1 & \tau_4 \\ \tau_1 & \tau_2 & \tau_3 & \tau_4 - 1 \end{bmatrix} \begin{bmatrix} {}_k V_1^i \\ {}_k V_2^i \\ {}_k V_3^i \\ {}_k V_4^i \end{bmatrix} + \hat{Z} I_s \quad (82)$$

where,  $[S]$  is the scattering matrix,  $\hat{Z} I_s$  accounts for external heat sources, and

$$Z_n = \frac{\Delta t}{2 \Delta \ell_n C_d} \quad (83)$$

*Connection* is the process by which reflected voltages at time-step  $k\Delta t$  ( ${}_k V_n^r$ ) are used to calculate incident voltages at time-step  $(k+1)\Delta t$  ( ${}_{k+1} V_n^i$ ). The connection process of

the TLM tetrahedral node is similar to that of the TLM triangular node (Milan and Gebremedhin, 2016).

The time evolution of the problem can be expressed as

$$[{}_{k+1}V^i] = [M][{}_kV^i] + [E] \quad (84)$$

$$[M] = [C][S] \quad (85)$$

$$[E] = [C][\hat{Z}I_S] + [B] \quad (86)$$

where,  $[C]$  is the connection matrix (Milan and Gebremedhin, 2016) and  $[B]$  accounts for the boundary condition effects. The elements of vector  $[B]$  are zero when the specific port is not in contact with a boundary. For boundary conditions, see the discussion in Section 2.4. The equation for calculating the steady-state solution can be obtained from Eq. (84) (Milan and Gebremedhin, 2016).

### 2.3. Calculating temperature and heat flux

Calculations for temperature and heat flux for the tetrahedral node are similar to the calculations for the triangular node. The temperature at the center of the node is expressed as

$${}_kT_c = {}_kV_c = [\tau][{}_kV^i] + \hat{Z}I_S = [\tau_1 \quad \tau_2 \quad \tau_3 \quad \tau_4] \begin{bmatrix} {}_kV_1^i \\ {}_kV_2^i \\ {}_kV_3^i \\ {}_kV_4^i \end{bmatrix} + \hat{Z}I_S \quad (87)$$

Calculation for the temperature between nodes follows the procedure described in (Milan and Gebremedhin, 2016). The heat flux is expressed as

$${}_k q''_{An} = \frac{{}_k T_{pn} - {}_k T_{cn}}{A_n R_n} \quad (88)$$

#### 2.4. Boundary conditions

Four types of boundary conditions can be considered in the connection process of TLM, and they are: adiabatic, temperature, heat flux, and convection. The effects of these boundary conditions in the TLM procedure for the triangular node was discussed in (Milan and Gebremedhin, 2016) and are similarly applied to the tetrahedral node except for the convection boundary condition, which has the electrical resistance calculated as

$$R_c = \frac{1}{hA} \quad (89)$$

and for which the convection heat transfer,  $h$  in  $W/(m^2 \text{ } ^\circ\text{C})$ , is defined as

$$q''_{LT} = h(T_B - T_p) \quad (90)$$

#### 2.5. Initial conditions

Initial values of the incident voltage in a node,  ${}_0 V_n^i$ , are assumed to be equal and expressed as

$${}_0 V_n^i = \frac{{}_0 T_c - \hat{Z} I_S}{\tau_1 + \tau_2 + \tau_3 + \tau_4} \quad (91)$$

#### 2.6. Convergence

The TLM approximation to the Fourier's conduction law is satisfied (Milan and Gebremedhin, 2016) when

$$1 \gg \eta_n \left| \frac{k-1 q''_{An}}{k q''_{An}} - 1 \right| \quad (92)$$

where,

$$\eta_n = \frac{A_n}{\Delta \ell_n^2} \frac{k}{\rho c} \frac{\Delta t (\Delta \ell_1 + \Delta \ell_2 + \Delta \ell_3 + \Delta \ell_4)}{4V_T} \quad (93)$$

## 2.7. Validation

To validate the TLM tetrahedral node, we used the geometry shown in Figure 10. The general equation for this problem is the Pennes' equation in differential form (Minkowycz and Sparrow, 2009; Pennes, 1948; Xu and Fu, 2011) that is expressed as

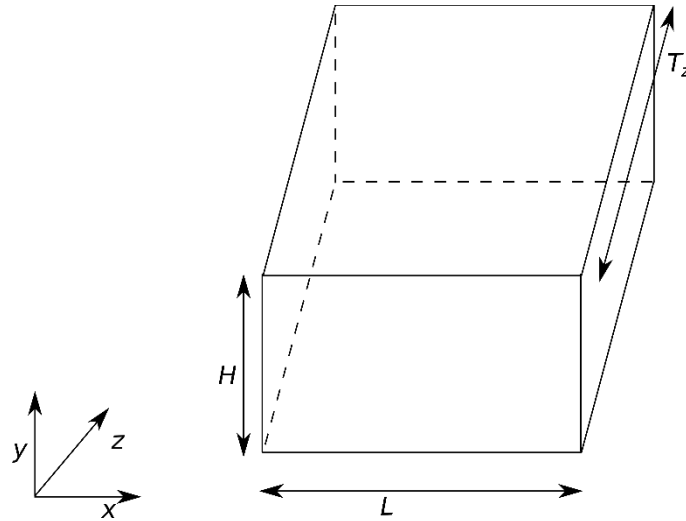


Figure 10. Computational domain for the analytical solution.  $H$  = height,  $L$  = length, and  $T_z$  = thickness.

$$\rho c \frac{\partial T}{\partial t} = -\nabla k \nabla T + \omega_b \rho_b c_b (T_b - T) V_T + q''' V_T \quad (94)$$

The following parameters were kept constant in solving the problem (Eq. (94)):  $L = 1$  mm,  $H = 0.75$  mm,  $T_z = 0.5$  mm,  $\rho = 1200$  kg/m<sup>3</sup>,  $c = 3200$  J/(kg °C),  $k = 0.3$  W/(m °C),  $\omega_b = 10^{-4}$  s<sup>-1</sup>,  $\rho_b = 1052$  kg/m<sup>3</sup>,  $c_b = 3600$  J/(kg °C),  $T_b = 37$  °C,  $q''' = 500$  W/m<sup>3</sup>,  $T_c = 37$  °C,  $T_\infty = 150$  °C,  $q''_x = 50,000$  W/m<sup>2</sup>, and  $q''_z = 25,000$  W/m<sup>2</sup>. These values were used to test the TLM tetrahedral node based on a worst-case scenario that has the following conditions: (1) the dimensions in  $x$ ,  $y$ , and  $z$  are different (*i.e.*,  $L \neq H \neq T_z$ ), (2) tissue thermal properties are different from blood thermal properties (*i.e.*,  $\rho \neq \rho_b$ ,  $c \neq c_b$ ,  $\rho c \neq \rho_b c_b$ ), and (3) the boundary conditions take extreme values.

Using the constant parameters listed above, and the boundary and initial conditions given in Table 2, Eq. (94) was solved using the principle of superposition and separation of variables. The solution of Eq. (94) is expressed as

$$T(x, y, z, t) = \sigma_z(y, z, t) + \Phi_z(y, z) + T_{2D}(x, y, t) \quad (95)$$

Table 2. Boundary and initial conditions for the problem geometry given in Figure 10.

|           | $T(x, y, z, t)$                   | $T_{2D}(x, y, t)$                      | $\Phi_z(y, z)$                         | $\sigma_z(x, y, t)$        |
|-----------|-----------------------------------|--|--|----------------------------|
| $x = 0$   | $\frac{dT}{dx} = 0$               | $\frac{dT_{2D}}{dx} = 0$               | -                                      | -                          |
| $x = L$   | $\frac{dT}{dx} = \frac{q_x''}{k}$ | $\frac{dT_{2D}}{dx} = \frac{q_x''}{k}$ | -                                      | -                          |
| $y = 0$   | $T = T_c$                         | $T_{2D} = T_c$                         | $\Phi_z = 0$                           | $\sigma_z = 0$             |
| $y = H$   | $T = T_\infty$                    | $T_{2D} = T_\infty$                    | $\Phi_z = 0$                           | $\sigma_z = 0$             |
| $z = 0$   | $\frac{dT}{dz} = 0$               | -                                      | $\frac{d\Phi_z}{dz} = 0$               | $\frac{d\sigma_z}{dz} = 0$ |
| $z = T_z$ | $\frac{dT}{dz} = \frac{q_z''}{k}$ | -                                      | $\frac{d\Phi_z}{dz} = \frac{q_z''}{k}$ | $\frac{d\sigma_z}{dz} = 0$ |
| $t = 0$   | $T = T_c$                         | $T_{2D} = T_c$                         | -                                      | $\sigma_z = -\Phi_z$       |

The solution for  $T_{2D}$  was reported in [9]. The solutions for  $\sigma_z$  and  $\Phi_z$  are

$$\Phi_z(y, z) = \sum_{m=1}^{\infty} C_{6m} \sin \lambda_m y \cosh \gamma z \quad (96)$$

$$\sigma_z(y, z, t) = \sum_{n=0}^{\infty} \sum_{m=1}^{\infty} C_{7nm} \sin \lambda_m y \cos \delta_n z \exp \left[ - \left( \lambda_m^2 + \delta_n^2 + \frac{W_b}{k} \right) \alpha t \right] \quad (97)$$

where

$$\alpha = \frac{k}{\rho c_p} \quad (98)$$

$$W_b = \omega_b \rho_b c_b \quad (99)$$

$$\lambda_m = \frac{m\pi}{H} \quad (100)$$

$$\delta_p = \frac{p\pi}{T_z} \quad (101)$$

$$\gamma = \sqrt{\frac{W_b}{k} + \lambda_m^2} \quad (102)$$

$$C_{6m} = \frac{2q_z''}{\lambda_m H k \gamma \sinh \gamma T_z} (1 - \cos \lambda_m H) \quad (103)$$

$$C_{7pm} = \frac{4q_z'' \cos \delta_p T_z}{\lambda_m H L k (\gamma^2 + \delta_p^2)} (\cos \lambda_m H - 1) \quad (104)$$

$$C_{7pm} \Big|_{p=0} = C_{70m} = \frac{2q_z''}{\lambda_m H T_z k \gamma^2} (\cos \lambda_m H - 1) \quad (105)$$

Heat flux was calculated from Fourier's conduction law.

The above solution was only meant to validate the TLM tetrahedral node procedure.

The problem does not represent any biological system, even though the heat flux at  $x =$

$L$  and at  $z = T_z$  could be assumed as environmental inputs of heat flow; the temperature at  $y = 0$  and  $y = H$  could represent measured values, and the adiabatic boundary condition at  $x = 0$  and  $z = 0$  could be produced from geometrical symmetry.

## **2.8. Effect of breast tumor on breast skin-surface temperature**

To show the potential application of the model that uses the TLM tetrahedral node, we solved a biological problem described by Amri et al. (2011). The solution of the problem was to determine the effect of blood perfusion, tumor heat production, and tumor size on breast skin-surface temperature. Using the same geometry (Fig. 11 in Amri et al., 2011), we calculated the maximum temperature difference at the skin surface for two cases, one with tumor and the other without tumor.

Figure 11 shows the problem geometry. The dimensions are: subcutaneous fat thickness,  $T_F = 5$  mm, gland thickness,  $H = 45$  mm, side lengths,  $L = 20$  mm, tumor depth = 20 mm and tumor diameter varying from 10 mm to 30 mm. Because of symmetry, a quarter of the geometry was used to solve the problem. The boundary conditions are: (1) convection heat transfer (Eq. (90)) at the skin surface with  $h = 13.5$  W/(m<sup>2</sup>-K) and  $T_B = 20$  °C, (2) constant temperature at the inner tissues boundary,  $T_c = 37$  °C, and (3) adiabatic conditions for all remaining boundaries.

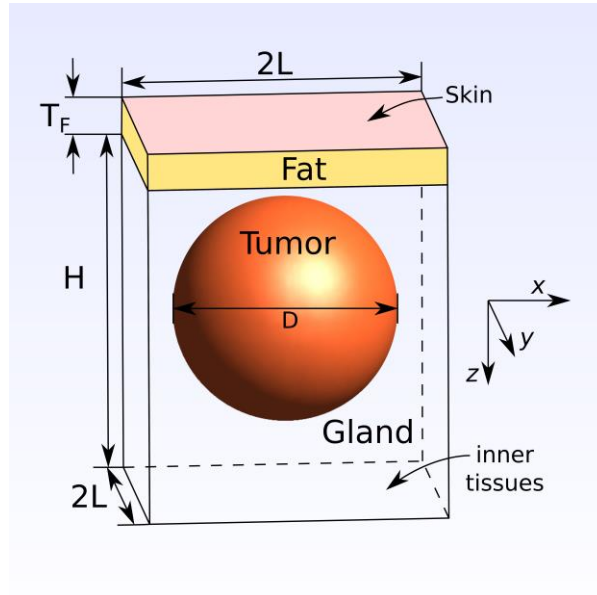


Figure 11. Computational domain for the breast with tumor.

The thermal characteristics were:  $\rho_f = 930 \text{ kg/m}^3$ ,  $c_f = 2770 \text{ J/(kg } ^\circ\text{C)}$ ,  $k_f = 0.21 \text{ W/(m } ^\circ\text{C)}$  and  $q_f''' = 400 \text{ W/m}^3$  for the subcutaneous fat,  $\rho = 1050 \text{ kg/m}^3$ ,  $c = 3770 \text{ J/(kg } ^\circ\text{C)}$  and  $k = 0.48 \text{ W/(m } ^\circ\text{C)}$  for the gland and tumor,  $q_g''' = 700 \text{ W/m}^3$  for gland, and  $\rho_b = 1100 \text{ kg/m}^3$ ,  $c_b = 3300 \text{ J/(kg } ^\circ\text{C)}$  and  $T_b = 37 \text{ } ^\circ\text{C}$  for blood (Amri et al., 2011; He et al., 2006). Metabolic heat generation for the tumor was calculated (Amri et al., 2011; Gautherie et al., 1975). Tumor blood flow was  $(c_b \omega_b) = 48,000 \text{ W/m}^3\text{-K}$  (Amri et al., 2011; Gautherie, 1980). The effect of four different combinations of blood perfusion for subcutaneous fat and gland were simulated and the values are shown in Table 3.

Table 3. Blood perfusions values (Amri et al., 2011; Ng and Sudharsan, 2001) used in the simulation to solve the breast tumor model (Figure 11).

| Tissue | $(c_b \omega_b)_1$<br>(W/m <sup>3</sup> -K) | $(c_b \omega_b)_2$<br>(W/m <sup>3</sup> -K) | $(c_b \omega_b)_3$<br>(W/m <sup>3</sup> -K) | $(c_b \omega_b)_4$<br>(W/m <sup>3</sup> -K) |
|--------|---|---|---|---|
| Fat    | 800   | 1600  | 800   | 1600  |
| Gland  | 2400  | 2400  | 3600  | 3600  |

## 2.9. Mesh-independent test

Mesh size influences the accuracy of a numerical solution. Finer meshes provide higher prediction accuracy but require a longer computing time to obtain one solution. A mesh-independent test was performed to obtain an acceptable relationship between mesh size and accuracy of the solution. Different mesh sizes were tested and changes in predictions were observed.

The mesh-independent test was performed simultaneously with model validation (Sec. 2.7). Effect of mesh size on model accuracy was analyzed using the following three mesh sizes: (1) 206 nodes and 460 ports, (2) 1,368 nodes and 2,928 ports, and (3) 69,941 nodes and 142,954 ports. The meshes were created using Gmsh software (Geuzaine and Remacle, 2009). Effect of time step ( $\Delta t$ ) on the accuracy of the model was also analyzed. The accuracy of temperature predictions was determined by

calculating the mean absolute percentage error for a simulation lasting 4 seconds. The accuracy of heat flux was determined by calculating the mean absolute difference rather than the mean absolute percentage error because heat flux could become near zero during the simulation. The accuracy of the model for estimating temperature and heat flux in a steady-state condition was also determined using the same procedure.

The mesh-independent test for the breast tumor model (Sec. 2.8) was performed by calculating the breast skin-surface temperature for blood perfusion  $(c_b \omega_b)_1$  (Table 3) with tumor diameter of 30 mm and without tumor. The maximum, minimum, and average temperature differences between the two cases were computed and were used to decide on the mesh size to be used for the remaining calculations. The meshes were created using Gmsh software (Geuzaine and Remacle, 2009).

### ***3. RESULTS AND DISCUSSION***

The difference between the tetrahedral nodes and the parallelepiped nodes (Milan et al., 2014) is that the tetrahedral nodes require additional approximation associated with Eq. (76) while the parallelepiped nodes require no such additional approximation. For this reason, the tetrahedral-node approach is more appropriate for problems of complex geometry, whereas the parallelepiped nodes, which use less approximations, are more appropriate for problems without geometrical complexities. The reason is that complex geometries could be fitted with less tetrahedral nodes than is the case with parallelepiped nodes. Tetrahedral and parallelepiped nodes could, however, be used in the same mesh to benefit from the advantages of both approaches.

The accuracy of the model using the tetrahedral node, as calculated in the validation (Sec. 2.7), is shown in Figure 12. The predicted temperatures from the TLM model and the analytical 3-D model agreed within 2% for a mesh size of 69,941 and a time step of 5ms. The increase in number of nodes led to a decrease in the length of the transmission-line ( $\Delta\ell_n$ ). The decrease of  $\Delta\ell_n$  improved the approximations related to Eq. (76). For the steady-state solution, the prediction accuracy increased in all cases except for the prediction of heat flux where there was no improvement between a mesh size of 1,368 nodes and 69,941 nodes.

For the time-domain solution, for a given mesh-size, decreasing the time-step ( $\Delta t$ ) increased the accuracy of the model because a decrease in  $\Delta t$  improved the requirement shown in Eq. (93). For large values of  $\Delta t$ , however, the accuracy of the model in predicting heat flux decreased when the mesh-size was increased because it increased the right-hand-side value of Eq. (93). This was observed because when only the mesh size was increased, and for large values of  $\Delta t$ ,  $\eta_n$  (Eq. (92)) increases and then, as predicted by Eq. (93), the accuracy of the TLM model decreased. Furthermore,  $\eta_n$  is proportional to  $\Delta\ell_n$  and  $\Delta t$  but inversely proportional to  $\Delta\ell_n^2$ . This means that, for a given value of  $\Delta t$ , the value of  $\eta_n$  will increase when the mesh size is increased (*i.e.*,  $\Delta\ell_n$  is decreased) and, hence, the accuracy of the model will decrease. For refined meshes, decreasing  $\Delta t$  increased the accuracy of the model considerably. For example, comparing the predicted heat flux using a mesh size of 1,368 nodes and 69,941 nodes resulted in lower value of  $\eta_n$  and, consequently, improved the time and space

approximation of TLM.

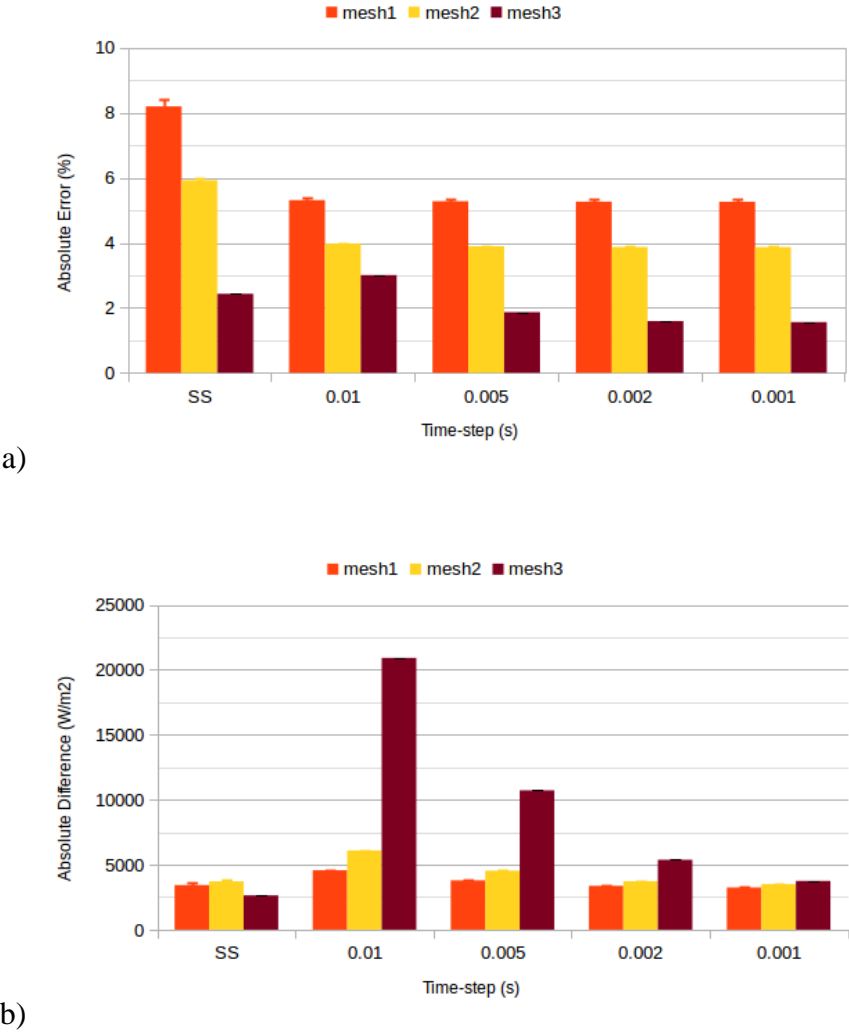


Figure 12. (a) Absolute percentage error in predicting the temperature, and (b) absolute difference in predicting the heat flux using the TLM tetrahedral node. Bars represent standard error, and *SS* represents steady-state condition. The mean error and absolute difference for the steady state correspond to the mean and standard error for all nodes and ports. For the problem solved in time domain, the mean error and absolute error for all the simulation time (mean values for each time step) are shown.

The longest computational time resulted when the mesh size of 69,941 nodes and 1ms time step were used. The computational time required to solve the analytical equations was 5.67 hours (using in-house algorithm optimized for Octave/Matlab). The computation time required to solve the same problem but using the TLM for a steady-state condition was only 2.28 min (4.86 GB peak RAM memory use). Solving the same problem in time-domain took 0.22 min (0.25 GB peak RAM memory use) and that was 1550 times faster than solving the analytical equations. This computational-time difference was expected because the analytical equations require solving infinity sums (Eqs. (96)-(97)), and the TLM steady-state solution involves the inversion of a matrix (high computational cost) whereas the TLM time-domain solution involves matrix multiplications.

Table 4 shows the mesh-independent test for the breast model with tumor. As the mesh size increases, the computing time and the RAM memory peak use also increases. The values for the average, minimum and maximum temperature difference at the skin surface oscillate between mesh sizes #1 to #6 but stabilize at mesh size #7 (Table 4). Mesh size #7 was used for the remaining computations.

Table 4. Number of nodes, results of minimum, average and maximum temperature, computing time and memory space used in the mesh-independent test for the breast tumor model.

| Mesh-size       | Number of nodes | T <sub>avg</sub> (°C) <sup>a</sup> | T <sub>min</sub> (°C) <sup>a</sup> | T <sub>max</sub> (°C) <sup>a</sup> | Computing time (min) <sup>b</sup> | RAM memory peak use (GB) <sup>b</sup> |
|-----------------|-----------------|------------------------------------|------------------------------------|------------------------------------|-----------------------------------|---------------------------------------|
| #1              | 9,962           | 0.35                               | 0.26                               | 0.50                               | 0.03                              | 0.24                                  |
| #2              | 12,534          | 0.37                               | 0.26                               | 0.53                               | 0.05                              | 0.30                                  |
| #3              | 15,213          | 0.36                               | 0.26                               | 0.51                               | 0.07                              | 0.49                                  |
| #4              | 21,352          | 0.38                               | 0.28                               | 0.54                               | 0.13                              | 0.70                                  |
| #5              | 31,089          | 0.37                               | 0.27                               | 0.53                               | 0.27                              | 1.41                                  |
| #6              | 48,044          | 0.38                               | 0.27                               | 0.53                               | 0.73                              | 2.26                                  |
| #7 <sup>c</sup> | 87,664          | 0.38                               | 0.28                               | 0.55                               | 2.57                              | 5.90                                  |
| #8              | 104,072         | 0.39                               | 0.28                               | 0.55                               | 4.02                              | 7.08                                  |
| #9              | 121,286         | 0.39                               | 0.28                               | 0.55                               | 4.81                              | 11.50                                 |
| #10             | 138,087         | 0.39                               | 0.28                               | 0.55                               | 7.11                              | 13.25                                 |

|     |         |      |      |      |       |       |
|-----|---------|------|------|------|-------|-------|
| #11 | 156,871 | 0.39 | 0.28 | 0.55 | 9.72  | 15.21 |
| #12 | 193,400 | 0.39 | 0.29 | 0.55 | 17.89 | 19.02 |

---

<sup>a</sup>Skin-surface temperature difference between a breast with tumor and without. Diameter (D) of tumor = 30 mm. Blood perfusion  $(c_b \omega_b)_1$  is given in Table 3.

<sup>b</sup>Computing time and peak RAM memory use for solving the problem with tumor.

<sup>c</sup>Mesh size used for all of the computations in this paper.

Figure 13 shows the maximum skin-surface temperature difference for the breast with and without tumor. Our model accurately replicates the temperature trend given in Amri et al. (2011). Figure 13 shows that the bigger the tumor the larger the maximum skin-surface temperature difference. Blood flow in the subcutaneous fat and gland tissues affect skin-temperature difference if the tumor diameter is greater than 15 mm. The largest temperature difference was at the lowest blood perfusion rate for subcutaneous fat and gland,  $(c_b \omega_b)_1$ . Furthermore, the maximum skin-surface temperature difference calculated using the tetrahedral TLM node was similar to that calculated using the TLM parallelepiped node reported by Amri et al. (2011). The mean difference between the two values was less than 6%. The difference between the two results, however small, may be because different mesh sizes were used. The paper by Amri et al. (2011) provided no mesh size or mesh-independent test.

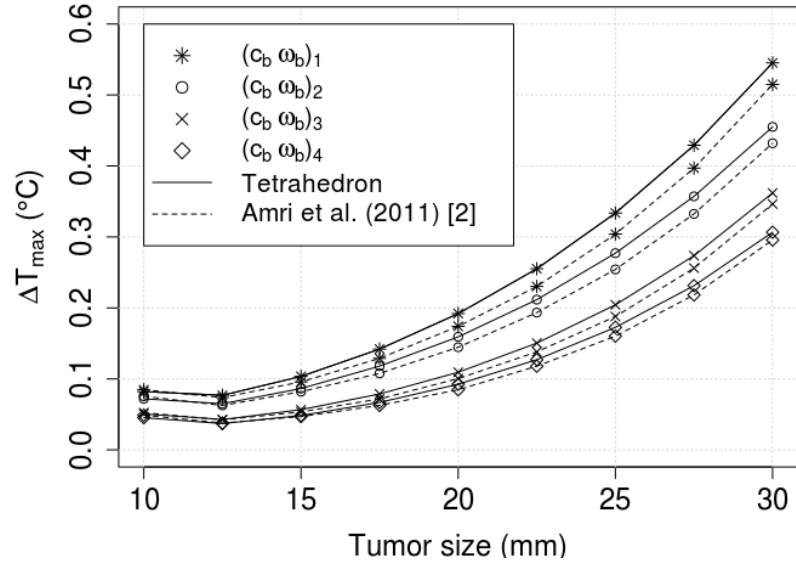


Figure 13. Maximum skin-surface temperature difference between a breast with tumor and without ( $\Delta T_{\max}$ ).  $(c_b \omega_b)_n$  represent different blood perfusion values (Table 3).

Based on the validations presented previously, it can be concluded that the TLM tetrahedral node has great potential in heat-transfer applications of biological systems. The advantages of the TLM tetrahedral node are that: (1) it allows to model complex geometries with time-dependent problems, and (2) it can include heat sources, blood perfusion, and different boundary conditions (adiabatic, temperature, heat flux, convection).

#### 4. CONCLUSIONS

The following specific conclusions can be drawn from this study:

- (1) The predicted temperature and heat flux values from the 3-D tetrahedral-node model were compared against the results obtained from an analytical solution,

and the results agreed within 2% for a mesh size of 69,941 nodes and a time step of 5ms.

- (2) The method was further validated against published results of maximum skin-surface temperature difference in a breast with and without tumor and the results agreed within 6%. The published results were obtained from a model that used the parallelepiped TLM node.
- (3) Use of Tetrahedral nodes requires less number of nodes in fitting irregular geometries compared to using parallelepiped nodes, and has great potential in the application of heat-transfer problems of biological systems. The model includes heat source, blood perfusion, boundary conditions (adiabatic, temperature, heat flux or convection) and initial conditions.
- (4) The computational time for a mesh size of 69,941 nodes and 1ms time step was 1550 times faster using the TLM tetrahedral node compared to the analytical computation.

### ***Acknowledgment***

Brazilian National Council of Technological and Scientific Development (Proc. 203312/2014-7) for scholarship to HFMM.

## REFERENCES

Alexander CK, Sadiku MNO. *Fundamentals of Electric Circuits (5th ed)*. McGraw-Hill: New York, NY, 2012.

Amri A, Saidane A, Pulko S. Thermal analysis of a three-dimensional breast model with embedded tumour using the transmission line matrix (tlm) method. *Comput Biol Med* 41(2):76-86, 2011.

Amri A, Pulko SH, Wilkinson, AJ. Potentialities of steady-state and transient thermography in breast tumour depth detection: A numerical study. *Comput Methods Programs Biomed* 123:68-80, 2016.

Bellia SA, Saidane A, Benzohra M, Saiter JM, Hamou A. Dimensional soft tissue thermal injury analysis using transmission line matrix (tlm) method. *Int J Numer Model* 21(6):531-549, 2008a.

Bellia SA, Saidane A, Hamou A, Benzohra M, Saiter JM. Transmission line matrix modelling of thermal injuries to skin. *Burns* 34(5):688-697, 2008b.

Bellil M, Bennaoum S. *Tlm modelling of laser thermal treatment of benign prostate hyperplasia*. International Conference on Control, Engineering & Information Technolog, pp 1-5, 2013.

Bellil M, Saidane A, Bennaoum S. *Transmission line matrix modelling of bioheat transfer in cryogenic therapy applications*. International Conference on Control, 73

Engineering & Information Technol, pp. 1-6, 2013.

de Cogan D. *Transmission Line Matrix (TLM) Techniques for Diffusion Applications*. Gordon and Breach Science Publishers: Amsterdam, Netherlands, 1998.

de Cogan D, Connor WJO, Pulko S. *Transmission Line Matrix in Computational Mechanics*. CRC Taylor & Francis: Boca Raton, FL, 2006.

Gautherie M, Quenneville Y, Gros CM. Metabolic heat production, growth rate and prognosis of early breast carcinomas. *Biomedicine* 22:328-336, 1975.

Gautherie M. Thermopathology of breast cancer: measurement and analysis of in vivo temperature and blood flow. *Ann N Y Acad Sci* 335(1):383-415, 1980.

Geuzaine C, Remacle JF. A three-dimensional finite element mesh generator with built-in pre- and post-processing facilities. *Int J Numer Meth Eng* 79:1309-1331, 2009.

He Y, Shirazaki M, Liu H, Himeno R, Sun Z. A numerical coupling model to analyse the blood flow, temperature, and oxygen transport in human breast tumor under laser irradiation. *Comput Biol Med* 36(12):1336-1350, 2006.

Maia ASC, Milan HFM, Gebremedhin KG. *Analytical and numerical modeling of skin surface temperature in livestock*. 20th International Congress of Biometeorology, pp. 1, 2014.

Minkowycz WJ, Sparrow EM. *Advances in Numerical Heat Transfer (volume 3)*. CRC

Press: Boca Raton, FL, 2009.

Milan HFM, Carvalho Jr CAT, Maia ASC, Gebremedhin KG. Graded meshes in bio-thermal problems with transmission-line modeling method. *J Therm Biol* 45:43-53, 2014.

Milan HFM, Gebremedhin KG. Triangular node for transmission-line modeling (TLM) applied to bio-heat transfer. *J Therm Biol* 62:116-122, 2016.

Ng EYK, Sudharsan NM. An improved three-dimensional direct numerical modelling and thermal analysis of a female breast with tumor. *Proc Inst Mech Eng H* 215(1):25-37, 2001.

Pennes HH. Analysis of tissue and arterial blood temperature in the resting human forearm. *J Appl Phys* 1(2):93-122, 1948.

Sewell P, Benson T, Christopoulos C, Thomas DWP, Vukovic A, Wykes J. Transmission-line modeling (TLM) based upon unstructured tetrahedral meshes. *IEEE T Microw Theory Tech* 53(6):1919-1928, 2005.

Sewell P, Wykes JG, Benson T, Thomas DWP, Vukovic A, Christopoulos C. Transmission line modelling using unstructured meshes. *IEE Proc-Sci Meas Technol* 151(6):445-448, 2004.

Xu F, Lu T. Introduction to skin biothermomechanics and thermal pain. Springer: Berlin, Germany, 2011.

CHAPTER 3: GENERAL NODE FOR TRANSMISSION-LINE MODELING (TLM)  
METHOD APPLIED TO BIO-HEAT TRANSFER

Hugo Fernando Maia Milan, Kifle G. Gebremedhin

Published in *International Journal of Numerical Modelling: Electronic Networks, Devices and Fields*: Milan HFM, Gebremedhin KG. General node for transmission-line modeling (TLM) method applied to bio-heat transfer. *Int J Num Model* e2455:1-13, 2018.

***Abstract***

Transmission-line modeling (TLM) is a numerical method used to solve coupled partial differential equations in time domain. Using TLM, the equations of the problem and a small control volume are represented by an electric network composed of nodes. In this paper, a general TLM node theory for bio-heat transfer that simplifies to existing node formulations is presented. This formulation allows the use of irregular node geometries, such as irregular quadrangles and hexahedrons, which are necessary to accurately model complex geometries of biological systems. Using irregular hexahedron nodes, solutions of skin-surface temperatures of a breast with tumor are demonstrated. This theory is based on two assumptions. The first is that the unit vector perpendicular to the border of the node is similar to the unit vector from the center of the node to the midpoint of its border, which is exact for regular geometries (e.g., rectangles in 2-D, and parallelepipeds in 3-D) and approximated for most irregular

geometries used in practice (e.g., triangles and quadrangles in 2-D, and tetrahedrons and hexahedrons in 3-D). This first assumption does not, however, hold for all geometries such as 3-D pyramids. The second assumption, which is controlled by an error parameter, is that the dispersive effect intrinsically modeled by the transmission-line inductor is negligible compared to the diffusive effect modeled by the resistor of the node. This general TLM node formulation facilitates algorithm development and increased flexibility, which improve the applicability of TLM to solve complex geometric problems, which are typical of most biological systems.

**Keywords:** bio-heat transfer, complex geometries, transmission-line modeling.

## ***1. INTRODUCTION***

Transmission-line modeling (TLM) method is a traditional numerical method used to solve systems of partial differential equations in time domain. The TLM principle is to substitute the computational domain by an equivalent network of circuit elements (Kron, 1945, 1948) and transmission lines (Johns and Beurle, 1971; Johns, 1977). The essential arrangement of the circuit elements and transmission lines is called node and the node represents the equations of the problem as well as a small control volume. The properties of the node and its elements give TLM its main advantages, which are stability (de Cogan, 1998; de Cogan et al., 2005) and non-requirement of matrix inversion for time-domain solutions (Christopoulos, 1995, 2006; Weiner, 2010). Because of these advantages, TLM has become an increasingly popular method to solve problems in heat transfer in biological tissues (Amri et al., 2011, 2016; Bellia et al., 2008ab; Bellil and Bennaoum, 2013; Bellil et al., 2013, 2015; Ijeh et al., 2017ab; Maia et al., 2014; Makhlouf et al., 2015, 2016ab; Milan, 2017; Milan and Gebremedhin, 2016abcd; Milan et al., 2014).

The limitation of the TLM method is that, for every control volume geometry, a new circuit node must be developed. The first developed TLM node formulation was for regular geometries (squares and cubes) (Bellia et al., 2008ab) and was later expanded to include graded elements (rectangles and parallelepipeds) (Milan et al., 2014) and orthogonal curvilinear elements (such as cylinders) (Austin and Pulko, 1993; Pulko et al., 1986). However, bio-heat-transfer problems have inherently complex geometries

that are difficult to accurately model using the node geometries previously described. To tackle this problem, we developed irregular triangular (Milan and Gebremedhin, 2016a) and tetrahedral (Milan and Gebremedhin, 2016b) node formulations that accurately model biological complex geometries. These formulations are not, however, general and do not extend to other geometries. In this paper, we propose a general TLM node theory that simplifies to existing node formulations and extends further to solve irregular quadrangles and hexahedrons. This formulation, therefore, allows solution of complex geometries, which are typical of most biological systems.

## **2. PROCEDURE**

In TLM (Christopoulos, 1995, 2006; de Cogan, 1998; de Cogan et al., 2005; Weiner, 2010), the computational domain is replaced by a network of transmission lines and circuit elements whose values are calculated based on the problem specification. This process is denoted *isomorphism*, and guarantees that the governing equations from the original problem have the same form as the resulting equations from the network. Inside the network, the problem is solved using *incident* and *reflected* voltages. Incident voltages travel inside the node from the transmission-line borders to the center of the node, where they are *scattered* and become reflected voltages traveling from the center to the borders. When reflected voltages reach the transmission-line border, they travel between *connected* nodes to become incident voltages in the neighboring nodes. How to enforce isomorphism using the general TLM node and how to compute scattering, connection, boundary conditions, initial conditions,

temperature, and heat flux are shown below.

## 2.1. Isomorphism

The theory of the general TLM node is based on performing energy balance on a general control volume. Figure 14 shows examples of control volumes in 1-D, 2-D, and 3-D. Inside the control volume, transmission lines connect the center of the node to the midpoint of its border. The connection point is called *port* and connects the node with its neighbors.

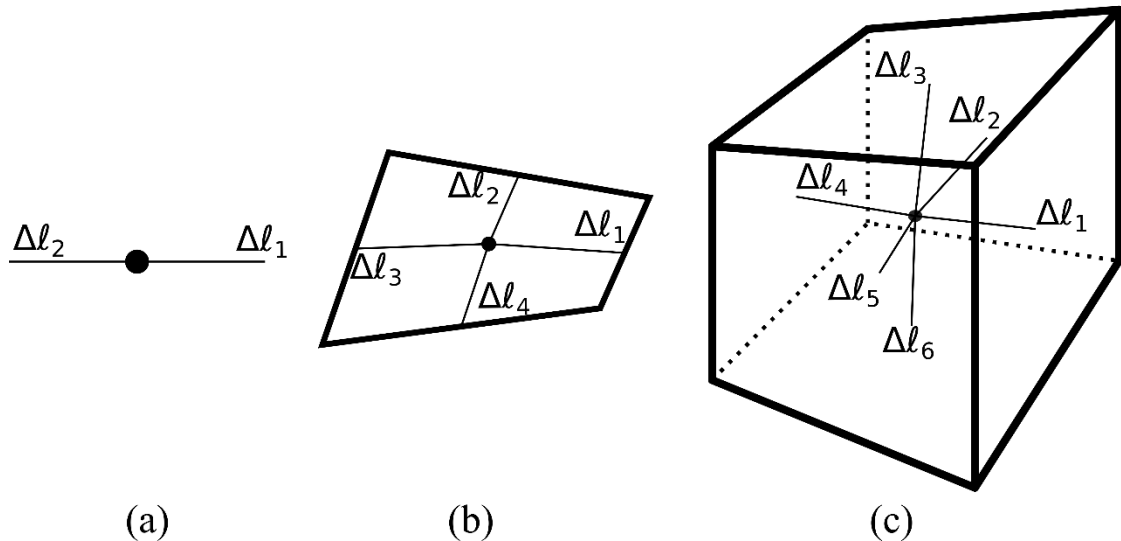


Figure 14. Example of control volumes for a general TLM node in (a) 1-D, (b) 2-D, and (c) 3-D. The dot represents the center of the geometry and  $\Delta l_n$  is the distance between the center and border  $n$ , which is defined as the length of the transmission line  $n$ . Transmission lines are represented by thin lines and control volume boundaries are represented by thick lines.

Assuming that heat flux is constant at boundary  $n$ , the Pennes (Pennes, 1948; Minkowycz and Sparrow, 2009) bio-heat energy conservation equation is expressed as

$$\rho c L_1 \frac{\partial T}{\partial t} = \sum_{n=1}^N \vec{q}_n L_{2,n} + \omega_b \rho_b c_b (T_b - T) L_1 + q''' L_1 \quad (106)$$

and the Fourier law is expressed as

$$\vec{q}_n = -k \frac{\partial T}{\partial \vec{L}_{2,n}} \quad (107)$$

where,  $\rho$  ( $\text{kg}/\text{m}^3$ ) = density,  $c$  ( $\text{J}/(\text{kg } ^\circ\text{C})$ ) = specific heat,  $T$  ( $^\circ\text{C}$ ) = temperature,  $t$  (s) = time,  $\vec{q}_n$  ( $\text{W}/\text{m}^2$ ) = heat flux in direction  $n$ ,  $\omega_b$  ( $\text{s}^{-1}$ ) = blood perfusion,  $\rho_b$  ( $\text{kg}/\text{m}^3$ ) = blood density,  $c_b$  ( $\text{J}/(\text{kg } ^\circ\text{C})$ ) = blood specific heat,  $T_b$  ( $^\circ\text{C}$ ) = blood temperature,  $q'''$  ( $\text{W}/\text{m}^3$ ) = heat sources,  $k$  ( $\text{W}/(\text{m } ^\circ\text{C})$ ) = thermal conductivity,  $N$  = number of borders,  $L_1$  and  $L_{2,n}$  are defined in Table 5, and  $\vec{L}_{2,n}$  = vector perpendicular to  $L_{2,n}$ .

Figure 15 shows the general TLM node circuit where resistors  $R_n$  represent heat conductivity in Fourier law, conductor  $G$  represents heat loss due to blood perfusion effects, current source  $I_S$  represents heat generation and blood perfusion effects, capacitors  $C_{dn}$  represent heat capacity, and inductors  $L_{dn}$  are artifacts from transmission-line theory. Using Kirchhoff voltage and current laws (Alexander and Sadiku, 2012), the node equation is written as

$$\sum_{n=1}^N C_{dn} \Delta \ell_n \frac{\partial V}{\partial t} + GV = \sum_{n=1}^N I_n + I_S \quad (108)$$

Table 5. Definition of  $L_1$  and  $L_{2,n}$  for 1-D, 2-D, and 3-D.  $L_1$  is a measure of node dimension and  $L_{2,n}$  is a measure of boundary  $n$  dimension.

|     | $L_1$  | $L_{2,n}$    |
|-----|--------|--------------|
| 1-D | Length | 1            |
| 2-D | Area   | Edge length  |
| 3-D | Volume | Surface area |

Assuming  $C_{dn} = C_d$ , the isomorphism between Eq. (106) and (108) is guaranteed when

$$V \equiv T \quad (109)$$

$$I_n \equiv \vec{q}_n L_{2,n} \quad (110)$$

$$C_d \equiv \frac{\rho c L_1}{\sum_{n=1}^N \Delta \ell_n} \quad (111)$$

$$G \equiv \omega_b \rho_b c_b L_1 \quad (112)$$

$$I_S \equiv \omega_b \rho_b c_b T_b L_1 + q''' L_1 \quad (113)$$

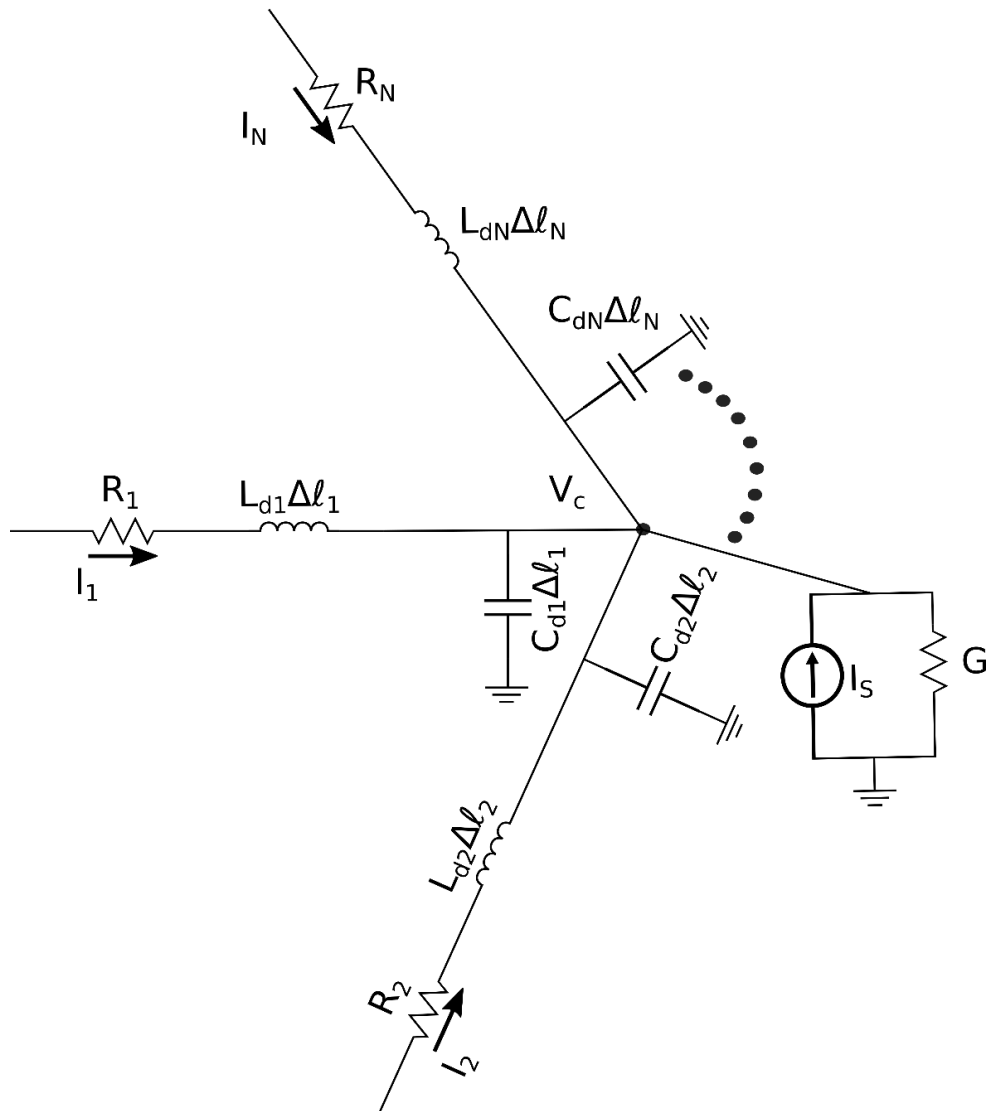


Figure 15. General node for the transmission line modeling method applied to a bio-heat transfer problem.  $V_c$  is voltage in the center of the node,  $I_n$  is current flowing through transmission line  $n$ ,  $L_{dn}$  and  $C_{dn}$  are, respectively, inductance and capacitance per unit length of transmission line  $n$ ,  $R_n$  is resistance connected in series with transmission line  $n$ ,  $I_S$  is current source connected to the center of the node, and  $G$  is conductance connected to the center of the node.

Analyzing the circuit between the center of the node and the port yields

$$I_n + \frac{L_{dn}}{R_n} \frac{\partial I_n}{\partial t} = - \frac{\Delta \ell_n}{R_n} \frac{\partial V}{\partial \vec{\ell}_n} \quad (114)$$

Assuming

$$\frac{\partial T}{\partial \vec{\ell}_n} \approx \frac{\partial T}{\partial \vec{L}_{2,n}} \quad (115)$$

$$|I_n| \gg \left| \frac{L_{dn}}{R_n} \frac{\partial I_n}{\partial t} \right| \quad (116)$$

where  $\vec{\ell}_n$  is the unit vector from the center of the node to port  $n$ , Eq. (114) is re-written as

$$I_n = - \frac{\Delta \ell_n}{R_n} \frac{\partial V}{\partial \vec{L}_{2,n}} \quad (117)$$

and the isomorphism between Eqs. (107) and (117) is guaranteed when

$$R_n \equiv \frac{\Delta \ell_n}{k L_{2,n}} \quad (118)$$

Note that this formulation is based on two assumptions. The first (Eq. (115)) is that the direction of transmission line  $n$  is similar to the perpendicular direction of the control volume boundary. For instance, in quadrangles (Figure 14b),  $\vec{\ell}_n$  is the unit vector from the center of the quadrangle to the midpoint of the border,  $\vec{L}_{2,n}$  is the unit vector

perpendicular to the direction of the boundary, and  $\theta$  is the angle between the vectors  $\vec{L}_{2,n}$  and  $\vec{\ell}_n$ . These two vectors are equal (i.e.,  $\theta = 0^\circ$ ) for regular geometries (e.g., rectangle and parallelepiped) and similar (i.e.,  $\theta \approx 0^\circ$ ) for irregular geometries used in practice (e.g., triangles, quadrangles, tetrahedrons, and irregular hexahedrons) as will be shown in the validation. The second assumption (Eq. (116)) is that, in the transmission line, diffusion dominates over dispersion. Transmission lines intrinsically model dispersion but the governing equation under consideration (Eq. (107)) only includes diffusion effects. This assumption that dispersion is negligible over diffusion can be verified by the following error parameter:

$$\xi_n = \frac{L_{2,n}}{L_1} \frac{k}{\rho c} \frac{\Delta t}{4\Delta\ell_n^2} \sum_{n=1}^N \Delta\ell_n \quad (119)$$

$$1 \gg \xi_n \left| \frac{{}_t-\Delta t q_n''}{{}_t q_n''} - 1 \right| \quad (120)$$

where  ${}_t q_n''$  represents heat flux in the direction of the transmission line  $n$  at time  $t$ .

It is important to note that, with minor modifications, Eqs. (108)-(44) can be simplified to the previously published formulations (Amri et al., 2011; Bellia et al., 2008ab; Bellil and Bennaoum, 2013; Bellil et al., 2013, 2015; Milan and Gebremedhin, 2016ab; Milan et al., 2014).

## 2.2. Scattering, connection, boundary conditions, initial conditions, temperature calculation, and heat flux calculation

Scattering is computed as the resultant voltage in the impedances  $Z_n$  of the Thévenin's equivalent circuit (Figure 16) of the general TLM node circuit (Figure 15):

$$Z_n = \frac{\Delta t}{2\Delta\ell_n C_{dn}} \quad (121)$$

$$\hat{Z} = \left[ G + \sum_{n=1}^N \frac{1}{Z_n} \right]^{-1} \quad (122)$$

$$\tau_n = 2 \frac{\hat{Z}}{Z_n} \quad (123)$$

$$[{}_k V^r] = [S][{}_k V^i] + \hat{Z} I_S \quad (124)$$

$$\begin{bmatrix} {}_k V_1^r \\ {}_k V_2^r \\ \vdots \\ {}_k V_N^r \end{bmatrix} = \begin{bmatrix} \tau_1 - 1 & \tau_2 & \cdots & \tau_N \\ \tau_1 & \tau_2 - 1 & \cdots & \tau_N \\ \vdots & \vdots & \ddots & \vdots \\ \tau_1 & \tau_2 & \cdots & \tau_N - 1 \end{bmatrix} \begin{bmatrix} {}_k V_1^i \\ {}_k V_2^i \\ \vdots \\ {}_k V_N^i \end{bmatrix} + \hat{Z} I_S \quad (125)$$

where, the subscript  $k$  refers to time  $t = k\Delta t$ .

Temperature at the center of the node is calculated from

$${}_k T_c = {}_k V_c = [\tau][{}_k V^i] + \hat{Z} I_S = [\tau_1 \quad \tau_2 \quad \cdots \quad \tau_N] \begin{bmatrix} {}_k V_1^i \\ {}_k V_2^i \\ \vdots \\ {}_k V_N^i \end{bmatrix} + \hat{Z} I_S \quad (126)$$

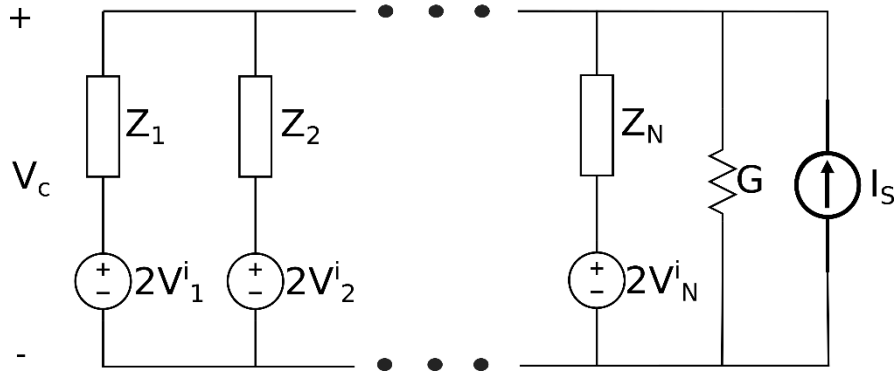


Figure 16. Thévenin's equivalent circuit of the general TLM node circuit (Figure 15).

$V_c$  represents voltage at the center of the node,  $Z_n$  represents impedance of transmission line  $n$ , and  $V_n^i$  represents incident voltage in transmission line  $n$ .

Connection and calculation of temperature between nodes and heat fluxes are as previously described (Milan and Gebremedhin, 2016a). Initial condition is expressed as

$${}_0V_n^i = \frac{{}_0T_c - \hat{Z}I_S}{\sum_{n=1}^N \tau_n} \quad (127)$$

Boundary conditions are modeled as previously described (Milan and Gebremedhin, 2016a).

### 2.3. Validation

Calculations were performed using the software TLMBHT (Milan, 2017) in Oryx Pro from System76, with Ubuntu 16.04, 512 GB PCIe M.2 SSD, 64 GB DDR4 RAM memory (2133 MHz), i7-6820HK (3.6 GHz), 8 GB GeForce GTX 980M. All meshes

were obtained using Gmsh (Geuzaine and Remacle, 2009).

Because the formulation described in this study reduces to published formulations, it can be said that the following node geometries are already validated: lines (Amri et al., 2011; Bellia et al., 2008ab; Bellil et al., 2013) and graded lines (Milan et al., 2014) in 1-D; squares (Amri et al., 2011; Bellia et al., 2008ab; Bellil and Bennaoum, 2013; Bellil et al., 2015), rectangles (Milan et al., 2014), and triangles (Milan and Gebremedhin, 2016a) in 2-D; cubes (Amri et al., 2011; Bellia et al., 2008ab), parallelepipeds (Milan et al., 2014), and tetrahedrons (Milan and Gebremedhin, 2016b) in 3-D. The validation performed in this paper is for non-previously described node elements, which are: irregular quadrangle in 2-D (Figure 17a), irregular hexahedron in 3-D (Figure 17b), and pyramids in 3-D (Figure 17c). For comparison, the regular counterparts of quadrangles and hexahedrons are included.

To validate irregular quadrangles, temperature and heat flux computed using TLM (Table 6) were compared with values obtained from an analytical solution of the problem shown in Figure 18a (for the analytical solution, refer to Milan and Gebremedhin, 2016a) with the following parameters:  $L = 0.75$  mm,  $H = 1$  mm,  $\rho = 1200$  kg/m<sup>3</sup>,  $c = 3200$  J/(kg °C),  $k = 0.3$  W/(m °C),  $\omega_b = 10^{-4}$  s<sup>-1</sup>,  $\rho_b = 1052$  kg/m<sup>3</sup>,  $c_b = 3600$  J/(kg °C),  $T_b = 37$  °C,  $q''' = 500$  W/m<sup>3</sup>,  $T_c = 37$  °C,  $T_\infty = 100$  °C, and  $q'' = 100,000$  W/m<sup>2</sup>.

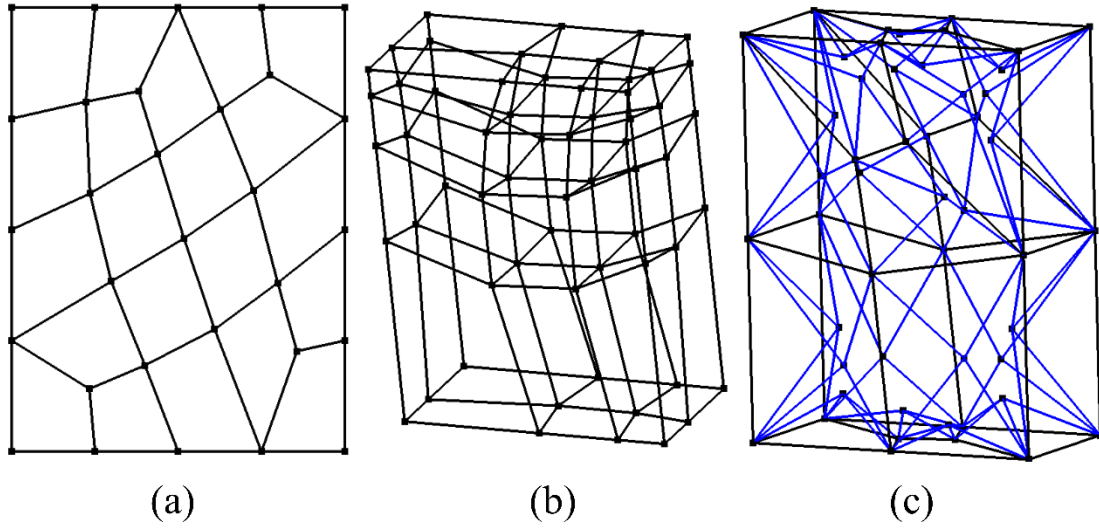


Figure 17. Example of meshes with (a) irregular quadrangles, (b) irregular hexahedrons, and (c) pyramids. In (c), pyramids (blue lines) were used to connect boundaries segmented with irregular quadrangles (black lines) with the domain segmented with tetrahedrons (not shown). Lines represent borders of geometry elements.

To validate irregular hexahedrons (Grandy, 1997) and pyramids, temperature and heat flux computed using TLM (Table 6 and Table 7) were compared with values obtained from an analytical solution of the problem shown in Figure 18b (for the analytical solution, refer to Milan and Gebremedhin, 2016b) with the following parameters:  $L = 1 \text{ mm}$ ,  $H = 0.75 \text{ mm}$ ,  $T_z = 0.375 \text{ mm}$ ,  $\rho = 1200 \text{ kg/m}^3$ ,  $c = 3200 \text{ J/(kg } ^\circ\text{C)}$ ,  $k = 0.3 \text{ W/(m } ^\circ\text{C)}$ ,  $\omega_b = 10^{-4} \text{ s}^{-1}$ ,  $\rho_b = 1052 \text{ kg/m}^3$ ,  $c_b = 3600 \text{ J/(kg } ^\circ\text{C)}$ ,  $T_b = 37 \text{ } ^\circ\text{C}$ ,  $q''' = 500 \text{ W/m}^3$ ,  $T_c = 37 \text{ } ^\circ\text{C}$ ,  $T_\infty = 100 \text{ } ^\circ\text{C}$ ,  $q''_x = 10,000 \text{ W/m}^2$ , and  $q''_z = 100,000 \text{ W/m}^2$ .

Table 6. Definition of meshes for regular and irregular quadrangles and regular hexahedrons. The meshes are defined in terms of number of nodes (#N), number of ports (#P), and the angle ( $\theta$ ) between vectors  $\vec{L}_{2,n}$  and  $\vec{\ell}_n$ .

|        | Regular Quadrangle |      |            | Irregular Quadrangle |      |                  | Regular Hexahedron |        |           |
|--------|--------------------|------|------------|----------------------|------|------------------|--------------------|--------|-----------|
|        | #N                 | #P   | $\theta^1$ | #N                   | #P   | $\theta$         | #N                 | #P     | $\theta$  |
| Mesh 1 | 64                 | 144  | $0 \pm 0$  | 76                   | 168  | $13.66 \pm 0.61$ | 504                | 1730   | $0 \pm 0$ |
| Mesh 2 | 256                | 544  | $0 \pm 0$  | 308                  | 648  | $12.36 \pm 0.28$ | 1512               | 4962   | $0 \pm 0$ |
| Mesh 3 | 1024               | 2112 | $0 \pm 0$  | 1193                 | 2450 | $10.04 \pm 0.12$ | 4032               | 12968  | $0 \pm 0$ |
| Mesh 4 | 4096               | 8320 | $0 \pm 0$  | 4801                 | 9730 | $9.83 \pm 0.06$  | 32256              | 100256 | $0 \pm 0$ |

<sup>1</sup>Mean value in degrees  $\pm$  standard error of the mean.

The validation problems were solved using time steps of 1 *ms*, 10 *ms*, or 100 *ms*, for a simulation time of 10 *s*. The accuracy in predicting temperature inside the node, and temperature and heat flux between nodes was computed for 100 time steps to reduce the computational burden in calculating the time-consuming analytical solutions. The evaluation metric for temperature was expressed in percentage error. The evaluation metric for heat flux was calculated by dividing the absolute difference between the heat flux calculated using TLM vs. the heat flux calculated using the analytical solution by the maximum heat flux input because heat fluxes could be near zero,

which renders percentage a misleading evaluation metric.

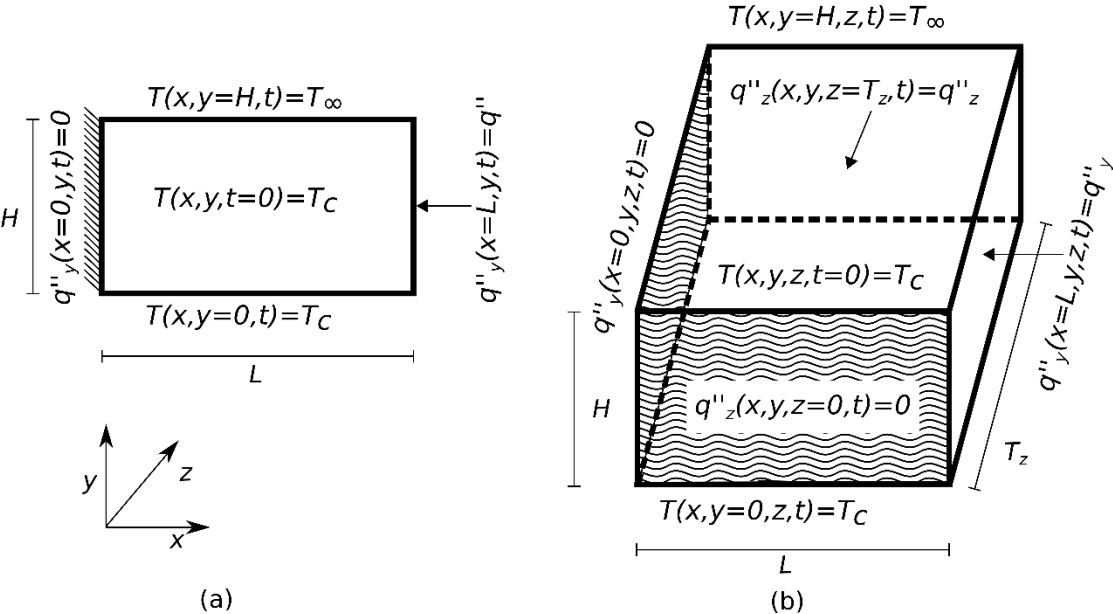


Figure 18. Problem domain for the analytical solutions in two-dimensions Milan and Gebremedhin, 2016a) (a) and three-dimensions (Milan and Gebremedhin, 2016b) (b).

The general TLM node was used to solve the effect of the presence of a breast tumor on skin-surface temperature of a tissue. The problem was solved using regular and irregular hexahedrons and the results were compared to values obtained previously using tetrahedrons (Milan and Gebremedhin, 2016b) and cubes (Amri et al., 2011). The problem geometry is shown in Figure 19 (which is the same geometry given in Figure 5 of Milan and Gebremedhin, 2016b, and Figure 11 of Amri et al., 2016), and has the following dimensions: subcutaneous fat thickness,  $T_{fat} = 5$  mm; gland thickness,  $H = 45$  mm; side lengths,  $L = 20$  mm; tumor center depth = 20 mm; tumor diameter,  $D$ , varying from 10 mm to 30 mm in steps of 2.5 mm. Because of symmetry,

only a quarter of the problem geometry was solved. Meshes composed of regular hexahedrons obtained from Gmsh were post processed in Octave (Eaton et al., 2015) to segment the tumor region with irregular (Figure 20a) or regular hexahedrons (Figure 20b).

Table 7. Definition of meshes for irregular hexahedrons and pyramids. The meshes are defined in terms of number of nodes (#N), number of ports (#P), and the angle ( $\theta$ ) between vectors  $\vec{L}_{2,n}$  and  $\vec{\ell}_n$ .

|        | Irregular Hexahedron |        |                     | Pyramid                      |                              |       |                     |                     |
|--------|----------------------|--------|---------------------|------------------------------|------------------------------|-------|---------------------|---------------------|
|        | #N                   | #P     | $\theta^1$          | #N <sub>P</sub> <sup>2</sup> | #N <sub>T</sub> <sup>3</sup> | #P    | $\theta_P^4$        | $\theta_T^5$        |
| Mesh 1 | 504                  | 1730   | 10.38<br>$\pm 0.08$ | 82                           | 512                          | 1270  | 41.84<br>$\pm 0.84$ | 34.82<br>$\pm 0.37$ |
| Mesh 2 | 1512                 | 4962   | 14.04<br>$\pm 0.06$ | 328                          | 2931                         | 6846  | 40.30<br>$\pm 0.41$ | 32.10<br>$\pm 0.15$ |
| Mesh 3 | 4032                 | 12968  | 10.57<br>$\pm 0.03$ | 690                          | 8955                         | 19980 | 37.95<br>$\pm 0.26$ | 29.37<br>$\pm 0.08$ |
| Mesh 4 | 32256                | 100256 | 10.58<br>$\pm 0.01$ | 1312                         | 19724                        | 43384 | 38.94<br>$\pm 0.20$ | 30.45<br>$\pm 0.06$ |

<sup>1</sup>Mean value in degrees  $\pm$  standard error of the mean; <sup>2</sup>number of pyramidal nodes;

<sup>3</sup>number of tetrahedral nodes; <sup>4</sup>angle  $\theta$  for pyramidal nodes; <sup>5</sup>angle  $\theta$  for tetrahedral nodes.

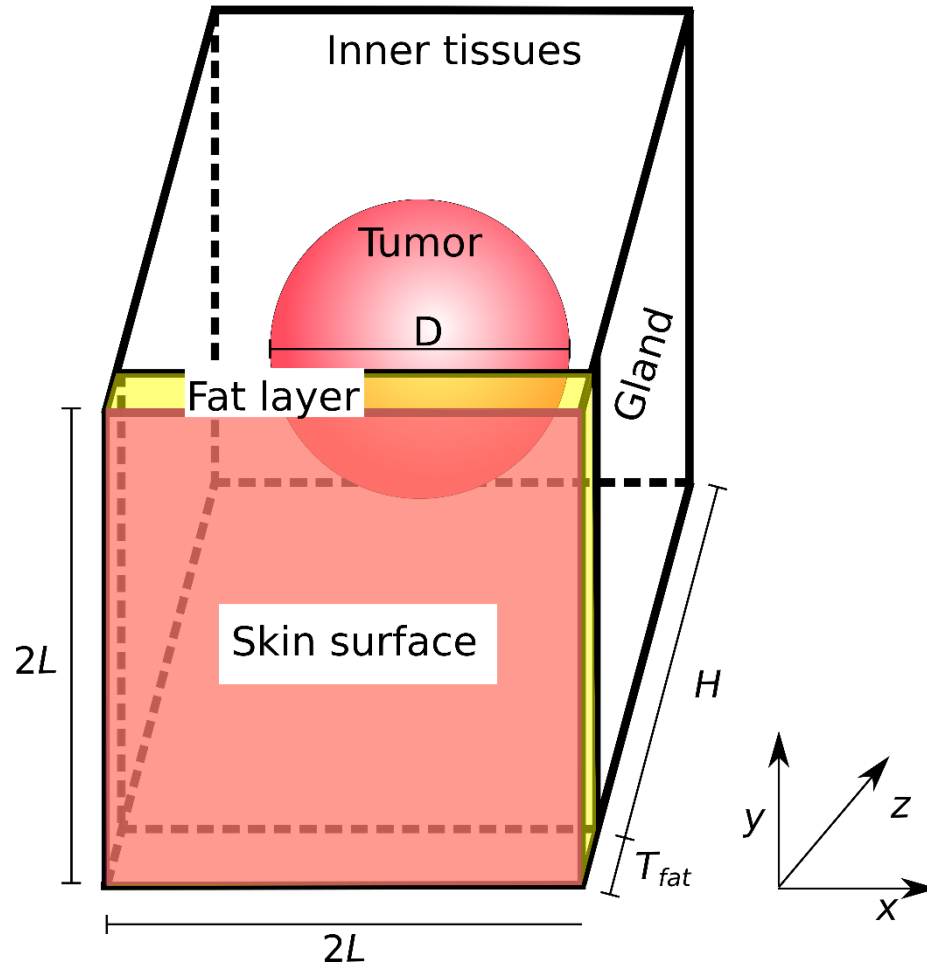


Figure 19. Problem domain for breast with tumor.

Thermal characteristics (Amri et al., 2011; He et al., 2006) for subcutaneous fat tissue were  $\rho_f = 930 \text{ kg/m}^3$ ,  $c_f = 2770 \text{ J/(kg } ^\circ\text{C)}$ ,  $k_f = 0.21 \text{ W/(m } ^\circ\text{C)}$ , and  $q_f''' = 400 \text{ W/m}^3$ .

Thermal characteristics (Amri et al., 2011; He et al., 2006) for gland tissue were  $\rho = 1050 \text{ kg/m}^3$ ,  $c = 3770 \text{ J/(kg } ^\circ\text{C)}$ ,  $k = 0.48 \text{ W/(m } ^\circ\text{C)}$ ,  $q_g''' = 700 \text{ W/m}^3$ . Thermal

characteristics (Amri et al., 2011; Gautherie, 1980; He et al., 2006) for tumor tissue were  $\rho = 1050 \text{ kg/m}^3$ ,  $c = 3770 \text{ J/(kg } ^\circ\text{C)}$ ,  $k = 0.48 \text{ W/(m } ^\circ\text{C)}$ ,  $(c_b \omega_b) = 48,000 \text{ W/(m}^3 \text{ } ^\circ\text{C)}$ ,  $q_t'''$  calculated accordingly to (Gautherie et al., 1975). Thermal characteristics for blood were [0]  $\rho_b = 1100 \text{ kg/m}^3$ ,  $c_b = 3300 \text{ J/(kg } ^\circ\text{C)}$ , and  $T_b = 37 \text{ } ^\circ\text{C}$ . Four blood perfusion values (Ng and Sudharsan, 2001) for subcutaneous fat and tumor tissues were used:  $(c_b \omega_b)_1 = 800 \text{ W/(m}^3 \text{ } ^\circ\text{C)}$  for subcutaneous fat tissue and  $(c_b \omega_b)_1 = 2,400 \text{ W/(m}^3 \text{ } ^\circ\text{C)}$  for gland tissue;  $(c_b \omega_b)_2 = 1,600 \text{ W/(m}^3 \text{ } ^\circ\text{C)}$  for subcutaneous fat tissue and  $(c_b \omega_b)_2 = 2,400 \text{ W/(m}^3 \text{ } ^\circ\text{C)}$  for gland tissue;  $(c_b \omega_b)_3 = 800 \text{ W/(m}^3 \text{ } ^\circ\text{C)}$  for subcutaneous fat tissue and  $(c_b \omega_b)_3 = 3,600 \text{ W/(m}^3 \text{ } ^\circ\text{C)}$  for gland tissue;  $(c_b \omega_b)_4 = 1,600 \text{ W/(m}^3 \text{ } ^\circ\text{C)}$  for subcutaneous fat tissue and  $(c_b \omega_b)_4 = 3,600 \text{ W/(m}^3 \text{ } ^\circ\text{C)}$  for gland tissue. Boundary condition at the skin surface was convection heat transfer with convection transfer coefficient  $h = 13.5 \text{ W/(m}^2 \text{ } ^\circ\text{C)}$  and convective temperature  $T_B = 20 \text{ } ^\circ\text{C}$ . Boundary condition at the inner tissues was constant temperature with  $T_c = 37 \text{ } ^\circ\text{C}$ . The remaining boundaries were considered to be adiabatic conditions. Mesh-independent test was performed by calculating the minimum, maximum, and average difference of skin-surface temperature for the cases without and with  $D = 30 \text{ mm}$  tumor for  $(c_b \omega_b)_1$ . The steady-state solution of this problem was obtained as described previously (Milan and Gebremedhin, 2016a).

### **3. RESULTS AND DISCUSSION**

This paper presents a general TLM formulation for bio-heat transfer that can be simplified to previously published formulations (Amri et al., 2011; Bellia et al.,

2008ab; Bellil and Bennaoum, 2013; Bellil et al., 2013, 2015; Milan and Gebremedhin, 2016ab; Milan et al., 2014). This formulation assumes that the unit vector normal to the border of the node is similar to the unit vector pointing from the center of the node to the midpoint of the border (Eq. (115)), which becomes exact for regular geometries such as rectangles and parallelepipeds. Furthermore, to model Fourier conduction law, the intrinsic transmission-line inductor dispersion effect was assumed negligible compared to the resistor diffusion effect (Eq. (116)). The validity of this assumption is controlled by the error parameter (Eq. (43)).

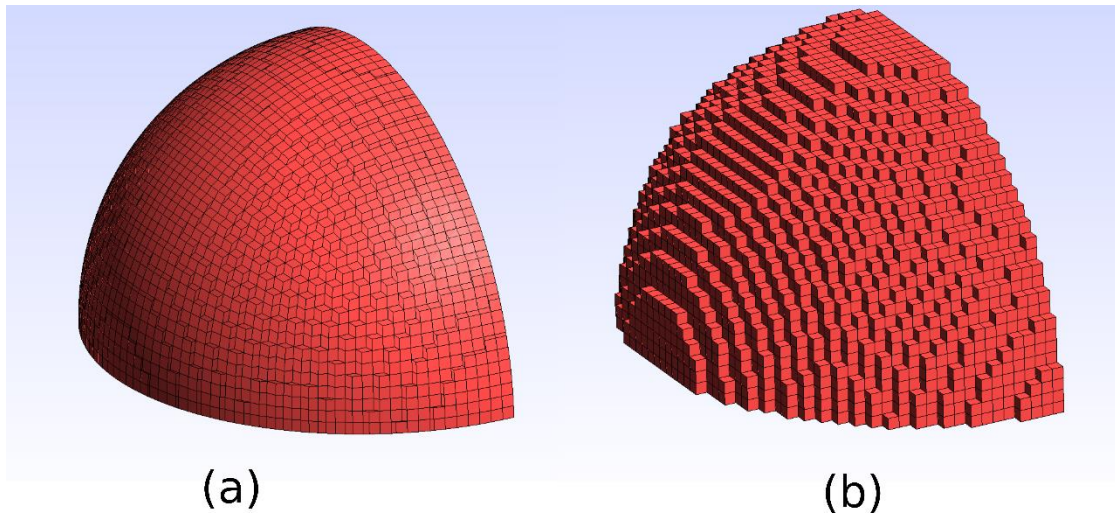


Figure 20. Representation of a quarter of a spherical tumor with diameter of 30 mm using irregular (a) and regular hexahedrons for mesh-size #7 show in Table 8.

Figure 21 shows the percentage temperature error for TLM compared with the analytical solutions and Figure 22 shows the absolute relative heat-flux difference. For quadrangles and hexahedrons, as expected, the errors decreased for smaller time steps

as well as when the number of nodes were increased. Furthermore, smaller errors were obtained for regular geometries likely because these geometries render Eq. (116) exact. The smallest observed mean percentage temperature errors and mean heat-flux differences were 0.04% and  $0.00029 \text{ Wm}^{-2}/\text{Wm}^{-2}$  (regular quadrangle), 0.56% and  $0.0199 \text{ Wm}^{-2}/\text{Wm}^{-2}$  (irregular quadrangle), 0.11% and  $0.0021 \text{ Wm}^{-2}/\text{Wm}^{-2}$  (regular hexahedron), and 1.65% and  $0.043 \text{ Wm}^{-2}/\text{Wm}^{-2}$  (irregular hexahedron). Since small errors were observed for quadrangles and hexahedrons, one can conclude that the general TLM node is valid for these geometries.

In contrast to quadrangles and hexahedrons, for pyramidal nodes, the resulting errors were high and did not decrease considerably for smaller time steps or when the number of nodes were increased. Although the mean percentage temperature error and heat-flux difference were reasonable (4.73% and  $0.093 \text{ Wm}^{-2}/\text{Wm}^{-2}$ ), very high percentage temperature errors and heat fluxes were observed ( $>100\%$  and  $>1 \text{ Wm}^{-2}/\text{Wm}^{-2}$ ). One possible explanation for these high errors would be that, for pyramids, Eq. (115) does not hold. Eq. (115) holds if  $\theta \approx 0^\circ$  but, as shown in Table 3,  $\theta \approx 40^\circ$  for pyramidal nodes.

Table 8 shows the result of the mesh-independent test for the breast with tumor model. For a similar number of nodes, the computing time and RAM memory peak use were bigger for hexahedron nodes when compared to tetrahedron nodes (Table 3 in Milan and Gebremedhin, 2016b), which is expected because the TLM node model for hexahedrons has a bigger number of ports for each node, which leads to reduction of

sparsity of the matrix (Milan and Gebremedhin 2016a) that was inverted to obtain the steady-state solutions. The main advantage of the TLM method is that the solution of time-domain problems does not require matrix inversion, which would lead to a reduction in computing time and RAM memory peak use as discussed in (Milan and Gebremedhin 2016b). Mesh-size #7 was chosen for the remaining simulation because it allows for a compromise between accuracy vs. computation time and RAM memory peak use and because a similar mesh size was used in the previous study (Milan and Gebremedhin 2016b).

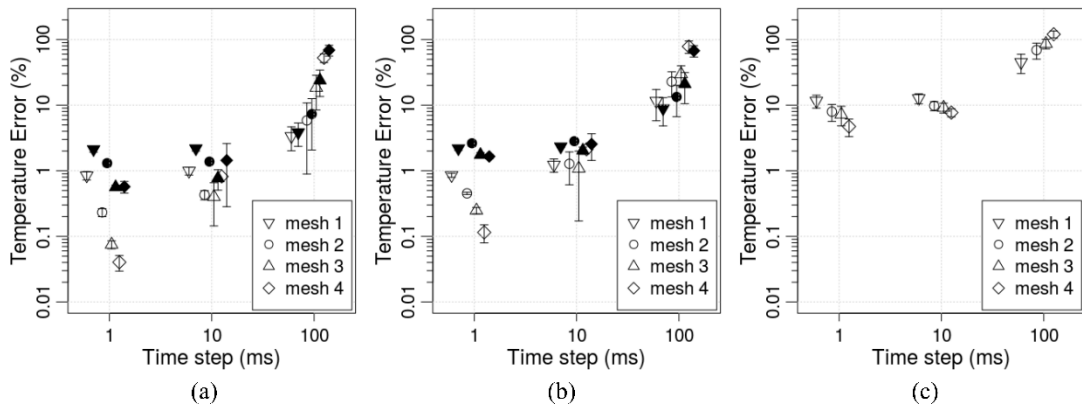


Figure 21. Mean and standard deviation of absolute temperature percentage error using the general TLM node vs. the analytical solutions for: (a) regular (□) and irregular (■) quadrangles, (b) regular (□) and irregular (■) hexahedrons, and (c) pyramids.

The values of the maximum difference in skin-surface temperature for the cases without and with tumor are given in Figure 23. All models showed a similar trend for

changes in tumor diameter and blood perfusion values. The maximum difference in skin-surface temperature is observed for bigger tumors and for lower values of blood perfusion. Compared to the values obtained in (Amri et al., 2011), the mean absolute difference for regular and irregular hexahedrons was 2.92% and 7.93%, respectively. These differences might be due to different mesh sizes (Amri et al., 2011; does not describe the mesh size used) or because of the better representation of curved tumor surfaces obtained by irregular hexahedrons (Figure 20).

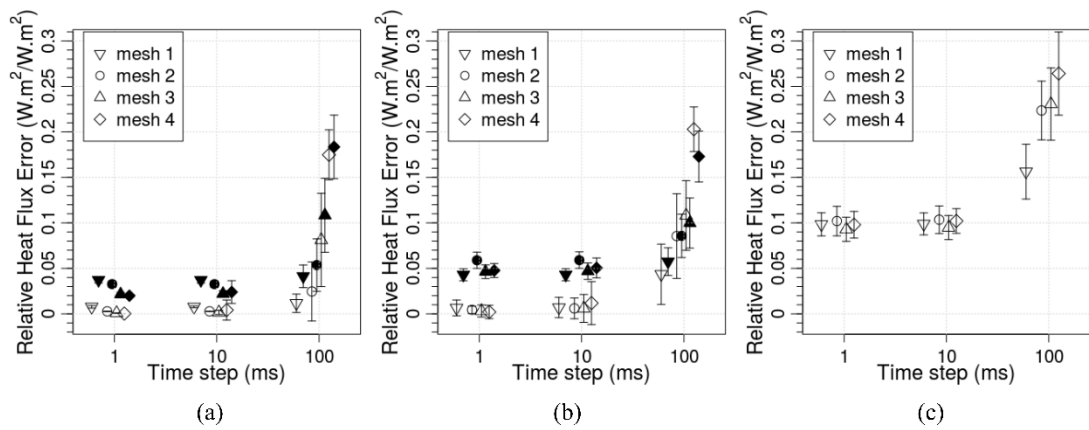


Figure 22. Mean and standard deviation of absolute heat-flux difference divided by maximum input heat flux (100,000 W/m<sup>2</sup>) using the general TLM node vs. the analytical solutions for: (a) regular (□) and irregular (■) quadrangles, (b) regular (□) and irregular (■) hexahedrons, and (c) pyramids.

Table 8. Mesh independent test for the breast with tumor model. The data shown for each mesh size is number of nodes, computing time and peak RAM memory use, and minimum, average, and maximum temperature difference for the models without vs. with  $D = 30$  mm tumor when using regular and irregular hexahedrons as well as the angle ( $\theta$ ) between vectors  $\vec{L}_{2,n}$  and  $\vec{\ell}_n$  computed for irregular hexahedrons.

| Mesh size       | Number of nodes | Regular Hexahedron          |                             |                             | Irregular Hexahedron        |                             |                             | $\theta^2$        | Comp. time (min) <sup>3</sup> | RAM mem. peak use (GB) <sup>3</sup> |
|-----------------|-----------------|-----------------------------|-----------------------------|-----------------------------|-----------------------------|-----------------------------|-----------------------------|-------------------|-------------------------------|-------------------------------------|
|                 |                 | $T_{avg}$ (°C) <sup>1</sup> | $T_{min}$ (°C) <sup>1</sup> | $T_{max}$ (°C) <sup>1</sup> | $T_{avg}$ (°C) <sup>1</sup> | $T_{min}$ (°C) <sup>1</sup> | $T_{max}$ (°C) <sup>1</sup> |                   |                               |                                     |
| #1              | 10,240          | 0.386                       | 0.297                       | 0.540                       | 0.370                       | 0.286                       | 0.512                       | 2.77<br>±<br>0.04 | 0.18                          | 1.04                                |
| #2              | 20,800          | 0.388                       | 0.299                       | 0.542                       | 0.373                       | 0.288                       | 0.517                       | 2.23<br>±<br>0.03 | 0.84                          | 3.06                                |
| #3              | 32,256          | 0.391                       | 0.300                       | 0.548                       | 0.375                       | 0.290                       | 0.519                       | 1.93<br>±<br>0.02 | 3.15                          | 6.88                                |
| #4              | 44,616          | 0.388                       | 0.298                       | 0.542                       | 0.375                       | 0.290                       | 0.520                       | 1.70<br>±<br>0.02 | 5.82                          | 10.54                               |
| #5              | 53,312          | 0.387                       | 0.298                       | 0.540                       | 0.376                       | 0.290                       | 0.520                       | 1.63<br>±<br>0.02 | 10.40                         | 16.60                               |
| #6              | 66,600          | 0.387                       | 0.298                       | 0.539                       | 0.377                       | 0.291                       | 0.521                       | 1.50<br>±<br>0.01 | 13.60                         | 20.84                               |
| #7 <sup>4</sup> | 79,872          | 0.387                       | 0.298                       | 0.539                       | 0.377                       | 0.291                       | 0.522                       | 1.43<br>±         | 22.94                         | 25.39                               |

|     |         |       |       |       |       |       |       |                   |        |       |
|-----|---------|-------|-------|-------|-------|-------|-------|-------------------|--------|-------|
|     |         |       |       |       |       |       |       | 0.01              |        |       |
| #8  | 99,416  | 0.386 | 0.297 | 0.537 | 0.377 | 0.291 | 0.522 | 1.31<br>±<br>0.01 | 42.34  | 32.32 |
| #9  | 114,048 | 0.385 | 0.297 | 0.536 | 0.378 | 0.292 | 0.522 | 1.27<br>±<br>0.01 | 51.08  | 36.36 |
| #10 | 132,848 | 0.385 | 0.296 | 0.535 | 0.378 | 0.292 | 0.523 | 1.20<br>±<br>0.01 | 76.43  | 61.53 |
| #11 | 160,000 | 0.385 | 0.296 | 0.534 | 0.378 | 0.292 | 0.523 | 1.14<br>±<br>0.01 | 118.79 | 64.12 |
| #12 | 186,984 | 0.385 | 0.297 | 0.535 | 0.378 | 0.292 | 0.523 | 1.07<br>±<br>0.01 | 237.20 | 64.48 |

---

<sup>1</sup>Difference for skin-surface temperature for the cases without and with  $D = 30$  mm tumor for  $(c_b \omega_b)_1$ ; <sup>2</sup>mean value in degrees  $\pm$  standard error of the mean computed for irregular hexahedrons (note that  $\theta = 0 \pm 0$  for regular hexahedrons); <sup>3</sup>average computing time and RAM memory peak use for solving the problems using regular and irregular hexahedrons in steady state; <sup>4</sup>mesh size chosen for the calculations in this paper.

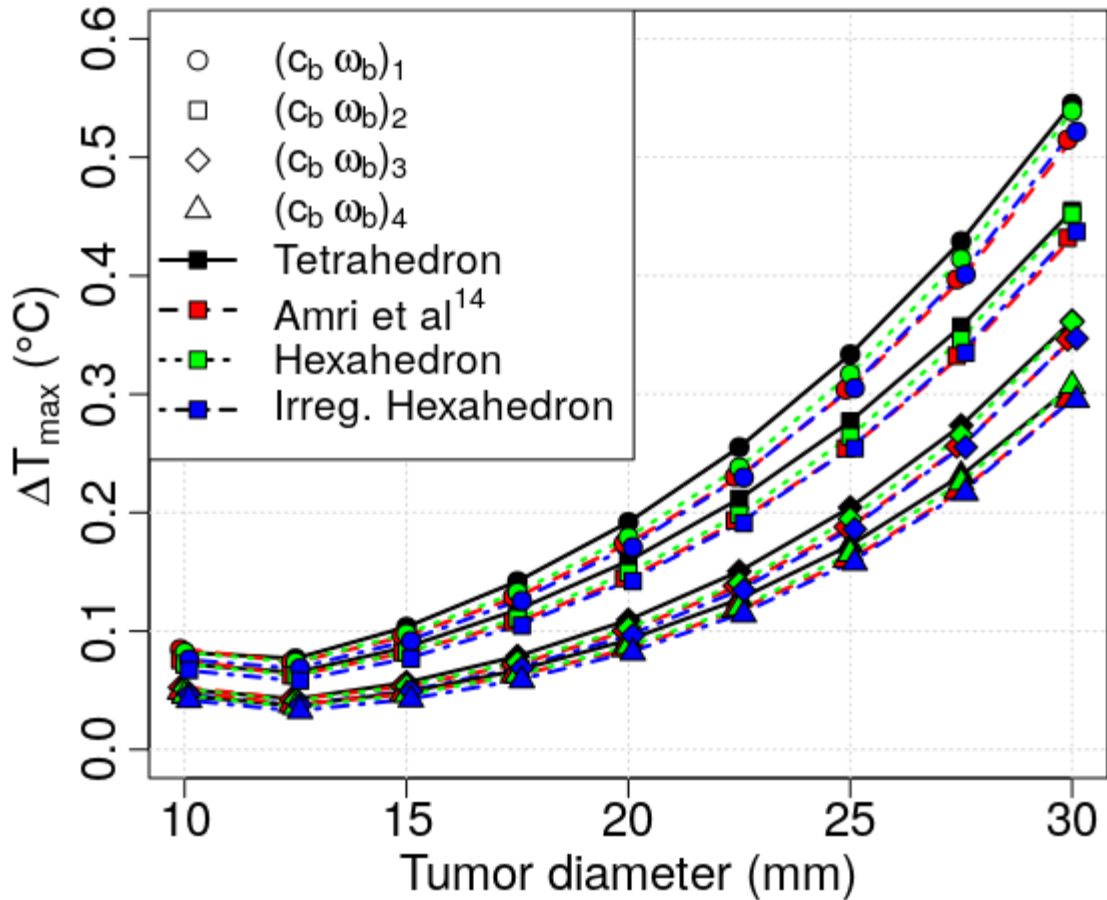


Figure 23. Maximum difference of skin-surface temperature between a breast without and with tumor of the indicated diameter and for the described blood perfusion values.

In addition to increased accuracy and possibility of simplifying the formulation of the node developed in this study to that of previous node formulations, this general framework facilitates algorithmic development because the same code can be reused for computing parameters of different node geometries. This versatility of being able to use different node geometries is essential in the development of bio-heat transfer models of complex geometrical problems. One such problem is modeling

bioenergetics of livestock. The challenge associated with bio-energetic modeling of livestock is to accurately determine the actual geometry of the animal (Milan et al., 2017). Different assumptions have been used (Gebremedhin and Wu, 2016; Gebremedhin et al., 2016; Turner et al., 1987ab) to simplify this problem and to reduce computational time. These assumptions obviously introduce errors in the prediction of the model (Mondaca and Choi, 2016). In the formulation developed in this study, the geometry of the animal could be accurately represented using fewer irregular nodes, which would result in more accurate predictions and reduced computational time.

#### ***4. CONCLUSION***

A general TLM node formulation was developed. The model can be used for different node geometries (lines and graded lines in 1-D; squares, rectangles, quadrangles, and triangles in 2-D; cubes, parallelepipeds, hexahedrons, and tetrahedrons in 3-D). This formulation simplifies to previously published formulations. Using this general TLM node, temperature and heat flux ratios were predicted for (a) regular and irregular quadrangles, and (b) regular and irregular hexahedrons. The results were compared against predictions obtained from an analytical model and agreed within 0.04% and 0.00029  $\text{Wm}^{-2}/\text{Wm}^{-2}$  for regular quadrangle, 0.56% and 0.0199  $\text{Wm}^{-2}/\text{Wm}^{-2}$  for irregular quadrangle, 0.11% and 0.0021  $\text{Wm}^{-2}/\text{Wm}^{-2}$  for regular hexahedron, and 1.65% and 0.043  $\text{Wm}^{-2}/\text{Wm}^{-2}$  for irregular hexahedron, respectively. For pyramids, while the mean agreement was 4.73% and 0.093  $\text{Wm}^{-2}/\text{Wm}^{-2}$ , higher errors were

observed ( $>100\%$  and  $>1 \text{ Wm}^{-2}/\text{Wm}^{-2}$ ). The general TLM formulation of irregular hexahedron nodes enables to solve bio-heat transfer problems of complex geometries. Solution of skin-surface temperature of a breast without and with tumor was demonstrated. The results agreed very well with those of published data. In fact, irregular hexahedrons seem to provide better representation of curved tumor surfaces.

### ***Acknowledgment***

Brazilian National Council of Technological and Scientific Development (Proc. 203312/2014-7) for scholarship to HFMM.

## REFERENCES

- Alexander CK, Sadiku MNO. *Fundamentals of Electric Circuits (5th ed)*. McGraw-Hill: New York, NY, 2012.
- Amri A, Saidane A, Pulko S. Thermal analysis of a three-dimensional breast model with embedded tumour using the transmission line matrix (tlm) method. *Comput Biol Med* 41(2):76-86, 2011.
- Amri A, Pulko SH, Wilkinson AJ. Potentialities of steady-state and transient thermography in breast tumour depth detection: A numerical study. *Comput Methods Programs Biomed* 123:68-80, 2016.
- Austin JD, Pulko SH. The use of general curvilinear orthogonal meshes in tlm heat conduction models. *Numer Heat Trans B* 24:107-125, 1993.
- Bellia SA, Saidane A, Benzohra M, Saiter JM, Hamou A. Dimensional soft tissue thermal injury analysis using transmission line matrix (tlm) method. *Int J Numer Model* 21(6):531-549, 2008a.
- Bellia SA, Saidane A, Hamou A, Benzohra M, Saiter JM. Transmission line matrix modelling of thermal injuries to skin. *Burns* 34(5):688-697, 2008b.
- Bellil M, Bennaoum S. *Tlm modelling of laser thermal treatment of benign prostate hyperplasia*. International Conference on Control, Engineering & Information Technology, pp. 1-5, 2013.

Bellil M, Saidane A, Bennaoum M. Numerical modelling for simulation and treatment planning of prostate thermal therapy. *Int J Numer Model* 28(5):540-550, 2015.

Bellil M, Saidane A, Bennaoum S. *Transmission line matrix modelling of bioheat transfer in cryogenic therapy applications*. International Conference on Control, Engineering & Information Technolog, pp. 1-6, 2013.

Christopoulos C. *The Transmission-Line Modeling Method*. IEEE Press: New York, NY, 1995.

Christopoulos C. *The Transmission-line Modeling (TLM) Method in Electromagnetics*. Morgan & Claypool: Williston, VT, 2006.

de Cogan D. *Transmission Line Matrix (TLM) Technique for Diffusion Applications*. Gordon and Breach Science Publishers: Amsterdam, Netherlands, 1998.

de Cogan D, Connor WJO, Pulko S. *Transmission Line Matrix in Computational Mechanics*. CRC Taylor & Francis: Boca Raton, FL, 2005.

Eaton JW, Bateman D, Hauberg S, Wehbring R. *GNU Octave version 4.2.0 manual: a high-level interactive language for numerical computations*. CreateSpace Independent Publishing Platform: Scotts Valley, CA, 2015.

Gautherie M. Thermopathology of breast cancer: measurement and analysis of in vivo temperature and blood flow. *Ann N Y Acad Sci* 335(1):383-415, 1980.

Gautherie M, Quenneville Y, Gros CM. Metabolic heat production, growth rate and prognosis of early breast carcinomas. *Biomedicine* 22:328-336, 1975.

Gebremedhin KG, Wu B. Modeling heat loss from the udder of a dairy cow. *J Therm Biol* 59:34-38, 2016.

Gebremedhin KG, Wu B, Perano K. Modeling conductive cooling for thermally stressed dairy cows. *J Therm Biol* 56:91-99, 2016.

Geuzaine C, Remacle JF. Gmsh: A 3-D finite element mesh generator with built-in pre- and post-processing facilities. *Int J Numer Meth Eng* 79:1309-1331, 2009.

Grandy J. *Efficient computation of volume of hexahedral cells*. Lawrence Livermore National Laboratory No. UCRL-ID—128886, CA, US, 1997.

He Y, Shirazaki M, Liu H, Himeno R, Sun Z. A numerical coupling model to analyse the blood flow, temperature, and oxygen transport in human breast tumor under laser irradiation. *Comput Biol Med* 36:1336-1350, 2006.

Ijjeh A, Makhlouf O, Cueille M, Dubard JL, Ney MM. *Dosimetry and hyperthermia computation in human tissues in presence of EM-waves using TLM method*. IEEE 11th European Conference on Antennas and Propagation, pp. 403-407, 2017a.

Ijjeh AA, Ney M. Local time-step TLM unstructured block meshing for electromagnetic and bio-thermal applications. *IEEE J Multiscale Multiply Comput Techn* 2:174-182, 2017b.

Johns PB, Beurle RL. Numerical solution of 2-dimensional scattering problems using a transmission-line matrix. *Proc IEE* 118(9):1203-1208, 1971.

Johns PB. A simple explicit and unconditionally stable numerical routine for the solution of the diffusion equation. *Int J Numer Meth Eng* 11:1307-1328, 1977.

Kron G. Equivalent circuits to represent the electromagnetic field equations. *Phys Rev* 64(3):126-128, 1948.

Kron G. Numerical solution of ordinary and partial differential equations by means of equivalent circuits. *J Appl Phys* 16:172-186, 1945.

Weiner M. *Electromagnetic Analysis Using Transmission-Line Variables*. 2<sup>nd</sup> ed., World Scientific: River Edge, NJ, 2010.

Maia ASC, Milan HFM, Gebremedhin KG. *Analytical and numerical modeling of skin surface temperature in livestock*. 20th International Congress of Biometeorology, pp. 1, 2014.

Makhlouf O, Cueille M, Dubard JL. *A new TLM algorithm to solve the Pennes's equation for dosimetry applications*. 45th European Microwave Conference, pp. 1-4, 2015.

Makhlouf O, Cueille M, Dubard JL. *TLM computation of temperature distribution in human head exposed to electromagnetic waves*. IEEE International Symposium on Antenna Propagation, pp. 1-2, 2016a.

Makhlouf O, Cueille M, Dubard JL. *TLM numerical thermal dosimetry in realistic environment*. IEEE Radio and Antenna Days of the Indian Ocean, pp. 1-2, 2016b.

Milan HFM. *TLMBHT – Transmission-line Modeling Method applied to BioHeat Transfer Problems*. Available at <https://github.com/hugomilan/tlmbht> (accessed in 11/12/17). DOI: 10.5281/zenodo.266350.

Milan HFM, Carvalho Jr CAT, Maia ASC, Gebremedhin KG. Graded meshes in bio-thermal problems with transmission-line modeling method. *J Therm Biol* 45:43-53, 2014.

Milan HFM, Gebremedhin KG. Triangular node for Transmission-Line Modeling (TLM) applied to bio-heat transfer. *J Therm Biol* 62:116-122, 2016a.

Milan HFM, Gebremedhin KG. Tetrahedral node for Transmission-Line Modeling (TLM) applied to Bio-heat Transfer. *Comput Biol Med* 79:243-249, 2016b.

Milan HFM, Gebremedhin KG. *Solving bioenergetics' problems with the transmission-line modeling (TLM) method*. ASABE Annual International Meeting, pp. 162420443:1-9, 2016c.

Milan HFM, Gebremedhin KG. *General formulation of transmission-line modeling (TLM) method applied to bio-energetics of endotherms*. ASABE Annual International Meeting, pp. 1700180:1-8, 2016d.

Milan HFM, Perano KM, Gebremedhin. *Procedures for measuring 3-D surface area and surface temperature of livestock*. VII Brazilian Congress of Biometeorology, Ambience, Behaviour and Animal Welfare, pp. 1-5, 2017.

Minkowycz WJ, Sparrow EM. *Advances in Numerical Heat Transfer*. Volume 3. CRC Press: Boca Raton, FL, 2009.

Mondaca M, Choi CY. An evaluation of simplifying assumptions in dairy cow computational fluid dynamic models. *Trans ASABE* 59(6):1575-1584, 2016.

Ng EYK, Sudharsan NM. An improved three-dimensional direct numerical simulation modelling and thermal analysis of a female breast with tumor. *Proc Inst Mech Eng H* 215(1):25-37, 2001.

Pennes HH. Analysis of tissue and arterial blood temperature in the resting human forearm, *J Appl Physiol* 1:93-122, 1948.

Pulko S, Mallik A, Johns PB. Application of transmission-line modelling (TLM) to thermal diffusion in bodies of complex geometry. *Int J for Numer Meth Eng* 23:2303-2312, 1986.

Turner LW, Blandford GE, Loewer OJ, Taul KL. Finite element model of heat transfer in the bovine. Part 1: theory. *Trans ASAE* 30(3):768-774, 1987a.

Turner LW, Loewer OJ, Taul KL, Munifering RB, Gay N. Finite element model of heat transfer in the bovine. Part 2: validation. *Trans ASAE* 30(3):775-781, 1987b.

## CHAPTER 4: PREDICTION OF OPTIMUM SUPPLEMENTAL HEAT FOR PIGLETS

Hugo Fernando Maia Milan, Alex Sandro Campos Maia, Kifle G. Gebremedhin

Published in *Transactions of the ASABE*: Milan HFM, Maia ASC, Gebremedhin KG. Prediction of optimum supplemental heat for piglets. *Trans ASABE* 62(2):321-342, 2019.

### ***Abstract***

The thermal environment of farrowing facilities is generally controlled at the thermo-neutral zone for sows (15°C to 19°C). This imposes thermal challenges for newborn piglets, which are thermally comfortable at temperatures 10°C to 20°C higher (32°C to 35°C). To satisfy the energetic requirements of piglets, supplemental heat is installed in creep or brooder areas. In this study, we determined optimum supplemental heat requirements (supplied by heating lamps) for piglets based on energy balance as a function of air temperature and animal body weight. We also determined the zone of least thermoregulation of piglets for a given weight when supplemental heat is not provided. Energy balance was calculated using an ensemble of mechanistic models of bio-heat transfer that predicts hair-coat temperature, skin temperature, and skin heat flux. Inputs to the ensemble of mechanistic models include air temperature, black-globe temperature, rectal temperature, and system parameters (e.g., thickness of internal tissues and thermal conductivities). Input temperatures were predicted from

measured air temperature in the pen and supplemental heat using machine learning. System parameters were measured or obtained from the literature and optimized using the Monte Carlo method. Ensemble predictions of hair-coat and skin temperature agreed within 3.5% with measured data. The ensemble-predicted zone of least thermoregulation agreed well with previous reports. Predicted optimum supplemental heat showed an exponential decay trend with increasing air temperature and/or animal weight. For air temperature between 15°C and 19°C, the predicted optimum supplemental heat was 266 to 344 W and 44 to 128 W for piglets weighing 1 kg and 20 kg, respectively. The predicted optimum supplemental heat was ~200 W lower for piglets at the end of the farrowing cycle (assuming weight of 20 kg) than at birth (assuming birth weight of 1 kg).

**Keywords:** Bio-heat equation; computational models; ensemble learning; piglets; precision livestock farming; supplemental heat; thermo-neutral zone.

## ***1. INTRODUCTION***

Classic studies (Mount, 1960, 1963; Stinn and Xin, 2014b) demonstrated that the zone of least thermoregulation for newborn piglets is 32°C to 35°C, which is 10°C to 20°C higher than the same zone for sows (15°C to 19°C). Because far-rowing facilities are usually maintained in the zone of least thermoregulation for sows, supplemental heat should be provided in creep or brooder areas to maintain the desired zone of least thermoregulation for piglets. A typical method of providing supplemental heat is heating lamps. The required supplemental heat provided by heating lamps was determined by studying animal behavior (Xin et al., 1997a, 1997b; Xin and Zhang, 1999; Zhou and Xin, 1999). Results from these studies suggested that the required supplemental heat decreased with increasing air temperature and weight or age of the piglets.

Providing the required supplemental heat for piglets can increase energy efficiency and animal welfare and comfort (Zhou and Xin, 1999). If only the required minimum supplemental heat is provided, then less energy will be used (Xin et al., 1997a). Furthermore, research (Vasdal et al., 2010a, 2010b) showed that not providing the required supplemental heat can lead to increased piglet mortality. For instance, piglets can be crushed by sows when avoiding high-intensity supplemental heat or suffer hypothermia when insufficient supplemental heat is provided.

It is therefore necessary to determine the optimum supplemental heat as a function of

air temperature and piglet weight or age. In this study, we established the optimum supplemental heat as a function of air temperature and body weight by minimizing the energy imbalance of the piglets.

## **2. MATERIALS AND METHODS**

Computer algorithms were written in Octave (Eaton et al., 2016) using the parallel package, except for machine learning algorithms, which were written in R (R Core Team, 2018) using the RStudio (RStudio Team, 2016), H2O (H2O.ai team, 2017), lme4 (Bates et al., 2015), and doMC (Revolution Analytics and Weston, 2017) packages. Data, algorithms, and all intermediary calculations are available online (Milan et al., 2018a; Milan, 2018). The computations involved were performed on an Oryx Pro from System76 with Pop-OS 17.10, 512 GB PCIe M.2 SSD, 64 GB DDR4 RAM (2133 MHz), i7-6820HK (3.6 GHz), and 8 GB GeForce GTX 980M.

### **2.1. Experimental measurements**

The research protocol and animal use were approved by the Animal Care and Use Committee of São Paulo State University (Protocol No. 9726/17 and FAPESP Proc. 17.519/14). The data collection procedure was reported by Gorczyca et al. (2018). For this study, ten 5-day-old Large White commercial lineage piglets were randomly selected from a farrowing facility. The facility had a suspended-floor pen with access to a brooder. Supplemental heat was not provided before starting the experiment. From 3:00 a.m. to 8:00 a.m., the piglets were kept inside the brooder, which had

dimensions of 1.5 m length  $\times$  1.0 m width  $\times$  0.8 m height, with a concrete floor, a 25 cm  $\times$  25 cm entrance, a cement rendered brick wall 20 cm thick, a plywood board ceiling 5 mm thick, and a heating lamp installed at approximately 0.45 m height. The pig-lets were divided into five groups of two. The groups were: (1) a control group without supplemental heat, and (2) experimental groups with the following supplemental heat (H) values: 60, 100, 160, and 200 W. The supplemental heat was provided with incandescent lamps (60 W IN10624, 100 W IN11024, Empalux; 160 W = 60 W + 100 W; 200 W = 100 W + 100 W).

Physiological responses were measured hourly from 4:00 a.m. to 8:00 a.m. Hair-coat surface temperature ( $T_h$ , °C) at the upper leg was measured using an infrared thermometer (model 568, Fluke, accuracy  $\pm 1^\circ\text{C}$ , emissivity adjusted to 0.98). Skin surface temperature ( $T_s$ , °C) at the upper leg was measured using a contact sensor (MLT422/AL, ADInstruments, accuracy  $\pm 0.2^\circ\text{C}$ ) connected to a temperature pod (ML309, ADInstruments, accuracy  $\pm 0.2^\circ\text{C}$ ). Rectal temperature ( $T_r$ , °C) was measured with a rectal temperature probe (MLT1403, ADInstruments, accuracy  $\pm 0.2^\circ\text{C}$ ) connected to a temperature pod (ML312, ADInstruments, accuracy  $\pm 0.2^\circ\text{C}$ ). The temperature pods were connected to a computer running PowerLab 16/32 (connected to LabChart, ADInstruments, Australia). Air temperature ( $T_a$ , °C) and relative humidity (RH, %) inside the brooder were measured using dataloggers with built-in sensors (HOBO U12-013, Onset Computer, accuracy  $\pm 0.35^\circ\text{C}$  and  $\pm 2.5\%$ ). Black-globe temperature in the brooder ( $T_g$ , °C) was measured using a sensor (TMC20-HD)

connected to one external channel of the same HOBO U12-013 (Onset Computer, accuracy  $\pm 0.35^\circ\text{C}$ ). Air temperature ( $T_{a,\text{pen}}$ ,  $^\circ\text{C}$ ) inside the pen was measured using a sensor (TMC20-HD) connected to one external channel of one HOBO U12-013 (Onset Computer, accuracy  $\pm 0.35^\circ\text{C}$ ). Irradiance ( $J$ ,  $\text{W m}^{-2}$ ) inside the brooder was measured one day using a portable pyranometer (CMP-22, Kipp and Zonen, The Netherlands).

Weight ( $w$ , kg) and diameter ( $D$ , m) of the piglets were measured daily. Hair-coat thickness ( $L_h$ , m) was measured at the lower back of the animal. Density of hairs ( $N_h$ , hairs  $\text{m}^{-2}$ ) was measured from hairs sampled from the lower back ( $1.0 \text{ cm}^2$  area) by counting the number of hairs in the sampled area. Hair length ( $H_L$ , m) and diameter ( $H_D$ , m) were measured from the ten longest hairs in the sample (da Silva and Maia, 2013) using a Mitutoyo digital micrometer. Thickness of the skin ( $L_s$ , m), fat ( $L_f$ , m), and muscle ( $L_m$ , m) layers were measured on 20 piglets (two days old) using ultrasound (500v, linear probe with 3.5 MHz, 13.5 cm, Aloka Ultrasound) between the thoracic and lower back (point P2) vertebrae, 6 cm below the mean line (ABCS, 1973).  $D$ ,  $w$ , and  $L_h$  were also measured for these piglets.

## **2.2. Data preprocessing**

The experiment was designed to collect 200 data points. Each data point consisted of  $T_r$ ,  $T_s$ ,  $T_h$ ,  $T_a$ ,  $T_g$ , RH,  $T_{a,\text{pen}}$ ,  $H$ , and  $J$ . Model development and validation used  $T_r$ ,  $T_s$ ,  $T_h$ ,  $T_a$ ,  $T_g$ ,  $T_{a,\text{pen}}$ , and  $H$ . The number of data points was reduced from 200 to 173

because of technical problems. Based on stratified random sampling (measurement time and supplemental heat were the strata), the 173 data points were divided between a training dataset (130 points = 75%) and a testing dataset (43 points = 25%; Hastie et al., 2003). In addition, mean values of each stratum were calculated (20 points) to determine the mean prediction error. The model was trained with the training dataset, and model accuracy was evaluated using the testing and mean datasets.

### 2.3. Mathematical modeling framework

Figure 24 shows the flowchart of our mathematical framework used to predict optimum supplemental heat ( $H_{opt}$ ),  $T_h$ ,  $T_s$ , and skin heat flux ( $q''_s$ ). The flow of input/output in the flowchart is as follows: distributions of system parameters (Table 36) are inputs to the Monte Carlo optimization method. The output from the Monte Carlo optimization method is a sample set  $i$  of system parameters, which is an input to the mechanistic model. Other inputs to the mechanistic model are  $T_a$ ,  $T_g$ ,  $T_r$ , and air temperature including the effect of supplemental heat ( $T_{a,in}$ ; see Sec. 2.8).  $T_a$ ,  $T_g$ ,  $T_r$ , and  $T_{a,in}$  are predicted using machine learning algorithms given  $T_{a,pen}$  and  $H$ . Outputs from the mechanistic model given the sampled set  $i$  of parameters are  $T_{h,i}$ ,  $T_{s,i}$ , and  $q''_{s,i}$ , which are inputs to the ensemble learning algorithm. The ensemble learning algorithm combines predictions from the mechanistic model to minimize an error metric (see the Sec. 2.7). Outputs from the ensemble are  $T_h$ ,  $T_s$ ,  $q''_s$ , and the equivalent air temperature ( $T_{a,eq}$ ) defined as  $q''_s(T_{a,eq}, 0) = q''_s(T_a, H)$ .  $T_{a,eq}$  is used as an input to calculate total heat production (THP,  $W m^{-2}$ ) because equations reported in the

literature do not account for the effects of H on changing THP (see Sec. 2.8). Other inputs to calculate THP include animal weight ( $w$ , kg) and animal surface area ( $A_s$ ,  $m^2$ ), predicted given  $w$ . THP, latent heat production ( $E_L$ ,  $W\ m^{-2}$ ; estimated from the literature, see Sec. 2.8), and sensible heat production ( $E_s = q''_s$ ) are inputs to the energy balance equation, which was bootstrapped to predict  $H_{opt}$ .

#### **2.4. Machine learning models to predict input temperatures**

Machine learning models were trained to predict inputs to the mechanistic model. Inputs to the mechanistic model were  $T_r$ ,  $T_a$ , and  $T_g$ , while  $T_r$ ,  $T_a$ , and  $T_g$  were predicted given H and  $T_{a,pen}$ . Farmers might measure air temperature above or outside the pen (but inside the barn). These two temperatures are likely similar to  $T_{a,pen}$ . The machine learning algorithms used in this study were ordinary linear regression with backward selection for regression coefficients, generalized linear square regression (with a Gaussian distribution) with elastic net regularization, random forests, gradient boosted machines, and deep learning with ReLU activation function. The machine learning models were trained using the training dataset, and hyperparameters were optimized using random search (Bergstra and Bengio, 2012) with 5-fold modular cross-validation to minimize the cross-validation mean squared error (MSE,  $^{\circ}C^2$ ), as described by Gorczyca et al. (2018). The performance of the best-fit models for each tested algorithm was evaluated using testing MSE, and their generalization capability was evaluated using dependence plots (Friedman, 2001). Selected models were retrained using the full (training and testing) dataset.

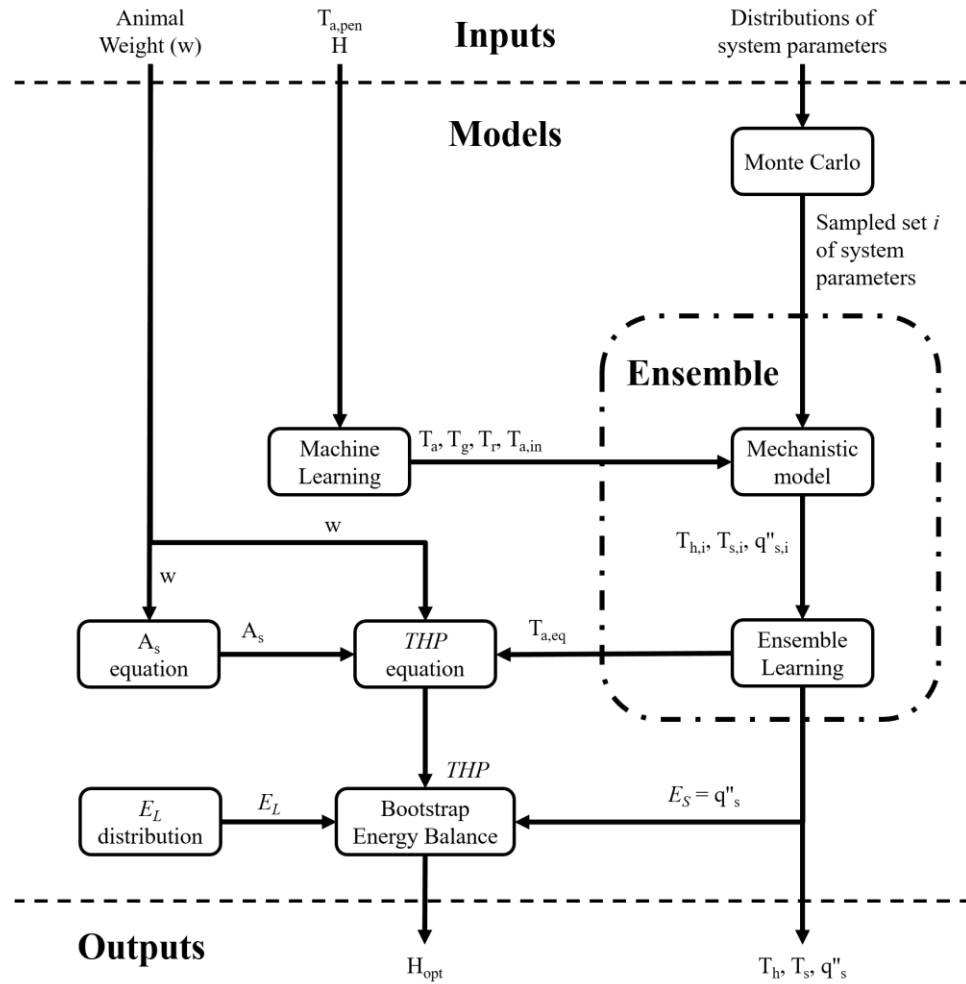


Figure 24. Flowchart of mathematical framework used to predict optimum supplemental heat ( $H_{opt}$ ), hair-coat temperature ( $T_h$ ), skin temperature ( $T_s$ ), and skin heat-flux ( $q''_s$ ). Boxes represent models. Arrows represent flow of input/output. See text for description.

## 2.5. Mechanistic model of bio-heat transfer

The mechanistic model predicts the temperature profile through the muscle, fat, skin, and hair-coat layers (Figure 25). Each layer can be divided into sublayers, which results in a total of  $n$  sublayers. Assuming 1-D and steady-state heat flux, and constant parameters in all sublayers, Pennes' energy conservation equation for biological tissues (Pennes, 1948) can be expressed as:

$$q_i'' = -k_i \frac{dT_i}{dx_i} \quad (128)$$

$$-\frac{dq_i''}{dx_i} + \omega_{b,i} \rho_{b,i} c_{b,i} (T_{b,i} - T_i) + q_{met,i}''' + q_{ext,i}''' = 0 \quad (129)$$

where  $i$  represents sublayer  $i$ ,  $q''$  is heat flux ( $\text{W m}^{-2}$ ),  $T$  is temperature ( $^{\circ}\text{C}$ ),  $k$  is thermal conductivity ( $\text{W m}^{-1} \text{ }^{\circ}\text{C}^{-1}$ ),  $x$  is the position direction between 0 and  $L$  (m),  $L_i$  is the length of sublayer  $i$  (m),  $\omega_b$  is blood perfusion rate ( $\text{m}^3 \text{ s}^{-1} \text{ m}^{-3}$ ),  $\rho_b$  is blood density ( $\text{kg m}^{-3}$ ),  $c_b$  is blood specific heat ( $\text{J kg}^{-1} \text{ }^{\circ}\text{C}^{-1}$ ),  $T_b$  is blood temperature ( $^{\circ}\text{C}$ ),  $q'''_{met}$  is metabolic heat generation per unit volume ( $\text{W m}^{-3}$ ), and  $q'''_{ext}$  is external heat generation per unit volume ( $\text{W m}^{-3}$ ).

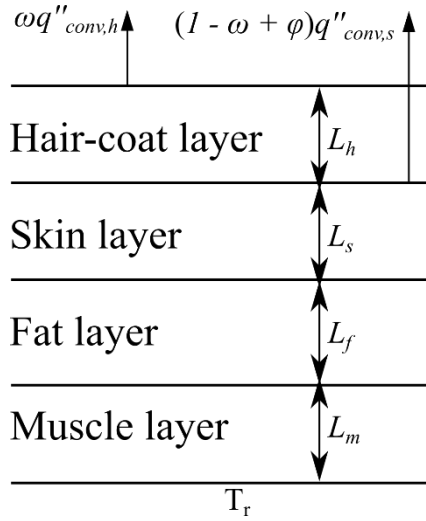


Figure 25. Control volume and boundary conditions for the mechanistic model. Subscripts  $m$ ,  $f$ ,  $s$ , and  $h$  represent muscle, fat, skin, and hair-coat layers, respectively;  $L_i$  represents thickness of layer  $i$ ;  $T_r$  represents rectal temperature used as a boundary condition;  $q''_{conv,i}$  represents convection heat transfer from the surface of layer  $i$ ;  $\omega$  is proportion of  $q''_{conv,h}$ ;  $\phi$  is additional proportion of  $q''_{conv,s}$ .

Eqs. (128) and (129) were analytically solved for the muscle, fat, and skin layers. The hair-coat layer was modeled using the radiation absorbing-emitting fibrous layer equation (Kowalski and Mitchell, 1979). This equation was numerically solved with finite differences. For completeness, all equations for solving the mechanistic model are given in Appendix A. Solutions for temperatures and heat fluxes of Eqs. (128) and (129) at the interfaces of sublayers can be assumed equal up to an offset, expressed as:

$$T_i(x_i = L_i) = T_{i+1}(x_{i+1} = 0) + T_o(x_{i+1} = 0) \quad (130)$$

$$q''_i(x_i = L_i) = q''_{i+1}(x_{i+1} = 0) + q''_o(x_{i+1} = 0) \quad (131)$$

where  $T_o$  ( $^{\circ}\text{C}$ ) and  $q''_o$  ( $\text{W m}^{-2}$ ) are the temperature and heat flux offsets, respectively, at the interfaces of sublayers. Eqs. (130) and (131) form an underdetermined system of  $2n - 2$  equations with  $2n$  unknowns. The solution of this system needs two boundary conditions, which were assumed to be  $T_r$  at  $x_1 = 0$  and convection at  $x_h = L_h$  (radiation was modeled following Kowalski and Mitchel, 1979). Because the density of hairs ( $N_h$ ) of piglets is one order of magnitude lower than of other non-glabrous animals (e.g., 150 hairs  $\text{cm}^{-2}$  vs. 5400 hairs  $\text{cm}^{-2}$  for cows; Gebremedhin et al., 1983), we can assume that the hair-coat does not provide full thermal isolation between the skin and the environment, which explains why  $T_s$  was observed to be as low as  $9^{\circ}\text{C}$  in cold air (Irving, 1956). To account for non-fully thermal isolation, convection heat transfer at the skin (included in  $q''_o$ ) and hair-coat surfaces were modeled as:

$$q''_h(x_h = L_h) = \omega q''_{conv,h} \quad (132)$$

$$q''_o(x_s = L_s) = (1 - \omega + \varphi) q''_{conv,s} \quad (133)$$

where  $\omega$  is the proportion of convection heat transfer at the hair-coat surface with values between 0 and 1,  $\varphi$  is the additional proportion of convection heat transfer at the skin surface with values between 0 and  $\omega$ ,  $q''_{conv,i}$  is convection heat transfer calculated at the surface of layer  $i$ , and subscripts  $h$  and  $s$  stand for the hair-coat and skin surfaces, respectively. With specified boundary conditions, the system of equations was solved using successive quadratic programming in Octave.

## 2.6. Monte Carlo optimization of system parameters

System parameters necessary to solve the system of equations (Eqs. (130) and (131)) were measured or obtained from the literature (Table 9). Because the parameters have intrinsic variabilities, their distributions were estimated from data, and these distributions were used in 10,000 samples of Monte Carlo optimization to select sets of system parameters that minimized the sum of MSEs for predicting  $T_s$  and  $T_h$ . The distributions were assumed to be independent between themselves. From Bayesian statistics theory (Gelman et al., 2013), prior probability distribution functions for optimization usually do not have a significant impact on the final optimized set of parameters, as long as the true set of parameters is included in the prior probability distribution. Hence, due to the lack of distributional data in the literature, the probability distribution functions in Table 9 were adjusted to cover previous values reported in the literature with 70% probability, leaving 30% for unlikely or non-reported values. In total, 10,002 sets of system parameters were evaluated, including 10,000 sampled sets, one set with traditional parameter values and measured input data (TM; i.e.,  $T_a$ ,  $T_g$ , and  $T_r$ ), and another set with traditional parameters and expected input data predicted using machine learning algorithms (TP).

Table 9. Traditional system parameters and distributions used to solve the mechanistic model.

| Parameter   | Traditional value <sup>[a]</sup> | Distribution <sup>[b]</sup>  | Reference  |
|---|----------------------------------|------------------------------|--|
| Animal  |                                  |                              |  |
| Volumetric heat capacity of blood (MJ m <sup>-3</sup> K <sup>-1</sup> )           | 4.1                              | $N(4.1,0.26)$                | Werner and Buse (1988)   |
| Blood temperature   | 1                                | $U(0.98,1.01)$               | Assumed  |
| multiplicative factor <sup>[c]</sup>  |                                  |                              |  |
| Diameter (cm)   | 10.5                             | $N(10.5,3.5)$                | Measured   |
| Muscle layer  |                                  |                              |  |
| #sublayers  | 1                                | $\text{round}(X_{10}^2 + 1)$ | Assumed  |
| Thickness (mm)  | 2                                | $N(2,1)$                     | Extrapolated from Fachinello et al. (2015) <sup>[d]</sup>                          |
| Thermal conductivity (W m <sup>-1</sup> K <sup>-1</sup> )                         | 0.53                             | $N(0.53,0.1)$                | Holmes (2018) <sup>[e]</sup>   |
| Blood perfusion (m <sup>3</sup> m <sup>-3</sup> s <sup>-1</sup> )×10 <sup>3</sup> | 2.5                              | $N(2.5,0.9)$                 | Duddy et al. (1984); van Woerkens et al. (1990, 1992); Upton (2008); Holmes (2018) |

|  |      |                              |  |
|--|------|------------------------------|--|
| Metabolic heat generation ( $\text{W m}^{-3}$ ) <sup>[f]</sup>             | 684  | $N(684,137)$                 | Werner and Buse (1988);<br>Ferreira and Yanagihara (2009)  |
| Fat layer  |      |                              |  |
| #sublayers   | 1    | $\text{round}(X_{10}^2 + 1)$ | Assumed  |
| Thickness (mm)   | 5    | $N(5,2.5)$                   | Measured   |
| Thermal conductivity ( $\text{W m}^{-1} \text{K}^{-1}$ )                   | 0.29 | $N(0.29,0.12)$               | Holmes (2018) <sup>[e]</sup>   |
| Blood perfusion ( $\text{m}^3 \text{m}^{-3} \text{s}^{-1}$ ) $\times 10^3$ | 2.5  | $N(2.5,1.34)$                | Tranquilli et al. (1982); Duddy et al. (1984); van Woerkens et al. (1990, 1992); Upton (2008); Holmes (2018) |
| Metabolic heat generation ( $\text{W m}^{-3}$ ) <sup>[f]</sup>             | 368  | $N(368,74)$                  | Werner and Buse (1988);<br>Ferreira and Yanagihara (2009)  |
| Skin layer   |      |                              |  |
| #sublayers   | 1    | $\text{round}(X_{10}^2 + 1)$ | Assumed  |
| Thickness (mm)   | 1    | $N(1,0.7)$                   | Measured   |
| Thermal conductivity ( $\text{W m}^{-1} \text{K}^{-1}$ )                   | 0.21 | $N(0.21,0.05)$               | Henriques Jr. and Moritz (1947)  |
| Blood perfusion ( $\text{m}^3 \text{m}^{-3} \text{s}^{-1}$ ) $\times 10^3$ | 1.55 | $N(1.55,0.50)$               | Tranquilli et al. (1982); Duddy  |

|  |                 |                       |  |
|--|-----------------|-----------------------|--|
| $s^{-1}) \times 10^3$  |                 |                       | et al. (1984); van Woerkens et al. (1990, 1992); Upton (2008); Holmes (2018) |
| Metabolic heat generation ( $W m^{-3}$ ) <sup>[f]</sup>                          | 368             | $N(368,74)$           | Werner and Buse (1988); Ferreira and Yanagihara (2009)                       |
| Additional proportion of convection heat transfer at the skin surface, $\varphi$ | 0               | $U(0, \omega)$        | Assumed  |
|  | Hair-coat layer |                       |  |
| #sublayers   | 20              | $round(X_{20}^2 + 1)$ | Determined <sup>[g]</sup>  |
| Thickness (mm)   | 2               | $N(2,1)$              | Measured   |
| Hair thermal conductivity ( $W m^{-1} K^{-1}$ ) <sup>[h]</sup>                   | 0.3             | $N(0.6,0.35)$         | Davis Jr. (1972); Davis Jr. and Birkebak (1974)                              |
| Hair density (#hairs $cm^{-2}$ ) <sup>2)</sup>                                   | 150             | $N(150,50)$           | Measured   |
| Hair diameter ( $\mu m$ )  | 95              | $N(95,20)$            | Measured   |
| Hair length (mm)   | 12              | $N(12,2.5)$           | Measured   |
| Proportion of convection heat transfer at the hair-                              | 1               | $U(0,1)$              | Assumed  |

coat surface,  $\omega$

Environment and predicted inputs

|   |      |                |           |
|---|------|----------------|-----------|
| Emissivity of black globe   | 0.95 | $U(0.92,0.99)$ | Assumed   |
| Air velocity inside the brooder ( $\text{m s}^{-1}$ ) <sup>[i]</sup>      | 0.5  | $N(0.5,0.25)$  | Assumed   |
| Mean radiant temperature multiplicative factor <sup>[j]</sup>             | 1    | $N(1,0.1)$     | Assumed   |
| Convective heat transfer coefficient multiplicative factor <sup>[j]</sup> | 1    | $N(1,0.1)$     | Assumed   |
| Offset for measured temperatures <sup>[k]</sup>                           | 0    | $N(0,0.35)$    | Datasheet |
| Standard error offset for predicted temperatures <sup>[l]</sup>           | 0    | $N(0,1)$       | Assumed   |

---

<sup>[a]</sup> Values that would traditionally be chosen by an expert if system parameters were not optimized. <sup>[b]</sup>  $N(\mu, \sigma)$  stands for normal distribution with mean  $\mu$  and standard deviation  $\sigma$ .  $U(v_l, v_u)$  represents a uniform distribution with lower limit  $v_l$  and upper limit  $v_u$ .  $X_k^2$  represents a chi-squared distribution with  $k$  degrees of freedom. The function  $\text{round}(\mu)$  rounds  $\mu$  to its nearest integer. Only physiologically reasonable sampled values were kept from random sampling (e.g., thickness  $\geq 0$ ). <sup>[c]</sup> Blood

126

temperature was assumed as the input rectal temperature. Blood temperature multiplicative factor accumulatively multiplies blood temperature values of previous sublayers, reducing blood temperature for sublayers near the interface skin-hair-coat. For instance, since the expected values of blood temperature multiplicative factor and number of tissue sublayers are 0.995 and 33, respectively, the expected blood temperature at the last skin sublayer is  $0.995^{33} \times 38^{\circ}\text{C} = 32.2^{\circ}\text{C}$  for rectal temperature equals to  $38^{\circ}\text{C}$ . <sup>[d]</sup> Thickness of muscle layer was below measurement resolution; values were extrapolated from measurements performed in older pigs. <sup>[e]</sup> Chato (1968) and Cohen (1977) as cited by Holmes (2018). <sup>[f]</sup> Values for humans. Standard deviation included 20% deviation of reported values. <sup>[g]</sup> Required number of sublayers division for hair-coat layer was determined through a mesh refinement study (see Appendix A). <sup>[h]</sup> Traditional value was assumed equal to the average thermal conductivities of deer (0.258 W/(m-K)) and bear (0.329 W/(m-K)) hairs and the distribution included value of human hairs (0.938 W/(m-K)). Effective thermal conductivity of the hair-coat layer was calculated (Kowalski and Mitchell, 1979). <sup>[i]</sup> Air velocity inside the brooder was assumed still. <sup>[j]</sup> Multiplicative factors were inserted to consider for misfits between predictive equations for mean radiant temperature and convective heat transfer coefficient, and for possible experimental measurement errors. <sup>[k]</sup> Offset adds to input measured temperatures to account for measurement error. <sup>[l]</sup> Standard error of prediction added to temperatures predicted using machine learning algorithms to compensate for prediction errors.

## 2.7. Ensemble learning

Ensemble learning consists of combining individual learners to increase prediction accuracy and to provide a standard deviation for the predictions (Sagi and Rokach, 2018). In this study, an individual learner consists of a sampled set of system parameters (see Table 9 for system parameters). Ensemble prediction and variance were calculated as:

$$T_{j,e,i} = \sum_{l=1}^L \eta_l T_{j,l} \quad (134)$$

$$\sigma_{j,e,i}^2 = -T_{j,e,i}^2 + \sum_{l=1}^L \eta_l T_{j,l}^2 \quad (135)$$

$$\sum_{l=1}^L \eta_l = 1; 0 \leq \eta_l \leq 1 \forall l \in [1, L] \quad (136)$$

where  $j$  refers to s (skin) or h (hair-coat),  $e$  refers to ensemble,  $i$  refers to data point  $i$ ,  $l$  refers to learner (set of system parameters)  $l$ ,  $L$  is the number of individual learners in the ensemble,  $\eta_l$  is the weight of learner  $l$  in the ensemble predictions,  $T_{j,l}$  refers to temperature at surface  $j$  estimated by learner  $l$ , and  $T_{j,e,i}$  and  $\sigma_{j,e,i}^2$  refer to ensemble temperature prediction and variance, respectively, at surface  $j$  for data point  $i$ .

Ideally, an ensemble provides accurate predictions (expressed by low MSE) with a tight confidence interval (expressed by low prediction variances) that makes the

measured data extremely likely given the ensemble predictions (expressed by a high likelihood). The objective function (for minimization) used to attain these three criteria was defined as:

$$obj = \lambda \text{MSE} + (\lambda - 1)\ell \quad (137)$$

$$\text{MSE} = \frac{1}{2n} \sum_{i=1}^n (T_{s,m,i} - T_{s,e,i})^2 + (T_{h,m,i} - T_{h,e,i})^2 \quad (138)$$

$$\begin{aligned} \ell = n \log(2\pi) + \frac{1}{2} \sum_{i=1}^n \log \sigma_{s,e,i}^2 + \frac{(T_{s,m,i} - T_{s,e,i})^2}{\sigma_{s,e,i}^2} + \log \sigma_{h,e,i}^2 \\ + \frac{(T_{h,m,i} - T_{h,e,i})^2}{\sigma_{h,e,i}^2} \end{aligned} \quad (139)$$

where, subscripts  $m$  refers to measured temperatures,  $n$  is number of data points,  $\ell$  is log-likelihood function, and  $\lambda$ , with values between 0 and 1, is tradeoff between minimizing MSE and maximizing  $\ell$  (equivalent to minimizing  $-\ell$ ). Values of  $\lambda$  were 0,  $10^{-4:0.25:-1}$ , 0.2:0.3:0.8,  $(1 - 10^{-1:0.25:-4})$ , and 1, where  $a:b:c$  represents a series of values from  $a$  to  $c$  with step  $b$ .

Ensemble learning can be divided into (a) learning which individual learners compose the ensemble and (b) learning values for  $\eta$ . Since exploring all possible combinations of individual learners is not computationally feasible (10,002! possibilities), three algorithms were considered for selecting individual learners: (1) naively selecting the first  $L$  sets of system parameters (individual learners) that minimized MSE, (2)

randomly selecting  $L$  sets of system parameters, and (3) greedy search for  $L$  sets of system parameters. For learning  $\eta$ , two algorithms were considered: (1) bagging, and (2) optimum weights. Bagging consists of assigning the same  $\eta$  for all learners in the ensemble. Optimum weights consists of minimizing (using successive quadratic programming in Octave) the objective function (Eq. (137)) through  $\eta$ .

The Jacobian and Hessian matrices for the optimum weights algorithm can be calculated as follow: let  $P$  be the  $2n \times L$  matrix with prediction to temperature  $j$  for data point  $i$  with individual learner  $l$  in row  $i$  and column  $l$  if  $j = s$  and at row  $n + i$  if  $j = h$ , and  $T_m$ ,  $T_e$ , and  $\sigma^2$  be  $2n \times 1$  vectors of the measured temperatures, predicted temperatures, and predicted inverse-variances with skin surface variables at positions 1 to  $n$  and hair-coat surface variables at positions  $(n + 1)$  to  $2n$ . Let the following notation denote element-wise operations:

$$(\zeta \odot \vartheta)_i = \zeta_i \vartheta_i \quad (140)$$

$$(\vartheta \wedge n)_i = \vartheta_i^n \quad (141)$$

$$(\Psi * \zeta)_{i,j} = \Psi_{i,j} \zeta_j \quad (142)$$

$$(\Psi \sqcap n)_{i,j} = \Psi_{i,j}^n \quad (143)$$

where,  $\zeta_j$  represents element  $j$  of vector  $\zeta$  and  $\Psi_{i,j}$  represents the element  $i,j$  (row, column) of matrix  $\Psi$ . Hence, the Jacobian and Hessian matrices can be calculated as follows:

$$J = \frac{\partial obj}{\partial \eta} = -\frac{\lambda}{n} P^t e_{rr} + (\lambda - 1) \left\{ \frac{1}{2} \left[ \frac{e_{rr}^2}{\sigma^4} - \sigma^{-2} \right] \Sigma^{-2'} + \left( \frac{e_{rr}}{\sigma^2} \right)^t P \right\}^t \quad (144)$$

$$H = \frac{\partial^2 obj}{\partial \eta^2} = \frac{\lambda}{n} P^t P + (\lambda - 1) \left\{ \left[ -2P^t \frac{e_{rr}}{\sigma^2} + \Sigma^{-2'} \left( \frac{1}{2} \sigma^{-4} - \frac{e_{rr}^2}{\sigma^6} \right) \right] \Sigma^{-2'} - \left( P^t \frac{e_{rr}^2}{\sigma^4} \right) P \right\} \quad (145)$$

$$e_{rr} = (T_m - T_e) \quad (146)$$

$$\frac{e_{rr}}{\sigma^2} = e_{rr} \odot \sigma^{-2} \quad (147)$$

$$\frac{e_{rr}}{\sigma^4} = \frac{e_{rr}}{\sigma^2} \odot \sigma^{-2} \quad (148)$$

$$\frac{e_{rr}^2}{\sigma^4} = \frac{e_{rr}}{\sigma^2} \wedge 2 \quad (149)$$

$$\frac{e_{rr}^2}{\sigma^6} = \frac{e_{rr}^2}{\sigma^4} \odot \sigma^{-2} \quad (150)$$

$$\sigma^{-4} = \sigma^{-2} \odot \sigma^{-2} \quad (151)$$

$$\Sigma^{-2'} = P \sqcap 2 - 2(P^t T_e)^t \quad (152)$$

where, superscript  $t$  represents matrix transpose operation. The optimization was constrained to Eq. (136), which has Jacobian equal to vector of ones with size  $L$ .

With 3 algorithms for selecting individual learners and 2 algorithms for computing weights, a total of 6 ensemble learning algorithms were considered. For naïve search for individual learners, a combination of the first 2 to 1,000 learners that minimized the MSE was considered. For random search, 5,000 combinations of up to 1,000 randomly selected learners were considered for bagging, while for optimum weights, the total number of learners in the ensemble was between 5 and 20 (because of the high computational time of the optimum weights algorithm and its tendency to select only a few non-zero weights; see Appendix E for computational times). Greedy search with bagging algorithm started with the learner with minimum MSE, calculated the objective function for the current ensemble plus one learner (for all learners that were not in the ensemble), added to the ensemble the learner that minimized the objective function, and searched for the next learner until the ensemble size was 1,000. Greedy search with optimum weights algorithm started with the first 20 learners with minimum MSE, added the next learner with minimum MSE to the ensemble, removed any learners with a zero weight, and added the next learner to the ensemble until all learners were considered for the ensemble.

Up to 28 ensemble candidates were selected given the criteria of minimum MSE, objective function (Eq. (137)), Akaike information criterion (AIC), Bayesian information criterion (BIC), or  $-\ell$ , calculated based on a 5-fold modular cross-validation (objective function for naïve and random search with bagging was considered for  $\lambda = 1$  only, that is, only for minimizing MSE). The set of candidate

ensembles was reduced to 6 by selecting, for each algorithm, the candidate ensemble with the lowest mean standard deviation for the testing dataset. Then, 3 candidates with maximum  $\ell$  for the test dataset were selected and the final ensemble was the one that minimized the sum of MSE and mean standard deviation squared for the testing dataset.

## 2.8. Energy balance

Energy balance of animals can be stated as (Collier and Gebremedhin, 2015)

$$E_F + E_{Met} = E_{Mai} + E_G + E_R + E_P + E_L + E_S \quad (153)$$

where,  $E_F$  (W m<sup>-2</sup>) is energy from feed,  $E_{Met}$  (W m<sup>-2</sup>) is energy from metabolism,  $E_{Mai}$  (W m<sup>-2</sup>) is energy required for maintenance,  $E_G$  (W m<sup>-2</sup>) is energy available for growth,  $E_R$  (W m<sup>-2</sup>) is energy available for reproduction purposes,  $E_P$  (W m<sup>-2</sup>) is energy available for production,  $E_L$  (W m<sup>-2</sup>) is energy transfer through latent heat exchange, and  $E_S$  (W m<sup>-2</sup>) is energy transfer through sensible heat exchanges. For piglets,  $E_R = E_P = 0$ . Hence, to improve production, the objective is to maximize  $E_G$  given  $E_F$ ,  $E_{Met}$ ,  $E_{Mai}$ ,  $E_L$ , and  $E_S$ , i.e.,

$$\max E_G = \max(E_F + E_{Met} - E_{Mai} - E_L - E_S) \quad (154)$$

Previous studies (Zhou and Xin, 1999; Collier and Gebremedhin, 2015) demonstrated that, given a specific feed composition (which affects  $E_F$ ) and genetics of animal (which affects  $E_{Met}$ ), maximum growth is observed at thermo-neutral conditions,

where the thermal component of  $E_{Mai}$  equilibrates with  $E_L$  and  $E_S$ . This implies that

$$\max E_G \Rightarrow \min |THP - E_L - E_S| \quad (155)$$

$$H_{opt} = \arg \min_H |THP - E_L - E_S| \quad (156)$$

where,  $THP$  ( $W m^{-2}$ ) is total heat production,  $H_{opt}$  (W) is optimum supplemental heat, and all energy terms were considered functions of  $T_a$ ,  $w$ , and  $H$ . Since increasing  $H$  results in increasing  $T_a$ , the additive effect of  $H$  on  $T_a$  was predicted using ordinary linear square regression (i.e., air temperature input to compute  $E_S$ ,  $T_{a,in}$ , was calculated as  $T_a + \alpha \times H$ , where  $\alpha$  is constant).  $E_S$ , which is equivalent to  $q''_s$ , was computed (similar to  $T_s$ ) using the best ensemble. For  $E_L$ , all research papers (Brown-Brandl et al., 2004, 2014; Stinn and Xin, 2014a) that measured latent heat production (LHP) of swine reported values of LHP from animal source, which includes evaporation from the following sources: cutaneous, respiratory, feces, urine, and dripping water. Since cutaneous evaporation is negligible in swine (McArthur, 1981), respiratory evaporation is the major component of piglets' LHP. However, LHP reported for swine was approximately one order of magnitude larger than respiratory heat transfer values reported for other livestock (Gebremedhin et al., 1981; Stevens, 1981; Maia et al., 2005, 2008, 2016; Berman, 2006; Camerero et al., 2016; Costa et al., 2018ab). Hence, LHP was assumed as a uniform random variable with values between those reported for livestock in non-heat stress conditions. Table 10 shows equations used to compute energy terms shown in Eq. (156).

Table 10. Equations used to compute energy terms in Eq. (156).

| Parameter  | Distribution <sup>[a]</sup>                                   | Reference                                       |
|--|---|---|
| Total heat production (W m <sup>-2</sup> ) <sup>[b]</sup>    | $N(10^{(0.715-0.0025T_{a,eq}+0.0211\log_{10} w)}, 0.15)w/A_s$ | Brown-Brandl et al. (2014)                      |
| Latent heat production (W m <sup>-2</sup> )                  | $U(0,15)$   | Assumed   |
| Sensible heat production (W m <sup>-2</sup> ) <sup>[c]</sup> | $N(q_s'', \sigma_{s,q})$                                      | Computed  |
| Surface area of the animal (m <sup>2</sup> )                 | $0.087w^{2/3}N(1,0.05)$                                       | Meeh (1879) cited by Lusk (1928) <sup>[d]</sup> |

<sup>[a]</sup>  $N(\mu, \sigma)$  stands for normal distribution with mean  $\mu$  and standard deviation  $\sigma$ .  $U(v_l, v_u)$  represents a uniform distribution with lower limit  $v_l$  and upper limit  $v_u$ . <sup>[b]</sup>  $w$  is animal weight,  $A_s$  is surface area of the animal, and  $T_{a,eq}$  is equivalent air temperature defined as  $q_s''(T_{a,eq}, 0) = q_s''(T_{a,in}, H)$ .  $T_{a,eq}$  was used to consider for the effect of supplemental heat (H) in the predicted total heat production (the regression

equation does not intrinsically include effects of supplemental heat). Standard deviation was obtained from literature. <sup>[c]</sup>  $q_s''$ : skin heat flux predicted using the best ensemble;  $\sigma_{s,q}$ : standard deviation of  $q_s''$  predicted using the best ensemble. <sup>[d]</sup> Meeh (1879) was not accessible. This regression equation was chosen because it was developed for swine and values predicted with it were close to values measured using 3D scanners (Milan et al., 2018b). Multiplicative normally distributed error was estimated from Brody (1945).

Because of uncertainties in the terms of Eq. (156), for each combination of  $T_a$  and  $w$ , the mean value of  $H_{opt}$  and its 95% confidence interval (lower and upper 2.5% of sampled values) that minimized Eq. (156) were obtained using 10,000 samples parametric bootstrap (Efron and Hastie, 2016).

### ***3. RESULTS AND DISCUSSION***

Data for  $D$ ,  $N_h$ ,  $H_L$ ,  $H_D$ ,  $L_h$ ,  $L_s$ ,  $L_f$ , and  $L_m$  were summarized in Table 9. These data, together with  $w$  and  $J$ , are given in Appendix B.

#### **3.1. Environmental data**

Figure 26 shows the environmental conditions the piglets were exposed to. When supplemental heat increased,  $T_a$  and  $T_g$  increased and RH decreased, as expected (Monteith and Unsworth, 2013).  $T_{a,pen}$  was similar for all stratum.

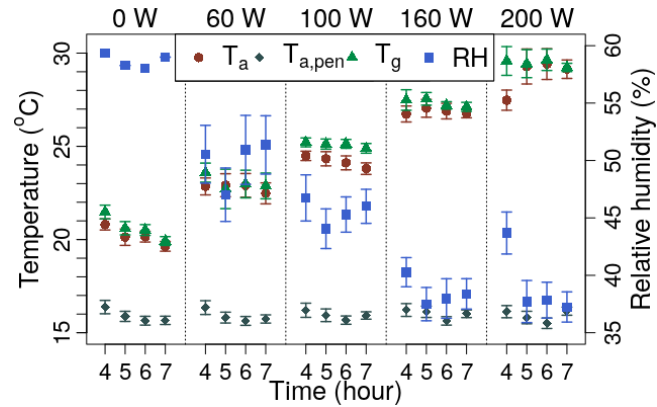


Figure 26. Experimental data (mean  $\pm$  standard error of the mean) for air ( $T_a$ ) and black-globe ( $T_g$ ) temperatures and relative humidity (RH) inside the brooder, and air temperature in the pen ( $T_{a,pen}$ ) stratified by measurement time and supplemental heat.

### 3.2. Machine learning models to predict input temperatures

Figure 27 shows training, cross-validation, and testing MSE for the best machine learning models (models with hyperparameters that minimized 5-fold modular cross-validation MSE). As expected, testing MSE (the best estimation of future model prediction errors; van der Vaart et al., 2006) was greater than training and cross-validation MSEs for  $T_a$  (Figure 27a) and  $T_g$  (Figure 27b) but not for  $T_r$  (Figure 27c), which can be explained by chance or because  $T_r$  is tightly regulated regardless of environmental conditions. Ordinary linear regression model was selected to predict  $T_a$ ,  $T_g$ , and  $T_r$  because of its low MSE and ability to generalize (no evidences of overfitting were observed in the generalization study reported in Appendix C). Figure 28a,b show performance of the best fit models using the mean dataset and Figure 28c shows absolute percentage error. Model predictions agreed very well with measured

values. Absolute errors were 1.38% for  $T_a$ , 0.96% for  $T_g$ , and 0.78% for  $T_r$ , based on the mean dataset.

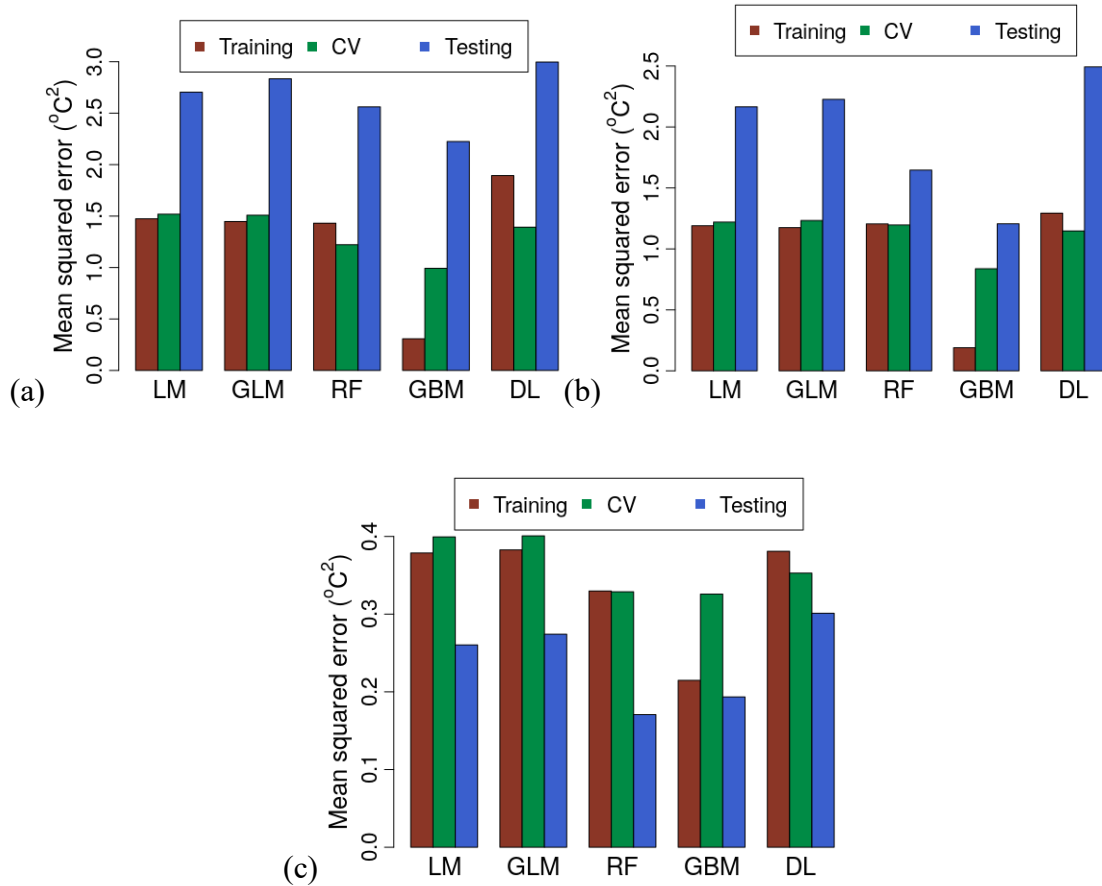


Figure 27. Performance of the best fit machine learning algorithms to predict air temperature inside the brooder ( $T_a$ ; a), black-globe temperature inside the brooder ( $T_g$ ; b), and rectal temperature ( $T_r$ ; c) given air temperature in the pen and supplemental heat. Mean squared error (MSE) for training, cross-validation (CV), and testing are shown. Selected model was LM for  $T_a$ ,  $T_g$ , and  $T_r$ . LM: ordinary linear regression with backwards selection; GLM: generalized linear regression model with elastic net

regularization; RF: random forests; GBM: gradient boosted machines; DL: deep learning with ReLU activation function.

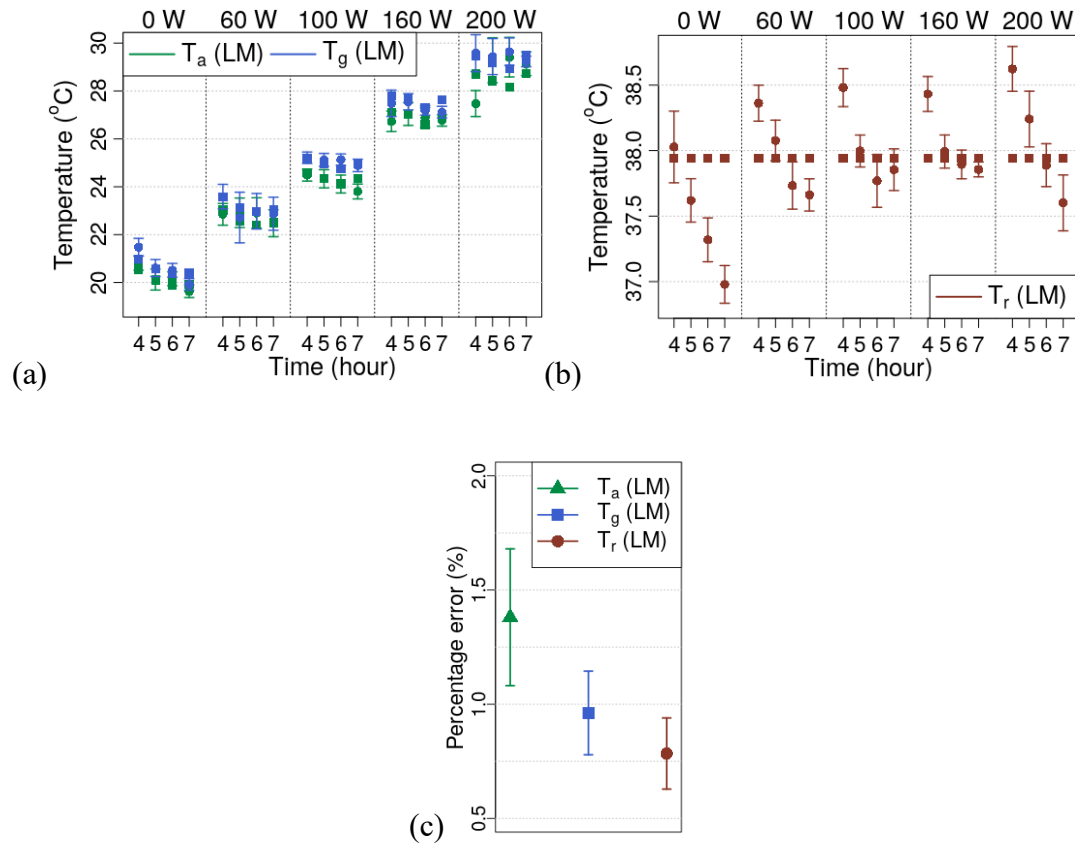


Figure 28. Measured (●) and predicted (■) air ( $T_a$ , a) and black-globe ( $T_g$ , a) temperatures inside the brooder and rectal temperature ( $T_r$ , b) for the mean dataset stratified by measurement time and supplemental heat. Absolute percentage errors of the predicted temperatures (c). Data shown are mean  $\pm$  standard error of the mean. Temperatures were predicted using ordinary linear regression with backwards selection (LM).

### 3.3. Monte Carlo optimization and ensemble learning

Figure 29a shows training and testing MSE for mechanistic model using the traditional set of system parameters with measured (TM) or expected (TP; predicted using machine learning algorithms) inputs ( $T_a$ ,  $T_g$ , and  $T_r$ ), and for the set of system parameters with minimum training MSE (optimized with Monte Carlo method). Monte Carlo optimization reduced training and testing MSE by 3.2 times compared to TM or TP. Fei et al. (2012) observed a similar reduction in error (from 7.5% to 1.5%) when Monte Carlo method was used to optimize parameters for a mechanistic model developed to predict internal temperature of lizards.

Figure 29b shows performance metrics for ensemble candidates. Apart from ensemble candidates obtained with random search with bagging, training and testing MSE of ensemble candidates were similar among themselves. The best performing ensemble candidate was greedy search with bagging. The best ensemble reduced training and testing MSE by 5% in addition to providing confidence intervals for predictions. To the best of our knowledge, this is the first attempt to include uncertainties through confidence intervals into bioenergetic models of livestock. Confidence intervals account for, at least partially, uncertainties in input temperatures predicted by machine learning algorithms and distribution of system parameters optimized through Monte Carlo optimization method as well as variability from experimental conditions and variability in the animals themselves. These last two variability components are, at least partially, accounted for by confidence intervals because the experimental data

were used for model optimization. Model optimization target minimization of MSE and variance components of the data that could not be explained by model predictions.

Although the space of ensemble sizes explored in this study was large (up to 1,000 individual learners, with 6 ensemble learning algorithms), the best performing ensembles typically had small sizes (2-4 individual learners). One explanation for obtaining the best performing ensembles with small sizes could be that all individual learners explored in this study were derived from the same mechanistic model, differing only on the input set of system parameters. As adding similar learners to an ensemble can reduce its diversity (Bonab and Can, 2016, 2017), and diverse ensembles usually outperform non-diverse ones (Bonab and Can, 2016, 2017), it could be the case that the best balance between diversity and ensemble size was obtained for small ensembles and that prediction accuracy could be further improved by developing a larger and more diverse ensemble.

In this study, the objective function used to combine sets of system parameters into ensembles was a linear combination between MSE and log-likelihood. Other possible objective functions could include variances of predictions, Akaike information criterion (AIC), or Bayesian information criterion (BIC). The effect of minimizing variances of predictions would likely be similar to minimizing MSE, given their similar formulation (note that, in this study, variances of predictions were assumed to be independent from each other, implying that variances of predictions were not equal to MSE). Minimizing AIC or BIC would be similar to maximizing log-likelihood but

favoring small sized ensembles, given that AIC and BIC are linear combinations of log-likelihood with penalizations for adding individual learners to the ensemble.

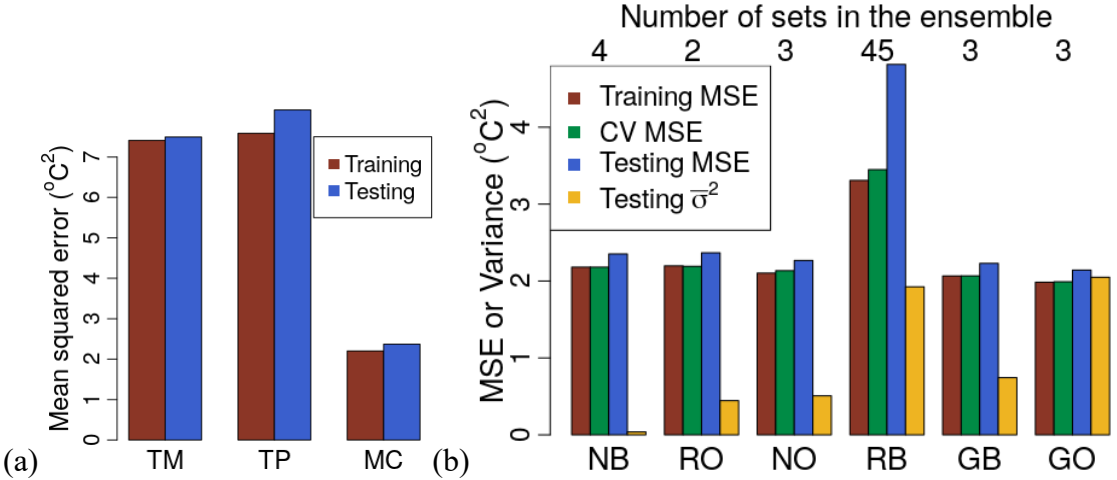


Figure 29. Performance of sets of system parameters (a) and ensembles (b) in predicting skin ( $T_s$ ) and hair-coat ( $T_h$ ) surface temperatures. Ensemble candidates are in the order from low-to-high (left-to-right) log-likelihood. The best performing ensemble candidate was GB. Performance metrics were mean squared error (MSE) evaluated in training, cross-validation (CV), and testing datasets, and mean standard deviation squared ( $\bar{\sigma}^2$ ) evaluated in the testing dataset (43 samples). CV MSE and  $\bar{\sigma}^2$  are only defined for ensembles. TM: traditional set of system parameters and measured input data; TP: traditional set of system parameters and expected input data predicted with machine learning algorithms; MC: set of system parameters drawn from Monte Carlo sampling method with minimum training MSE; NB: ensemble obtained with naïve search and bagging; RO: ensemble obtained with random search with optimum weights; NO: ensemble obtained with naïve search and optimum

weights; RB: ensemble obtained with random search and bagging; GB: ensemble obtained with greedy search and bagging; GO: ensemble obtained with greedy search and optimum weights.

Figure 30 shows measured and predicted  $T_h$  (Figure 30a) and  $T_s$  (Figure 30b), their absolute percentage error (Figure 30c), and predicted  $q''_s$  (Figure 30d). Figure 31 shows surface plots for the relationship between  $H$  (x axis) and  $T_a$  (y axis) with  $T_h$ ,  $T_s$ , and  $q''_s$  (color gradients and contours). Regression approximations for mean values of  $T_h$ ,  $T_s$ , and  $q''_s$  are given in Appendix D. The final ensemble predictions agreed with measured values with absolute errors of 2.09% and 3.04% in the mean dataset for  $T_h$  and  $T_s$ , respectively. Observed errors are lower than errors reported in other studies. Turnpenny et al. (2000ab) reported 7% error for  $T_s$  of pigs obtained using a mechanistic model. Loughmiller et al. (2001) reported 3.5% error for predicting mean body-surface temperature for pigs using a linear regression model. Costa et al. (2010) reported 5.5% error for predicting surface temperature for piglets using a linear regression model. The only study that reported smaller errors was Gorczyca et al. (2018), where machine learning algorithms were used to predict  $T_h$  and  $T_s$  and reported errors of 1.35% and 0.62%, respectively, given  $T_a$ ,  $T_g$ ,  $H$ , and measurement time. Since the dataset for this study and for Gorczyca et al. (2018) is the same, this indicates that prediction errors obtained from mechanistic models could be further reduced by including circadian thermoregulation mechanisms or by solving dynamic mechanistic models that consider previous measurements of environment and

physiological responses. This can be accomplished using numerical methods (Milan and Gebremedhin, 2018).

Mean absolute difference between measured and predicted  $T_h$  and  $T_s$  was lower than 1 °C, which is within the measurement error for  $T_h$  ( $\pm 1^\circ\text{C}$ ) but not for  $T_s$  ( $\pm 0.2^\circ\text{C}$ ). This result implies that there is great potential in developing interconnected models, such as interconnecting Monte Carlo optimization, machine learning algorithms, mechanistic models, and ensemble learning. Interconnected models have the potential to provide predictions for individual animals, even under the same environmental conditions. This means that farmers would be able to obtain individualized information for management and intervention purposes in real-time.

### **3.4. Energy balance**

Figure 32 shows surface plots for the relationship between animal weight ( $x$ -axis) and air temperature ( $y$ -axis) with  $H_{opt}$  and energy flux imbalance (color gradients and contours). Air temperature values in Figure 32 are for  $H = 0$  W (input air temperature for calculations was  $T_{a,in}$ , which is  $T_a$  added by the effect of  $H$ ; see Sec. 2.8 and Appendix D). For practical purposes, mean values of  $H_{opt}$  given  $T_a$  and  $w$  (Figure 32) are shown in Table 11, and a polynomial regression approximation is given in Appendix D. For  $T_a$  at the zone of least thermoregulation for sows ( $15^\circ\text{C}$  to  $19^\circ\text{C}$ ), predicted  $H_{opt}$  is 266 to 334 W and 44 to 128 W for piglets with weights of 1 kg and 20 kg, respectively. Assuming 1 kg for birth weight and 20 kg for weight at the end of

the farrowing cycle, supplying  $H_{opt}$ , instead of constant-intensity supplemental heat, could help farms become more energy efficient, as can be noted by the  $\sim 200$  W difference in  $H_{opt}$  for 1 kg versus 20 kg.

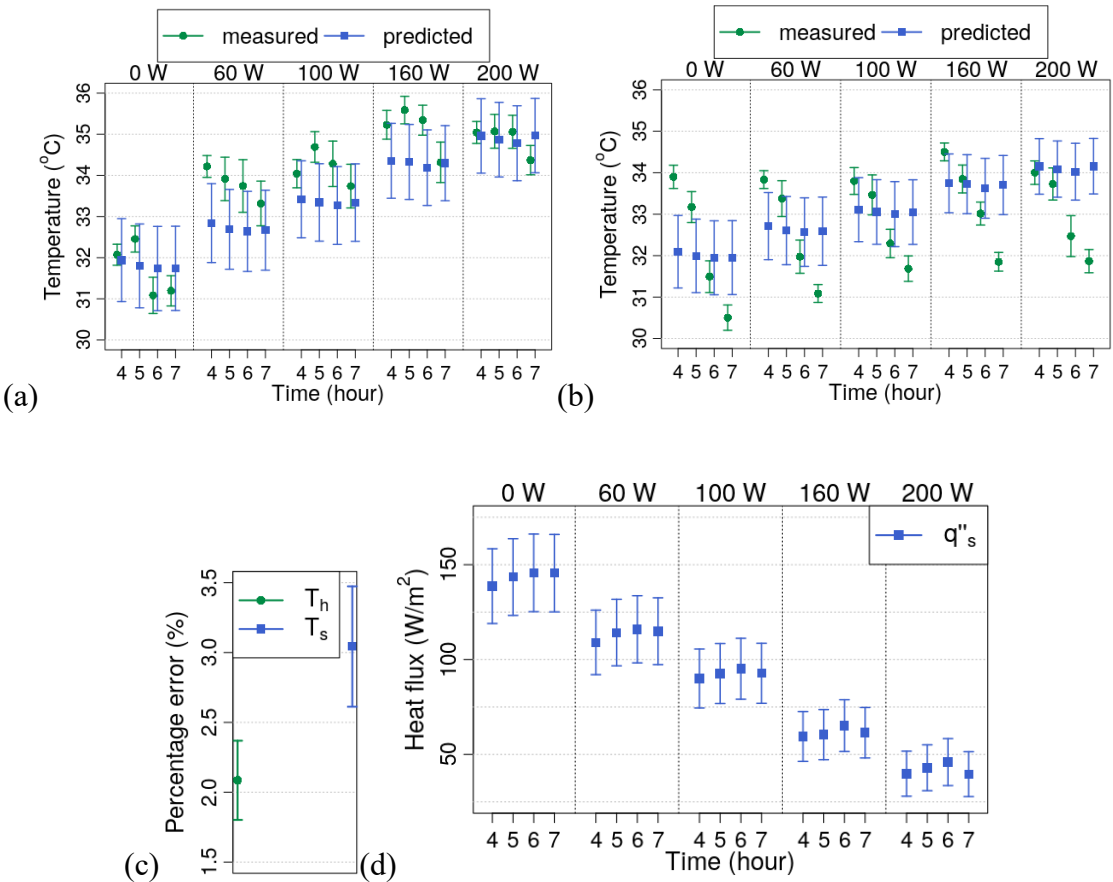


Figure 30. Hair-coat ( $T_h$ ; a) and skin ( $T_s$ ; b) surface temperatures, and skin-surface heat flux ( $q''_s$ ; d) predicted using the best performing ensemble (greedy search with bagging) for the mean dataset (stratified by measurement time and supplemental heat), and (c) absolute percentage errors of the predicted temperatures. Measured values and absolute percentage errors are presented as mean  $\pm$  standard error of the mean.

Predicted values are presented as mean  $\pm$  standard deviation of the mean.

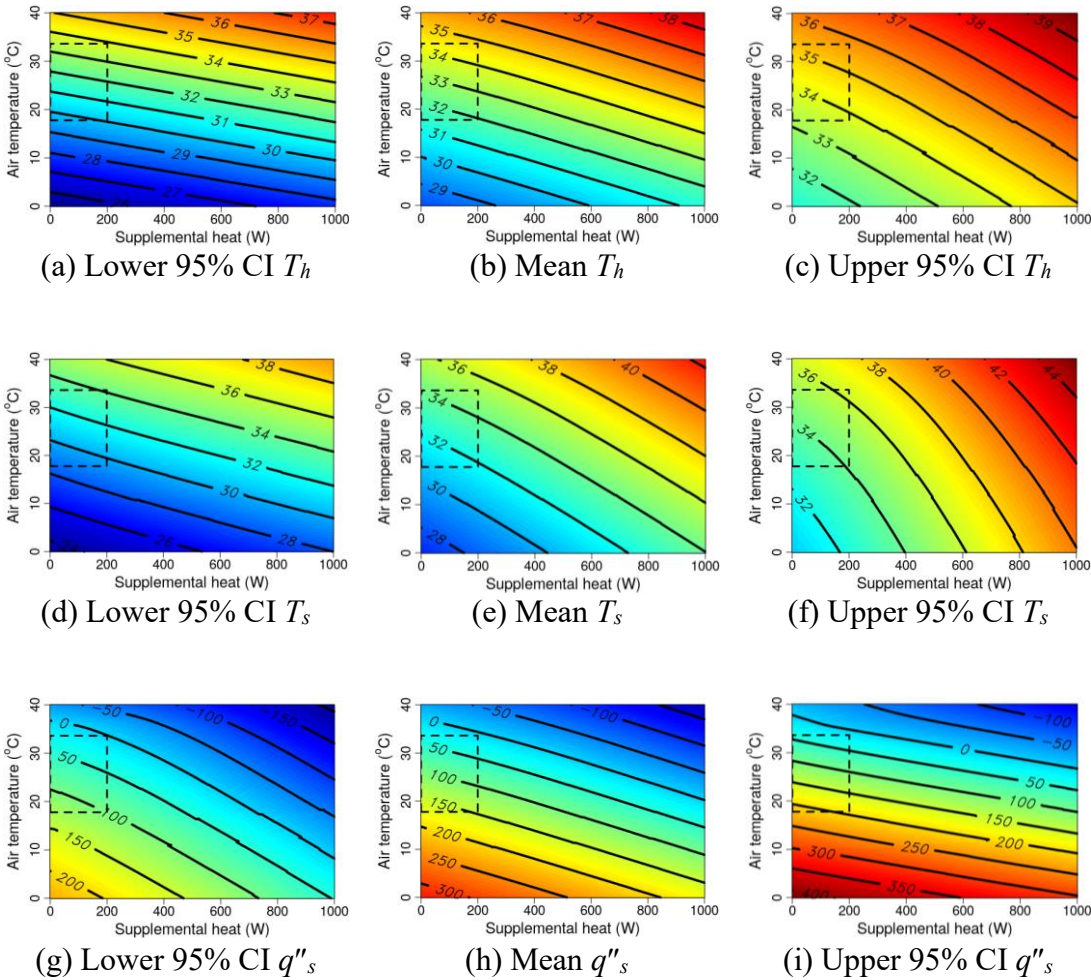


Figure 31. Surface plots for the relationship between supplemental heat ( $x$ -axis) and air temperature ( $y$ -axis) with hair-coat surface temperature ( $T_h$ ,  $^{\circ}\text{C}$ ), skin surface temperature ( $T_s$ ,  $^{\circ}\text{C}$ ), and skin surface heat flux ( $q''_s$ ,  $\text{W m}^{-2}$ ). Plots show (a) lower 95% confidence interval (CI), (b) mean, and (c) upper 95% CI for  $T_h$ ; (d) lower 95% CI, (e) mean, and (f) upper 95% CI for  $T_s$ ; and (g) lower 95% CI, (h) mean, and (i) upper 95% CI for  $q''_s$ .  $T_h$ ,  $T_s$ , and  $q''_s$  are shown using color gradients and contours. Color

gradients are the same for each set of plots (a-c, d-f, and g-i). Numbers and lines on the surface plots indicate contours. Dashed rectangles represent range of measured experimental data.

One possible explanation for the variabilities in Figure 32 is the uncertainties in the mathematical framework. Because model optimization was based on minimizing the error in predicting the physiological temperatures of piglets, other possible explanations include intra- and intervariability of the piglets, thermoregulation, and behavioral adaptations (Wheeler et al., 2008; Vasdal et al., 2009, 2010a, 2010b). Previous studies reported that supplemental heat usage decreased with increasing animal age (Xin et al., 1997a, 1997b) and air temperature (Xin et al., 1999; Zhou and Xin, 1999). Our results show that these conditions are explained by energy imbalance that occurs as the animals increase in weight or because of increased air temperature.

Table 11. Mean predicted optimum supplemental heat ( $H_{opt}$ , W) for piglets given air temperature ( $T_a$ , rows) and animal weight (w, columns).

| $T_a$<br>(°C) | Animal Weight (kg) |     |     |     |     |     |     |     |     |     |     |     |     |     |     |     |     |     |     |     |
|---------------|--------------------|-----|-----|-----|-----|-----|-----|-----|-----|-----|-----|-----|-----|-----|-----|-----|-----|-----|-----|-----|
|               | 1                  | 2   | 3   | 4   | 5   | 6   | 7   | 8   | 9   | 10  | 11  | 12  | 13  | 14  | 15  | 16  | 17  | 18  | 19  | 20  |
| 0             | 584                | 555 | 533 | 516 | 501 | 488 | 477 | 466 | 456 | 446 | 437 | 429 | 421 | 414 | 407 | 400 | 393 | 387 | 380 | 374 |
| 1             | 567                | 538 | 517 | 500 | 485 | 472 | 460 | 449 | 439 | 430 | 421 | 413 | 404 | 397 | 390 | 384 | 377 | 370 | 364 | 358 |
| 2             | 550                | 522 | 501 | 483 | 469 | 456 | 444 | 433 | 423 | 414 | 405 | 396 | 388 | 381 | 373 | 366 | 361 | 354 | 348 | 341 |
| 3             | 534                | 505 | 484 | 467 | 452 | 439 | 428 | 417 | 407 | 397 | 388 | 380 | 372 | 364 | 357 | 350 | 343 | 338 | 331 | 325 |
| 4             | 517                | 488 | 468 | 451 | 436 | 423 | 411 | 400 | 391 | 381 | 372 | 364 | 356 | 348 | 341 | 334 | 327 | 321 | 314 | 310 |
| 5             | 501                | 472 | 451 | 434 | 420 | 407 | 395 | 384 | 374 | 365 | 356 | 348 | 340 | 332 | 325 | 318 | 311 | 304 | 298 | 292 |
| 6             | 484                | 455 | 434 | 418 | 403 | 390 | 378 | 368 | 358 | 348 | 340 | 331 | 323 | 316 | 308 | 301 | 294 | 288 | 281 | 275 |
| 7             | 468                | 439 | 418 | 401 | 387 | 374 | 362 | 351 | 341 | 332 | 323 | 315 | 307 | 299 | 292 | 285 | 278 | 272 | 265 | 259 |
| 8             | 451                | 422 | 401 | 384 | 370 | 357 | 346 | 335 | 325 | 316 | 307 | 298 | 290 | 283 | 276 | 269 | 262 | 255 | 249 | 243 |
| 9             | 434                | 406 | 384 | 368 | 353 | 341 | 329 | 318 | 308 | 299 | 290 | 282 | 274 | 267 | 259 | 252 | 245 | 239 | 233 | 226 |
| 10            | 418                | 389 | 368 | 351 | 336 | 324 | 312 | 302 | 292 | 283 | 274 | 266 | 258 | 250 | 243 | 236 | 229 | 223 | 216 | 210 |
| 11            | 401                | 372 | 351 | 334 | 320 | 307 | 296 | 285 | 275 | 266 | 257 | 249 | 241 | 234 | 226 | 219 | 213 | 206 | 200 | 194 |
| 12            | 384                | 355 | 335 | 318 | 303 | 290 | 279 | 269 | 259 | 249 | 241 | 232 | 225 | 217 | 210 | 203 | 196 | 190 | 183 | 177 |
| 13            | 367                | 339 | 318 | 301 | 287 | 274 | 262 | 252 | 242 | 233 | 224 | 216 | 208 | 200 | 193 | 186 | 180 | 173 | 167 | 161 |
| 14            | 351                | 322 | 301 | 284 | 270 | 257 | 245 | 235 | 225 | 216 | 207 | 199 | 192 | 184 | 177 | 170 | 163 | 157 | 150 | 144 |
| 15            | 334                | 305 | 284 | 268 | 253 | 240 | 229 | 218 | 208 | 199 | 191 | 183 | 175 | 167 | 160 | 153 | 146 | 140 | 134 | 128 |
| 16            | 317                | 288 | 268 | 251 | 236 | 224 | 212 | 201 | 191 | 182 | 174 | 166 | 158 | 151 | 143 | 137 | 130 | 123 | 117 | 111 |
| 17            | 300                | 271 | 251 | 234 | 220 | 207 | 195 | 185 | 175 | 165 | 157 | 149 | 141 | 134 | 127 | 120 | 113 | 107 | 100 | 94  |
| 18            | 283                | 254 | 234 | 217 | 203 | 190 | 178 | 168 | 158 | 149 | 140 | 132 | 124 | 117 | 110 | 103 | 96  | 90  | 84  | 78  |
| 19            | 266                | 237 | 217 | 200 | 186 | 173 | 162 | 151 | 141 | 132 | 123 | 115 | 107 | 100 | 93  | 86  | 80  | 73  | 67  | 61  |
| 20            | 249                | 220 | 200 | 183 | 169 | 156 | 144 | 134 | 124 | 115 | 106 | 98  | 90  | 83  | 76  | 69  | 63  | 56  | 50  | 44  |
| 21            | 232                | 203 | 183 | 166 | 152 | 139 | 128 | 117 | 107 | 98  | 89  | 81  | 73  | 66  | 59  | 52  | 45  | 40  | 33  | 27  |
| 22            | 214                | 186 | 166 | 149 | 135 | 122 | 110 | 100 | 90  | 81  | 72  | 64  | 56  | 49  | 42  | 35  | 28  | 22  | 16  | 10  |
| 23            | 197                | 169 | 148 | 132 | 117 | 105 | 93  | 83  | 73  | 64  | 55  | 47  | 39  | 32  | 25  | 18  | 11  | 5   | 0   | 0   |
| 24            | 180                | 152 | 131 | 115 | 100 | 88  | 76  | 66  | 56  | 47  | 38  | 30  | 22  | 15  | 8   | 0   | 0   | 0   | 0   | 0   |
| 25            | 163                | 134 | 114 | 97  | 83  | 70  | 59  | 49  | 39  | 30  | 21  | 13  | 5   | 0   | 0   | 0   | 0   | 0   | 0   | 0   |
| 26            | 145                | 117 | 96  | 80  | 66  | 53  | 42  | 31  | 22  | 12  | 4   | 0   | 0   | 0   | 0   | 0   | 0   | 0   | 0   | 0   |
| 27            | 128                | 100 | 79  | 63  | 48  | 36  | 25  | 14  | 4   | 0   | 0   | 0   | 0   | 0   | 0   | 0   | 0   | 0   | 0   | 0   |
| 28            | 110                | 82  | 62  | 45  | 31  | 18  | 7   | 0   | 0   | 0   | 0   | 0   | 0   | 0   | 0   | 0   | 0   | 0   | 0   | 0   |
| 29            | 93                 | 65  | 44  | 28  | 14  | 0   | 0   | 0   | 0   | 0   | 0   | 0   | 0   | 0   | 0   | 0   | 0   | 0   | 0   | 0   |
| 30            | 75                 | 47  | 27  | 10  | 0   | 0   | 0   | 0   | 0   | 0   | 0   | 0   | 0   | 0   | 0   | 0   | 0   | 0   | 0   | 0   |
| 31            | 58                 | 29  | 9   | 0   | 0   | 0   | 0   | 0   | 0   | 0   | 0   | 0   | 0   | 0   | 0   | 0   | 0   | 0   | 0   | 0   |
| 32            | 40                 | 12  | 0   | 0   | 0   | 0   | 0   | 0   | 0   | 0   | 0   | 0   | 0   | 0   | 0   | 0   | 0   | 0   | 0   | 0   |
| 33            | 22                 | 0   | 0   | 0   | 0   | 0   | 0   | 0   | 0   | 0   | 0   | 0   | 0   | 0   | 0   | 0   | 0   | 0   | 0   | 0   |
| 34            | 4                  | 0   | 0   | 0   | 0   | 0   | 0   | 0   | 0   | 0   | 0   | 0   | 0   | 0   | 0   | 0   | 0   | 0   | 0   | 0   |

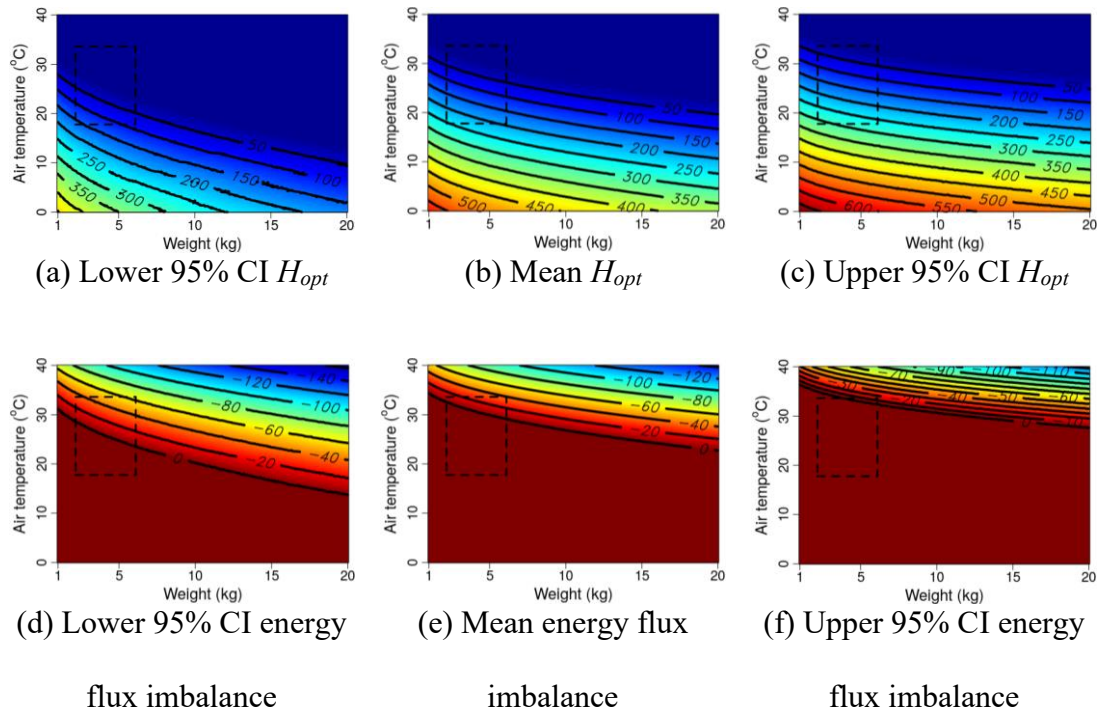


Figure 32. Surface plots for the relationship between animal weight ( $x$ -axis) and air temperature ( $y$ -axis) with optimum supplemental heat ( $H_{opt}$ , W) and energy flux imbalance ( $W m^{-2}$ ). Plots show (a) lower 95% confidence interval (CI), (b) mean, and (c) upper 95% CI for  $H_{opt}$ , and (d) lower 95% CI, (e) mean, and (f) upper 95% CI for energy flux imbalance.  $H_{opt}$  and energy flux imbalance are shown using color gradients and contours. Color gradients are the same for each set of plots (a-c and d-f). Numbers and lines in the surface plots indicate contour plots. Negative values in energy flux imbalance plots (d-f) represent piglets gaining energy flux. Dashed rectangles represent range of measured data.

In this study, unlike previous studies, the zone of least thermoregulation was determined mechanistically by minimizing the energy imbalance between total heat

149

production and latent and sensible heat losses (Eq. (155)). Figure 33 shows a comparison of the zone of least thermoregulation obtained in this study (when supplemental heat was not provided,  $H = 0$  W) with the recommendations by Harmon and Xin (1995) and Brown-Brandl et al. (2004). The zone of least thermoregulation described by Harmon and Xin (1995) is within the mean and upper 95% confidence interval of the zone calculated from the mathematical framework formulated in this article. The zone of least thermoregulation reported by Brown-Brandl et al. (2004) was calculated from an equation developed based on recommendations from the Midwest Plan Service (MWPS, 1983). The zone of least thermoregulation reported by Brown-Brandl et al. (2004) does not agree with our results for newborn piglets (~1 kg) but agrees well for older piglets. Another study that determined the zone of least thermoregulation for piglets was Mount (1960). Mount's study was based on calorimetric measurements and behavioral observations of piglets and reported 34°C to 35°C, 30°C to 35°C, and 25°C to 30°C for piglets weighing 1 to 2 kg, 2 to 4 kg, and 4 to 8 kg, respectively. The zone of least thermoregulation determined by Mount (1960) is within the confidence interval of the results obtained in our study. The curve in Figure 33 shifts downward with increasing  $H$ , which implies that piglets remain in their zone of least thermoregulation even when the temperature is cooler.

Despite uncertainties in predicting the zone of least thermoregulation using our mathematical model, our data agree well with data obtained from the literature. Uncertainties in our predictions include (1) uncertainties in input temperatures

predicted by the machine learning algorithms, (2) uncertainties in the optimization of system parameters from the Monte Carlo optimization method, (3) uncertainties in bootstrapping predictions for the zone of least thermoregulation, (4) experimental condition variabilities, and (5) animal variability. Furthermore, predicted confidence intervals are not symmetrical around the mean because the joint probability distribution of the predicted zone of least thermoregulation was estimated using parametric bootstrap, which estimates a non-parametric joint probability distribution function that does not need to be symmetrical. As expected, uncertainties increase as predictions are made farther away from the range of measured data.

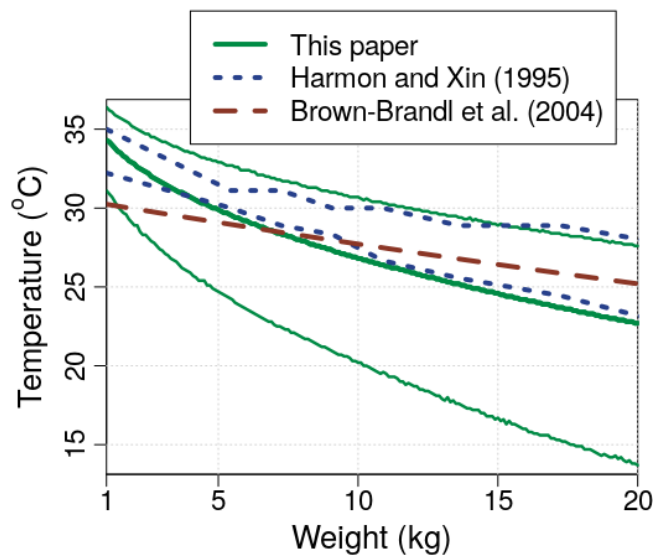


Figure 33. Zone of least thermoregulation of piglets when supplemental heat is not provided. Thinner solid lines represent lower and upper 95% confidence interval for our result. Plots from Harmon and Xin (1995) represent their suggested optimum temperature ranges. Range of measured data is 2.2-6.1 kg and 17.8-33.6 °C.

### 3.5. Limitations of the model

Optimization of our mathematical framework relied on data collected from one farrowing cycle, from one sow, at one farm, during one period of the year (August, the last winter month), and in one country (Brazil). If our mathematical framework was trained using data from diverse sources, its predictive power would increase. This emphasizes the need for large and diverse public datasets, which could be used to develop sophisticated models. However, no such public dataset, besides the dataset from this research (Milan et al., 2018a), exists.

The mechanistic model used in this study assumed that heat flow is 1-D and steady-state. In addition, the hair-coat layer was assumed as a pure absorbing-emitting fibrous layer without providing full thermo-isolation for convection heat transfer. Animals are complex 3-D geometries with surfaces that might be exposed to different thermal conditions. For example, a piglet lying down and in contact with littermates could have four distinct heat transferring regions: (1) conduction heat transfer with the floor, (2) conduction heat transfer with littermates, (3) convection and radiation heat transfer with the environment, and (4) convection and radiation heat transfer with the environment and incident radiation from the supplemental heat source. A hair-coat layer is a scattering-absorbing-emitting fibrous layer (Tong and Teng, 1980; Modest, 2013), and the effects of neglecting radiation scattering are unknown. Because the density of the hair-coat of piglets is small, we assumed that the hair-coat layer does not provide full isolation for convection heat transfer. An alternative approach would

be to treat the hair-coat as a porous medium (Khaled and Vafai, 2003; Datta 2007, 2016). This approach would, however, increase the computation time and memory use (see Appendix E for computation times).

Because of a lack of distribution data, the distributions of system parameters (Table 9) and energy component terms (Table 10) were assumed to be independent. The independence assumption is known to not hold in all cases. For example, piglets with a thicker fat layer are more likely to have a thicker muscle layer, which violates the independence assumption. Another example is that, on hot days, which would decrease  $E_S$ , pigs might increase  $E_L$  and decrease THP to maintain thermal equilibrium, which again violates the independence assumption. Such correlation between energy terms was partially considered through  $T_{a,eq}$  (instead of  $T_{a,in}$  or  $T_a$ ; see the Energy Balance section) used to calculate THP. Despite these limitations, our mathematical formulation provided reasonable predictions.

Machine learning or statistical models can provide more accurate predictions than fundamentally based models (Gorczyca et al., 2018). However, predictions from machine learning or statistical models are not guaranteed to generalize to ranges outside the dataset nor to comply with first principles (e.g., Figure 37 to Figure 39). Fundamentally based models, however, provide insights into bioenergetics and can be generalized to ranges outside the dataset. To the best of our knowledge, this is the first study that combines machine learning and fundamentally based models. All predictions from the combined model, different from predictions solely from machine

learning models, comply with first principles built into the fundamentally based model. Will predictions from the combined model extrapolate to ranges outside the dataset? Evidence suggesting that predictions from the integrated model should not be extrapolated was not observed. In addition, extrapolated predictions from the combined model comply with first principles. However, further investigation of the extrapolation capabilities of integrated models is required.

#### ***4. CONCLUSION***

The following conclusions can be drawn from this study:

- A bioenergetic model that incorporates machine learning, Monte Carlo optimization, a mechanistic bio-heat transfer model, and ensemble learning was developed. The bioenergetic model was used to predict optimum supplemental heat, hair-coat temperature, and skin temperature for piglets.
- Ordinary linear regression with backward selection resulted in predictions of air, black-globe, and rectal temperatures with errors equal to 1.38%, 0.96%, and 0.78%, respectively, in the mean dataset.
- Monte Carlo optimization of system parameters reduced the mean squared error of predicted skin and hair-coat temperatures by 3.2 times.
- Ensemble learning improved the prediction accuracy of skin and hair-coat temperatures by 5% and added confidence intervals to the predictions. The errors were 3.04% for skin temperature and 2.09% for hair-coat temperature in

the mean dataset.

- Optimum supplemental heat for piglets as a function of air temperature and body weight, together with its 95% confidence interval, was calculated based on energy balance (Figure 33 and Table 11). Optimum supplemental heat decreased in an exponential decay fashion with increasing air temperature and/or body weight. Predictions from this model would allow development of efficient supplemental heat as a function of air temperature and body weight.
- For air temperature between 15°C to 19°C, the optimum supplemental heat was 266 to 344 W and 44 to 128 W for piglets at birth (assuming 1 kg) and at the end of the farrowing cycle (assuming 20 kg), respectively. This means that ~200 W could be saved by providing the optimum supplemental heat for animals at the end of the farrowing cycle versus for newborn piglets.
- The zone of least thermoregulation (when supplemental heat is not provided), along with its 95% confidence interval, was calculated for piglets of specified body weight, and the results agreed well with published data (Figure 33).

### ***Acknowledgment***

Funding was provided by the Brazilian National Council of Technological and Scientific Development (CNPq, Proc. 203312/2014-7), the São Paulo Research Foundation (FAPESP, Proc. 17.519/14), and USDA Hatch funds as part of the W-3173 Regional Project through Cornell University. We thank Michael T. Gorczyca for help with machine learning and ensemble techniques and Leandro Zuccherato

Camerro, Dr. Cintia Carol de Melo Costa, and Dr. Carolina Cardoso Nagib Nascimento for help with data collection. Dr. Luciano Hauschild of the Swine Research Center of São Paulo State University provided the animals and allowed us to use his facility, and Alicia Zem Fraga of the Swine Research Center of São Paulo State University helped with ultrasound measurements.

## ***APPENDIX A: SOLUTION PROCEDURE FOR THE MECHANISTIC MODEL***

### **A1. Solution procedure for mechanistic model**

Figure 34 shows the control volume and the conditions imposed between sublayers (Eqs. (130) and (131)). The bio-heat equation (Pennes, 1948) can be analytically solved independently from the solution of the other sublayers. Similarly, the radiation absorbing-emitting fibrous layer approximation for the hair-coat layer (Kowalski and Mitchell, 1979) can be numerically solved independently from the solution of the other sublayers.

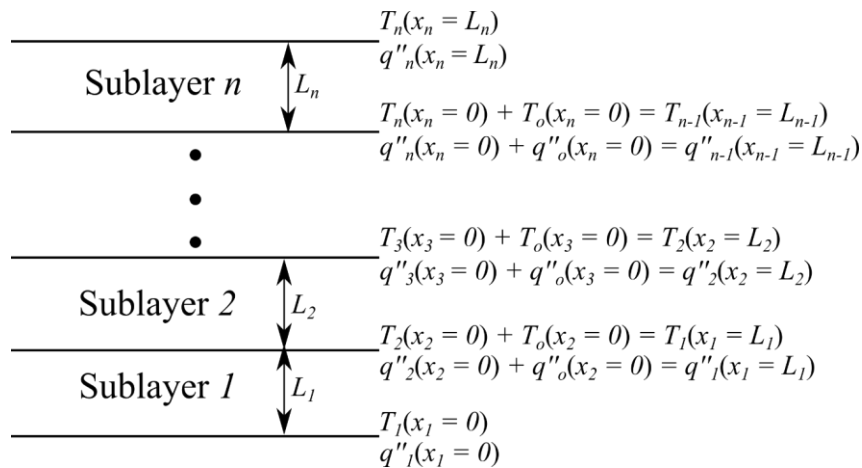


Figure 34. Control volume and conditions imposed between sublayers.

## A2. Analytical solution of the bio-heat equation

The solution to Eqs. (128) and (129), for  $\omega_{b,i} \neq 0$ , is

$$T_i(x_i) = T_{b,i} + \frac{q'''_{met,i} + q'''_{ext,i}}{\omega_{b,i}\rho_{b,i}c_{b,i}} + \beta_{1,i} \sinh\left(x_i \sqrt{\frac{\omega_{b,i}\rho_{b,i}c_{b,i}}{k_i}}\right) + \beta_{2,i} \cosh\left(x_i \sqrt{\frac{\omega_{b,i}\rho_{b,i}c_{b,i}}{k_i}}\right) \quad (157)$$

$$q''_i(x_i) = -\beta_{1,i}\sqrt{k_i\omega_{b,i}\rho_{b,i}c_{b,i}} \cosh\left(x_i \sqrt{\frac{\omega_{b,i}\rho_{b,i}c_{b,i}}{k_i}}\right) - \beta_{2,i}\sqrt{k_i\omega_{b,i}\rho_{b,i}c_{b,i}} \sinh\left(x_i \sqrt{\frac{\omega_{b,i}\rho_{b,i}c_{b,i}}{k_i}}\right) \quad (158)$$

and, for  $\omega_{b,i} = 0$ ,

$$T_i(x_i) = \frac{-q'''_{met,i} + q'''_{ext,i}}{2k_i} x_i^2 + \beta_{1,i} x_i + \beta_{2,i} \quad (159)$$

$$q''_i(x_i) = (q'''_{met,i} + q'''_{ext,i})x_i - k_i\beta_{1,i} \quad (160)$$

## A3. Numerical solution of the absorbing-emitting radiation fibrous layer equation

The absorbing-emitting radiation fibrous layer equation (Kowalski and Mitchell, 1979) is given below. Temperatures in this equation are in Kelvin. This model assumes that hairs are purely absorptive (radiation is not reflected nor scattered) and

emit as black-bodies.

$$\begin{aligned}
& k_{eff}(x) \frac{d^2 T(x)}{dx^2} + 2\alpha\sigma T_s^4 E_2[\alpha x] + 2\alpha\sigma T_{MR}^4 E_2[\alpha(L_h - x)] \\
& + 2\sigma \int_0^x \alpha^2 T^4(x) E_1[\alpha(x - x')] dx' \\
& + 2\sigma \int_x^{L_h} \alpha^2 T^4(x) E_1[\alpha(x' - x)] dx' - 4\alpha\sigma T^4(x) = 0
\end{aligned} \tag{161}$$

$$k_{x'}(x) = \frac{A_F}{A_T} (k_h(x) - k_a) + k_a \tag{162}$$

$$k_{y'}(x) = \frac{k_a(\tau - D)}{\tau} + \frac{Dk_a k_h(x)}{Dk_a + (\tau - D)k_h(x)} \tag{163}$$

$$k_{eff}(x) = \frac{k_{x'}(x) + k_{y'}(x)}{2} \tag{164}$$

$$\frac{A_F}{A_T} = \min\left(1, \frac{NH_L \pi D^2}{L_h 4}\right) \tag{165}$$

$$\tau = \max\left(D, \sqrt{\frac{L_h}{N_h H_L}}\right) \tag{166}$$

$$\alpha = \frac{2}{3\pi} ND \tag{167}$$

$$E_n(\gamma) = \int_1^{\infty} \frac{e^{-\gamma t}}{t^n} dt \quad (168)$$

$$E_{n+1}(\gamma) = \frac{1}{n} [e^{-\gamma} - \gamma E_n(\gamma)] \quad (169)$$

where  $k_{eff}$  (W/(m-K)) is effective thermal conductivity of the hair-coat layer,  $k_x$  (W/(m-K)) is thermal conductivity in the direction perpendicular to the skin,  $k_y$  (W/(m-K)) is thermal conductivity in the direction parallel to the skin,  $k_a$  (W/(m-K)) is air thermal conductivity,  $\alpha$  is absorption coefficient,  $\sigma = 5.670373 \times 10^{-8}$  kg/(s<sup>3</sup>-K<sup>4</sup>) is Stefan-Boltzmann constant,  $E_n$  is exponential integral of order  $n$ ,  $T_{MR}$  (K) is mean radiant temperature,  $A_F/A_T$  is cross-sectional area of hairs per unit area,  $\tau$  (m) is average hairs spacing. Eq. (161) is subject to the boundary condition of  $T(x = 0) = T_s$  and convection heat transfer at  $x = L_h$ . The heat flux at the surface of the skin can be calculated as

$$q_s'' = -k_{eff}(x) \frac{dT(x)}{dx} + \sigma T_s^4 - 2\sigma T_{MR}^4 E_3[\alpha L_h] - 2\sigma \int_0^{L_h} \alpha T^4(x) E_2[\alpha x'] dx' \quad (170)$$

$$+ q_o''(x_s = L_s)$$

where  $q_o''$  (W/m<sup>2</sup>) is heat flux offset (Eqs. (130) and (131)). Eqs. (161) and (170) were solved using finite differences (see Figure 35 for the discretization space) using the following equations:

$$\begin{aligned}
& \frac{k_{eff,i}}{\Delta x^2} (T_{i-1} - 2T_i + T_{i+1}) + 2\sigma T_s^4 \alpha E_2 \left[ \frac{2i-3}{2} \Delta x \alpha \right] \\
& + 2\sigma \sum_{\substack{j=2 \\ j \neq i}}^N \alpha T_j^4 \left\{ E_2 \left[ \left( |i-j| - \frac{1}{2} \right) \Delta x \alpha \right] \right. \\
& \left. - E_2 \left[ \left( |i-j| + \frac{1}{2} \right) \Delta x \alpha \right] \right\} \\
& + 2\sigma \alpha T_h^4 \left\{ E_2 \left[ \left( N-i + \frac{1}{2} \right) \Delta x \alpha \right] - E_2[(N-i+1)\Delta x \alpha] \right\} \\
& + 2\sigma \alpha T_{MR}^4 E_2[(N-i+1)\Delta x \alpha] - 4\sigma T_i^4 \alpha E_2 \left[ \frac{\Delta x}{2} \alpha \right] = 0
\end{aligned} \tag{171}$$

$$\begin{aligned}
q_s'' &= \frac{k_{eff,1}}{\Delta x} (T_s - T_2) + 2\sigma T_s^4 E_3 \left[ \frac{\Delta x}{2} \alpha \right] - 2\sigma T_{MR}^4 E_3[N\Delta x \alpha] \\
& - 2\sigma \sum_{i=2}^N T_i^4 \left\{ E_3 \left[ \frac{2i-1}{2} \Delta x \alpha \right] - E_3 \left[ \frac{2i+1}{2} \Delta x \alpha \right] \right\} \\
& - 2\sigma T_h^4 \left\{ E_3 \left[ \frac{2N-1}{2} \Delta x \alpha \right] - E_3[N\Delta x \alpha] \right\} + q_o''(x_s = L_s)
\end{aligned} \tag{172}$$

$$q_h'' = q_{conv,h}'' = \frac{k_{eff,N-1}}{\Delta x} (T_{N-1} - T_h) = h(T_h - T_a) \tag{173}$$

$$\Delta x = \frac{L_h}{N} \tag{174}$$

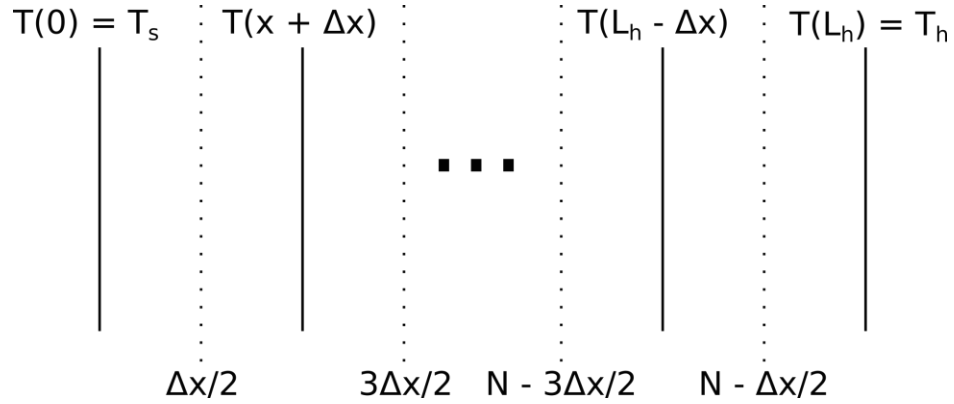


Figure 35. Finite difference discretization space used to solve Eqs. (161) and (170).

Temperature at  $0 \leq x < \Delta x/2$  is assumed equal to the skin-surface temperature ( $T_s$ ). Temperatures at  $(2i - 1)\Delta x/2 \leq x < (2i + 1)\Delta x/2$  is assumed equal to  $T(x + i\Delta x)$ . Temperature at  $(L_h - \Delta x/2) \leq x \leq L_h$  is assumed equal to the hair-coat surface temperature ( $T_h$ ).

Eqs. (161) and (170), together with the boundary condition  $T(x = 0) = T_s$ , form a system of  $N + 1$  non-linear equations ( $N$  forms of Eq. (172) and one Eq. (173)) with  $N + 1$  unknowns. This system of non-linear equations was solved using sequential quadratic programming in Octave with the following equations

$$e = (AT + ET^4 + b)^t(AT + ET^4 + b) \quad (175)$$

$$J = \frac{\partial e}{\partial T} = 2[(AT + ET^4 + b)^t(A + 4E * T^3)]^t \quad (176)$$

$$H = \frac{\partial^2 e}{\partial T^2} = 2(A + 4E * T^3)(A + 4E * T^3)^t + \text{diag}[(12E * T^2)^t(AT + ET^4 + b)] \quad (177)$$

$$(AT + ET^4 + b) = 0 \quad (178)$$

$$J_{cc} = (A + 4E * T^3) \quad (179)$$

where  $T$  is an  $(N + 1) \times 1$  vector of the temperatures,  $T^n$  is an  $(N + 1) \times 1$  vector of the  $n$ th power of the temperatures,  $A$  and  $E$  are  $(N + 1) \times (N + 1)$  matrices,  $b$  is a  $(N + 1) \times 1$  vector,  $e$  is the objective function (for minimization),  $J$  is the  $(N + 1) \times 1$  Jacobian matrix of the objective function,  $H$  is the  $(N + 1) \times (N + 1)$  Hessian matrix of the objective function, Eq. (178) is the equality constraint condition, and  $J_{cc}$  is the  $(N + 1) \times (N + 1)$  Jacobian matrix of the equality constraint condition.

The tolerance for solving the sequential quadratic programming was set to  $\sqrt{\text{eps}} = 1.4901 \times 10^{-8}$ , where  $\text{eps}$  is the machine precision of the computer used. If the sequential quadratic programming algorithm did not converge, and if the objective function value and the maximum absolute value of the equality constraint (Eq. (179)) were either greater than 10, the set of system parameters was discarded.

#### **A4. Coupled solution of bio-heat equation and absorbing-emitting radiation fibrous layer equation**

The solution procedure for combining the bio-heat equation and the absorbing-emitting radiation fibrous layer equation is as follows:

1. Start with initial values for  $T$  in all points.
2. Solve absorbing-emitting radiation fibrous layer equations.

3. Update predicted skin-surface heat flux (Eq. (172)).
4. Recalculate analytical solutions with updated predicted skin-surface heat flux.
5. Recalculate  $T_s$ .
6. If the change between  $T_s$  in previous and the current iteration is lower than a tolerance (a tolerance of  $\sqrt{\epsilon ps}$  was used), the calculation is ended, otherwise return to 2.

#### **A5. Equations to calculate convection heat transfer and mean radiant temperature**

Convection heat transfer was calculated as (da Silva and Maia, 2013)

$$q''_{conv} = h(T - T_a) \quad (180)$$

$$h = \frac{k_a N_u}{D} \quad (181)$$

where,  $k_a$  (W/(m-°C)) is air thermal conductivity,  $D$  (m) is diameter of the animal, and  $N_u$  is Nusselt Number.  $k_a$  was calculated as

$$k_a = \rho_a c_a D_a \quad (182)$$

$$D_a = 1.888 \times 10^{-5} + 1.324 \times 10^{-7} T_a \quad (183)$$

$$c_a = 1005.2 + 0.4577 \exp\left(\frac{T_a}{32.07733}\right) \quad (184)$$

$$\rho_a = \frac{3.481965P_a}{T_a + 273.15} \quad (185)$$

$$P_a = 101.325 \exp \left[ \frac{-zg}{287.04(T_a + 273.15)} \right] \quad (186)$$

$$g = 9.78013 + 8.18 \times 10^{-5}L_t + 1.168 \times 10^{-5}L_t^2 - 3.1 \times 10^{-6}z \quad (187)$$

where,  $g$  (m/s<sup>2</sup>) is gravity,  $P_a$  (kPa) is air pressure,  $\rho_a$  (kg/m<sup>3</sup>) is air density,  $c_a$  (J/(kg<sup>1</sup>-°C)) is air specific heat,  $D_a$  (m<sup>2</sup>/s) is air thermal diffusivity,  $z$  (m) is elevation, and  $L_t$  (decimal degrees) latitude.  $L_t = 21.2583^\circ$  and  $z = 595$  m for the experimental facility (Jaboticabal, Brazil).

Nusselt number was obtained by approximate the piglet to a cylinder with airflow perpendicular to it.

$$N_u = \begin{cases} N_u^F & 0.08 \geq \xi \\ [(N_u^N)^{3.5} + (N_u^F)^{3.5}]^{1/3.5} & 0.08 < \xi < 3 \\ N_u^N & 3 \leq \xi \end{cases} \quad (188)$$

$$N_u^F = 0.3 + \frac{0.62R_e^{1/2}P_r^{1/3}}{[1 + (0.4/P_r)^{2/3}]^{1/4}} \left[ 1 + \left( \frac{R_e}{282,000} \right)^{5/8} \right]^{4/5} \quad (189)$$

$$N_u^N = \left\{ 0.6 + \frac{0.387(G_r P_r)^{1/6}}{[1 + (0.559/P_r)^{9/16}]^{8/27}} \right\}^2 \quad (190)$$

$$\xi = \frac{G_r}{R_e^2} \quad (191)$$

$$Re = \frac{u_a d}{\nu_a} \quad (192)$$

$$Gr = \frac{g d^3 |T_i - T_a|}{\nu_a^2 (T_a + 273.15)} \quad (193)$$

$$Pr = \frac{\rho_a c_a \nu_a}{k_a} \quad (194)$$

$$\nu_a = 1.32743 \times 10^{-5} + 9.22286 \times 10^{-8} T_a \quad (195)$$

where,  $Nu^F$  is Nusselt number for forced convection,  $Nu^N$  is Nusselt number for natural convection,  $Re$  is Reynolds number,  $Gr$  is Grashof number,  $Pr$  is Prandtl number,  $u_a$  (m/s) is air velocity inside the brooder,  $\nu_a$  (m<sup>2</sup>/s) is air kinematic viscosity, and  $T_i$  (°C) is the temperature of the surface temperature being used to calculate convection heat transfer (h = hair-coat, s = skin).

The mean radiant temperature ( $T_{MR}$ , °C) was calculated based on an energy balance of the black-globe (da Silva and Maia, 2013):

$$T_{MR} = \left[ \frac{h_g}{\sigma \varepsilon} (T_g - T_a) + (T_g + 273.15)^4 \right]^{1/4} - 273.15 \quad (196)$$

$$h_g = \frac{k_a Nu_{u,g}}{d_g} \quad (197)$$

$$N_{u,g} = \begin{cases} N_{u,g}^F & 0.08 \geq \xi_g \\ [(N_{u,g}^N)^4 + (N_{u,g}^F)^4]^{1/4} & 0.08 < \xi_g < 3 \\ N_{u,g}^N & 3 \leq \xi_g \end{cases} \quad (198)$$

$$\xi_g = \frac{G_{r,g}}{R_{e,g}^2} \quad (199)$$

$$N_{u,g}^F = 2 + (0.4R_{e,g}^{1/2} + 0.06R_{e,g}^{2/3})P_r^{0.4} \left( \frac{\nu_a \rho_a}{\nu_{a,g} \rho_{a,g}} \right)^{1/4} \quad (200)$$

$$N_{u,g}^N = 2 + \frac{0.589(G_{r,g}P_r)^{1/4}}{[1 + (0.469/P_r)^{9/16}]^{4/9}} \quad (201)$$

$$G_{r,g} = \frac{gd_g^3|T_g - T_a|}{\nu_a^2(T_a + 273.15)} \quad (202)$$

$$R_{e,g} = \frac{u_a d_g}{\nu_a} \quad (203)$$

where  $T_g$  (°C) is black-globe temperature,  $d_g$  (0.15 m) is black-globe diameter,  $\nu_{a,g}$  and  $\rho_{a,g}$  are, respectively,  $\nu_a$  and  $\rho_a$  calculated using  $T_g$ .

## A6. Mesh-size independent study

The solution of absorbing-emitting radiation fibrous layer equations depends on  $N$  (number of sublayers of the hair-coat layer). A low number for  $N$  results in a poor finite-difference approximation of the derivatives and integrals of Eqs. (161) and (170). A high number for  $N$  results in high computational time and memory use. To

166

find the number  $N$  that would give a balance between accuracy and computational resources use, a mesh-size independent study was performed using the traditional values of Table 9 with increasing values of  $N$  and measured  $T_a$ ,  $T_g$ , and  $T_r$ . The study consisted in calculating minimum, mean, and maximum values of  $T_s$  and  $T_h$  by solving the mechanistic model for the training dataset. Figure 36 shows the result of the mesh-size independent test.  $N = 20$  was chosen because the minimum, mean, and maximum values of  $T_s$  and  $T_h$  changed by  $\leq 0.31\%$  compared to  $N = 100$  at a fraction of 4.78% of the computational time.

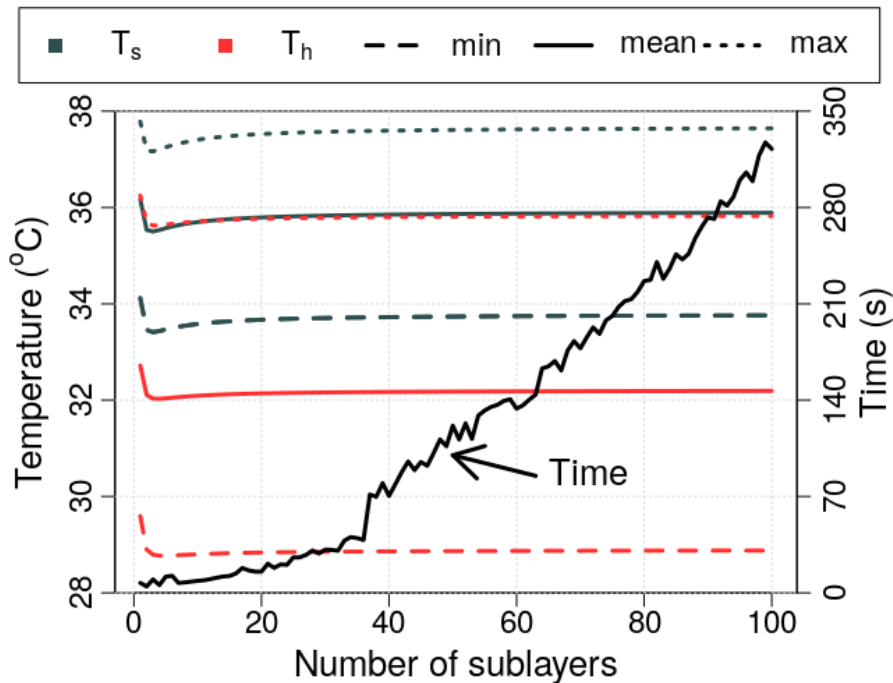


Figure 36. Mesh-size independent study.  $T_s$ : skin surface temperature;  $T_h$ : hair-coat surface temperature; min: minimum value for the training dataset; mean: mean value for the training dataset; max: maximum value for the training dataset.

## ***APPENDIX B: PHYSICAL VARIABLES AND IRRADIANCE DATA***

Table 12 shows physical variables of piglets and Table 13 shows irradiance of the supplemental heat.

Table 12. Physical measurements of piglets. Values expressed in mean  $\pm$  standard deviation (number of samples).

| Variable                                   | Value <sup>[a]</sup>          | Value <sup>[b]</sup>   |
|--|-------------------------------|------------------------|
| Hair diameter ( $\mu\text{m}$ )            | 97.525 $\pm$ 10.882 (40)      | -                      |
| Density of hairs (#hairs/cm <sup>2</sup> ) | 153.750 $\pm$ 36.257 (40)     | -                      |
| Hair Length (mm)                           | 12.026 $\pm$ 1.171 (40)       | -                      |
| Thickness of hair coat (mm)                | 2 $\pm$ 0 (40) <sup>[c]</sup> | 2.385 $\pm$ 0.794 (20) |
| Thickness of fat (mm)                      | -                             | 5.214 $\pm$ 1.351 (20) |
| Thickness of skin (mm)                     | -                             | 1.037 $\pm$ 0.342 (20) |
| Piglets weight (kg)                        | 3.767 $\pm$ 1.288 (40)        | 1.630 $\pm$ 0.295 (20) |
| Piglets diameter (cm)                      | 10.126 $\pm$ 1.283 (30)       | 8.284 $\pm$ 0.532 (20) |

<sup>[a]</sup> Population of piglets used to measure thermo-variables. <sup>[b]</sup> Population of piglets used to measure thickness of internal tissues. <sup>[c]</sup> Resolution was 1 mm.

Table 13. Irradiance of the supplemental heat.

| Supplemental heat | Irradiance             |
|-------------------|------------------------|
| 0 W               | 0.00 W/m <sup>2</sup>  |
| 60 W              | 31.25 W/m <sup>2</sup> |
| 100 W             | 44.00 W/m <sup>2</sup> |
| 160 W             | 71.75 W/m <sup>2</sup> |
| 200 W             | 94.75 W/m <sup>2</sup> |

## ***APPENDIX C: MACHINE LEARNING ALGORITHMS***

### **C1. Ordinary linear regression with backwards selection**

Eqs. (204)-(207) show the fitting from the ordinary linear regression with backwards selection, where  $R^2_{adj}$  is adjusted coefficient of determination,  $N_i(0, \sigma)$  represents normal distribution with standard error  $\sigma$  and the subscripts represent  $e$  = residual errors,  $p$  = piglet random variable,  $h$  = hour random variable (4am, 5am, 6am, or 7am). Note that  $R^2_{adj}$  is not defined for linear mixed-effect models (Eq. (206)). All terms in the equations are statistically significant.

$$T_a = 6.0967 + 0.882T_{a,pen} + 41.872 \times 10^{-3}H + N_e(0,1.342); R_{adj}^2 = 0.8465 \quad (204)$$

$$T_g = 7.2529 + 0.8388T_{a,pen} + 43.384 \times 10^{-3}H + N_e(0,1.207); R_{adj}^2 = 0.8785 \quad (205)$$

$$T_r = 37.9115 + N_p(0,0.2697) + N_h(0,0.3521) + N_e(0,0.4850) \quad (206)$$

$$T_{a,in} = T_a + 41.9683 \times 10^{-3}H + N_e(0,1.233); R_{adj}^2 = 0.9475 \quad (207)$$

## C2. Generalization study

Dependence plots (Friedman, 2001) for predicting  $T_a$  (Figure 37),  $T_g$  (Figure 38), and  $T_r$  (Figure 39) given  $T_{a,pen}$  and  $H$  are shown below. Deep learning resulted in curved non-linear functions with predictions that did not change considerable outside the range of the experimental data. Gradient boosted machines and random forests partitioned the experimental data region into several decision spaces, which were extended with constant values outside the range of the experimental data. Generalized linear regression resulted in predictions similar to predictions from ordinary linear regression with backwards selection. This is expected given their similar formulation, differing that coefficients not supported by the data were removed for ordinary linear regression with backwards selection.

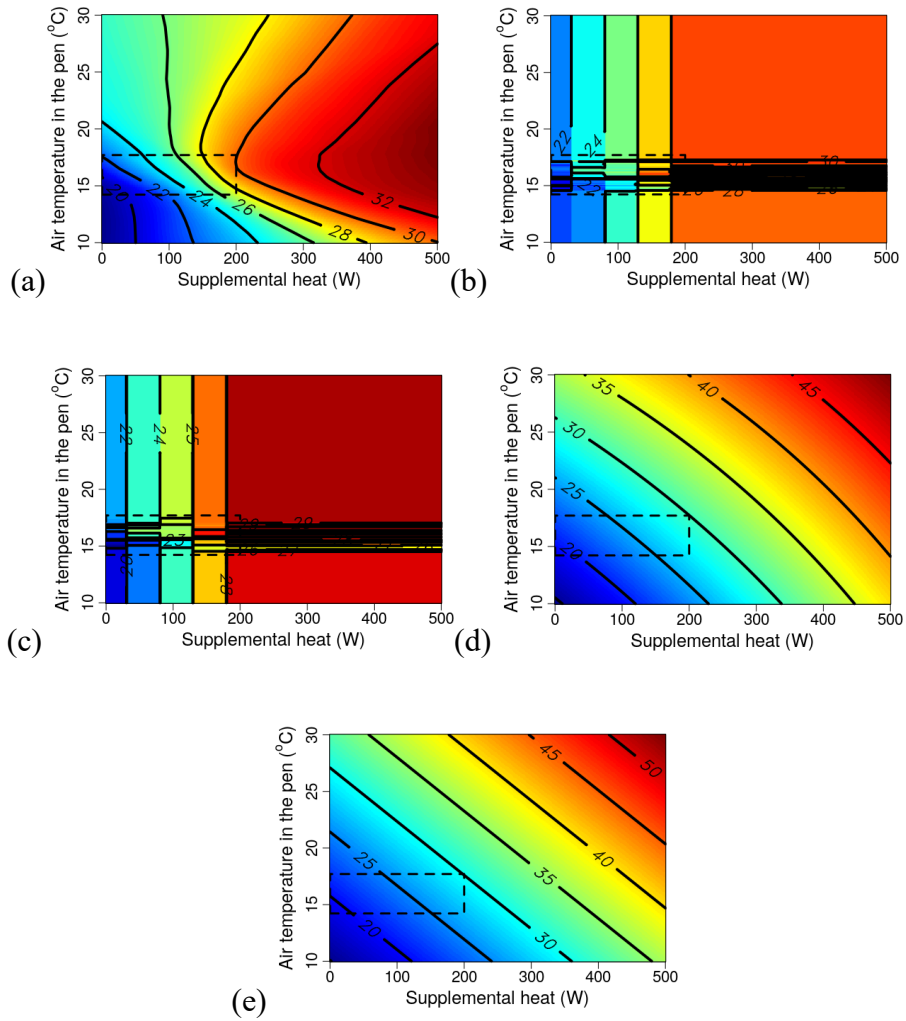


Figure 37. Dependence plot for predicting air temperature inside the brooder ( $T_a$ ) using (a) deep learning with ReLU activation function, (b) gradient boosted machines, (c) random forests, (d) generalized linear regression with elastic net regularization, and (e) ordinary linear regression with backwards selection. Dashed rectangle represents range of measured experimental data.

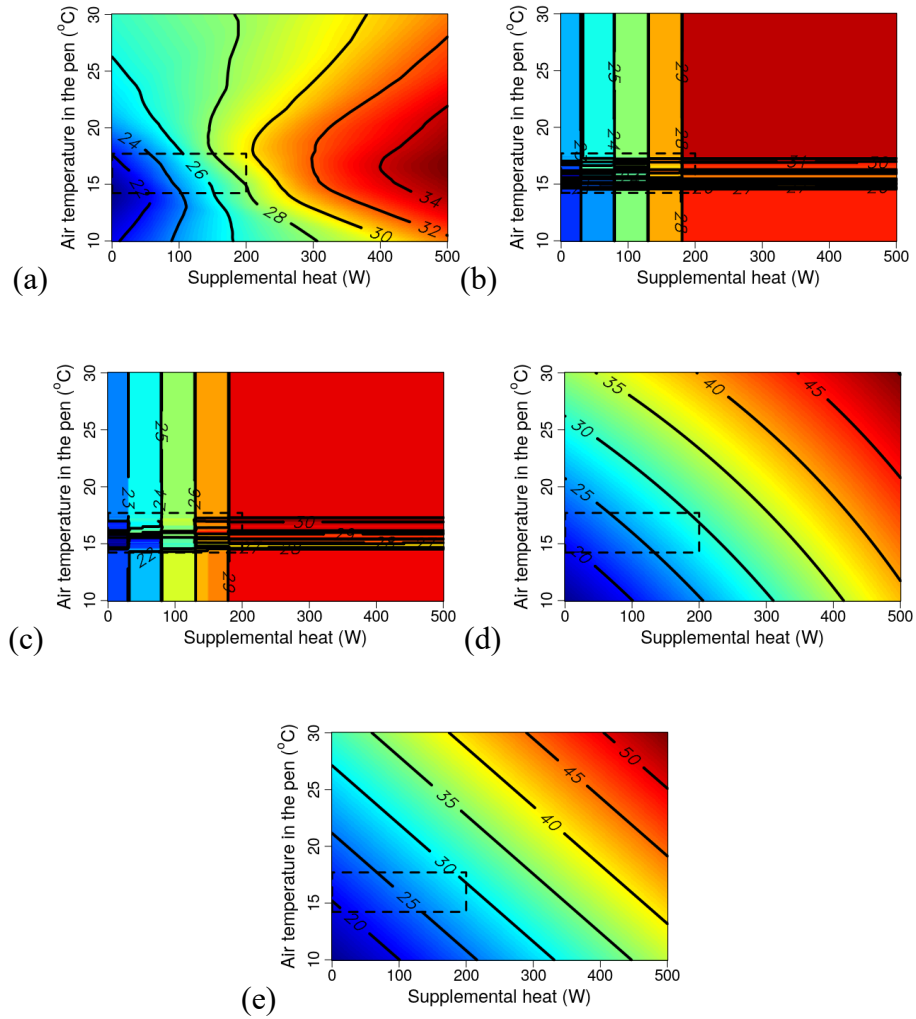


Figure 38. Dependence plot for predicting black-globe temperature inside the brooder ( $T_g$ ) using (a) deep learning with ReLU activation function, (b) gradient boosted machines, (c) random forests, (d) generalized linear regression with elastic net regularization, and (e) ordinary linear regression with backwards selection. Dashed rectangle represents range of measured experimental data.

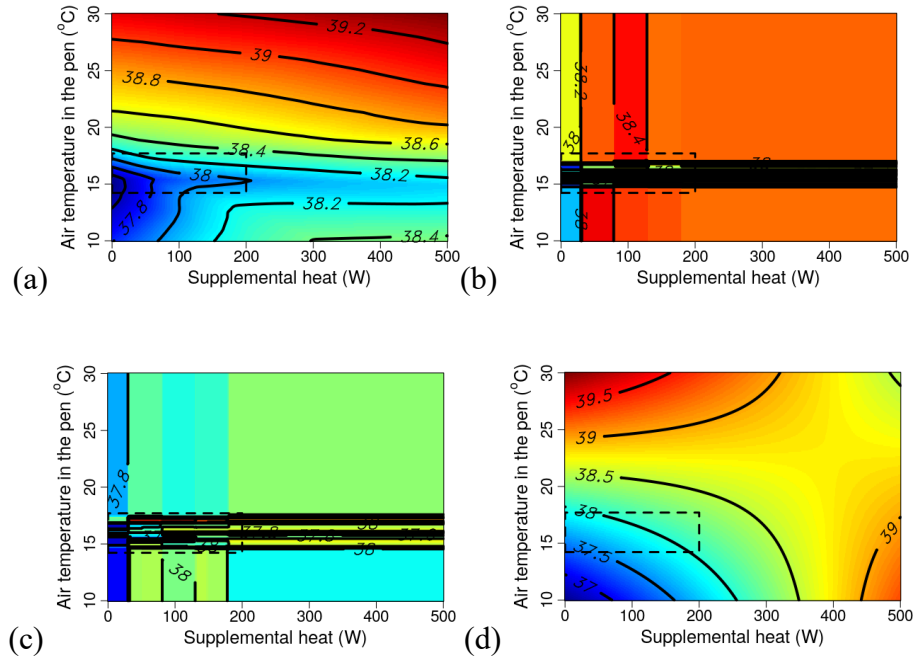


Figure 39. Dependence plot for predicting rectal temperature ( $T_r$ ) using (a) deep learning with ReLU activation function, (b) gradient boosted machines, (c) random forests, and (d) generalized linear regression with elastic net regularization. Predictions using ordinary linear regression with backwards selection were independent of input data:  $T_r = 37.91$  °C. Dashed rectangle represents range of measured experimental data.

#### ***APPENDIX D: LINEAR REGRESSION APPROXIMATIONS***

Linear regression approximations for mean values of  $T_h$ ,  $T_s$ ,  $q''_s$ , and  $H_{opt}$  are shown in Eqs. (211)-(208), where  $R^2_{adj}$  is adjusted coefficient of determination,  $N_e(0, \sigma)$  represents normal distribution of the residual errors with standard error  $\sigma$ .

Table 14 shows quantiles of the residues obtained using these equations.

$$\begin{aligned}
T_h = & 27.03 + 180.4 \times 10^{-3}T_a + 874.2 \times 10^{-6}T_a^2 + 6.538 \times 10^{-3}H \\
& + 403.3 \times 10^{-9}H^2 + 6.285 \times 10^{-6}T_aH - 773.8 \times 10^{-9}T_a^2H \\
& + 5.17 \times 10^{-9}T_aH^2 + 380.6 \times 10^{-12}T_a^2H^2 \\
& + N_e(0,0.0109); R_{adj}^2 = 1
\end{aligned} \tag{208}$$

$$\begin{aligned}
T_s = & 28.25 + 169 \times 10^{-3}T_a + 325 \times 10^{-6}T_a^2 + 2.857H + 190.5 \times 10^{-9}H \\
& + 7.549 \times 10^{-6}T_aH - 374.5 \times 10^{-9}T_a^2H \\
& + 2.496 \times 10^{-9}T_aH^2 + 182 \times 10^{-12}T_a^2H^2 \\
& + N_e(0,0.007); R_{adj}^2 = 1
\end{aligned} \tag{209}$$

$$\begin{aligned}
q_s'' = & 323.4 - 8.096T_a - 158 \times 10^{-3}T_a^2 - 138.1 \times 10^{-3}H \\
& - 9.259 \times 10^{-6}H - 365.7 \times 10^{-6}T_aH + 18.33 \times 10^{-6}T_a^2H \\
& - 117.3 \times 10^{-9}T_aH^2 - 8.958 \times 10^{-9}T_a^2H^2 \\
& + N_e(0,0.3359); R_{adj}^2 = 1
\end{aligned} \tag{210}$$

$$\begin{aligned}
H_{opt} = \max & (0,5986 - 16.24T_a - 43.12 \times 10^{-3}T_a^2 + 966.3 \times 10^{-6}T_a^3 \\
& - 23.83w + 1.056w^2 - 21.32 \times 10^{-3}w^3 - 0.2105T_a w \\
& + 28.19 \times 10^{-3}T_a^2 w - 892.4 \times 10^{-6}T_a^3 w + 39 \times 10^{-3}T_a w^2 \\
& - 4.52 \times 10^{-3}T_a^2 w^2 + 138.1 \times 10^{-6}T_a^3 w^2 \\
& - 1.608 \times 10^{-3}T_a w^3 + 180.5 \times 10^{-6}T_a^2 w^3 \\
& - 5.442 \times 10^{-6}T_a^3 w^3 + N_e(0,1.528)); R_{adj}^2 = 0.9999
\end{aligned} \tag{211}$$

Table 14. Quantile of the residues obtained using linear regression approximation for Eqs. (211)-(208).

| Var <sup>[a]</sup>                   | Min    | 1Q     | Med    | 3Q    | Max   |
|--------------------------------------|--------|--------|--------|-------|-------|
| T <sub>h</sub> (°C)                  | -0.029 | -0.007 | 0.000  | 0.008 | 0.034 |
| T <sub>s</sub> (°C)                  | -0.027 | -0.004 | -0.001 | 0.005 | 0.031 |
| q'' <sub>s</sub> (W/m <sup>2</sup> ) | -1.457 | -0.220 | 0.043  | 0.214 | 1.310 |
| H <sub>opt</sub> (W)                 | -3.151 | 1.100  | -0.086 | 0.963 | 8.454 |

<sup>[a]</sup> Var: variable; Min: minimum; 1Q: first quantile; Med: median; 3Q: third quantile; Max: maximum; T<sub>h</sub>: hair-coat temperature; T<sub>s</sub>: skin-surface temperature; q''<sub>s</sub>: skin heat flux; H<sub>opt</sub>: optimum supplemental heat.

### ***APPENDIX E: COMPUTATIONAL TIMES***

Table 15 shows computational times for training, evaluating performance, and obtaining predictions using machine learning algorithms.

It took, on average, 167.79 ms to calculate predictions for a data point using a set of system parameters for the mechanistic model. In total (130 data points × 10,002 sets of parameters = 1.3 million data points), it took 60.60 h to run the Monte Carlo optimization method.

Table 15. Computational times (in seconds) for training, evaluating performance, and obtaining predictions using machine learning algorithms.

| Algorithm <sup>[a]</sup> | Training  | Evaluation | Predictions <sup>[b]</sup> |
|--------------------------|-----------|------------|----------------------------|
| GLM                      | 1,382.61  | 213.14     | 65.64                      |
| RF                       | 1,620.87  | 516.01     | 76.83                      |
| GBM                      | 395.13    | 788.10     | 71.13                      |
| DL                       | 22,758.39 | 2,571.27   | 683.33                     |

<sup>[a]</sup> GLM: generalized linear regression model with elastic net regularization; RF: random forests; GBM: gradient boosted machines; DL: deep learning with ReLU activation function; ordinary linear regression with backwards selection was not included because its computational time was low (~2s). <sup>[b]</sup> Total of 193 prediction points (173 for the dataset + 20 for the mean dataset) for each of the 1,000 tested models for each algorithm (2,000 for DL).

Table 16 shows computational times for ensemble learning algorithms.

To calculate the energy balance, predictions for  $q''_s$  were first obtained for  $T_a = 0:0.1:40^\circ\text{C}$  and  $H = 0:1:1000 \text{ W}$  (total of 401,401 data points) using the best performing ensemble, which took 128.79 h. Then, it took 28.39 h to calculate the energy balance using 10,000 samples parametric bootstrap.

Table 16. Computational times (in seconds) to train and obtain predictions using ensemble learning algorithms.

| Algorithm <sup>[a]</sup> | Training   | Predictions <sup>[b]</sup> |
|--------------------------|------------|----------------------------|
| NB                       | 10.69      | 23.15                      |
| RB                       | 491.67     | 107.07                     |
| GB                       | 39,587.50  | 39.92                      |
| NO                       | 267,931.18 | 30.64                      |
| RO                       | 31,809.92  | 14.01                      |
| GO                       | 4,020.63   | 110.71                     |

[a] NB: naïve search and bagging; RB: random search and bagging; GB: greedy search and bagging; NO: naïve search and optimum weights; RO: random search and optimum weights; GO: greedy search and optimum weights. <sup>[b]</sup> Predictions for the testing dataset (43 data points) using the best ensemble from each algorithm.

## REFERENCES

- ABCS. Brazilian method to classify carcasses [in Portuguese]. Technical Note No. 2. Estrela, Rio Grande do Sul, Brazil: Brazilian Association of Swine Producers, 1973.
- Bates D, Machler M, Bolker B, Walker S. Fitting linear mixed-effects models using lme4. *J Stat Software* 67(1):1-48, 2015.
- Bergstra J, Bengio Y. Random search for hyper-parameter optimization. *Mach Learn Res* 13:281-305, 2012.
- Berman. Extending the potential of evaporative cooling for heat-stress relief. *J Dairy Sci* 89(10):3817-3825, 2006.
- Bonab HR, Can F. A theoretical framework on the ideal number of classifiers for online ensembles in data streams. *Proc 25th ACM Intl Conf on Information and Knowledge Management* (pp. 2053-2056). New York, NY: ACM, 2016.
- Bonab HR, Can F. Less is more: A comprehensive framework for the number of components of ensemble classifiers. *IEEE Trans Neural Network Learn Syst* 14(8):1-7, 2017.
- Brody S. *Bioenergetics and growth with special reference to the efficiency complex in domestic animals*. New York, NY: Reinhold, 1945.
- Brown-Brandl TM, Hayes MD, Xin H, Nienaber, JA, Li H, Eigenberg RA, Stinn JP,

Shepherd T. Heat and moisture production of modern swine. *ASHRAE Trans* 120(1):469-489, 2014.

Brown-Brandl TM, Nienaber JA, Xin H, Gates RS. A literature review of swine heat production. *Trans ASAE* 47(1):259-270, 2004.

Camerro LZ, Maia ASC, Neto MC, Costa CC, Castro PA. Thermal equilibrium responses in Guzerat cattle raised under tropical conditions. *J Therm Biol* 60:213-221, 2016.

Chato JC. A method for the measurement of thermal properties of biological materials. In J. C. Chato (Ed.), *Proc ASME Symp on Thermal Problems in Biotechnology* (pp. 16-25). New York, NY: ASME, 1968.

Cohen ML. Measurement of the thermal properties of human skin: A review. *J Invest Dermatol* 69(3):333-338, 1977.

Collier RJ, Gebremedhin KG. Thermal biology of domestic animals. *Ann Rev Animal Biosci* 3(1):513-532, 2015.

Costa CC, Maia ASC, Brown-Brandl TM, Neto MC, Fonseca VF. Thermal equilibrium of Nellore cattle in tropical conditions: An investigation of circadian pattern. *J Thermal Biol* 74:317-324, 2018b.

Costa CC, Maia ASC, Nascimento ST, Nascimento CC, Neto MC, Fonseca VF. Thermal balance of Nellore cattle. *Intl J Biometeorol* 62(5):723-731, 2018a.

Costa LN, Redaelli V, Magnani D, Cafazzo S, Amadori M, Razzauoli E, Verga M, Luzi F. Preliminary study of the relationship between skin temperature of piglets measured by infrared thermography and environmental temperature in a vehicle in transit. In A. Pugliese, A. Gaiti, & C. Boiti (Eds.), *Veterinary science* (pp. 193-197). Berlin, Germany: Springer, 2010.

da Silva RG, Maia ASC. *Principles of animal biometeorology*. New York, NY: Springer, 2013.

Datta AK. Porous media approaches to studying simultaneous heat and mass transfer in food processes: I. Problem formulations. *J Food Eng* 80(1):80-95, 2007.

Datta AK. Toward computer-aided food engineering: Mechanistic frameworks for evolution of product, quality, and safety during processing. *J Food Eng* 176:9-27, 2016.

Davis Jr LB. Energy transfer in fur. PhD diss. Lexington, KY: University of Kentucky, Department of Mechanical Engineering, 1972.

Davis Jr LB, Birkebak RC. On the transfer of energy in layers of fur. *Biophys J* 14:249-268, 1974.

Duddy J, Hayden TL, Bourne DW, Fiske WD, Benedek IH, Stanley D, Gonzalez A, Heierman W. Physiological model for distribution of sulfathiazole in swine. *J Pharm Sci* 73(11):1525-1528, 1984.

Eaton JW, Bateman D, Hauberg S, Wehbring R. GNU Octave version 4.0.0 manual: A high-level interactive language for numerical computations. Retrieved from <http://www.gnu.org/software/octave/doc/interpreter/>, 2016.

Efron B, Hastie T. *Computer age statistical inference: Algorithms, evidence, and data science*. Cambridge, UK: Cambridge University Press, 2016.

Fachinello MR, Pozza PC, Moreira I, Carvalho PL, Castilha LD, Pasquetti TJ, Esteves LAC, Huepa LM. Effect of passion fruit seed meal on growth performance, carcass, and blood characteristics in starter pigs. *Trop Animal Health Prod* 47(7):1397-1403, 2015.

Fei T, Skidmore AK, Venus V, Wang T, Schlerf M, Toxopeus B, van Overijssel S, Bian M, Liu Y. A body temperature model for lizards as estimated from the thermal environment. *J Therm Biol* 37(1):56-64, 2012.

Ferreira MS, Yanagihara JI. A transient three-dimensional heat transfer model of the human body. *Intl Comm Heat Mass Transfer* 36(7):718-724, 2009.

Friedman JH. Greedy function approximation: A gradient boosting machine. *Ann Stat* 29(5):1189-1232, 2001.

Gebremedhin KG, Cramer CO, Porter WP. Predictions and measurements of heat production and food and water requirements of Holstein calves in different environments. *Trans ASAE* 24(3):715-720, 1981.

Gebremedhin KG, Porter WP, Cramer CO. Quantitative analysis of the heat exchange through the fur layer of Holstein calves. *Trans ASAE* 26(1):188-193, 1983.

Gelman A, Carlin JB, Stern HS, Dunson DB, Vehtari A, Rubin DB. *Bayesian data analysis*. Boca Raton, FL: CRC Press, 2013.

Gorczyca MT, Milan HFM, Maia ASC, Gebremedhin KG. Machine learning algorithms to predict core, skin, and hair-coat temperatures of piglets. *Comput Electron Agric* 151:286-294, 2018.

H2O.ai team. H2O: R interface for H2O: R package ver. 3.16.0.2. Retrieved from <https://CRAN.R-project.org/package=h2o>, 2017.

Harmon JD, Xin H. Environmental guidelines for confinement swine housing. Publication PM 1536. Ames, IA: Iowa State University Extension, 1995.

Hastie T, Tibshirani R, Friedman J. *The elements of statistical learning*. New York, NY: Springer, 2003.

Henriques Jr FC, Moritz AR. Studies of thermal injury: I. The conduction of heat to and through skin and the temperatures attained therein. A theoretical and an experimental investigation. *American J Pathol* 23(4):530-549, 1947.

Holmes KR. Thermal properties. Retrieved from <https://users.ece.utexas.edu/~valvano/research/Thermal.pdf>, 2018.

Irving L. Physiological insulation of swine as bare-skinned mammals. *J Appl Physiol* 9(3):414-420, 1956.

Khaled AR, Vafai K. The role of porous media in modeling flow and heat transfer in biological tissues. *Intl J Heat Mass Transfer* 46(26):4989-5003, 2003.

Kowalski GJ, Mitchell JW. An analytical and experimental investigation of the heat transfer mechanism within fibrous media. *Trans ASME* 79:402-1215, 1979.

Loughmiller JA, Spire MF, Dritz SS, Fenwick BW, Hosni MH, Hogge SB. Relationship between mean body surface temperature measured by use of infrared thermography and ambient temperature in clinically normal pigs and pigs inoculated with *Actinobacillus pleuropneumoniae*. *American J Vet Res* 62(5):676-681, 2001.

Lusk G. *The elements of the science of nutrition* (4th ed.). New York, NY: Academic Press, 1928.

Maia ASC, da Silva RG, Loureiro CM. Respiratory heat loss of Holstein cows in a tropical environment. *Intl J Biometeorol* 49:332-336, 2005.

Maia ASC, Nascimento ST, Nascimento CC, Gebremedhin KG. Thermal equilibrium of goats. *J Therm Biol* 58:43-49, 2016.

Maia ASC, Silva RG, Loureiro CM. Latent heat loss of Holstein cows in a tropical environment: A prediction model. *Revista Brasileira de Zootecnia* 37(10):1837-1843, 2008.

McArthur AJ. Thermal resistance and sensible heat loss from animals. *J Therm Biol* 6(1):43-47, 1981.

Milan HFM. ANABHT: Analytical solver for steady-state bioheat transfer problems in 1D. <http://doi.org/10.5281/zenodo.1432539>, 2018.

Milan HFM, Gebremedhin KG. General node for transmission-line modeling (TLM) method applied to bio-heat transfer. *Intl J Numer Model* 31(5):e2455, 2018.

Milan HFM, Maia ASC, Gebremedhin KG. Data for mechanistic modeling of bio-heat transfer of piglets. <https://doi.org/10.17605/OSF.IO/FSQXJ>, 2018a.

Milan HFM, Moura GA, Castro PA, Maia ASC, Gebremedhin KG. Measurement of 3-D surface area of piglets. *Proc. 10th Intl. Livestock Environment Symp. (ILES X)* (pp. 1-6). St. Joseph, MI: ASABE. <https://doi.org/10.13031/iles.18-060>, 2018b.

Modest MF. Chapter 10: The radiative transfer equation in participating media (RTE). In M. F. Modest (Ed.), *Radiative heat transfer* (3rd ed., pp. 279-302). Boston, MA: Academic Press. <https://doi.org/10.1016/B978-0-12-386944-9.50010-8>, 2013.

Monteith J, Unsworth M. *Principles of environmental physics: Plants, animals, and the atmosphere*. Boston, MA: Academic Press, 2013.

Mount LE. The influence of huddling and body size on the metabolic rate of the young pig. *J Agric Sci* 55(1):101-105, 1960.

Mount, L. E. (1963). Environmental temperature preferred by the young pig. *Nature*, 199(4899), 1212-1213. <https://doi.org/10.1038/1991212a0>

MWPS. Structures and environment handbook. Ames: Iowa State University, MidWest Plan Service, 1983

Pennes HH. Analysis of tissue and arterial blood temperatures in the resting human forearm. *J Appl Physiol* 1(2):93-122, 1948.

R Core Team. R: A language and environment for statistical computing. Vienna, Austria: R Foundation for Statistical Computing, 2018.

Revolution Analytics, Weston S. doMC: For each parallel adaptor for 'parallel'. Retrieved from <https://CRAN.R-project.org/package=doMC>, 2017.

RStudio Team. RStudio: Integrated development environment for R. Boston, MA: RStudio, Inc. Retrieved from [www.rstudio.com](http://www.rstudio.com), 2016.

Sagi O, Rokach L. Ensemble learning: A survey. *Wiley Interdisciplinary Rev: Data Mining and Knowledge Discovery* 8(4):e1249, 2018.

Stevens DG. A model of respiratory vapor loss in Holstein dairy cattle. *Trans ASAE* 24(1):151-153, 1981.

Stinn JP, Xin H. Heat and moisture production rates of a modern U.S. swine breeding, gestation, and farrowing facility. *Trans ASABE* 57(5):1517-1528, 2014a.

Stinn JP, Xin H. Heat lamp vs. heat mat as localized heat source in swine farrowing crate. *Animal Industry Report* 660:ASL R2931, 2014b.

Tong TW, Tien CL. Analytical models for thermal radiation in fibrous insulations. *J Thermal Insul* 4(1):27-44, 1980.

Tranquilli WJ, Parks CM, Thurmon JC, Benson GJ, Koritz GD, Manohar M, Theodorakis MC. Organ blood flow and distribution of cardiac output in nonanesthetized swine. *American J Vet Res* 43(5):895-897, 1982.

Turnpenny JR, McArthur AJ, Clark JA, Wathes CM. Thermal balance of livestock: 1. A parsimonious model. *Agric Forest Meteorol* 101(1):15-27, 2000a.

Turnpenny JR, Wathes CM, Clark JA, McArthur AJ. Thermal balance of livestock: 2. Applications of a parsimonious model. *Agric Forest Meteorol* 101(1):29-52, 2000b.

Upton RN. Organ weights and blood flows of sheep and pig for physiological pharmacokinetic modelling. *J Pharmacol Toxicol Methods* 58(3):198-205, 2008.

Van der Vaart AW, Dudoit S, van der Laan MJ. Oracle inequalities for multi-fold cross validation. *Stat Decisions* 24(3):351-371, 2006.

Van Woerkens LJ, Duncker DJ, Huigen RJ, Van Der Giessen WJ, Verdouw PD. Redistribution of cardiac output caused by opening of arteriovenous anastomoses by a combination of azaperone and metomidate. *Br J Anaesthesia* 65(3):393-399, 1990.

van Woerkens LJ, Man in't Veld AJ, van der Giessen WJ, van Meegen J, Boomsma F, Verdouw PD. Effect of epinine on systemic hemodynamics and regional blood flow in conscious pigs. *J Cardiovasc Pharmacol* 19(4):580-586, 1992.

Vasdal G, Glaerum M, Melisova M, Boe KE, Broom DM, Andersen IL. Increasing the piglets' use of the creep area: A battle against biology? *Appl Animal Behav Sci* 125(3):96-102, 2010a.

Vasdal G, Mogedal I, Boe KE, Kirkden R, Andersen IL. Piglet preference for infrared temperature and flooring. *Appl Animal Behav Sci* 122(2):92-97, 2010b.

Vasdal G, Wheeler EF, Boe KE. Effect of infrared temperature on thermoregulatory behaviour in suckling piglets. *Animal* 3(10):1449-1454, 2009.

Werner J, Buse M. Temperature profiles with respect to inhomogeneity and geometry of the human body. *J Appl Physiol* 65(3):1110-1118, 1988.

Wheeler EF, Vasdal G, Flo A, Boe KE. Static space requirements for piglet creep area as influenced by radiant temperature. *Trans ASABE* 51(1):271-278, 2008.

Xin H, Zhang Q. Preference for lamp or mat heat by piglets at cool and warm ambient temperatures with low to high drafts. *Appl Eng Agric* 15(5):547-551, 1999.

Xin H, Zhou H, Bound DS. Heat lamp usage by neonatal piglets. Swine Research Report 33. Ames, IA: Iowa State University, 1997b.

Xin H, Zhou H, Bundy DS. Comparison of energy use and piglet performance between conventional and energy-efficient heat lamps. *Appl Eng Agric* 13(1):95-99, 1997a.

Zhou H, Xin H. Effects of heat lamp output and color on piglets at cool and warm environments. *Appl Eng Agric* 15(4):327-330, 1999.

CHAPTER 5: PREDICTION OF BIOENERGETIC RESPONSES OF DAIRY-COWS  
USING THE TRANSMISSION-LINE MODELING (TLM) METHOD

Hugo Fernando Maia Milan, Kifle G. Gebremedhin

*In Preparation.*

***Abstract***

Heat stress costs \$2 billion to American farmers every year. To reduce the loss from heat stress, farmers provide heat reduction systems to the animals, such as shades, ventilation, sprinklers, and conductive cooling. To assist farmers in deciding which heat reduction system to install, given animal performance and environmental conditions of the region, researchers have developed bioenergetic models. Bioenergetic models provide insights into animal energy balance and thermal comfort. The limitation of existing bioenergetic models is the assumption of steady-state heat transfer (i.e., thermal comfort does not depend on previous the environmental conditions an animal was exposed to), although experimental data suggests that animals respond dynamically to the environment. The main limitation on providing dynamic predictions of bioenergetic responses is likely because of the high computational cost (RAM memory and computation time) of the numerical models commonly used (e.g., finite difference method, finite element method, and finite volume method). In this research, we developed a dynamic bioenergetic for dairy-cows using the transmission-line modeling (TLM) method. The advantage of the TLM

is the intrinsic modeling of the dynamic response, allowing for fast and accurate computations. The TLM bioenergetic model consisted of two 1-D mediums composed of muscle, fat, skin, and hair-coat layers (black vs. white). The model predicts temperatures (e.g., internal, skin surface, and hair-coat surface), heat fluxes (e.g., internal, skin surface, hair-coat surface, convection, and radiation), metabolic heat flux, respiratory variables (respiration rate, tidal volume, expired air temperature), respiratory heat transfer (evaporation and convection), sweating rate, and cutaneous evaporation. The accuracy of the model in predicting skin surface and hair-coat surface temperatures was better than 5%.

**Keywords** Bio-heat equation, bioenergetics, computational models, dairy-cows, precision livestock farming, transmission-line modeling.

### ***Highlights***

- A transmission-line modeling (TLM) bioenergetic model of dairy-cows was developed.
- The model was validated using experimental data.
- Predictions of skin surface and hair-coat surface temperatures were accurate within 5%.

Table 17. Nomenclature table.

Nomenclature

---

|            |  |
|------------|--|
| $c$        | Specific heat, $\text{J kg}^{-1} \text{ } ^\circ\text{C}^{-1}$   |
| $d$        | Diameter, m  |
| $d_{preg}$ | Days in pregnancy  |
| $f_w$      | Proportion of white hair-coat surface area   |
| $h$        | Convection transfer coefficient  |
| $k$        | Thermal conductivity, $\text{W m}^{-1} \text{ } ^\circ\text{C}^{-1}$   |
| $n$        | Number of samples/iterations/nodes   |
| $n_N$      | Number of nodes  |
| $n_{SM}$   | Fractional number of iterations (total equals to $n_{SM} \times n_N$ ) to solve the scattering multiplication matrix |
| $n_{SS}$   | Number of iterations to solve the steady-state inversion matrix equation   |
| $q''$      | Heat flux, $\text{W m}^{-2}$   |
| $q'''$     | Volumetric heat, $\text{W m}^{-3}$   |

|                  |   |
|------------------|---|
| $t$              | Time, s   |
| $A$              | Animal surface area, $m^2$  |
| $D$              | Diffusivity, $m^2 s^{-1}$   |
| $HD$             | Hair density, $m^{-2}$  |
| $HL$             | Hair length, m  |
| $L$              | Length, m   |
| $M$              | Milk production, kg   |
| $N(\mu, \sigma)$ | Normal distribution with mean $\mu$ and standard deviation $\sigma$ |
| $Q$              | Heat, W   |
| $RH$             | Relative humidity, %  |
| $RR$             | Respiration rate, respirations per minute (RPM)                     |
| $S(a)$           | Step function, defined as 1 when $a$ is positive and 0 otherwise    |
| $SR$             | Sweating rate, $g h^{-1} m^{-2}$                                    |
| $T$              | Temperature, $^{\circ}C$  |
| $T_{exp}$        | Expired air temperature, $^{\circ}C$                                |

|                  |  |
|------------------|--|
| $U_I(a, b)$      | Uniform integer distribution from $a$ to $b$   |
| $U_R(a, b)$      | Uniform real distribution from $a$ to $b$  |
| $V_t$            | Tidal volume, $\text{m}^3 \text{respiration}^{-1}$   |
| $W$              | Animal weight, kg  |
| $Weibull(a, b)$  | Weibull distribution (a long tail distribution), with shape parameter $a$ and scale parameter $b$                  |
| $X^2_n$          | Chi-squared distribution with $n$ degrees  |
| $\delta$         | Laminar boundary thickness   |
| $\lambda(T)$     | Latent heat of vaporization at temperature $T$ : $2,500.7879 - 2.3737T$ (da Silva & Maia, 2013), $\text{J g}^{-1}$ |
| $\rho$           | Density, $\text{kg m}^{-3}$  |
| $\omega_{blood}$ | Blood perfusion, $\text{m}^3 \text{s}^{-1} \text{m}^{-3}$  |
| $\Delta t$       | Time-step, s   |
| $\Psi(T)$        | Saturated vapor density at temperature $T$ (Wagner & Pruß, 2002), $\text{kg m}^{-3}$                               |

---

**Subscripts**

- $\square_a$  Denotes a variable of the air
- $\square_A$  Denotes a variable for the animal
- $\square_b$  Denotes a variable for the black hair-coat
- $\square_{blood}$  Denotes a variable for the blood
- $\square_c$  Denotes a variable for the core of the animal
- $\square_{ce}$  Denotes a variable for cutaneous evaporation
- $\square_{evap}$  Denotes a variable for evaporation
- $\square_{conv}$  Denotes a variable for convection
- $\square_{end}$  Denotes a variable at a specific end time
- $\square_f$  Denotes a variable for the fat
- $\square_h$  Denotes a variable for the surface of the hair-coat
- $\square_{ht}$  Denotes a variable for heat transfer
- $\square_i$  Denotes a variable at the internal boundary of the model

|                 |   |
|-----------------|---|
| $\square_{ini}$ | Denotes a variable at a specific initial time             |
| $\square_{im}$  | Denotes a variable for the internal tissue metabolic heat |
| $\square_m$     | Denotes a variable for the muscle                         |
| $\square_{mes}$ | Denotes the measured value of a variable                  |
| $\square_{met}$ | Denotes a variable for the metabolism                     |
| $\square_p$     | Denotes the predicted value of a variable                 |
| $\square_r$     | Denotes a variable for the respiratory system             |
| $\square_s$     | Denotes a variable at the surface of the skin             |
| $\square_{sk}$  | Denotes a variable for the skin                           |
| $\square_v$     | Denotes a variable for vapor mass transfer                |
| $\square_w$     | Denotes a variable for the white hair-coat                |

---

## ***1. INTRODUCTION***

Heat stress costs \$2 billion to the dairy industry every year (Ferreira et al., 2016; St-Pierre et al., 2003). This huge cost comes from the negative effects of heat stress (Bernabucci et al., 2014; Kadzere et al., 2002), which include decreased milk production (West, 2003), decreased fertility rate (Rensis and Scaramuzzi, 2003; Wolfenson et al., 2000), impaired animal welfare (Polsky and von Keyserlingk, 2017; Silanikove, 2000), increased health risks (Bernabucci et al., 2010), and increased production costs (Ferreira et al., 2016; St-Pierre et al., 2003). A heat-stressful environment is defined as an environment where animals cannot dissipate their internal energy (Collier and Gebremedhin, 2015). To allow animals to dissipate their internal energy and to mitigate the negative effects of heat-stress, farmers provide heat reduction systems, such as shades (Maia et al., 2020; Schütz et al., 2010), ventilation (Turner et al., 1992), sprinklers (Chen et al., 2015; Turner et al., 1992), and conductive cooling (Ortiz et al., 2015; Perano et al., 2015). The most challenging decision is which of these systems a farmer should provide given the productive performance of the animals and the environmental conditions of the region of the farm.

To help farmers decide which heat reduction system to install, researchers have developed bioenergetic mathematical models of energy balance. Previous studies developed simple, resistor-based (Berman, 2004, 2005; McArthur, 1981; McGovern and Bruce, 2000) to complex, numerically-based (Drewry et al., 2018; Gebremedhin and Wu, 2016; Mondaca and Choi, 2016; Radoń et al., 2014) models. These models

were focused on investigating the effects of several heat reduction systems, such as shades (Gebremedhin et al., 1997; Jiang et al., 2005), ventilation (Gebremedhin and Wu, 2001, 2003, 2005; Shen et al., 2013), sprinkles (Kimmel et al., 1991), and conductive cooling (Bastian et al., 2003; Mondaca et al., 2013).

The main limitation of current bioenergetic models is their steady-state simplification, although experimental data suggests a strong time-dependence of bioenergetic responses on previous environmental conditions (Gaughan et al., 2000). The main limitations with providing dynamic predictions of bioenergetic responses are likely the high computational costs (computational time and RAM memory requirements) of numerical methods classically used in our field. These methods (e.g., finite element method, FEM, finite difference method, FDM, and finite volume method, FVM) are based on matrix inversion computations, which possess high computational costs. To the best of our knowledge, only one study has included time-dependence effects on predictions of bioenergetic responses of beef cattle (Turner et al., 1987ab).

The transmission-line modeling (TLM) method is a fast time-domain numerical method developed to predict bioenergetic responses (Milan et al., 2014; Milan and Gebremedhin, 2018). Differently from classical numerical methods based on matrix inversion computations, the TLM is based on a simple highly sparse matrix multiplications (Milan and Gebremedhin, 2016b). TLM computations were shown to be 1,550 faster than analytical solutions of time-domain bioheat propagations (based

on the truncation of an infinite series solution) while maintaining a high accuracy better than 2% (Milan and Gebremedhin, 2016a).

The objective of this paper is to develop and validate a TLM model to predict bioenergetics responses of dairy-cows, such as temperatures, heat fluxes, and energy balance. The TLM was used to model two 1-D mediums composed of muscle, fat, skin, and hair-coat layers. The two mediums differed by the color of the hair-coat (black vs. white). The model incorporates heat exchange through metabolism, respiratory ventilation (evaporation and convection), cutaneous evaporation, convection, and radiation.

## ***2. MATERIALS AND METHODS***

Computer algorithms were written in C++. Data analysis was performed in R (R Core Team, 2018) using RStudio (RStudio Team, 2016). Algorithms and all intermediary calculations are available online (Milan, 2020). The computations involved were performed on an Oryx Pro from System76 with Pop-OS 19.04, 512 GB PCIe M.2 SSD, 64 GB DDR4 RAM (2133 MHz), i7-6820HK (3.6 GHz), and 8 GB GeForce GTX 980M.

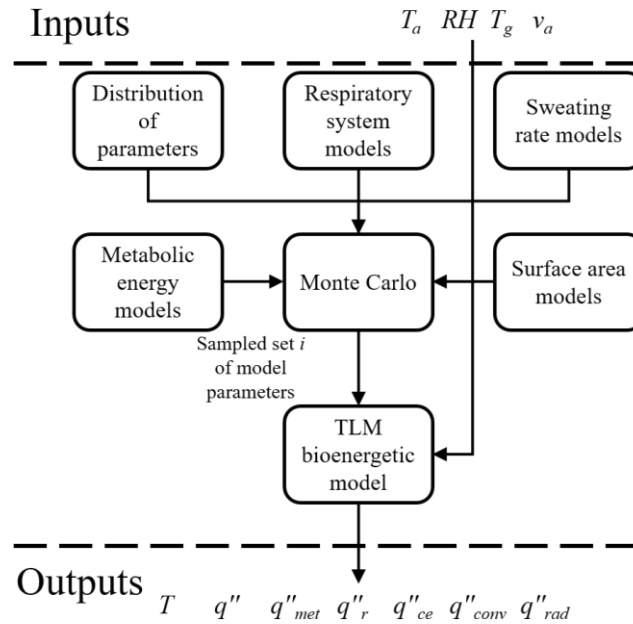


Figure 40. Flowchart of the modeling procedure. The transmission-line modeling (TLM) bioenergetic model predicts several bioenergetics variables, including 1) temperatures at any position in the control volume ( $T$ , °C), 2) heat fluxes at any position in the control volume ( $q''$ ,  $W m^{-2}$ ), 3) metabolic heat generation ( $q''_{met}$ ,  $W m^{-2}$ ), 4) respiratory evaporation and convection heat transfer ( $q''_r$ ,  $W m^{-2}$ ), 5) cutaneous evaporation heat transfer ( $q''_{ce}$ ,  $W m^{-2}$ ), 6) convection heat transfer ( $q''_{conv}$ ,  $W m^{-2}$ ), and 7) radiation heat transfer ( $q''_{rad}$ ,  $W/m^2$ ). The model inputs are the environmental conditions: 1) air temperature ( $T_a$ , °C), 2) relative humidity ( $RH$ , %), 3) air velocity ( $v_a$ ,  $m s^{-1}$ ), and 4) black-globe temperature ( $T_g$ , °C).

Figure 40 shows the flowchart of the modeling procedure. The model inputs are the environmental conditions: 1) air temperature ( $T_a$ , °C), 2) relative humidity ( $RH$ , %), 3) air velocity ( $v_a$ ,  $m s^{-1}$ ), and 4) black-globe temperature ( $T_g$ , °C). The Monte Carlo

method was used to optimize the set of parameters of the TLM bioenergetic model (Figure 41). The inputs for the Monte Carlo optimization method were distribution of parameters (measured and previously reported data) and modeling equations (Appendix A). The TLM bioenergetic model predicts several bioenergetics responses, including 1) temperatures at any position in the control volume ( $T$ , °C), 2) heat fluxes at any position in the control volume ( $q''$ ,  $W m^{-2}$ ), 3) metabolic heat generation ( $q''_{met}$ ,  $W m^{-2}$ ), 4) respiratory evaporation and convection heat transfers ( $q''_r$ ,  $W m^{-2}$ ), 5) cutaneous evaporation heat transfer ( $q''_{ce}$ ,  $W m^{-2}$ ), 6) convection heat transfer ( $q''_{conv}$ ,  $W m^{-2}$ ), and 7) radiation heat transfer ( $q''_{rad}$ ,  $W/m^2$ ).

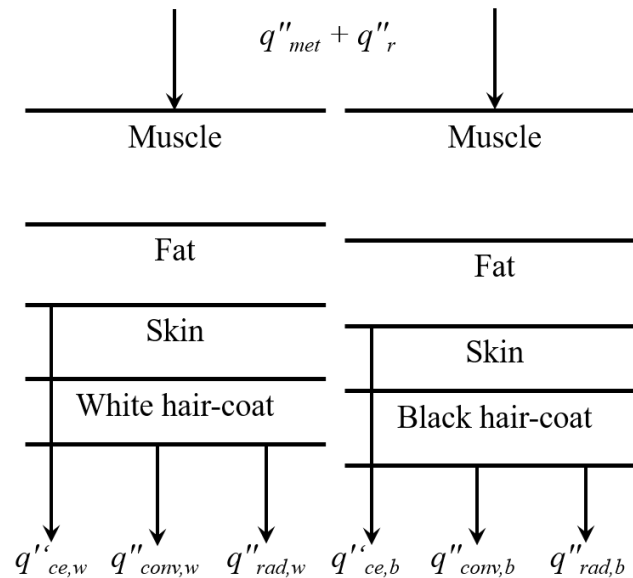


Figure 41. Control volume and boundary conditions of the transmission-line modeling (TLM) bioenergetic model.  $q''_{met}$  ( $W m^{-2}$ ) represents metabolic heat generation,  $q''_r$  ( $W m^{-2}$ ) represents respiratory evaporation and convection heat transfer,  $q''_{ce}$  ( $W m^{-2}$ ) represents cutaneous evaporation heat transfer,  $q''_{conv}$  ( $W m^{-2}$ ) represents convection

heat transfer,  $q''_{rad}$  (W/m<sup>2</sup>) represents radiation heat transfer,  $\square_w$  represents variables for to the model with white hair-coat, and  $\square_b$  represents variables for the model with black hair-coat.

## 2.1. Model description

Figure 41 shows the control volume and boundary conditions for the TLM bioenergetic model. The control volume (Figure 41) was divided into 4 layers (muscle, fat, skin, and hair-coat) and each layer was divided into sublayers, which have parameters independent from each other. For this control volume, the Pennes' energy conservation equation for biological tissues (Pennes, 1948) can be expressed as

$$q'' = -k \frac{dT}{dx} \quad (212)$$

$$\rho c \frac{\partial T}{\partial x} = -\frac{dq''}{dx} + q'''_{blood} + q'''_{itm} + q'''_{ext} \quad (213)$$

$$q'''_{blood} = \omega_{blood} \rho_{blood} c_{blood} (T_{blood} - T) \quad (214)$$

where  $q''$  (W m<sup>-2</sup>) is heat flux,  $T$  (°C) is temperature,  $k$  (W m<sup>-1</sup> °C<sup>-1</sup>) is thermal conductivity,  $x$  (m) is position,  $q'''_{blood}$  (W m<sup>-3</sup>) is blood volumetric heat generation,  $q'''_{itm}$  (W m<sup>-3</sup>) is internal tissue metabolic volumetric heat generation,  $q'''_{ext}$  (W m<sup>-3</sup>) is external volumetric heat generation,  $\omega_{blood}$  (m<sup>3</sup> m<sup>-3</sup> s<sup>-1</sup>) is blood perfusion rate,  $\rho_{blood}$  (kg m<sup>-3</sup>) is blood density,  $c_{blood}$  (J kg<sup>-1</sup> °C<sup>-1</sup>) is blood specific heat, and  $T_{blood}$  (°C) is

blood temperature. As we demonstrated (Milan and Gebremedhin, 2016ab, 2018), these modeling equations can be solved using the TLM method for general node geometries (Milan et al., 2014, Milan and Gebremedhin, 2016ab, 2018). To save computational time in the optimization procedure, we solved Eqs. (212)-(214) using the one-dimensional graded-node formulation (Milan et al., 2014) within the general TLM node framework (Milan and Gebremedhin, 2018).

We developed two one-dimensional TLM models, one representing each hair-coat color. The two one-dimensional TLM models are connected through animal parameters (Table 18-Table 21, e.g., weight and surface area), core temperature ( $T_c$ , °C), internal heat fluxes ( $q''_{met}$  and  $q''_r$ , W m<sup>-2</sup>), and the same environmental conditions. All other parameters of the models are independent.

$T_c$  was calculated as follows:

$$T_c(t + \Delta t) = T_c(t) - \frac{q''_c(t)\Delta t}{AWc_A} \quad (215)$$

$$q''_c = q''_{s,w}f_w + q''_{s,b}(1 - f_w) - q''_{met} - q''_{resp} \quad (216)$$

where  $q''_c$  (W m<sup>-2</sup>) represents net heat flux leaving the control volume,  $\Delta t$  (s) represents time-step,  $A$  (m<sup>2</sup>) represents animal surface area (Table 21),  $W$  (kg) represents animal weight,  $c_A$  (J kg<sup>-1</sup> °C<sup>-1</sup>) represents animal specific heat,  $f_w$  represents proportion of white hair-coat surface area,  $q''_s$  (W m<sup>-2</sup>) represents total skin surface heat flux (cutaneous evaporation heat flux,  $q''_{ce}$ , and conduction heat flux,  $q''_{cond,s}$ ).  $q''_r$

(Table 22-Table 27),  $q''_{met}$  (Table 28-Table 31), and  $q''_{ce}$  (Table 32) were calculated based on equations reported in the literature. For  $q''_r$ , different waveforms were considered (Table 22). The sweating rate could be cyclic (Eq. (221), Gebremedhin et al., 2010). Convection ( $q''_{conv}$ ,  $W m^{-2}$ ) and radiation ( $q''_{rad}$ ,  $W m^{-2}$ ) heat flux were calculated as previously defined (Milan et al., 2019).

Because of the non-linearities in the model, the initialization of the model consisted of 1) calculating the TLM matrices (Milan and Gebremedhin, 2016b), 2) inversely solving the steady-state inversion matrix equation (Milan and Gebremedhin, 2016b), for at most  $n_{SS}$  times, until the temperature at the internal boundary ( $T_i$ , °C),  $T_s$ , and  $T_h$  changed less than a threshold of 0.01 °C, and 3) solving the scattering multiplication matrix equation (Milan and Gebremedhin, 2016b)  $n_N$  times, for at most  $n_{SM}$  times, until the maximum time derivatives of  $T_i$ ,  $T_s$ , and  $T_h$  were less than a threshold of 0.01 °C s<sup>-1</sup>.

A mesh validation procedure was followed to optimize the choices of  $n_N$  and  $\Delta t$  (Appendix B).

## 2.2. Experimental data processing

To validate the model, we used the dry dairy-cow experimental data of PLFBD that was cleaned (Precision Livestock Farming Big Data, Milan et al., 2020). To train and validate the model (Gorczyca et al., 2018), the data ( $n = 45,473$  for  $T_{s,w}$ ,  $n = 57,154$  for  $T_{s,b}$ ,  $n = 40,405$  for  $T_{h,w}$ ,  $n = 62,864$  for  $T_{h,b}$ ) was divided into testing (~25%,  $n =$  203

12,175 for  $T_{s,w}$ ,  $n = 17,002$  for  $T_{s,b}$ ,  $n = 12,570$  for  $T_{h,w}$ ,  $n = 16,434$  for  $T_{h,b}$ ) and training. The training dataset was divided into 5-fold cross-validation datasets (28,152, 28,232, 25,726, 25,248, and 25,834 for  $T_{s,w}$ , 32,389, 30,514, 32,282, 32,177, and 33,246 for  $T_{s,b}$ , 23,525, 21,911, 22,288, 22,153, and 21,463 for  $T_{h,w}$ , and 35,772, 37,042, 38,383, 38,358, and 36,165 for  $T_{h,b}$ ). The division of the data was in continuous segments of samples (training:  $n = 32$  for  $T_{s,w}$ ,  $n = 46$  for  $T_{s,b}$ ,  $n = 26$  for  $T_{h,w}$ ,  $n = 45$  for  $T_{h,b}$ ; testing:  $n = 10$  for  $T_{s,w}$ ,  $n = 15$  for  $T_{s,b}$ ,  $n = 9$  for  $T_{h,w}$ ,  $n = 15$  for  $T_{h,b}$ ; CV: 26, 26, 25, 26, and 25 for  $T_{s,w}$ , 37, 37, 37, 36, and 37 for  $T_{s,b}$ , 21, 21, 21, 20, and 21 for  $T_{h,w}$ , and 36, 36, 36, 36, and 36 for  $T_{h,b}$ ).

### 2.3. Model optimization

System parameters necessary to solve the equations representing the TLM bioenergetic model (Figure 40 and Figure 41) were measured or obtained from the literature (Appendix A). Because of the intrinsic variability of the parameters, we estimated the distribution of the parameters based on data, adjusting the probability distribution of the parameters to cover the reported data with at least 70% probability (leaving 30% for unlikely or non-reported values). In the sampling procedure for the different modeling equations (e.g., predictive equation for  $q''_{met}$ ), we sampled how many predictive equations were going to be used, their partial contributions (which sum up to 1), and random factors (to adjust for misfits). The distributions were assumed to be independent between themselves. Only physically possible parameters were accepted by the sampling procedure (e.g., length greater than zero). From

204

Bayesian statistics theory (Gelman et al., 2013), prior probability distribution functions usually do not have a significant impact on the final result, as long as the true set of parameters is included in the prior probability distribution.

These distributions were used in the Monte Carlo optimization method, sampling 10,000 sets, to select the sets of system parameters that minimized the cross-validation value of the following objective function:

$$\text{MSE}(x) = \frac{1}{n_x} \sum_{j=1}^{n_x} (x_m - x_p)^2 \quad (217)$$

$$\text{obj}_j = \text{MSE}(T_{s,w,j}) + \text{MSE}(T_{s,b,j}) + \text{MSE}(T_{h,w,j}) + \text{MSE}(T_{h,b,j}) \quad (218)$$

$$\text{obj} = \frac{1}{n_{CV}} \sum_{j=1}^{n_{CV}} \text{obj}_j \quad (219)$$

For most predictions, the prediction time did not match the time of the measurement. In these cases, the predicted values were linearly interpolated using the predicted value at a time-step before the measurement time and another after.

### ***3. RESULTS AND DISCUSSION***

Figure 42 shows the MSE for the predictions using the traditional set of inputs and the set optimized with the Monte Carlo optimization method. The MSE for the optimized set was 3.6 times lower than using the traditional set. The mean absolute percentage

error of the predictions were 3.93%, 4.07%, 4.26%, and 4.18% for  $T_{s,w}$ ,  $T_{s,b}$ ,  $T_{h,w}$ , and  $T_{h,b}$ , respectively.

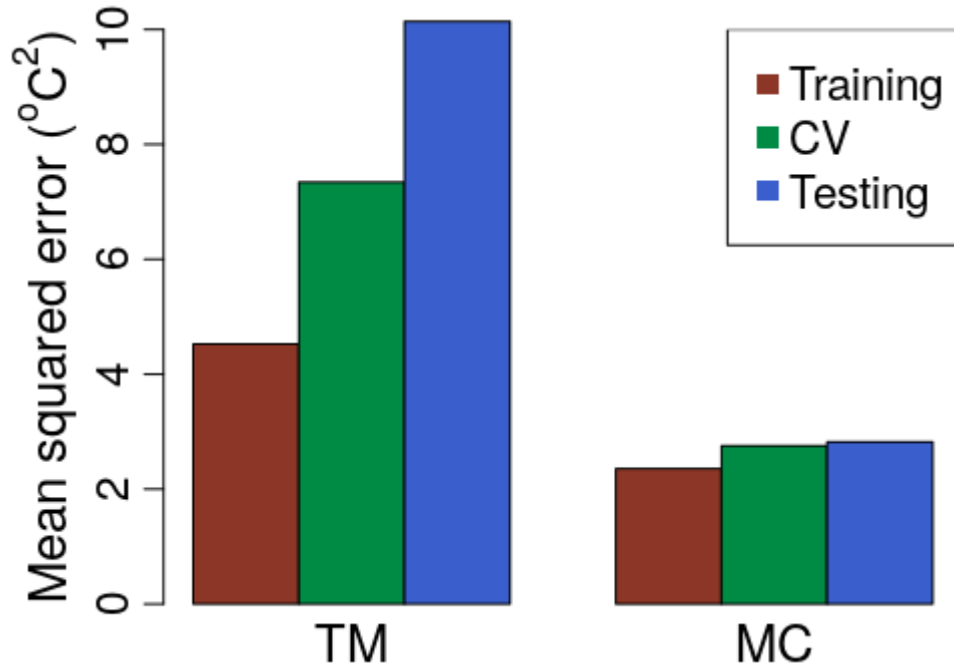


Figure 42. Mean squared error for the training, cross-validation (CV), and testing datasets using the traditional set of system parameters (TM) and the set of system parameters optimized using the Monte Carlo optimization method (MC).

#### 4. CONCLUSION

The following conclusions can be drawn from this study:

- A transmission-line modeling (TLM) bioenergetic model was developed to predict bioenergetic responses of dairy-cows.
- The TLM bioenergetic model consisted of two 1-D medium, one with white

and another with black hair-coat color.

- The predictions of skin surface and hair-coat surface temperatures for the medium with the white hair-coat color were 3.93% and 4.26%, respectively.
- The predictions of skin surface and hair-coat surface temperatures for the medium with the black hair-coat color were 4.07% and 4.18%, respectively.

***Acknowledgement***

Funding: Brazilian National Council of Technological and Scientific Development (CNPq, Proc. 203312/2014-7) and the USDA/Hatch (Washington, DC) funds as part of the W-3173 Regional Project through Cornell University.

***APPENDIX A: MODEL PARAMETERS***

Table 18. Traditional values and distributions for parameters related to the transmission-line modeling configuration, animal, blood, and the environment.

| Parameter                              | Traditional value | Distribution      | Reference              |
|--|-------------------|-------------------|------------------------|
| <hr/> Transmission-line modeling <hr/> |                   |                   |                        |
| Time-step ( $\Delta t$ ), s            | 0.1               | Weibull(0.42, 10) | Validated (Appendix B) |

Number of iterations to solve - - Calculated  
the steady-state inversion  
matrix equation ( $n_{SS}$ )

Fractional number of - - Calculated  
iterations to solve the  
scattering multiplication  
matrix ( $n_{SM}$ )

---

Animal

---

|  |      |                 |  |
|--|------|-----------------|--|
| Diameter ( $d_A$ ), m                                | 0.75 | $N(0.75, 0.02)$ | Measured   |
| Weight ( $W$ ), kg                                   | 850  | $N(700, 200)$   | Measured, Maia et al. (2005ab), Santos et al. (2017) |
| Proportion of white hair-coat surface area ( $f_w$ ) | 0.5  | $U_R(0, 1)$     | Assumed  |
| Specific heat ( $c_A$ ), $J\ kg^{-1}\ ^\circ C^{-1}$ | 3600 | $N(3600, 100)$  | Assumed  |

---

Blood

|  |      |                   |                        |
|--|------|-------------------|------------------------|
| Volumetric heat capacity of blood ( $\rho_{blood}C_{blood}$ ), MJ m <sup>-3</sup> °C <sup>-1</sup> | 4.1  | $N(4.1, 0.26)$    | Werner and Buse (1988) |
| Blood temperature multiplicative factor <sup>a</sup>   | 1    | $U_R(0.98, 1.01)$ | Assumed                |
| Environment  |      |                   |                        |
| Black-globe emissivity   | 0.95 | $U_R(0.92, 0.99)$ | Assumed                |
| Mean radiant temperature multiplicative factor <sup>b</sup>  | 1    | $N(1, 0.1)$       | Assumed                |
| Convective heat transfer coefficient multiplicative factor <sup>b</sup>                            | 1    | $N(1, 0.1)$       | Assumed                |
| Convective vapor mass transfer coefficient multiplicative factor <sup>b</sup>                      | 1    | $N(1, 0.1)$       | Assumed                |
| Vapor mass transfer  | 1    | $N(1, 0.1)$       | Assumed                |

diffusivity      multiplicative  
factor<sup>b</sup>

---

<sup>a</sup>Blood temperature was assumed equal to the core temperature times the accumulated blood temperature multiplicative factor (Milan et al., 2019). <sup>b</sup>Multiplicative factors were inserted to account for misfits between predictive equations for mean radiant temperature and convective heat transfer coefficient, and for possible experimental measurement errors.

Table 19. Traditional values and distributions for parameters for muscle, skin, and fat layers.

| Parameter               | Traditional value | Distribution                  | Reference |
|-------------------------|-------------------|-------------------------------|-----------|
| <b>Muscle</b>           |                   |                               |           |
| Number of sublayers     | 1                 | $\text{round}(X_{10}^2 + 1)$  | Assumed   |
| Number of nodes         | 100               | $\text{round}(X_{100}^2 + 1)$ | Validated |
| Thickness ( $L_m$ ), mm | 66                | $N(66, 13)$                   | Measured  |

|  |      |                               |           |
|--|------|-------------------------------|-----------|
| Thermal conductivity ( $k_m$ ), W m <sup>-1</sup> °C <sup>-1</sup>                                     | 0.53 | $N(0.53, 0.1)$                | Assumed   |
| Density ( $\rho_m$ ), kg m <sup>-3</sup>   | 1000 | $N(1000, 100)$                | Assumed   |
| Specific heat ( $c_m$ ), J kg <sup>-1</sup> °C <sup>-1</sup>   | 3600 | $N(3600, 100)$                | Assumed   |
| Blood perfusion ( $\omega_{blood,m}$ ), 10 <sup>3</sup> m <sup>3</sup> m <sup>-3</sup> s <sup>-1</sup> | 2.5  | $N(2.5, 0.9)$                 | Assumed   |
| Internal volumetric heat ( $q'''_{im,m}$ ), W m <sup>-3</sup>  | 684  | $N(684, 137)$                 | Assumed   |
| <hr/>  |      |                               |           |
| Fat  |      |                               |           |
| <hr/>  |      |                               |           |
| Number of sublayers  | 1    | $\text{round}(X_{10}^2 + 1)$  | Assumed   |
| Number of nodes  | 100  | $\text{round}(X_{100}^2 + 1)$ | Validated |
| Thickness ( $L_f$ ), mm  | 11   | $N(11, 4)$                    | Measured  |
| Thermal conductivity ( $k_f$ ), W m <sup>-1</sup> °C <sup>-1</sup>                                     | 0.29 | $N(0.29, 0.12)$               | Assumed   |

1

|  |      |                |         |
|--|------|----------------|---------|
| Density ( $\rho_f$ ), kg m <sup>-3</sup>   | 1000 | $N(1000, 100)$ | Assumed |
| Specific heat ( $c_f$ ), J kg <sup>-1</sup> °C <sup>-1</sup>   | 3600 | $N(3600, 100)$ | Assumed |
| Blood perfusion ( $\omega_{blood,f}$ ), 10 <sup>3</sup> m <sup>3</sup> m <sup>-3</sup> s <sup>-1</sup> | 2.5  | $N(2.5, 1.34)$ | Assumed |
| Internal volumetric heat ( $q'''_{im,f}$ ), W m <sup>-3</sup>  | 368  | $N(368, 74)$   | Assumed |

---

 Skin
 

---

|   |      |                               |           |
|---|------|-------------------------------|-----------|
| Number of sublayers   | 1    | $\text{round}(X_{10}^2 + 1)$  | Assumed   |
| Number of nodes   | 100  | $\text{round}(X_{100}^2 + 1)$ | Validated |
| Thickness ( $L_{sk}$ ), mm  | 5    | $N(5, 0.3)$                   | Measured  |
| Thermal conductivity ( $k_{sk}$ ), W m <sup>-1</sup> °C <sup>-1</sup> | 0.21 | $N(0.21, 0.05)$               | Assumed   |

212

|   |      |                |         |
|---|------|----------------|---------|
| Density ( $\rho_{sk}$ ), kg m <sup>-3</sup>   | 1000 | $N(1000, 100)$ | Assumed |
| Specific heat ( $c_{sk}$ ), J kg <sup>-1</sup> °C <sup>-1</sup>   | 3600 | $N(3600, 100)$ | Assumed |
| Blood perfusion ( $\omega_{blood,sk}$ ), 10 <sup>3</sup> m <sup>3</sup> m <sup>-3</sup> s <sup>-1</sup> | 1.55 | $N(1.55, 0.5)$ | Assumed |
| Internal volumetric heat ( $q'''_{ims,sk}$ ), W m <sup>-3</sup>   | 367  | $N(367, 74)$   | Assumed |

Table 20. Traditional values and distributions for parameters for black and white hair-coat colors.

| Parameter           | Traditional value | Distribution                  | Reference |
|---------------------|-------------------|-------------------------------|-----------|
| White hair-coat     |                   |                               |           |
| Number of sublayers | 1                 | $\text{round}(X_{10}^2 + 1)$  | Assumed   |
| Number of nodes     | 100               | $\text{round}(X_{100}^2 + 1)$ | Validated |

|  |      |                               |           |
|--|------|-------------------------------|-----------|
| Thickness ( $L_w$ ), mm  | 3    | $N(3, 1)$                     | Measured  |
| Thermal conductivity ( $k_b$ ), $\text{W m}^{-1} \text{ } ^\circ\text{C}^{-1}$ | 0.6  | $N(0.6, 0.35)$                | Assumed   |
| Density ( $\rho_w$ ), $\text{kg m}^{-3}$                                       | 1000 | $N(1000, 100)$                | Assumed   |
| Specific heat ( $c_w$ ), $\text{J kg}^{-1} \text{ } ^\circ\text{C}^{-1}$       | 3600 | $N(3600, 100)$                | Assumed   |
| <hr/>  |      |                               |           |
| Black hair-coat  |      |                               |           |
| <hr/>  |      |                               |           |
| Number of sublayers  | 1    | $\text{round}(X_{10}^2 + 1)$  | Assumed   |
| Number of nodes  | 100  | $\text{round}(X_{100}^2 + 1)$ | Validated |
| Thickness ( $L_b$ ), mm  | 2.5  | $N(2.5, 0.9)$                 | Measured  |
| Thermal conductivity ( $k_b$ ), $\text{W m}^{-1} \text{ } ^\circ\text{C}^{-1}$ | 0.6  | $N(0.6, 0.35)$                | Assumed   |
| Density ( $\rho_b$ ), $\text{kg m}^{-3}$                                       | 1000 | $N(1000, 100)$                | Assumed   |
| Specific heat ( $c_b$ ), $\text{J kg}^{-1} \text{ } ^\circ\text{C}^{-1}$       | 3600 | $N(3600, 100)$                | Assumed   |

Table 21. Animal surface area model. Both hair-coat colors have the same model. Brody (1945) model was used for the set with traditional parameters (see Berman, 2005).

| Animal surface area<br>(A), m <sup>2</sup> | Random<br>factor  | Reference  |
|--|-------------------|--|
| $0.14W^{0.56}$                             | $\times N(1,0.1)$ | Brody (1945)   |
| $0.13W^{5/9}$                              | $\times N(1,0.1)$ | Finch (1985)   |
| $0.14W^{5/9}$                              | $\times N(1,0.1)$ | Finch (1985)   |
| $0.105W^{2/3}$                             | $\times N(1,0.1)$ | Meeh (1879) <sup>a</sup> and Rubner (1902) <sup>a</sup> as cited<br>by Lusk (1928) |
| $0.2616W^{0.44}$                           | $\times N(1,0.1)$ | Johnson et al. (1961)  |
| $0.2098W^{0.48}$                           | $\times N(1,0.1)$ | Johnson et al. (1961)  |
| $0.147W^{0.56}$                            | $\times N(1,0.1)$ | Eltin (1926)   |

<sup>a</sup>Reference not accessible.

Heat transfer from the respiratory system was modeled using 4 waveforms: constant, square, sinusoidal, and exponential. Each waveform implies a different multiplication factor for the total heat transfer from the respiratory system (Table 22). For the constant waveform, heat flux was calculated at each time-step. For the remaining waveforms, the total heat flux (integrated over the period of the waveform, defined as  $60/RR$ ) was equal to the heat flux calculated using the constant waveform when the waveform begins.

Table 22. Respiratory system waveform multiplication factor. Both hair-coat colors have the same model. The constant waveform was used for the set with traditional parameters.

|            | Respiratory system waveform <sup>abc</sup>  | Random factors    |
|------------|---|-------------------|
| Constant   | 1   |                   |
| Square     | $\frac{1}{f} [1 - S(t - t_m)]$  | $f \sim U_R(0,1)$ |
| Sinusoidal | $\frac{\pi t_{end} - t_{ini}}{2 t_m - t_{ini}} \sin\left(\pi \frac{t - t_{ini}}{t_m - t_{ini}}\right) [1 - S(t - t_m)]$ | $f \sim U_R(0,1)$ |

$$\text{Exponential} \quad \frac{f_2}{(1-f)[f_2-1+\exp(f_2)]} \left\{ \begin{array}{l} 1 \\ - \exp\left(-f_2 \frac{t-t_{ini}}{t_{end}-t_{ini}}\right) \\ - \left[1 - \exp\left(-f_2 \frac{t-t_m}{t_{end}-t_m}\right)\right] S(t) \\ - t_m \end{array} \right\} \quad \begin{array}{l} f \sim U_R(0,1) \\ f_2 \sim Weibull(2, 4.5) \end{array}$$

---

<sup>a</sup> $t_{ini}$  refers to the initial time of the waveform and  $t_{end} = t_{ini} + 60/RR$ . <sup>b</sup> $f$  represents the fraction of the waveform that is not zero (square and sinusoidal waveforms) or the fraction of the respiration period where the waveform is increasing (exponential waveform). <sup>c</sup> $t_m$  represents the point of inflection of the waveform, calculated as  $t_m = t_{in} + 60f/RR$ .

Table 23. Respiration rate models. Both hair-coat colors have the same model. Maia et al. (2005a) model was used for the set with traditional parameters.

| Respiration rate ( $RR$ ), RPM           | Random factor     | Reference           |
|--|-------------------|---------------------|
| $\max(0, 3.07 + 0.71T_a + 0.044T_a^2)$   | $\times N(1,0.2)$ | Maia et al. (2005a) |
| $\exp(2.966 + 0.0218T_a + 0.00069T_a^2)$ | $\times N(1,0.2)$ | Stevens (1981)      |

|                             |            |                        |
|-----------------------------|------------|------------------------|
| $\max(0, -1,660 + 43.8T_c)$ | $+N(1,20)$ | Thompson et al. (2011) |
| $\max(0, -2,226 + 59T_c)$   | $+N(1,20)$ | Thompson et al. (2011) |

---

Table 24. Tidal volume models. Both hair-coat colors have the same model. Maia et al. (2005a) model was used for the set with traditional parameters.

| Tidal volume ( $V_t$ ), $\text{m}^3 \text{ respiration}^{-1}$ | Random factor     | Reference           |
|---|-------------------|---------------------|
| $\frac{RR - 2}{-755.32 + 161.93(RR - 2) + 1.97(RR - 2)^2}$    | $\times N(1,0.2)$ | Maia et al. (2005a) |
| $\max(1.9, \min(4.3, 0.4 + 0.006W))$                          | $\times N(1,0.2)$ | Berman (2005)       |
| $0.0189RR^{-0.493}$   | $\times N(1,0.2)$ | Stevens (1981)      |

---

Table 25. Expired air temperature models. Both hair-coat colors have the same model. Maia et al. (2005a) model was used for the set with traditional parameters.

| Expired air temperature ( $T_{exp}$ ), °C   | Random factor     | Reference           |
|---|-------------------|---------------------|
| $947 + 1.18T_a - 0.01278T_a^2$              | $\times N(1,0.2)$ | Maia et al. (2005a) |
| $17 + 0.3T_a + \exp(0.01611RH + 0.0387T_a)$ | $\times N(1,0.2)$ | Stevens (1981)      |

Table 26. Respiratory system convection heat transfer models. Both hair-coat colors have the same model. Maia et al. (2008) model was used for the set with traditional parameters.

| Respiratory system convection heat transfer<br>( $q''_{r,conv}$ ), W m <sup>-2</sup> | Random factor                  | Reference           |
|--|--------------------------------|---------------------|
| $\frac{V_t RR \rho_a c_{pa}}{60A} (T_{exp} - T_a)$                                   | In the calculated coefficients | Maia et al. (2008)  |
| $16.35 - 1.74T_a + 0.02T_a^2 - 0.0016T_a^3$  | $\times N(1,0.2)$              | Maia et al. (2005a) |

Table 27. Respiratory system evaporation heat transfer models. Both hair-coat colors have the same model. The first Maia et al. (2008) model was used for the set with traditional parameters.

| Respiratory system evaporation heat transfer<br>( $q''_{r, evap}$ ), $W m^{-2}$                | Random factor                  | Reference           |
|--|--------------------------------|---------------------|
| $\frac{V_t RR \lambda(T_a)}{60A} \left( \Psi(T_{exp}) - \frac{\Psi(T_s) RH}{100} \right)$      | In the calculated coefficients | Maia et al. (2008)  |
| $2.17 \exp\left(\frac{T_a - 9.11}{8.49}\right)$  | $\times N(1,0.2)$              | Maia et al. (2008)  |
| $54.5 \exp\left(\frac{26.04 - RH}{22.82}\right)$   | $\times N(1,0.2)$              | Maia et al. (2008)  |
| $0.5966 + 0.815RR - 0.0059RR^2$  | $\times N(1,0.2)$              | Maia et al. (2005a) |
| $1.1 \times 10^{-5} RR^{2.78}$   | $\times N(1,0.1)$              | McArthur (1987)     |
| $+ \frac{\lambda(T_a)}{0.027RR + 0.5} \left( \Psi(T_{exp}) - \frac{\Psi(T_s) RH}{100} \right)$ |                                |                     |

Metabolic heat models were divided into effects of environmental condition models ( $f_{met,env}$ , Table 28), basal metabolic heat ( $Q_{met,basal}$ , W, Table 29), milk production metabolic heat model ( $Q_{met,milk}$ , W, Table 30), and pregnancy metabolic heat model ( $Q_{met,preg}$ , W, Table 31):

$$Q_{met} = f_{met,env}(Q_{met,basal} + Q_{met,milk} + Q_{met,preg}) \quad (220)$$

Table 28. Models for the effect of the environment on the metabolic heat. Both hair-coat colors have the same model. Pedersen and Sällvik (2002) model was used for the set with traditional parameters.

| Metabolic heat multiplier ( $f_{met,env}$ ) | Random factor      | Reference                                      |
|---|--------------------|--|
| 1   |                    |  |
| $1 + 0.004(20 - T_a)$                       | $\times N(1, 0.1)$ | Pedersen and Sällvik (2002)                    |
| $1 + 4 \times 10^{-5}(20 - T_a)^3$          | $\times N(1, 0.1)$ | Strom (4) <sup>a</sup> as cited by CIGR (1984) |

<sup>a</sup>Reference not accessible.

Table 29. Basal metabolic heat models. Both hair-coat colors have the same model. Pedersen and Sällvik (2002) model was used for the set with traditional parameters.

| Basal metabolic heat models ( $Q_{met,basal}$ ), W | Random factor      | Reference   |
|--|--------------------|---|
| $5.6W^{0.75}$                                      | $\times N(1, 0.1)$ | Pedersen and Sällvik (2002)                       |
| $3.874W^{0.75}$                                    | $\times N(1, 0.1)$ | Berman (2005)                                     |
| $5.52W^{0.75}$                                     | $\times N(1, 0.1)$ | Landis (1) <sup>a</sup> as cited by CIGR (1984)   |
| $6.36W^{0.73}$                                     | $\times N(1, 0.1)$ | Bruce (2) <sup>a</sup> as cited by CIGR (1984)    |
| $6.6W^{0.73}$                                      | $\times N(1, 0.1)$ | Eriksson (3) <sup>a</sup> as cited by CIGR (1984) |
| $5.2W^{0.73}$                                      | $\times N(1, 0.1)$ | Strom (4) <sup>a</sup> as cited by CIGR (1984)    |
| $6.6W^{0.75}$                                      | $\times N(1, 0.1)$ | CIGR (1999)                                       |
| $A(1022.962 - 21.5394Tc)$                          | $\times N(1,0.1)$  | McArthur (1987), Worstell and Brody (1953)        |
| $6.06W^{1/3}$                                      | $\times N(1, 0.1)$ | Heusner (1982)                                    |

$W^{0.75} \times N(0.65, 0.15)$  Yan et al. (1997), Dong et al. (2015),  
 Xue, Yan et al. (2011), Strathe et al.  
 (2011)

---

<sup>a</sup>Reference not accessible.

Table 30. Milk production metabolic heat model. Both hair-coat colors have the same model. Pedersen and Sällvik (2002) model was used for the set with traditional parameters.

| Milk production metabolic heat<br>( $Q_{met,milk}$ ), W | Random factor      | Reference   |
|---|--------------------|---|
| 22M   | $\times N(1, 0.1)$ | Pedersen and Sällvik (2002)                       |
| 22.2M   | $\times N(1, 0.1)$ | Bruce (2) <sup>a</sup> as cited by CIGR (1984)    |
| 21.7M   | $\times N(1, 0.1)$ | Eriksson (3) <sup>a</sup> as cited by CIGR (1984) |
| 30M   | $\times N(1, 0.1)$ | Strom (4) <sup>a</sup> as cited by CIGR           |

(1984)

$22M \times N(1, 0.1)$  CIGR (1999)

---

<sup>a</sup>Reference not accessible.

Table 31. Pregnancy metabolic heat model. Both hair-coat colors have the same model. Pedersen and Sällvik (2002) model was used for the set with traditional parameters.

| Pregnancy metabolic heat<br>( $Q_{met, preg}$ ), W | Random factor      | Reference   |
|--|--------------------|---|
| $1.6 \times 10^{-5} d_{preg}^3$                    | $\times N(1, 0.1)$ | Pedersen and Sällvik (2002)                       |
| $12.5e^{0.01d_{preg}}$                             | $\times N(1, 0.1)$ | Bruce (2) <sup>a</sup> as cited by CIGR (1984)    |
| $1.6 \times 10^{-5} d_{preg}^3$                    | $\times N(1, 0.1)$ | Eriksson (3) <sup>a</sup> as cited by CIGR (1984) |
| $1.6 \times 10^{-5} d_{preg}^3$                    | $\times N(1, 0.1)$ | Strom (4) <sup>a</sup> as cited by CIGR (1984)    |

---

$$1.6 \times 10^{-6} d_{preg}^3 \times N(1, 0.1) \quad \text{CIGR (1999)}$$

<sup>a</sup>Reference not accessible.

Each sampled sweating rate model was considered constant or cyclic (the probability of a cyclic model was equal to 0.5). Cyclic models were multiplied by the following factor:

$$f_{sw} = a_0 + \sum_{i=1}^N a_i \sin(2\pi f_i t + \alpha_i) \quad (221)$$

where amplitude factor ( $a_i$ )  $\sim U_R(0, 1)$ , frequency components ( $f_i$ )  $\sim Weibull(0.5, 0.4)$  (based on data from Gebremedhin et al., 2010) as long as  $f_i < 2/\Delta t$  (to respect the Nyquist theorem for maximum frequency; Oppenheim & Schaffer, 2009), and the angle components ( $\alpha_i$ )  $\sim U_R(0, 2\pi)$ .

Table 32. Sweating rate models. Each hair-coat color may have a different model. Collier et al. (2008) model was used for the set with traditional parameters.

| Sweating rate ( $SR$ ), $\text{g h}^{-1} \text{m}^{-2}$   | Random factor      | Reference             |
|---|--------------------|-----------------------|
| $\begin{cases} 4.2976T_h - 71.289 & \text{if } T_h \geq 35^\circ\text{C} \\ 1.1665T_h^2 - 64.166T_h + 894.35 & \text{if } T_h \geq 27.5^\circ\text{C} \\ 46.895 & \text{otherwise} \end{cases}$ | $\times N(1, 0.3)$ | Collier et al. (2008) |

|   |  |
|---|--|
| $\frac{\left(\Psi(T_a) - \frac{\Psi(T_s)RH}{100}\right)}{\frac{1}{h_v} + \frac{\delta}{D_v}}$   | <p>In the Gebremedhin<br/>calculated and Wu<br/>coefficient<sup>a</sup> (2003)</p> |
| $\frac{3,600}{\lambda(T_s)} 85.18 \exp\left(\frac{T_a - 24.92}{7.96}\right)$  | <p>× <math>N(1,0.3)</math> Maia et al.<br/>(2005b)</p>                             |
| $\frac{3,600}{\lambda(T_s)} 301.27 \exp\left(\frac{26.92 - RH}{21.53}\right)$   | <p>× <math>N(1,0.3)</math> Maia et al.<br/>(2005b)</p>                             |
| $\frac{3,600}{\lambda(T_s)} 91.97 \exp\left(\frac{T_h - 33.11}{2.73}\right)$  | <p>× <math>N(1,0.3)</math> Maia et al.<br/>(2005b)</p>                             |
| $\frac{3,600}{\lambda(T_s)} \begin{cases} 7,191 - 465.42T_h + 7.5309T_h^2 & \text{if } T_h \geq 30.9^\circ\text{C} \\ 0.1 & \text{otherwise} \end{cases}$ | <p>× <math>N(1,0.4)</math> Santos et al.<br/>(2017)</p>                            |
| $\frac{3,600}{\lambda(T_s)} \left[ 31.5 + 3.67 \exp\left(\frac{T_s - 27.9}{2.19115}\right) \right]$   | <p>× <math>N(1,0.3)</math> da Silva and<br/>Maia (2011)</p>                        |
| $3.6 \left[ 4 + \exp\left(\frac{T_s - 32}{1.58}\right) \right]$   | <p>× <math>N(1,0.4)</math> Gatenby<br/>(1986)</p>                                  |
| $\begin{cases} 64,699 - 3,462T_c + 46.4T_c^2 & \text{if } T_c \geq 37.3^\circ\text{C} \\ 122.256 & \text{otherwise} \end{cases}$                          | <p>× <math>N(1,0.4)</math> Finch et al.</p>  |

(1982)

$$\max(0, 93,528 + 4,575T_c - 55.6T_c^2) \quad \text{Finch et al.}$$

$\times N(1,0.4)$  (1982)

$$0.085 \exp(0.22T_s)$$

$\times N(1,0.4)$  Thompson et al. (2011)

$$0.015 \exp(0.25T_s)$$

$\times N(1,0.4)$  Thompson et al. (2011)

$$\frac{3,600}{\lambda(T_s)} 8.18 \exp\left(\frac{T_a - 15.32}{5.2}\right)$$

$\times N(1,0.2)$  Maia et al. (2008)

$$\frac{3,600}{\lambda(T_s)} 299.63 \exp\left(\frac{26.04 - RH}{12.71}\right)$$

$\times N(1,0.2)$  Maia et al. (2008)

---

<sup>a</sup>The coefficients were calculated as  $D_v = D_a N(1,0.1)$ ,  $h_v = D_v h_{ht} / k_a N(1,0.1)$ , and  $\delta = L_h N(1,0.1)$ .

## ***APPENDIX B: MESH VALIDATION***

The mesh validation procedure consisted of investigating which combination of  $n_N$  and  $\Delta t$  result in valid (not not-a-numbers) precise predictions. For this study, we used the traditional set of parameters, with one sublayer for each layer, with each layer with the

same number of nodes such that  $n_N \sim 4 + 4 \times \text{round}[\text{Weibull}(1, 1,000)]$  and  $\Delta t \sim \text{Weibull}(0.42, 10)$ . 50,000 samples were used for this study.

The following generalized additive model (GAM, Wood, 2017), developed in the R environment using the `mgcv` package (Wood, 2011), was used to investigate the probability of obtaining valid predictions:

$$f(n_N, \Delta t) = a_0 + s(n_N) + s(\Delta t) + ti(n_N, \Delta t) + N(0, \sigma) \quad (222)$$

$$p(n_N, \Delta t) = \frac{1}{1 + \exp[f(n_N, \Delta t)]} \quad (223)$$

where  $f(n_N, \Delta t)$  represents the link function,  $a_0$  represents the intercept coefficient,  $s(x)$  represents a smooth function of  $x$ ,  $ti(\dots)$  represents a smooth function for the interaction between its inputs ( $n_N$  and  $\Delta t$  in this case), and  $p(n_N, \Delta t)$  represents the probability of observing a valid prediction. This model explained 97.80% of the deviance and correctly predicted 99.00% of valid predictions and 99.48% of invalid predictions (Figure 43). For the simulation, we set the threshold  $n_N \times \Delta t = 2,000$ , which correctly predicted 99.20% of valid predictions and 98.45% of invalid predictions.

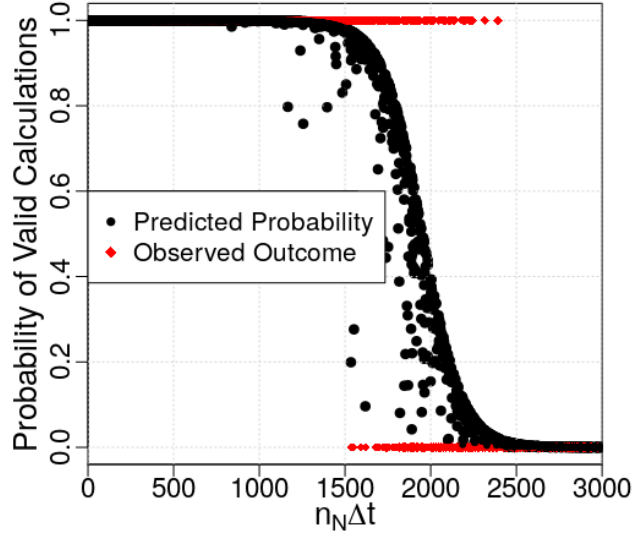


Figure 43. Probability of observing valid predictions vs. number of nodes ( $n_N$ )  $\times$  time-step ( $\Delta t$ ).

To investigate if the values of the sampled parameters would provide precise predictions, we developed GAM models as expressed in Eq. (224) and investigated how  $T_s$  and  $T_h$  change with  $n_N$  and  $\Delta t$ . The deviance explained by the GAM models were 97.00% for  $T_{s,w}$  (Figure 44a), 97.00% for  $T_{s,b}$  (Figure 44b), 97.10% for  $T_{h,w}$  (Figure 44c), and 97.10% for  $T_{s,w}$  (Figure 44d). Assuming that the precise predictions thresholds are 35.10 °C for  $T_{s,w}$ , 35.10 °C for  $T_{s,b}$ , 34.40 °C for  $T_{h,w}$ , and 34.40 °C for  $T_{s,w}$ , the maximum  $n_N$  given  $\Delta t$  can be described by the following equation ( $R^2 = 0.9999$ ; Figure 45).

$$\max(n_N) = 67,805.6 - 116,513.4\Delta t + 48,878.9\Delta t^2 + N(0,33.18) \quad (224)$$

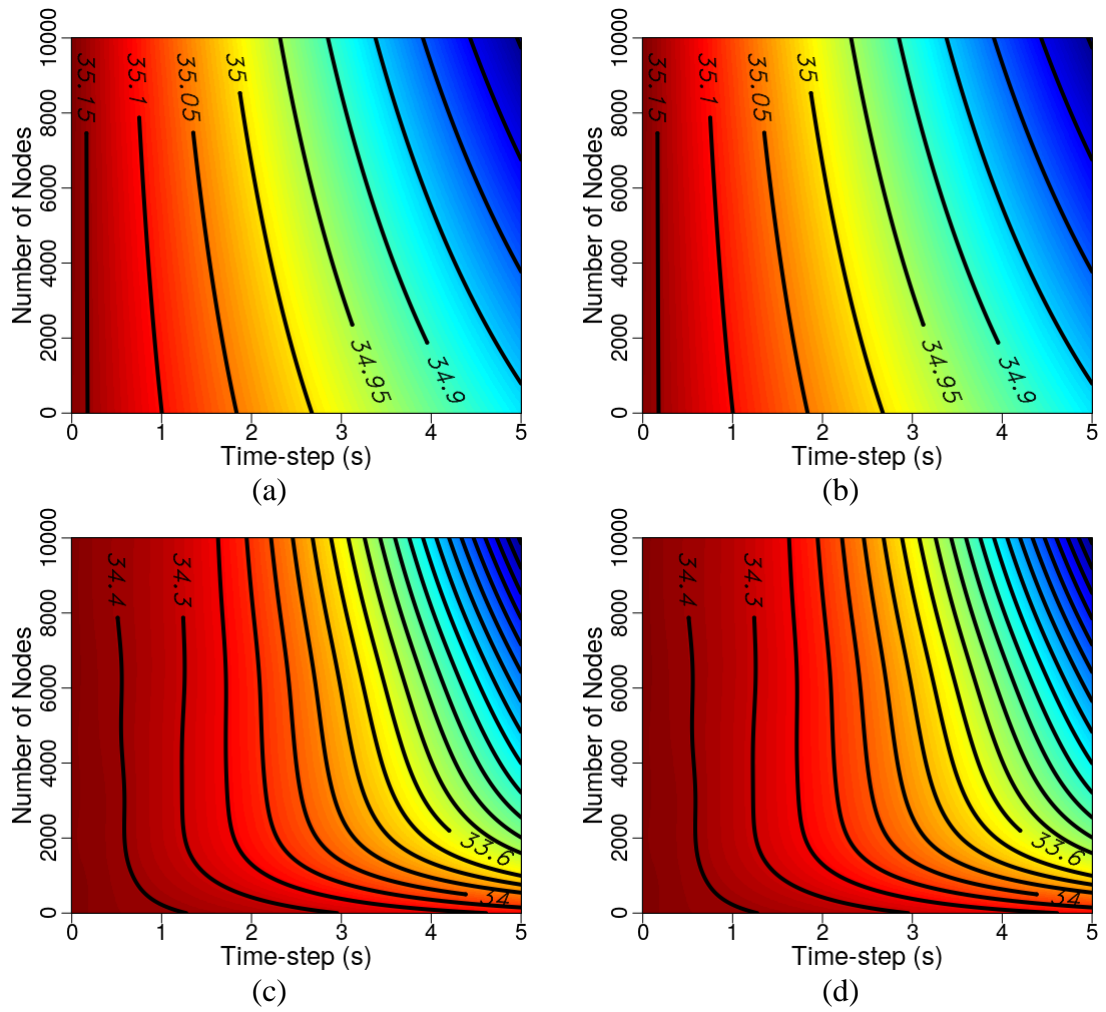


Figure 44. Skin surface temperature ( $T_s$ , a and b) and hair-coat surface temperature ( $T_h$ , c and d) for white ( $T_{s,w}$  in a and  $T_{h,w}$  in b) and black ( $T_{s,b}$  in c and  $T_{h,b}$  in d) hair-coat colors.

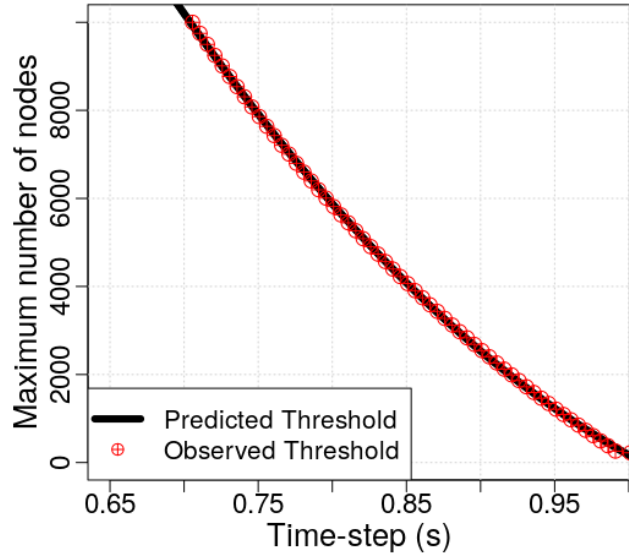


Figure 45. Observed and predicted (using Eq. (224)) maximum number of nodes, given time-step, that provides precise predictions.

## REFERENCES

- Bastin KR, Gebremedhin KG, Scott NR. A finite difference model to determine conduction heat loss to a water-filled mattress for dairy cows. *Trans ASABE* 46(3):773-780, 2003.
- Berman A. Tissue and external insulation estimates and their effects on prediction of energy requirements and of heat stress. *J Dairy Sci* 87:1400-1412, 2004.
- Berman A. Estimates of heat stress relief needs for Holstein dairy cows. *J Anim Sci* 83(6):1377-1384, 2005.
- Bernabucci U, Biffani S, Buggiotti L, Vitali A, Lacetera N, Nardone A. The effects of heat stress in Italian Holstein dairy cattle. *J Dairy Sci* 97:471-486, 2014.
- Bernabucci U, Lacetera N, Baumgard LH, Rhoads RP, Ronchi B, Nardone A. Metabolic and hormonal acclimation to heat stress in domesticated ruminants. *Animal* 4:1167-1183, 2010.
- Brody S. *Bioenergetics and Growth with Special Reference to the Energetic Efficiency Complex in Domestic Animals*. New York, NY: Reinhold Publishing Corporation, pp. 354-403, 1945.
- Chen JM, Schütz KE, Tucker CB. Cooling cows efficiently with sprinklers: physiological responses to water spray. *J Dairy Sci* 98:6925-6938, 2015.

CIGR. *Climatization of Animal Houses*. Aberdeen, Scotland: Scottish Farm Buildings Investigation Unit, 1984.

CIGR. *Handbook of Agricultural Engineering Volume II: Animal Production & Aquacultural Engineering*. St. Joseph, USA: American Society of Agricultural Engineers, 1999.

Collier RJ, Collier JL, Rhoads RP, Baumgard LH. Invited review: genes involved in the bovine heat stress response. *J Dairy Sci* 91:335-354, 2008

Collier RJ, Gebremedhin KG. Thermal biology of domestic animals. *Ann Rev Anim Biosci* 3:513-532, 2015.

da Silva RG, Maia ASC. Evaporative cooling and cutaneous surface temperature of Holstein cows in tropical conditions. *R Bras Zootec* 40(5):1143-1147, 2011.

da Silva RG, Maia ASC. *Principles of Animal Biometeorology*. New York, NY: Springer, 2013.

Rensis FD, Scaramuzzi RJ. Heat stress and seasonal effects on reproduction in the dairy cow—a review. *Theriogenology* 60:1139-1151, 2003.

Dong LF, Yan L, Ferris CP, McDowell DA. Comparison of maintenance energy requirement and energetic efficiency between lactating Holstein-Friesian and other groups of dairy cows. *J Dairy Sci* 98:1136-1144, 2015.

Drewry JL, Mondaca MR, Luck BD, Choi CY. A computational fluid dynamics model of biological heat and gas generation in a dairy holding area. *Trans ASABE* 61(2):449-460, 2018.

Elting EC. A formula for estimating surface area of dairy cattle. *J Agric Sci* 33(3):269-279, 1926.

Ferreira FC, Gennari RS, Dahl GE, De Vries A. Economic feasibility of cooling dry cows across the United States. *J Dairy Sci* 99:9931-9941, 2016.

Finch VA, Bennett IL, Holmes CR. Sweating response in cattle and its relation to rectal temperature, tolerance of sun and metabolic rate. *J Agri Sci* 99:479-487, 1982.

Finch VA. Comparison of non-evaporative heat transfer in different cattle breeds. *Aust J Agric Res* 36:497-508, 1985.

Gatenby RM. Exponential relation between sweat rate and skin temperature in hot climates. *J Agri Sci* 106:175-183, 1986.

Gaughan JB, Holt SM, Hahn GL, Mader TL, Eigenberg R. Respiration rate – is it a good measure of heat stress in cattle? *Asian-Aus J Anim Sci*, 13(C), 329-332, 2000.

Gebremedhin KG, Lee CN, Hillman PE, Collier RJ. Physiological responses of dairy cows during extended solar exposure. *Trans ASABE* 53(1):239-247, 2010.

Gebremedhin KG, Wu B. CFD development and simulation of flow fields in

ventilated spaces with multiple occupants. *Trans ASAE* 44(6):1839-1850, 2001.

Gebremedhin KG, Wu BX. Characterization of flow field in a ventilated space and simulation of heat exchange between cows and their environment. *J Therm Biol* 28:301-319, 2003.

Gebremedhin KG, Wu B. Simulation of flow field of a ventilated and occupied animal space with different inlet and outlet conditions. *J Therm Biol* 30:343-353, 2005.

Gebremedhin KG, Wu B. Modeling heat loss from the udder of a dairy cow. *J Therm Biol* 59:34-38, 2016.

Gelman A, Carlin JB, Stern HS, Dunson DB, Vehtari A, Rubin DB. *Bayesian Data Analysis*. New York, NY: CRC Press, 2013.

Gorczyca MT, Milan HFM, Maia ASC, Gebremedhin KG. Machine learning algorithms to predict core, skin, and hair-coat temperatures of piglets. *Comput Electron Agric* 151:286-294, 2018.

Heusner AA. Energy metabolism and body size: Is the 0.75 mass exponent of Kleiber's equation a statistical artifact? *Respir Physiol* 48:1-12, 1982.

Johnson HD, Ragsdale AC, Sikes JD, Kennedy JI, O'Bannon Jr. EB, Hartman D. *Research Bulletin 770: Surface Area Determinations of Beef and Dairy Calves During Growth at 50° and 80°F Environmental Temperatures*. In *Environmental Physiology and Shelter Engineering with Special Reference to Domestic Animals* (pp. 235

1-27), 1961.

Kadzere CT, Murphy MR, Silanikove N, Maltz E. Heat stress in lactating dairy cows: a review. *Livest Prod Sci* 77:59-91, 2002.

Kimmel E, Arkin H, Broday D, Berman A. A model of evaporative cooling in a wetted hide. *J Agric Eng Res* 49:227-241, 1991.

Lusk G. *The Elements of the Science of Nutrition* (4<sup>th</sup> ed.). New York, NY: Academic Press, 1928.

Maia ASC, Culhari EA, Fonsêca VFC, Milan HFM, Gebremedhin KG. Photovoltaic panels as shading resources for livestock. *In Preparation*, 2020.

Maia ASC, da Silva RG, Loureiro CMB. Respiratory heat loss of Holstein cows in a tropical environment. *Int J Biometeorol* 49(5):332-336, 2005a.

Maia ASC, da Silva RG, Loureiro CMB. Sensible and latent heat loss from the body surface of Holstein cows in a tropical environment. *Int J Biometeorol* 50(1):17-22, 2005b.

Maia ASC, da Silva RG, Loureiro CMB. Latent heat loss of Holstein cows in a tropical environment: a prediction model. *R Bras Zootec* 37(10):1837-1843, 2008.

McArthur AJ. Thermal resistance and sensible heat loss from animals. *J Therm Biol* 6:43-47, 1981.

McArthur AJ. Thermal interaction between animal and microclimate: a comprehensive model. *J Therm Biol* 126:203-238, 1987.

McGovern RE, Bruce JM. A model of the thermal balance for cattle in hot conditions. *J Agric Eng Res* 77(1):81-92, 2000.

Milan HFM. TLMBHT1D: One-dimensional TLM model. Algorithm *In Preparation*, 2020.

Milan HFM, Carvalho Jr. CAT, Maia ASC, Gebremedhin KG. Graded meshes in bio-thermal problems with transmission-line modeling method. *J Therm Biol* 45:43-53, 2014.

Milan HFM, Gebremedhin KG. Tetrahedral node for transmission-line modeling (TLM) applied to bio-heat transfer. *Comp Biol Med* 79:243-249, 2016a.

Milan HFM, Gebremedhin KG. Triangular node for transmission-line modeling (TLM) applied to bio-heat transfer. *J Therm Biol* 62(Pt B):116-122, 2016b.

Milan HFM, Gebremedhin KG. General node for transmission-line modeling (TLM) method applied to bio-heat transfer. *Int J Numer Model* 31(5):e2455, 2018

Milan HFM, Maia ASC, Costa CCM, Perano KM, Gorczyca MT, Moura GAB, Castro PA, Fonsêca VFC, Hariharan B, Chiquitelli Neto M, Gebremedhin KG. Precision livestock farming big data: PLFBD. *In Preparation*, 2020.

Milan HFM, Maia ASC, Gebremedhin KG. Prediction of optimum supplemental heat for piglets. *Trans ASABE* 62(2):321-342, 2019.

Mondaca M, Choi CY. An evaluation of simplifying assumptions in dairy cow computational fluid dynamics model. *Trans ASABE* 59(6):1575-1584, 2016.

Mondaca M, Rojano F, Choi CY, Gebremedhin KG. A conjugate heat and mass transfer model to evaluate the efficiency of conductive cooling for dairy cattle. *Trans ASABE* 56(6):1471-1482, 2013.

Oppenheim AV, Schaffer RW. *Discrete-Time Signal Processing* (3rd ed.). New York, NY: Pearson, 2009.

Ortiz XA, Smith JF, Rojano F, Choi CY, Bruer J, Steele T, Schuring N, Allen J, Collier RJ. Evaluation of conductive cooling of lactating dairy cows under controlled environmental conditions. *J Dairy Sci* 98:1759-1771, 2015.

Pedersen S, Sällvik K. *Heat and Moisture Production at Animal and House levels*. Horsens, Denmark: Research Centre Bygholm, 2002.

Pennes HH. Analysis of tissue and arterial blood temperatures in the resting human forearm. *J Appl Phys* 1(2):93-122, 1948.

Perano KM, Usack JG, Angenent LT, Gebremedhin KG. Production and physiological responses of heat-stressed lactating dairy cattle to conductive cooling. *J Dairy Sci* 98:5252-5261, 2015.

Polsky L, von Keyserlingk MAG. Invited review: effects of heat stress on dairy cattle welfare. *J Dairy Sci* 100:8645-8657, 2017.

R Core Team. *R: A Language and Environment for Statistical Computing*. Vienna, Austria: R Foundation for Statistical Computing, 2019.

Radoń J, Bieda W, Lendelová J, Pogran S. Computational model of heat exchange between dairy cow and bedding. *Comput Electron Agric* 107:29-37, 2014

RStudio Team (2018). *RStudio: Integrated Development Environment for R*. Boston, USA: RStudio, Inc.

Santos SGCG, Saraiva EP, Pimenta Filho EC, Gonzaga Neto S, Fonsêca VFC, Pinheiro AC, Almeida MEV, Amorim MLCM. The use of simple physiological and environmental measures to estimate the latent heat transfer in crossbred Holstein cows. *Int J Biometeorol* 61(2):217-225, 2017.

Schütz KE, Rogers AR, Poulouin YA, Cox NR, Tucker CB. The amount of shade influences the behavior and physiology of dairy cattle. *J Dairy Sci* 93:125-133, 2010.

Shen X, Zhang G, Wu W, Bjerg B. Model-based control of natural ventilation in dairy buildings. *Comput Electron Agri* 94:47-57, 2013.

Silanikove N. Effects of heat stress on the welfare of extensively managed domestic ruminants. *Livest Prod Sci* 67:1-18, 2000.

St-Pierre NR, Cobanov B, Schnitkey G. Economic losses from heat stress by US livestock industries. *J Dairy Sci* 86(E):E52-E77, 2003.

Stevens DG. A model of respiratory vapor loss in Holstein dairy cattle. *Trans ASAE* 24(1):151-153, 1981.

Strathe AB, Dijkstra J, France J, Lopez S, Yan T, Kebreab E. A Bayesian approach to analyze energy balance data from lactating dairy cows. *J Dairy Sci* 94:2520-2531, 2011.

Thompson VA, Fadel JG, Sainz RD. Meta-analysis to predict sweating and respiration rates for *Bos indicus*, *Bos Taurus*, and their crossbreds. *J Anim Sci* 89:3973-3982, 2011.

Turner LW, Blandford GE, Loewer OJ, Taul KL. Finite element model of heat transfer in the bovine. Part 1: theory. *Trans ASAE* 30(3):768-774, 1987a.

Turner LW, Loewer OJ, Taul KL, Munifering RB, Gay N. Finite element model of heat transfer in the bovine. Part 2: validation. *Trans ASAE* 30(3):775-781, 1987b.

Turner LW, Chastain JP, Hemken RW, Gates RS, Crist WL. Reducing heat stress in dairy cows through sprinklers and fan cooling. *Appl Eng Agric* 8(2):251-256, 1992.

Wagner W, Pruß A. The IAPWS formulation 1995 for the thermodynamic properties of ordinary water substance for general and scientific use. *J Phys Chem Ref Data* 31(2):387-535, 2002.

Werner J, Buse M. Temperature profiles with respect to inhomogeneity and geometry of the human body. *J Appl Phys* 65:1110-1118, 1988.

West JW. Effects of heat-stress on production in dairy cattle. *J Dairy Sci* 86:2131-2144, 2003.

Wolfenson D, Roth Z, Meidan R. Impaired reproduction in heat-stressed cattle: basic and applied aspects. *Anim Reprod Sci* 60-61:535-547, 2000.

Wood SN. Fast stable restricted maximum likelihood and marginal likelihood estimation of semiparametric generalized linear models: Estimation of Semiparametric Generalized Linear Models. *J Royal Stat Soc B* 73:3-36, 2011.

Wood SN. *Generalized Additive Models: An Introduction in R* (2<sup>nd</sup> ed.). Boca Raton, FL: CRC Press, 2017.

Worstell DM, Brody S. *Research Bulletin 20: Comparative Physiology Reactions of European and India Cattle to Changing Temperature*. In *Environmental Physiology and Shelter Engineering with Special Reference to Domestic Animals* (pp. 1-44), 1953.

Xue B, Yan T, Ferris CF, Mayne CS. Milk production and energy efficiency of Holstein and Jersey-Holstein crossbred dairy cows offered diets containing grass silage. *J Dairy Sci* 94:1455-1464, 2011.

Yan T, Gordon FJ, Agnew RE, Porter MG, Patterson DC. The metabolizable energy requirement for maintenance and the efficiency of utilisation of metabolizable energy  
241

for lactation by dairy cows offered grass silage-based diets. *Livest Prod Sci* 51:141-150, 1997.

CHAPTER 6: TECHNICAL NOTE: DEVICE FOR MEASURING RESPIRATION  
RATE OF CATTLE UNDER FIELD CONDITIONS

Hugo Fernando Maia Milan, Alex Sandro Campos Maia, Kifle G. Gebremedhin

Published in *Journal of Animal Science*: Milan HFM, Maia ASC, Gebremedhin KG.

Technical Note: Device for measuring respiration rate of cattle under field conditions.

*J Anim Sci* 94:5434-5438, 2016.

***Abstract***

Respiration rate (RR) is one of the physiological responses used to gage the level of heat stress in cattle. Respiration rate is usually measured by counting chest movement of the animal. This procedure has some disadvantages including that the person who is doing the counting must be trained to ensure accurate results, the animals must be preconditioned to the presence of the observer, and the presences of the observer may influence the behavior and activity of the animals or their position in the pen. In this study, a device that continuously records RR without restraining the animal was developed. The device is lightweight, cheap, easy to install, and more importantly, does not interfere with the activities of the animal. The device is mounted in a halter and is placed around the neck of the subject. The device measures air temperature near the nostrils of the animal and RR is calculated as the number of oscillations of the temperature. The RR measured by the device were compared against RR observed by counting the flank movement (for 60s, repeated every 10 min) of five Nellore cattle,

one animal per day, and the results show no statistical difference ( $p = 0.45$ ) between the two methods. This demonstrates that this device can be used to continuously measure RR of cattle under field conditions.

**Keywords:** Cattle, Continuous measurement, Measuring device, Respiration rate.

## ***1. INTRODUCTION***

Respiration rate (RR) is the first visible response of cattle to heat stress and oscillates with thermal environment. Researches have shown that RR is correlated to levels of solar radiation (Spain and Spiers, 1996; Maia et al., 2015), relative humidity (McLean, 1972; McLean and Calvert, 1972), heat stress level and welfare (Fraser and Broom, 2007), and can be used to indirectly quantify respiratory volume (Hanh et al., 1997; Gaughan et al., 2000; Eigenberg et al., 2002, 2005; Maia et al., 2005; da Silva and Maia, 2013). Therefore, continuous monitoring of RR could be used to accurately capture actual responses of cattle under field conditions.

Several approaches have been developed to continuously monitor RR. These include: wearing spirometry masks (Maia et al., 2014), use of belts around chest of animals (DeShazer, 2009), and use of surgical implant (cardiopulmonary transmitter for large animals, [www.datasci.com](http://www.datasci.com), 2016).

The measurement of RR using a spirometry mask requires training and restraining animals. This procedure interferes with the behavior of animals and does not represent actual field conditions. The problem with wearing a belt around the chest of the animal is that other animals may try to remove or chew it and any such behavior interferes with the reading of the signal or even sensor damage. In surgical implants, the signal is transmitted by telemetry and thus the area where the animal is kept need to be restricted. In addition, the effect of the implant on the behavior of animals is not well

known. We came across one reference (Eigenberg et al., 2000, who cited personal communication with Hahn, 1998) that suggested the possibility of monitoring RR by using temperature sensors positioned near the nostrils of animals.

The objective of this study was to develop and assemble a device for measuring RR of cattle in their natural habitat by monitoring changes in temperature near the nostrils.

## ***2. MATERIALS AND METHODS***

Animal use and handling was approved by the committee for animal care and use from FCAV/UNESP under the number 8410/15. The experimental study was conducted at the São Paulo State University, Campus of Jaboticabal, Brazil (latitude 21°25'S) during the month of July of 2016, from 0800 h to 1700 h. Five male Nelore cattle (age 26 months, weight ~500 kg) were used in this study. Animals did not receive any specific training besides wearing the system (Figure 46) two days prior to the experiment. The animals were each provided with 30 m<sup>2</sup> stall with a shade area of 10 m<sup>2</sup>. They were fed 60:40 sorghum silage: concentrate at 0900 h and 1500 h.

Respiration rates were measured between 0800h and 1700h for each animal by counting flank movement for 60 seconds every 10 minutes (54 samples). The experimental period was one day for each animal. At the same time, respiration rates were measured using the device. Air temperature near the nostrils of the animals was measured using temperature sensors (PT100, PPG101A1, accuracy  $\pm 0.15^{\circ}\text{C}$ , U.S. Sensor, [www.ussensor.com](http://www.ussensor.com)). The temperature sensor was protected by a metallic case

and the sensor was shaped in a “J” form to add stiffness and avoid movement of the sensor when the animal moves its head. The diameter of the tip of the metallic case was large enough to avoid introduction of noise from contact of the sensor against the nostril tissue.

The electronic device, which was mounted on top of the halter and protected by the metallic case, was programmed to record air temperature at a rate of 100 Hz (greater than the theoretical minimum of 2 Hz for maximum of 60 RPM, accordingly to Nyquist theorem). Within the electronic device, the temperature signal was filtered (low pass filter, 1 kHz), amplified (611x), converted to digital data, and stored in a thumb drive for post-processing using a computer software (MaiaRR, Maia and Milan, 2016). The flowchart of these steps is shown in Figure 47. In the software, spectrum components of the temperature signal below 0.17 Hz and above 1.67 Hz were removed using the Fast Fourier Transform (FFT) algorithm. Then, RR was automatically calculated by counting the number of oscillations of the signal. These procedures are necessary to accurately measure the smallest temperature variation inside the nostrils. Different variants of sensor, filter, amplification, algorithms were tested and yielded similar results.

Environmental parameters (air temperature, relative humidity and black globe temperature) were recorded every 3 minutes using HOBO data logger (Onset Computer Corp., Bourne, MA). Black globe temperature was measured using a thermocouple (Type K) inserted into the center of a hollow 0.15-m diameter copper

sphere painted black placed one meter above the ground, (da Silva and Maia, 2013). Short-wave solar radiation (sum of diffused and direct) on a horizontal surface in the 200 to 3600 nm spectral range was measured using a portable pyranometer every 10 minutes (Model CMP-22, Kipp and Zonen, Delft, Netherlands).

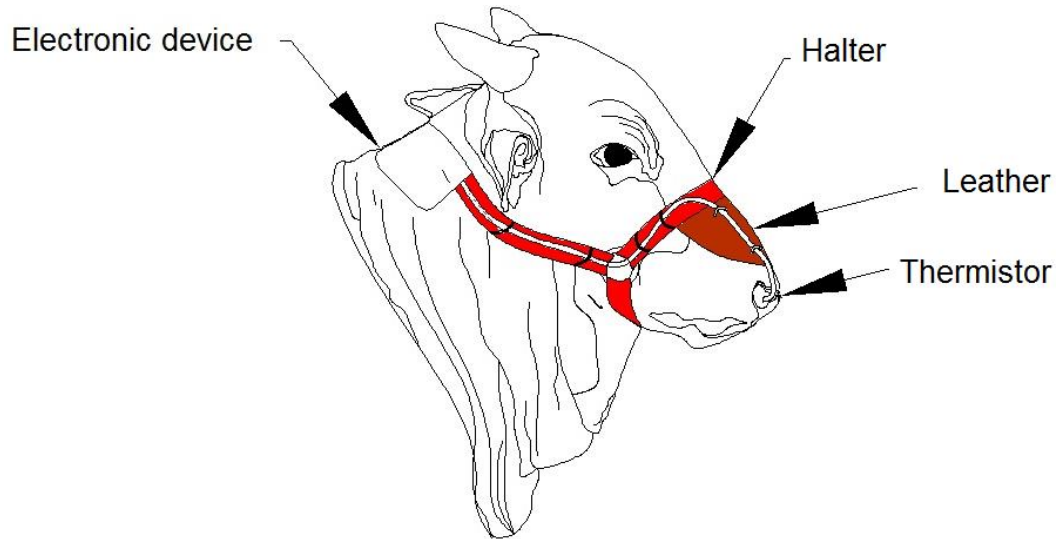


Figure 46. Schematic of the halter. Electronic device and temperature sensor are contained in the halter.

The data obtained from the two methods were analyzed to test for statistical difference using a multiple linear regression model (PROC GLM, SAS Institute, Version 8), according to Littell et al. (2006). In addition, RR measured by counting chest movements was linearly regressed against RR measured using the device in R (R Core Team, 2016).

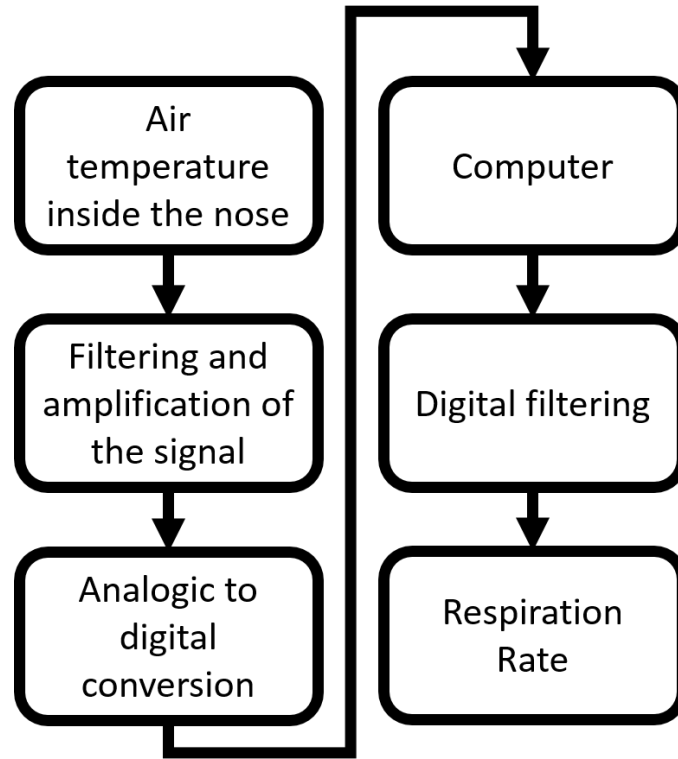


Figure 47. Flowchart of the device. The respiration rate is calculated from the number of oscillations of the temperature signal (shown in the inset of Figure 48). Patent of the device is pending.

### 3. RESULTS AND DISCUSSION

The multiple linear regression model is expressed as

$$Y_{ijk} = a + M_i + (MA)_{ij} + H_k + (MH)_{ik} + b_1 T_A + b_2 H_R + b_3 R_S + e_{ijk}$$

where,  $Y_{ijk}$  represents RR observed in the hour class  $k$ , in animal  $j$ , and by method  $i$ ;  $a$  is the intercept;  $M$  is the fixed effect of the  $i^{th}$  method (device or counting);  $MA$  is the interaction of the  $i^{th}$  method with  $j^{th}$  animal;  $H$  is the fixed effect of the  $k^{th}$  hour class;

$MH$  is the interaction between the  $i^{th}$  method within the  $k^{th}$  hour class;  $b_1$ ,  $b_2$  and  $b_3$  are linear regression coefficients for air temperature, relative humidity and solar radiation, respectively;  $e_{ijk}$  is the residual term.

Figure 48 shows the results of the air temperature measured near the nostrils of one experimental animal. The insert in Figure 48 is a zoomed-in image of air temperature inside the nostrils and shows that the temperature oscillates and the number of oscillations is equivalent to or is a measure of respiration rate. Figure 49 and Figure 50 are comparisons of RR between both methods of measurements for Animal 1, and mean values of measurements of the 5 animals, respectively. From these two figures, we observe that: (1) the mean respiration rates are lower than 30 breaths/min, which means that the animals were not thermally stressed, (2) the mean values of the measurements by both methods are very similar. The main difference is that the standard error associated with the flank counting was, as expected, higher than that measured by the device. A regression plot (Figure 51) of RR measured by counting chest movement against RR measured by the electronic device shows a strong correlation ( $R^2 = 0.95$ ). Table 33 shows the mean values of RR measured by the two methods. The results show that the means are pretty much in agreement (within 2 respirations per minute for 80% of the times). It can be concluded, therefore, that the values measured using the device are accurate and consistent. Figure 52 shows the environmental conditions (air temperature, relative humidity and solar radiation) that the animals were exposed to during the experiment.

Table 33. Comparison between respiration rates measured using the device and counting the flank movement of the animals.

| Animal | Method   | n    | Mean $\pm$ SEM,<br>breathes min <sup>-1</sup> |
|--------|----------|------|---|
| 1      | Device   | 540  | 22 $\pm$ 0.15                                 |
|        | Counting | 48   | 24 $\pm$ 0.56                                 |
| 2      | Device   | 348  | 18 $\pm$ 0.13                                 |
|        | Counting | 49   | 19 $\pm$ 0.52                                 |
| 3      | Device   | 540  | 24 $\pm$ 0.16                                 |
|        | Counting | 39   | 28 $\pm$ 1.24                                 |
| 4      | Device   | 463  | 17 $\pm$ 0.16                                 |
|        | Counting | 54   | 19 $\pm$ 0.50                                 |
| 5      | Device   | 540  | 17 $\pm$ 0.14                                 |
|        | Counting | 54   | 16 $\pm$ 0.30                                 |
| Mean   | Device   | 2431 | 20 $\pm$ 0.09                                 |
|        | Counting | 244  | 20 $\pm$ 0.33                                 |

The results show no statistical difference ( $p > 0.45$ ) for method of measurement nor for the interaction between method and time of measurement (hour) ( $p = 0.88$ ). At  $p = 0.05$  significance level, time of measurement showed isolated statistical significance on RR ( $p = 0.045$ ). The statistical analysis confirms that RR measurements taken by the device and by counting the flank movement are similar.

The use of the device requires no observer and provides continuous and accurate measurement. Furthermore, the halter can easily be installed/removed from the animal.

From the perspective of the animals wearing the device, we saw no discomfort. In fact, the animals were feeding and drinking water freely. Considering the robustness and accuracy of the device, and given that the activities/behavior of the animals are not altered in any way, we can confidently conclude the applicability of measuring respiration rate by measuring the temperature oscillations near the nostril of cattle.

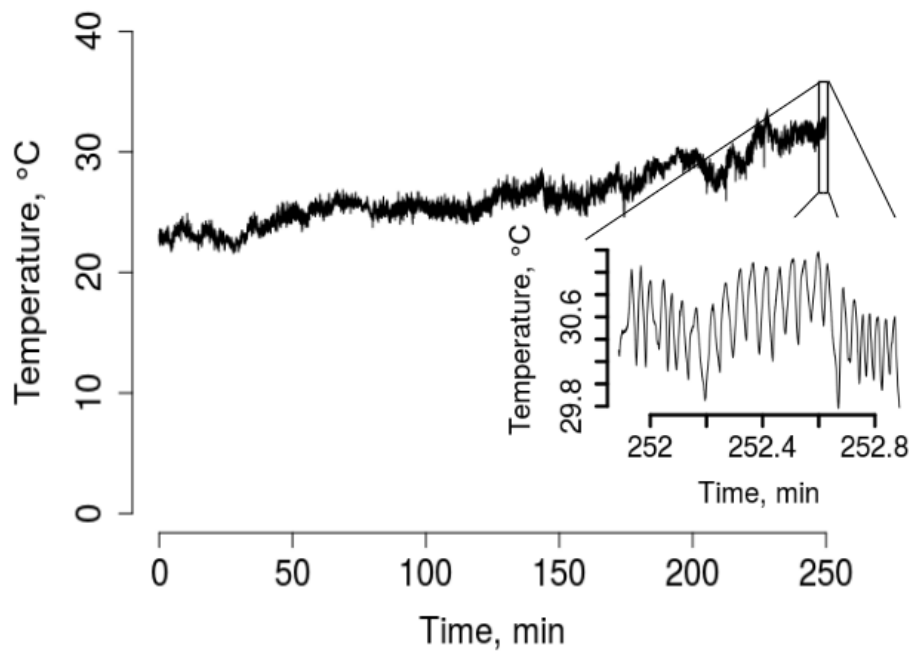


Figure 48. Air temperature measurement near the nostrils of the animal. The inset is a zoomed-in image of the temperature reading of one-minute segment.

#### **4. CONCLUSIONS**

The following conclusions could be drawn from this study:

1. A device that provides continuous and accurate measurement of respiration

rates (RR) of cattle under field conditions was developed and assembled. The device is lightweight, easy to install, cheap and is protected from potential damage.

2. The respiration rate measured using the device were validated against RR data measured by counting the flank movement of animals, and the results were not statistically different ( $p = 0.45$ ).

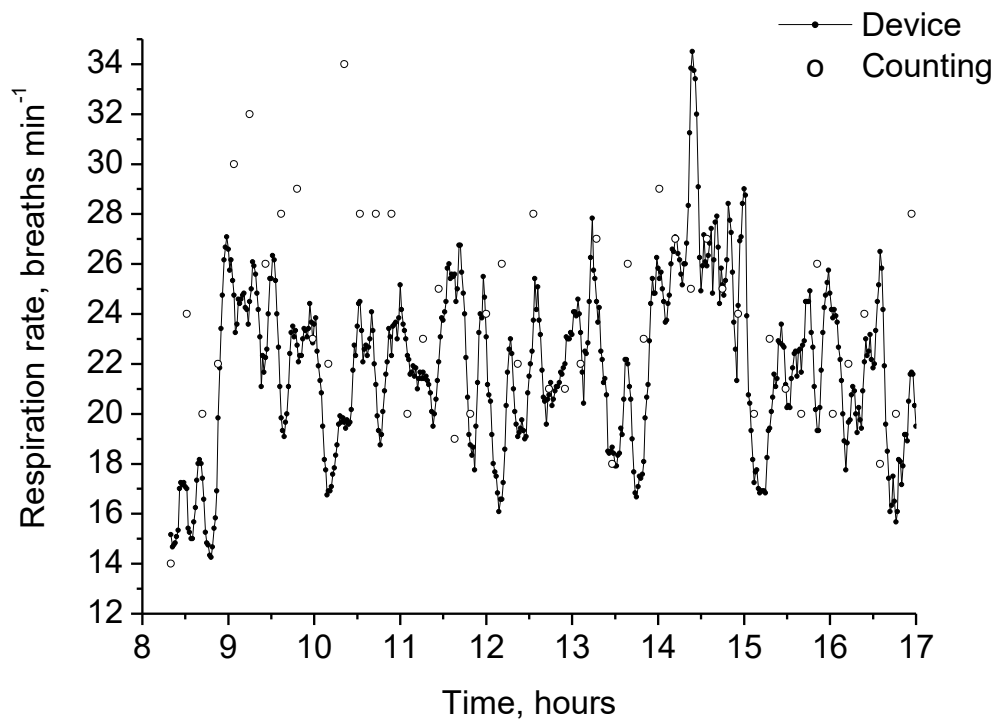


Figure 49. Respiration rate measured using the device and by counting the flank movements of Animal 1.

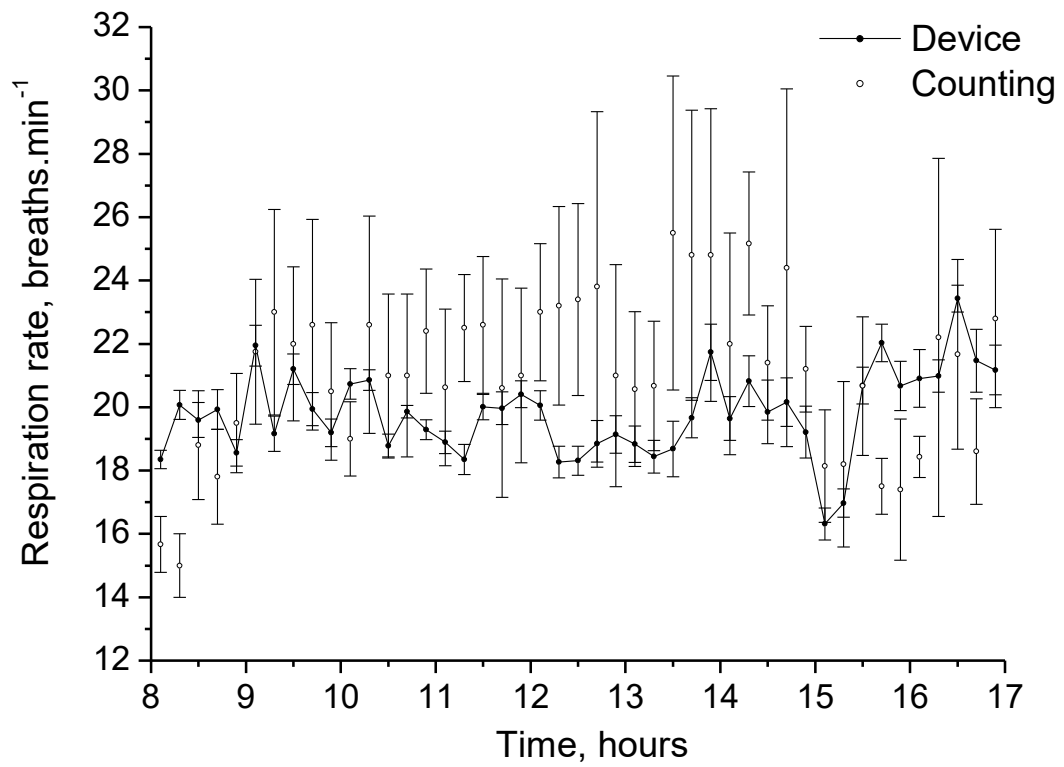


Figure 50. Respiration rate measured using the device and by counting the flank movements of the animals (mean  $\pm$  SEM).

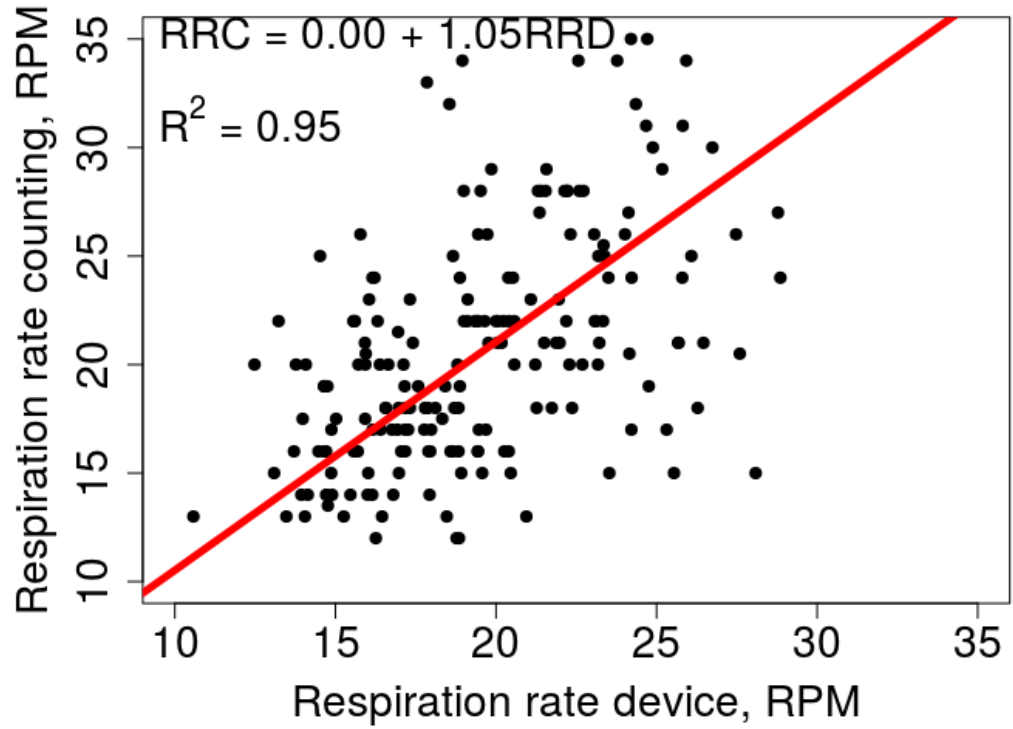


Figure 51. Linear regression of respiration rate measured by counting flank movement (RRC) against respiration rate measured by the device (RRD) in respirations per minute (RPM).

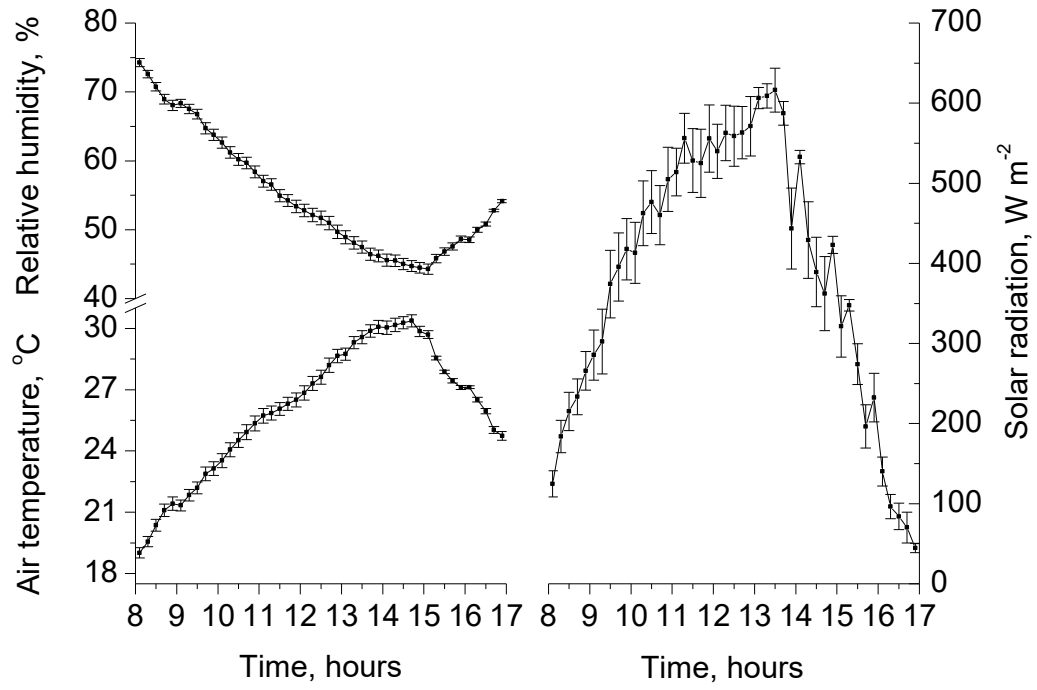


Figure 52. Measured environmental variables (mean  $\pm$  SEM).

## REFERENCES

- DeShazer JA. *Livestock Energetics and Thermal Environmental Management*. ASABE: St. Joseph, MI, 2009.
- Eigenberg RA, Brown-Brandl TM, Nienaber JA. Development of a respiration rate monitor for swine. *Trans ASAE* 45(5):1599-1603, 2002.
- Eigenberg RA, Hahn GL, Nienaber JA, Brown-Brandl TM, Spiers DE. Development of a new respiration rate monitor for cattle. *Trans ASAE* 43(3):723-728, 2000.
- Eigenberg RA, Brown-Brandl TM, Nienaber JA, Hahn GL. Dynamics response indicators of heat stress in shaded and non-shaded feedlot cattle. Part 2: Predictive relationships. *Biosystems Eng* 91(1):111-118, 2005.
- Fraser AF, Broom DM. *Domestic animal behavior and welfare (4th ed)*. CABI: Cambridge, MA, 2007.
- Gaughan JBS, Holt SM, Hahn GL, Mader TL, Eigenberg RA. Respiration rate: Is it a good measure of heat stress in cattle? *Asian-Aus J Anim Sci* 13(C):329-332, 2000.
- Hanh GL, Parkhurst AM, Gaughan JB. *Cattle respiration rate as a function of ambient temperature*. ASABE Conference, St Joseph, MI, Paper N. MC97-121, 1997.
- Littell RC, Milliken GA, Stroup WW, Wolfinger RD, Schabenberger O. *SAS for Mixed Models (2nd ed)*. SAS Institute Inc: Cary, NC, 2006

Maia ASC, da Silva RG, Loureiro CMB. Respiratory heat loss of Holstein cows in a tropical environment. *Int J Biometeorol* 49(5): 332-336, 2005.

Maia ASC, Gebremedhin KG, Nascimento ST, Carvalho MD, Simão BR, Camerero LZ, Chiquitelli Neto M. *Development of facial masks for indirect calorimetric studies for livestock*. CSBE/ASABE Joint Meeting Presentation, pp. 1-4, 2014.

Maia ASC, da Silva RG, Nascimento ST, Nascimento CCN, Pedroza HP, Domingos HGT. Thermoregulatory responses of goats in hot environments. *Int J Biometeorol* 59:1025–1033, 2015.

Maia ASC, Milan HFM. RR *Respiratory Rate – Frequência respiratória de animais de grande porte em condições de campo*. Registered in Brazil, BR 51 2016 000418-5, 2016.

McLean JA. On the calculation of heat production from open-circuit calorimetric measurements. *Br J Nutr* 27:597-600, 1972.

McLean JA, Calvert DJ. Influence of air humidity on the partition of heat exchanges of cattle. *J Agric Sci* 78:303-307, 1972.

da Silva RG, Maia ASC. *Principles of animal biometeorology*. Springer: New York, NY, 2013.

R Core Team. *R: A language and environment for statistical computing*. R Foundation for Statistical Computing: Vienna, Austria, 2016.

Spain JN, Spiers DE. Effects of supplemental shade on thermoregulatory response of calves to heat challenge in a hutch environment. *J Dairy Sci* 79:639-646, 1996.

## CHAPTER 7: MACHINE LEARNING ALGORITHMS TO PREDICT CORE, SKIN, AND HAIR-COAT TEMPERATURES OF PIGLETS

Michael T. Gorczyca, Hugo F. M. Milan, Alex S. C. Maia, Kifle G. Gebremedhin

Published in *Computers and Electronics in Agriculture*: Gorczyca MT, Milan HFM, Maia ASC, Gebremedhin KG. Machine learning algorithms to predict core, skin, and hair-coat temperatures of piglets. *Comput Electron Agric* 151:286-294, 2018.

### ***Abstract***

Internal-body (core) and surface temperatures of livestock are important information that indicate heat stress status and comfort of animals. Previous studies focused on developing mechanistic and empirical models to predict these temperatures. Mechanistic models based on bioenergetics of animals often require parameters that may be difficult to obtain (e.g., thickness of internal tissues). Empirical models, on the other hand, are data-based and often assume linear relationships between predictor (e.g., air temperature) and response (e.g., internal-body temperature) variables although, from the theory of bioenergetics, the relationship between the predictor and the response variables is non-linear. One alternative to consider non-linearity is to use machine learning algorithms to predict physiological temperatures. Unlike mechanistic models, machine learning algorithms do not depend on biophysical parameters, and, unlike linear empirical models, machine learning algorithms automatically select the predictor variables and find non-linear functions between predictor and response

variables. In this paper, we tested four different machine learning algorithms to predict rectal ( $T_r$ ), skin-surface ( $T_s$ ), and hair-coat surface ( $T_h$ ) temperatures of piglets based on environmental data. From the four algorithms considered, *deep neural networks* provided the best prediction for  $T_r$  with an error of 0.36%, *gradient boosted machines* provided the best prediction for  $T_s$  with an error of 0.62%, and *random forests* provided the best predictions for  $T_h$  with an error of 1.35%. These three algorithms were robust for a wide range of inputs. The fourth algorithm, *generalized linear regression*, predicted at higher errors and was not robust for a wide range of inputs. This study supports the use of machine learning algorithms (specifically deep neural networks, gradient boosted machines, and random forests) to predict physiological temperature responses of piglets.

**Keywords:** Bioenergetics; machine learning; piglets; precision livestock farming; temperature.

### ***Highlights***

- Prediction of temperatures of livestock using machine learning.
- Environmental data were the predictors.
- Random forest, gradient boosting machine, and deep neural networks performed well.
- Generalized linear regression underperformed on generalization and robustness tests.

## ***1. INTRODUCTION***

One of the current challenges in agriculture is to increase food production to feed the world's growing population while considering environmental responsibilities and the comfort of the biological object (livestock; Hunter et al., 2017). In animal production, the challenge is in developing precision livestock farming techniques (Van Hertem et al., 2017; Wathes et al., 2008) to increase animal comfort and production. These techniques (Guarino et al., 2017) are focused on continuous monitoring of animal health, comfort, and production indicators, such as internal-body and skin-surface temperature. These temperatures indicate the health status and production levels of animals (Da Silva and Maia, 2013; Soerensen and Pedersen, 2015), as well as their heat stress level, estimated to cost the swine industry \$300 million each year (St-Pierre et al., 2003).

Heat stress is a major issue that decreases animal welfare (Silanikove, 2000), production (Nienaber et al., 1999), reproduction (Wolfenson et al., 2000), and growth potential (Collin et al., 2001). To cope with heat stress, pigs rely on behavioral (Vasdal et al., 2009) and physiological (Brown-Brandl et al., 2001, 2014; Robertshaw, 2006) responses. Because of the importance of monitoring heat stress of pigs (Shao and Xin, 2008), and the difficulty of measuring the necessary parameters that indicate heat stress (McCafferty et al., 2015), two classical approaches are used to estimate heat stress of animals: (1) mechanistic modelling, and (2) empirical modelling.

Mechanistic models are based on the biophysical understanding of conservation of energy, momentum, and mass in live animals (Collier and Gebremedhin, 2015; DeShazer, 2009). Using conservation equations, a governing equation for the problem is formulated and solved analytically or numerically. The limitations of analytical and numerical models are the assumption that internal and/or superficial temperatures are known, or a simple mathematical relationship exists between them, and/or some of the parameters are also difficult to obtain (e.g., thickness of internal tissues, etc.). Furthermore, mechanistic models reveal that the relationship between environmental and physiological responses are non-linear (Hensley et al., 2013; Milan and Gebremedhin, 2016ab; McArthur, 1981).

Empirical models are data-based and usually assume a linear relationship between predictor variables (e.g., air temperature) and the response variable (e.g., internal-body temperature). These relationships are chosen by the researcher and has a considerable impact on the accuracy of the model (Mostaço et al., 2015; Pathak et al., 2009; Ramirez, 2017; Soerensen and Pedersen, 2015).

A third approach that is receiving increased attention from swine researchers are machine learning and computer vision algorithms (Kamilaris and Prenafeta-Boldú, 2018). Recent applications include monitoring animal behavior (Cross et al., 2018; Lao et al., 2016; Nasirahmadi et al., 2017; Shao and Xin, 2008), and weight (Kashiha et al., 2014; Shi et al., 2016; Wongsriworaphon et al., 2015). In this paper, we propose the use of machine learning algorithms to predict internal-body temperature, skin-

surface temperature, and hair-coat surface temperature of piglets from environmental variables. The advantage of this approach compared to mechanistic models is that it does not rely on biophysical parameters. The advantage of this approach compared to empirical models is that it automatically finds a non-linear function from the data, removing the subjectivity from the researcher choosing the relationship between predictor and response variables. To the best of our knowledge, this is the first study that applies machine learning algorithms to predict physiological temperatures of livestock.

## ***2. MATERIALS AND METHODS***

### **2.1. Experimental Measurements**

Animal use and research protocol were approved by the Animal Care and Use Committee from São Paulo State University (FAPESP Proc. 17.519/14). The experiment was conducted in Jaboticabal, São Paulo, Brazil (21°15'40" South Latitude and 595 m elevation) for five consecutive days. Ten 5-days-old piglets (weight =  $3.76 \pm 0.41$  kg, mean  $\pm$  SEM) from the commercial lineage "Large White" were randomly selected from the same farrowing. The farrowing was not provided with supplemental heat. The selected piglets were randomly separated into 5 groups (2 piglets in each group) and managed inside a brooder (1.0 x 1.0 x 1.0 m<sup>3</sup>) from 3 a.m. to 8 a.m. Physiological measurements were performed hourly and started one hour after the piglets were inside the brooder (i.e., from 4 a.m. to 8 a.m.) to allow for

adaptation to the environment. Four of the five groups were provided with supplemental heat (lamps) with intensities of 60 W, 100 W, 160 W, or 200 W. The fifth group (control) was not provided with supplemental heat.

Skin-surface temperature ( $T_s$ , °C) at the upper leg of the animal was measured with a skin-temperature probe (MLT422/AL, ADInstruments, accuracy  $\pm 0.2^\circ\text{C}$ ) and rectal temperature ( $T_r$ , °C) was measured with a rectal temperature probe (MLT1403, ADInstruments, accuracy  $\pm 0.2^\circ\text{C}$ ). These probes were connected to thermistor pods (ML309, ADInstruments), and the pods were connected to a data acquisition system (PL3516/P, PowerLab 16/35 and LabChart Pro, ADInstruments) that recorded data every second for approximately 5 minutes. Hair-coat-surface temperature ( $T_h$ , °C) at the upper leg was measured with an infrared thermometer (Model 568, Fluke, accuracy  $\pm 1^\circ\text{C}$ ). Air temperature ( $T_a$ , °C) and relative humidity (RH, %) inside the brooder were measured every minute (HOBO U12 Temp/RH, Onset, accuracy  $\pm 0.35^\circ\text{C}$  and  $\pm 2.5\%$ ). Black globe temperature ( $T_g$ , °C) inside the brooder was measured using a 15-cm dia. black globe installed 10 cm above the ground (thermocouple TMC20-HD, datalogger U12-013, accuracy  $\pm 0.35^\circ\text{C}$ , Onset).

## **2.2. Model Development**

### *2.2.1. Data Processing*

The experiment was designed to provide 200 data points. Each individual data point contained the time of measurement (in hours), intensity of the supplemental heat,  $T_a$ ,

RH,  $T_g$ ,  $T_r$ ,  $T_s$ , and  $T_h$ . Time of measurement, intensity of supplemental heat,  $T_a$ , and  $T_g$  were used as predictors of  $T_r$ ,  $T_s$ , and  $T_h$ . RH was not used as a predictor variable because 22% of the data was lost due to sensor failure. Further technical problems led to a reduction in the number of collected datapoints from 200 to 173. Correlations of the variables, mean and standard error of the mean were calculated. The univariate number of the outliers in the dataset was calculated using the z-score method at 2.5 standard deviations above or below the mean (Cousineau and Chartier, 2010).

The dataset was divided into training and testing datasets (Hastie et al., 2003). The training dataset was used to develop the machine learning models and the testing dataset was used to evaluate the predictive performance of the models. The training dataset consisted of 130 data points (75% of the dataset) and the testing dataset consisted of 43 points (25% of the dataset). The testing dataset was first obtained using stratified random sampling for each combination of time of measurement/intensity of supplemental heat (strata). This approach ensured that the testing dataset contained at least two data points from each stratum. Mean values were calculated for each strata of the dataset (yielding 20 data points) to determine the mean percentage error of each model for every stratum.

### *2.2.2. Overview of Machine Learning models*

The machine learning algorithms used in this study were generalized linear regression model with elastic net regularization (GLM; Zou and Hastie, 2005), random forests (RF; Breiman, 2001), gradient boosted machines (GBM; Natekin and Knoll, 2013),

and deep neural networks (feedforward neural networks) with the ReLU activation function (DNN; Goodfellow et al., 2016). Each algorithm has hyperparameters that influence the model learned from the data.

GLM is ordinary linear regression with penalty terms in the  $L_1$  (sum of magnitudes) and  $L_2$  (sum of squares) norms of the linear regression coefficients. The penalties shrink irrelevant regression coefficients and limit the impact of collinearity between the predictor variables (Zou and Hastie, 2005). The objective function of the GLM model is described as

$$\min_{\beta, \beta_0} \frac{1}{2N} \sum_{i=1}^N (x_i^T \beta + \beta_0 - y_i)^2 + \lambda \left[ \alpha \|\beta\|_1 + \frac{1}{2} (1 - \alpha) \|\beta\|_2^2 \right]$$

where,  $\beta, \beta_0$  are regression coefficients, the summation represents the squared residual errors,  $x_i$  is the predictor variable from the  $i^{th}$  row of data,  $y_i$  is the predicted variable from the  $i^{th}$  row of data,  $\lambda$  is the severity of penalty applied, and  $\alpha$  distributes the penalty between  $L_1$  ( $\|\beta\|_1$ ) and squared  $L_2$  ( $\|\beta\|_2^2$ ) norms of the regression coefficients. The hyperparameters are  $\lambda$  and  $\alpha$ .

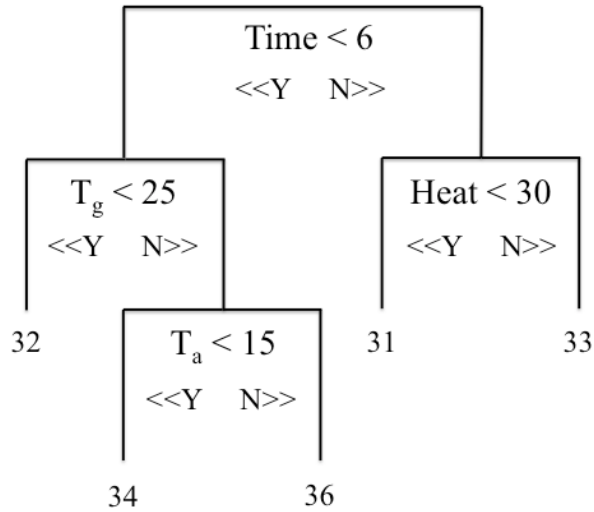


Figure 53. Example of a decision tree for predicting hair-coat surface temperature. A decision tree is developed by segmenting the input space into structured outputs. Each decision (e.g., Time < 6) represents a split of the tree. A leaf is the end node of the tree (e.g., the node with the value of 31 for Time  $\geq 6$  and Heat < 30). Random forests are based on creating several decision trees and averaging their output. Gradient boosted machines are based on creating several sequential decision trees, where new trees focus on improving the prediction accuracy of previous trees, and linearly combining the predictions of these trees. Time: time of measurement (hours); Heat: intensity of supplemental heat (W);  $T_a$ : air temperature ( $^{\circ}\text{C}$ );  $T_g$ : black globe temperature ( $^{\circ}\text{C}$ ).

The RF and GBM models rely on decision trees, which are simple predictive models that stratify the input data space into output areas. The output-area prediction of decision trees is the mean of the response variables from the training dataset that fall in that output area (Figure 53). For RF, several decision trees are developed

independently from different subsets of the training dataset as well as from the different predictor variables. The prediction of the RF is the average of the predictions from all decision trees. The hyperparameters for RF are number of decision trees, minimum number of observations in a leaf, number of variables used to develop each split in a decision tree, and the maximum depth of the decision trees. For the GBM model, decision trees are developed sequentially, where each new decision tree is designed to improve on the predictive performance of the previous decision trees. The hyperparameters of the GBM are nearly the same as the hyperparameters for the RF, except GBM uses all predictor variables in a dataset for each split. GBM also has the learning rate of the sequential trees and an annealing rate (the influence of sequential trees on the final prediction output) as hyperparameters.

DNN algorithms provide flexible and robust approaches to develop nonlinear machine learning models. Feedforward neural networks, the type of DNN used in this study, consist of an input layer, hidden layers of unobserved variables, and an output layer (Figure 54). Given an input vector  $x$ , the output of hidden layer  $h$  is computed as follows:

$$h = f(\theta + Wx)$$

where,  $\theta$  is a vector of offsets,  $W$  is a matrix of weights, and  $f$  is a user selected activation (non-linear) function (ReLU was used in this study). The output from  $f$  (i.e.,  $h$ ) is an input for the next layer. This process is repeated until the output layer is reached. The variable calculated for the output layer, the prediction of the feedforward

neural network, is calculated similarly as  $h$  but with a different activation function. In this study, the activation function for the output layer was the identity function, which is equivalent to linear regression with the variables of the last hidden layer. The hyperparameters for the DNN model are the number of hidden layers, number of neurons in each hidden layer, mini-batch size (the number of observations used in each iteration in the model optimization process), epochs (the number of times the whole training dataset is used in training), dropout percentage (the percentage of weights not updated during a mini-batch iteration to avoid overfitting; Srivastava et al., 2014), and  $\rho$  and  $\varepsilon$  (hyperparameters of the ADADELTA optimization framework; Zeiler, 2012).

### *2.2.3. Training and Testing Machine Learning Models*

The objective of this paper was to develop machine learning models to predict  $T_r$ ,  $T_s$ , and  $T_h$  using  $T_a$ ,  $T_g$ , time of measurement, and intensity of supplemental heat as predictors. The machine learning models were trained in R (R Core Team, 2017) using the H2O package (The H2O.ai Team, 2017) with modular 5-fold cross-validation (Hastie et al., 2003). To develop the machine learning models, a random search for hyperparameter optimization (Bergstra and Bengio, 2012) was performed on the hyperparameter space described in Table 34. For GLM, RF, and GBM, 1000 random searches were performed (resulting in 1000 trained models for each of these algorithms). For DNN, because of its inherently larger hyperparameter space, 2000 random searches were performed (resulting in 2000 trained deep neural network

models). Computations were performed on an Oryx Pro from System76, with Pop-OS 17.10, 512 GB PCIe M.2 SSD, 64 GB DDR4 RAM memory (2133 MHz), i7-6820HK (3.6 GHz), 8 GB GeForce GTX 980M.

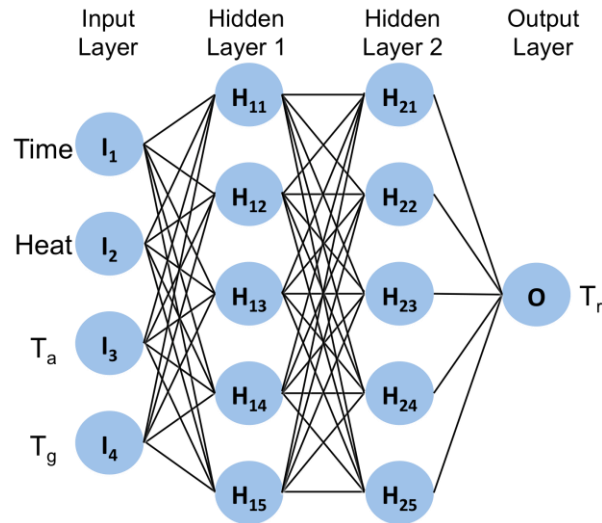


Figure 54. Feedforward neural network. Each input variable represents one neuron ( $I_n$ ) that connects to every hidden neuron in the first hidden layer ( $H_{1m}$ ). Each hidden neuron is a non-linear function (activation function), where the outputs of the hidden neurons in the previous hidden layer are inputs to the hidden neurons in the next hidden layer. The outputs of the last hidden layer are inputs to the output neuron ( $O$ ), which provides the prediction of the neural network. Time: time of measurement (hours); Heat: intensity of supplemental heat (W);  $T_a$ : air temperature ( $^{\circ}\text{C}$ );  $T_g$ : black globe temperature ( $^{\circ}\text{C}$ );  $I_n$ : input neuron  $n$ ;  $H_{nm}$ : hidden neuron  $m$  of hidden layer  $n$ ;  $O$ : output neuron;  $T_r$ : rectal temperature ( $^{\circ}\text{C}$ ).

The mean squared error (MSE) was used as the evaluation metric (Hastie et al., 2003).

We used cross-validation MSE to select the best performing model from each algorithm. Of these best performing models, the overall best model was the one that minimized MSE on the testing dataset.

Robustness and generalization of the best models were tested using partial dependence plots (Friedman, 2001) for 5 artificial datasets. Each dataset was designed to test how the models would perform under different conditions. Four artificial datasets had  $T_a = [-20, 100]$  °C,  $T_g = [-20, 100]$  °C, time of measurement = [0, 24] h, or intensity of supplemental heat = [0, 1000] W, while keeping the remaining predictor variables at their mean values. The fifth artificial dataset consisted of 10,000 random combinations of these artificial values to further test how change in the predictor variables would affect the prediction from the machine learning models.

### ***3. RESULTS AND DISCUSSION***

#### **3.1. Environmental data**

Figure 55 shows the measured environmental data from the dataset stratified for the different time of measurement and intensity of supplemental heat while Table 35 shows the coefficients of correlation, mean, standard error of the mean, and number of outliers. As expected (Monteith and Unsworth, 2013),  $T_a$  and  $T_g$  increased when the intensity of the supplemental heat increased while RH decreased.

Table 34. Hyperparameter space used to sample hyperparameters for training the machine learning algorithms.

| Hyperparameter            | Distribution <sup>1</sup> | Hyperparameter               | Distribution <sup>1</sup>  |
|---------------------------|---------------------------|------------------------------|----------------------------|
| Random Forests            |                           | Generalized Linear Model     |                            |
| #Trees                    | $\mathcal{U}_d(10, 250)$  | $\lambda$                    | $10^{\mathcal{U}(-10,0)}$  |
| MNOL <sup>2</sup>         | $\mathcal{U}_d(1, 30)$    | $\alpha$                     | $\mathcal{U}(0, 1)$        |
| NVS <sup>3</sup>          | $\mathcal{U}_d(1, 4)$     | Deep Neural Network          |                            |
| Max. Tree Depth           | $\mathcal{U}_d(1, 100)$   | #Hidden layers               | $\mathcal{U}_d(1, 4)$      |
| Gradient Boosted Machines |                           | #Neurons                     | $\mathcal{U}_d(1, 250)$    |
| #Trees                    | $\mathcal{U}_d(1, 100)$   | Dropout percentage           | $\mathcal{U}(0, 0.33)$     |
| MNOL <sup>2</sup>         | $\mathcal{U}_d(1, 20)$    | Epochs                       | $\mathcal{U}_d(1, 10^4)$   |
| Max. Tree Depth           | $\mathcal{U}_d(1, 100)$   | Mini-batch size <sup>4</sup> | $\mathcal{U}_d(1, 130)$    |
| Learning rate             | $\mathcal{U}(0.001, 1)$   | $\rho$                       | $\mathcal{U}(0.75, 0.999)$ |

Annealing

$U(0.8, 1) \mid \epsilon$

$10^{U(-10, -6)}$

<sup>1</sup> $U_a(a, b)$  stands for uniform discrete random distribution from  $a$  to  $b$ ;  $U(a, b)$  stands for uniform random distribution from  $a$  to  $b$ . <sup>2</sup>MNOL: minimum number of observations in a leaf. <sup>3</sup>NVS: number of variables used in each split. <sup>4</sup>The maximum number corresponds to the number of observations in the training dataset.

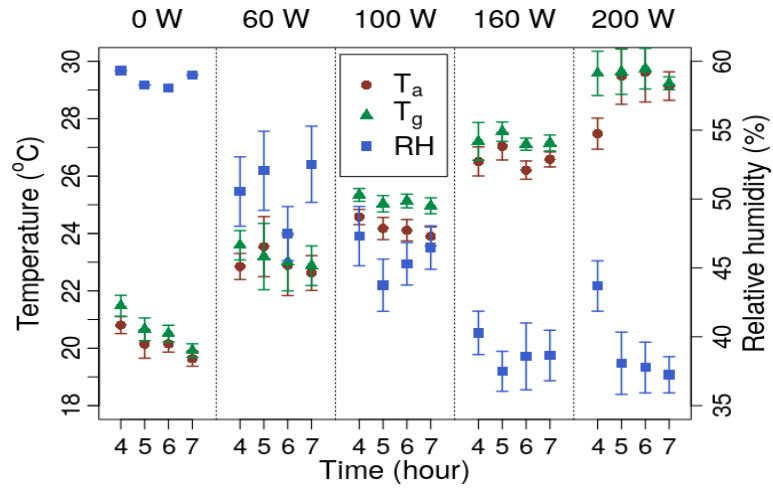


Figure 55. Experimental data (mean +/- standard error of the mean) for air temperature ( $T_a$ ), black-globe temperature ( $T_g$ ), and relative humidity (RH) separated by time of measurement and intensity of supplemental heat.

Table 35. Correlation coefficients, mean and standard error of the mean, and number of univariate outliers of the measured data. The number of outliers is displayed on the rightmost column, the mean and standard error of each data variable is displayed on the main diagonal of the table, and the correlation coefficients are displayed on the remaining entries of the table. No outliers were removed from training and testing datasets.

| Var. <sup>1</sup> | Hour    | Heat     | T <sub>a</sub> | T <sub>g</sub> | RH <sup>2</sup> | T <sub>r</sub> | T <sub>s</sub> | T <sub>h</sub> | #Outliers |
|-------------------|---------|----------|----------------|----------------|-----------------|----------------|----------------|----------------|-----------|
|                   | 5.490   |          |                |                |                 |                |                |                |           |
| Hour              | ± 1.149 | -0.009   | -0.020         | -0.075         | -0.110          | -0.497         | -0.699         | -0.214         | 0         |
|                   |         | 101.850  |                |                |                 |                |                |                |           |
| Heat              | -0.009  | ± 72.441 | 0.891          | 0.912          | -0.706          | 0.330          | 0.225          | 0.642          | 0         |
|                   |         |          | 24.455         |                |                 |                |                |                |           |
| T <sub>a</sub>    | -0.020  | 0.891    | ± 3.424        | 0.969          | -0.590          | 0.287          | 0.258          | 0.743          | 3         |
|                   |         |          |                | 25.068         |                 |                |                |                |           |
| T <sub>g</sub>    | -0.075  | 0.912    | 0.969          | ± 3.464        | -0.596          | 0.306          | 0.282          | 0.740          | 0         |
|                   |         |          |                |                | 43.888          |                |                |                |           |
| RH <sup>2</sup>   | -0.110  | -0.706   | -0.590         | -0.596         |                 | -0.063         | 0.071          | -0.275         | 0         |

± 7.833

---

|       |        |       |       |       |        |                   |                   |                   |   |
|-------|--------|-------|-------|-------|--------|-------------------|-------------------|-------------------|---|
| $T_r$ | -0.497 | 0.330 | 0.287 | 0.306 | -0.063 | 37.917<br>± 0.637 | 0.493             | 0.418             | 5 |
| $T_s$ | -0.699 | 0.225 | 0.258 | 0.282 | 0.071  | 0.493             | 32.803<br>± 1.506 | 0.428             | 2 |
| $T_h$ | -0.214 | 0.642 | 0.743 | 0.740 | -0.275 | 0.418             | 0.428             | 33.836<br>± 1.864 | 3 |

---

<sup>1</sup>Variables: Hour: time of measurement (hour); Heat: intensity of supplemental heat (W);  $T_a$ : air temperature (°C);  $T_g$ : black globe temperature (°C); RH: relative humidity (%);  $T_r$ : rectal temperature (°C);  $T_s$ : skin-surface temperature (°C);  $T_h$ : hair-coat surface temperature (°C). <sup>2</sup>Number of samples for RH was 132.

### 3.2. Performance of machine learning models

Figure 56 shows the MSE of the best performing machine learning models (that minimized cross-validation MSE) using cross-validation, training dataset, and testing dataset. Table 36 shows the hyperparameters for these models. Figure 57 shows the training and testing MSE of these models for the training iterations. The GLM model converged at one iteration, but the other models required more than ten iterations to converge. The best overall model (based on minimum testing MSE), was DNN for  $T_r$ ,

GBM for  $T_s$ , and RF for  $T_h$ .

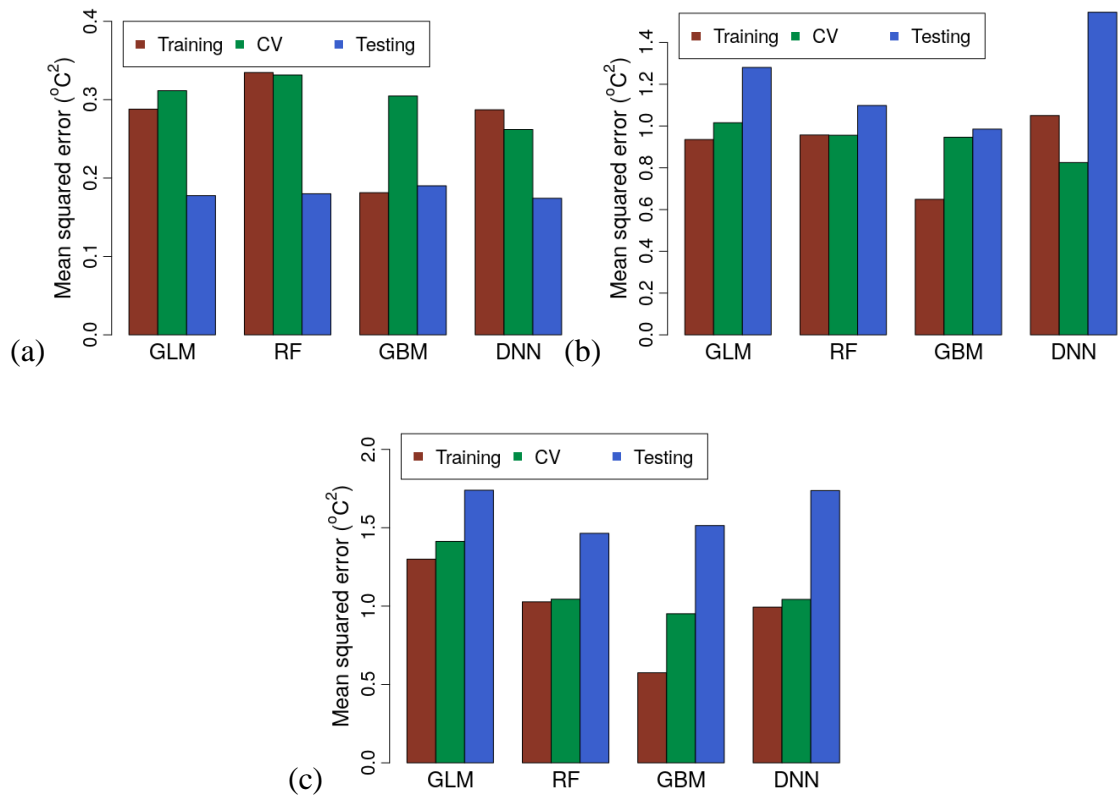


Figure 56. Performance of the best machine learning models for predicting rectal ( $T_r$ ; a), skin-surface ( $T_s$ ; b), and hair-coat surface ( $T_h$ ; c) temperatures. GLM: generalized linear regression model with elastic net regularization; RF: random forests; GBM: gradient boosted machines; DNN: deep neural network with ReLU activation function.

Table 36. Hyperparameters of the best machine learning models.

| Hyperparameter <sup>1</sup> | T <sub>r</sub>          | T <sub>s</sub>     | T <sub>h</sub>         |
|-----------------------------|-------------------------|--------------------|------------------------|
| Random Forests              |                         |                    |                        |
| #Trees                      | 61                      | 46                 | 236                    |
| MNOL <sup>2</sup>           | 4                       | 6                  | 2                      |
| NVS <sup>3</sup>            | 1                       | 3                  | 2                      |
| Max. Tree Depth             | 72                      | 26                 | 82                     |
| Gradient Boosted Machines   |                         |                    |                        |
| #Trees                      | 80                      | 60                 | 25                     |
| MNOL <sup>2</sup>           | 20                      | 12                 | 10                     |
| Max. Tree Depth             | 29                      | 2                  | 41                     |
| Learning Rate               | 0.351                   | 0.504              | 0.398                  |
| Annealing                   | 0.976                   | 0.882              | 0.808                  |
| Generalized Linear Model    |                         |                    |                        |
| $\lambda$                   | $1.632 \times 10^{-10}$ | 0.240              | $8.749 \times 10^{-7}$ |
| $\alpha$                    | 0.244                   | 0.453              | 0.409                  |
| Deep Neural Network         |                         |                    |                        |
| #Hidden Layers              | 2                       | 4                  | 2                      |
| #Neurons <sup>4</sup>       | (242, 190)              | (11, 53, 241, 230) | (65, 20)               |

|                                 |                        |                          |                        |
|---------------------------------|------------------------|--------------------------|------------------------|
| Dropout Percentage <sup>4</sup> | (0.13, 0.19)           | (0.06, 0.19, 0.17, 0.06) | (0.03, 0.04)           |
| Epochs                          | 14                     | 14.567                   | 12.129                 |
| Mini-Batch Size                 | 53                     | 128                      | 82                     |
| $\rho$                          | 0.876                  | 0.946                    | 0.914                  |
| $\varepsilon$                   | $2.855 \times 10^{-7}$ | $5.604 \times 10^{-7}$   | $5.646 \times 10^{-8}$ |

<sup>1</sup>Hyperparameters of the best machine learning models to predict rectal temperature ( $T_r$ , °C), skin-surface temperature ( $T_s$ , °C), and hair-coat surface temperature ( $T_h$ , °C).

<sup>2</sup>MNOL: minimum number of observations in a leaf. <sup>3</sup>NVS: number of variables used in each split. <sup>4</sup>The numbers in parenthesis represent the value used for each hidden layer.

Figure 58a shows the prediction output from the best machine learning algorithms using the mean dataset and Figure 58b shows the absolute percentage error. The model predictions are very close to the measured values. The observed mean absolute errors of  $T_r$ ,  $T_s$ , and  $T_h$ , were 0.36%, 0.62% and 1.35%, respectively (Figure 58b). These errors are lower than those previously reported from either statistical or mechanistic models. Mostaçó et al. (2015) predicted rectal temperatures of pigs with 2.5% error using multiple linear regression for air enthalpy and tympanic temperature (known to be correlated with internal body temperature; Korthals et al., 1995). Costa et al. (2010) predicted surface temperature of piglets with 5.5% error using a linear regression model. Loughmiller et al. (2001) predicted mean body-surface temperature of pigs with 3.5% error using a linear regression model. Turnpenny et al. (2000ab) developed

a mechanistic model and the resulting error was 7% for predicting skin-surface temperature of pigs.

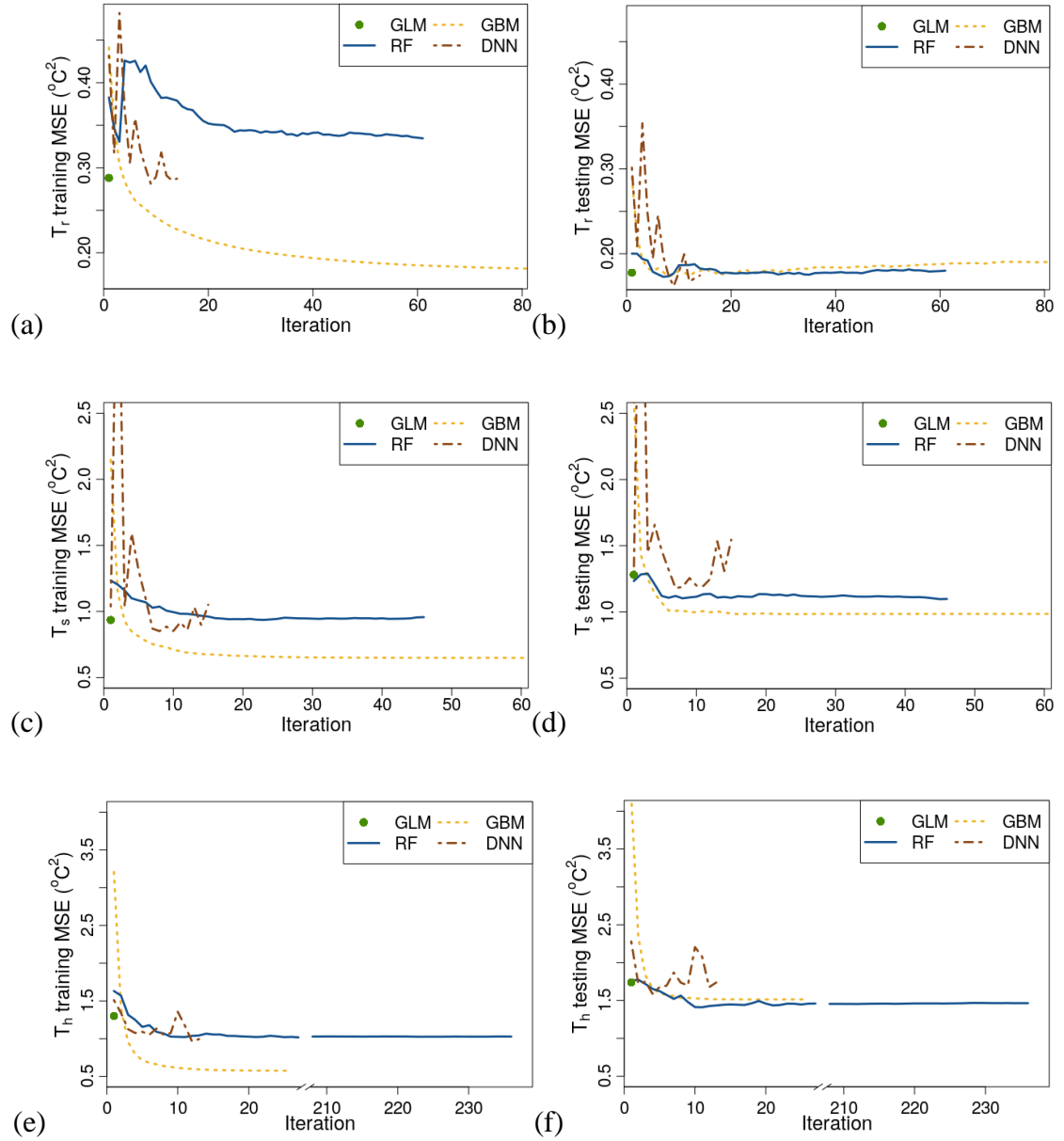


Figure 57. Mean squared error (MSE) on the training (a, c, e) and testing (b, d, f) datasets for predicting rectal ( $T_r$ ; a, b), skin-surface ( $T_s$ ; c, d), and hair-coat surface

( $T_h$ ; e, f) temperatures using the best performing machine learning models.

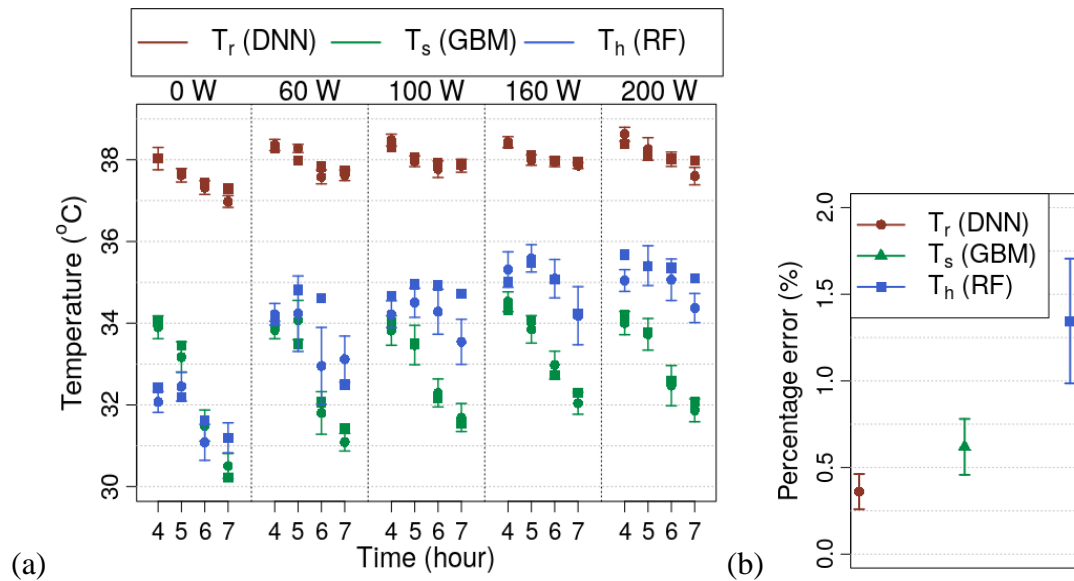


Figure 58. Measured ( $\bullet$ ) and predicted ( $\blacksquare$ ) rectal ( $T_r$ ), skin-surface ( $T_s$ ), and hair-coat surface ( $T_h$ ) temperatures for the mean dataset stratified by (a) time of measurement and intensity of supplemental heat, and (b) absolute percentage errors of the predicted temperatures. Measured values and absolute percentage errors are presented as mean  $\pm$  standard error of the mean. Temperatures were predicted from the best performing machine learning models. RF: random forests; GBM: gradient boosted machines; DNN: deep neural network with ReLU activation function.

### 3.3. Test of robustness and generalization of the best machine learning models.

Figure 59, Figure 60, and Figure 61 show the partial dependence plots (Friedman, 2001) from the effect of changing one predictor variable (while keeping the remaining predictor variables at their mean values) on  $T_r$ ,  $T_s$ , and  $T_h$ , respectively. These figures

show, with the exception of GLM, that the machine learning models were robust with respect to the input variables because they did not produce unexpected predictions. GLM, which fits linear functions for the predictor variables, however, produced relationships that are counter to expectations, such as decreasing  $T_s$  and  $T_r$  while increasing  $T_g$ .

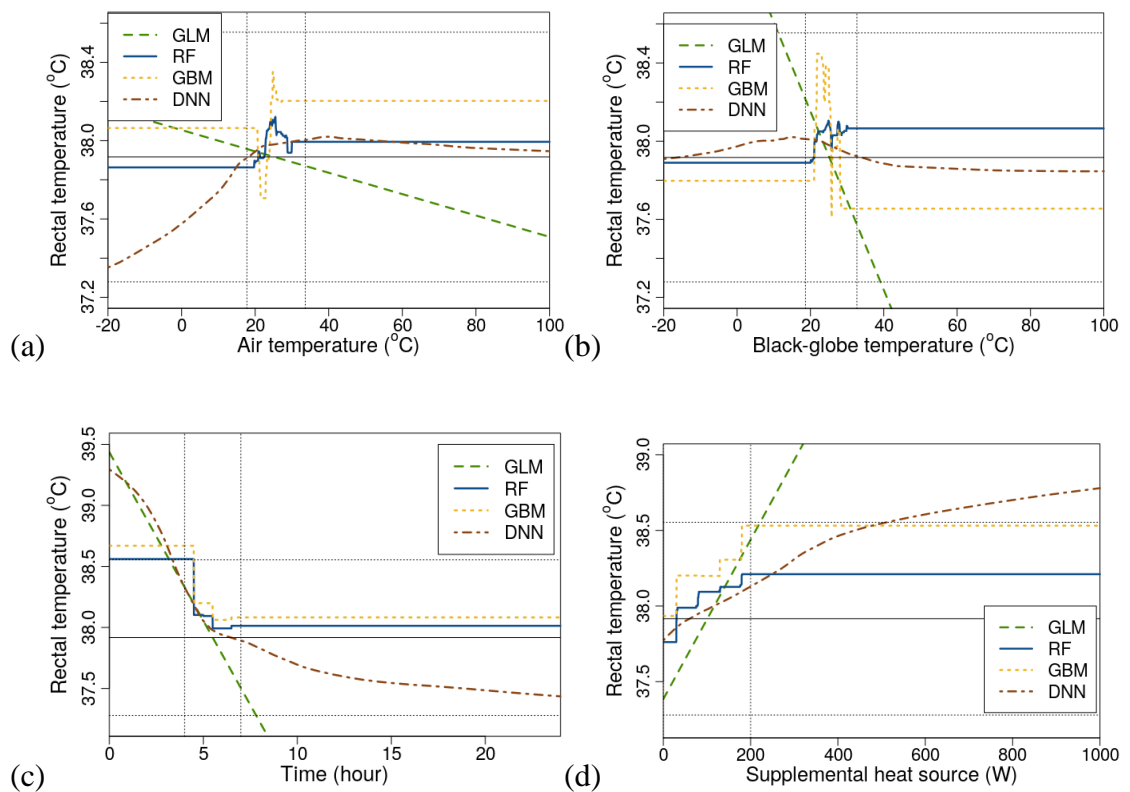


Figure 59. Test of robustness and generalization of the best machine learning models in predicting rectal temperature when changing (a) air temperature, (b) black-globe temperature, (c) time of measurement, or (d) intensity of supplemental heat, while keeping the remaining predictor variables at their mean values. The vertical dashed lines represent the range of the measured predictor variable. The horizontal solid line

represents the mean rectal temperature, and the horizontal dashed lines represent the mean rectal temperature  $\pm$  one standard deviation from the mean.

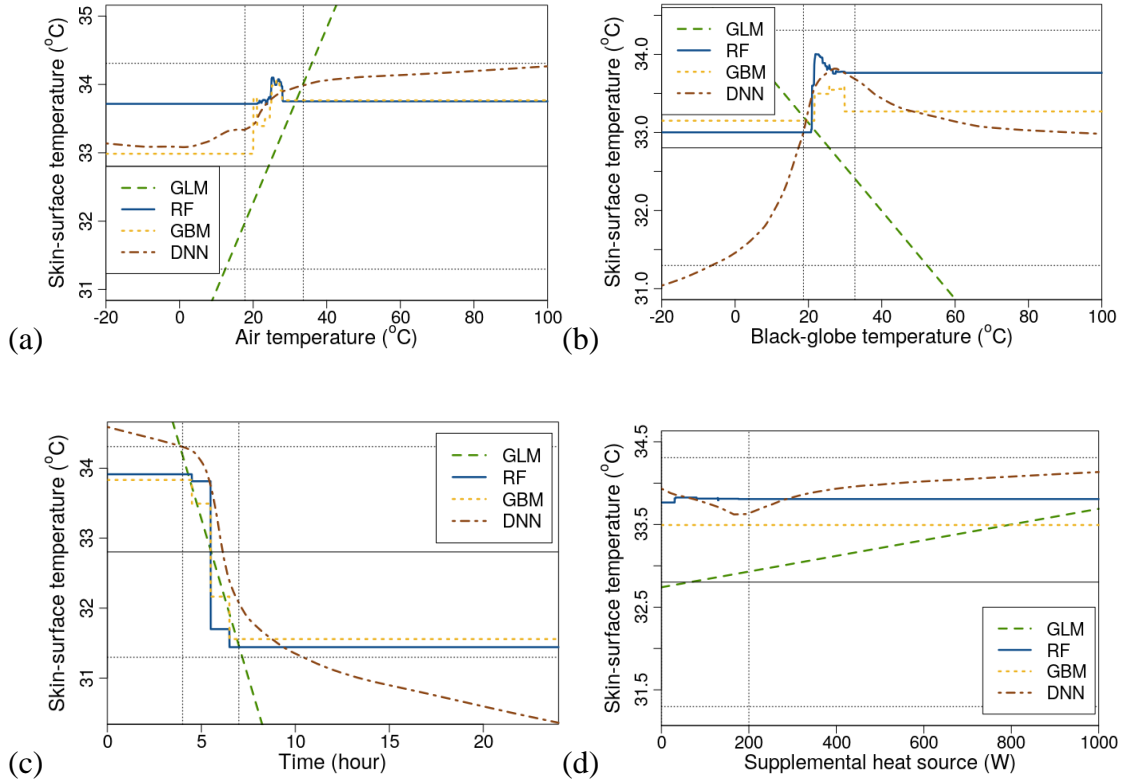


Figure 60. Test of robustness and generalization of the best machine learning models in predicting skin-surface temperature when changing (a) air temperature, (b) black-globe temperature, (c) time of measurement, or (d) intensity of supplemental heat, while keeping the remaining predictor variables at their mean values. The vertical dashed lines represent the range of the measured predictor variable. The horizontal solid line represents the mean skin-surface temperature, and the horizontal dashed lines represent the mean skin-surface temperature  $\pm$  one standard deviation from the mean.

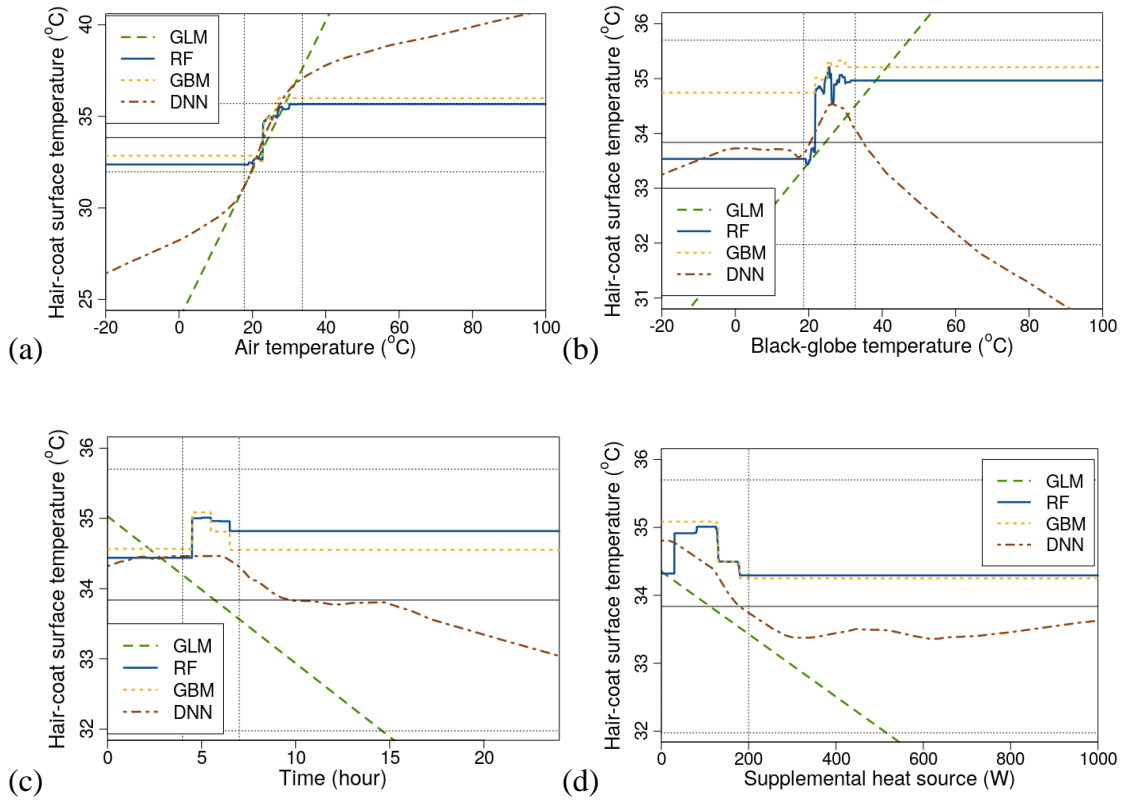


Figure 61. Test of robustness and generalization of the best machine learning models in predicting hair-coat surface temperature when changing (a) air temperature, (b) black-globe temperature, (c) time of measurement, or (d) intensity of supplemental heat, while keeping the remaining predictor variables at their mean values. The vertical dashed lines represent the range of the measured predictor variable. The horizontal solid line represents the mean hair-coat surface temperature, and the horizontal dashed lines represent the mean hair-coat surface temperature  $\pm$  one standard deviation from the mean.

Figure 62 shows the effect of randomly changing all predictor variables on  $T_r$ ,  $T_s$ , and  $T_h$ , which are predicted by the best performing machine learning models. This figure  
284

shows that temperature predictions using GLM resulted in higher variance, which means that GLM is not robust to changes in the predictor variables. The predictions from RF, GBM, and DNN were, however, closer to the mean measured values and the variance of their predictions was lower, which means that these algorithms are robust to changes in the predictor variables.

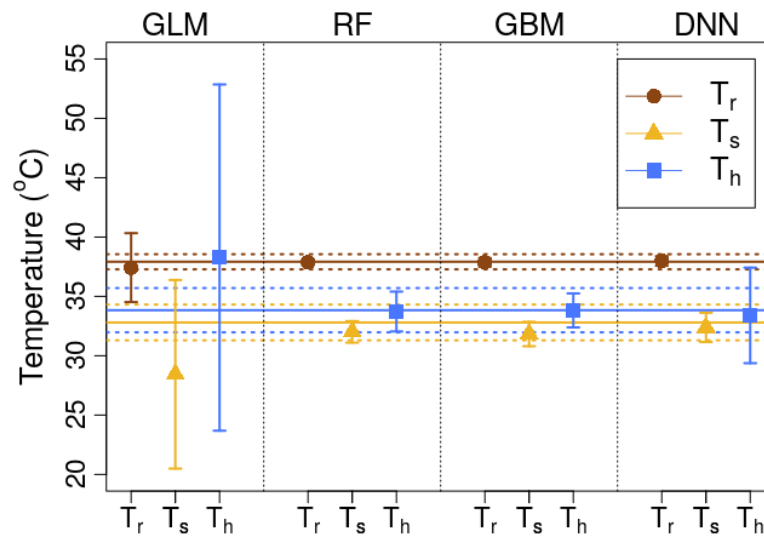


Figure 62. Test of robustness and generalization of the best machine learning models in predicting rectal ( $T_r$ ), skin-surface ( $T_s$ ), and hair-coat surface ( $T_h$ ) temperatures when randomly changing air temperature, black-globe temperature, time of measurement, and intensity of supplemental heat. Points represent mean  $\pm$  one standard deviation of the mean (10,000 samples). Horizontal solid lines represent mean temperatures, and horizontal dashed lines represent mean  $\pm$  one standard deviation of the mean.

### **3.4. Limitations and potential applications of machine learning models**

The main limitations of machine learning models are that they are data-based as well as time-consuming and computationally expensive to train. In addition, if the training dataset is noisy or the model is trained inappropriately, then, the model may “learn” noise instead of the non-linear relationships that may exist between the predictor variables and the response variable (Natekin and Knoll, 2013). We showed in Sec. 3.3 that all algorithms considered in this study, except GLM, were robust to changes in the predictor variables. It should be noted, however, that the models were trained and tested from the same data population. This means that the models proposed in this study should not be applied to different data sets obtained from other livestock species. If a model is, however, trained with a larger dataset obtained from several livestock species, it would provide accurate predictions within the population represented by the dataset. It is also important to note that in this study,  $T_a$  and  $T_g$  were the only environmental predictor variables. Future studies may include other environmental predictor variables (e.g., relative humidity and heat stress indices) and spatio-temporal parameters (e.g., time of the year), which could improve model performance.

Training and validation of the four machine learning models considered in this study took ~9.5 hours to complete. Most of this time was spent on training the models (~8 hours in total; GLM = 50 min; RF = 35 min; GBM = 30 min; DNN = 6 h). The time to compute one prediction was ~0.3 ms, which is faster than the computing time required

for analytical or numerical models (Milan and Gebremedhin, 2016b).

Our results suggest that machine learning algorithms, particularly RF, GBM, and DNN were found to be accurate in predicting rectal temperature ( $T_r$ ), skin-surface temperature ( $T_s$ ), and hair-coat surface ( $T_h$ ) temperature, but not GLM. The main advantage of machine learning models is that only data is needed to train the non-linearity of the data. For mechanistic models, the non-linearity comes from the assumptions made in solving the conservation equations. Since machine learning algorithms predict temperatures that are necessary to solve mechanistic models, one possible application of machine learning algorithms would be to provide inputs to mechanistic models.

#### ***4. CONCLUSIONS***

Four machine learning algorithms were trained to predict rectal temperature, skin-surface temperature, and hair-coat surface temperature of piglets based on environmental data. Deep neural networks, gradient boosted machines, and random forests were the best algorithms, based on the lowest mean squared error on the testing dataset, to predict rectal, skin-surface, and hair coat-surface temperatures, respectively. The mean absolute percentage errors calculated using the mean dataset were 0.36% for rectal temperature, 0.62% for skin-surface temperature and 1.35% for hair coat-surface temperature. These three algorithms, different from generalized linear regression models, were robust to a wide range of inputs. The data supports the

use of machine learning algorithms to predict physiological temperatures of livestock, and these temperature predictions can be used as inputs to mechanistic models. The combination of mechanistic and machine learning algorithms has the potential to provide more information about thermal-comfort status of livestock.

***Acknowledgment***

Funding: Brazilian National Council of Technological and Scientific Development (CNPq, Proc. 203312/2014-7), São Paulo Research Foundation (FAPESP, Proc. 17.519/14), and the USDA/Hatch (Washington, DC) funds as part of the W-273 Regional Project through Cornell University.

## REFERENCES

- Bergstra J, Bengio Y. Random search for hyper-parameter optimization. *J Mach Learn Res* 13:281-305, 2012.
- Breiman L. Random forests. *Machine Learning* 45:5-32, 2001.
- Brown-Brandl TM, Eigenberg RA, Nienaber JA, Kachman SD. Thermoregulatory profile of a newer genetic line of pigs. *Livest Prod Sci* 71:253-260, 2001.
- Brown-Brandl TM, Hayes MD, Xin H, Nienaber JA, Li H, Eigenberg RA, Stinn JP, Shepherd T. Heat and moisture production of modern swine. *ASHRAE Trans* 120(1):469-489, 2014.
- Collier RJ, Gebremedhin KG. Thermal biology of domestic animals. *Ann Rev Anim Biosci* 3:513-532, 2015.
- Collin A, van Milgen J, Dubois S, Noblet J. Effect of high temperature on feeding behaviour and heat production in group-housed young pigs. *Br J Nutr* 86:63-70, 2001.
- Costa LN, Redaelli V, Magnani D, Cafazzo S, Amadori M, Razzauoli E, Verga M, Luzi F. *Preliminary study of the relationship between skin temperature of piglets measured by infrared thermography and environmental temperature in a vehicle in transit.* LXIV Annual Meeting of The Italian Society for Veterinary Sciences pp. 193-197, 2010.
- Cousineau D, Chartier S. Outliers detection and treatment: a review. *Int J Psychol Res* 289

3(1), 58-67, 2010.

Cross AJ, Rohrer GA, Brown-Brandl TM, Cassady JP, Keel BN. Feed-forward and generalised regression neural networks in modelling feeding behaviour of pigs in the grow-finish phase. *Biosys Eng* 173:124-133, 2018

Da Silva RG, Maia ASC. *Principles of animal biometeorology*. Springer: New York, NY, 2013.

DeShazer JA. *Livestock Energetics and Thermal Environmental Management*. ASABE: St. Joseph, MI, 2009.

Friedman JH. Greedy function approximation: a gradient boosting machine. *Ann Stat* 1189-1232, 2001.

Goodfellow I, Bengio Y, Courville A. *Deep Learning*. MIT Press: Cambridge, MA, 2016.

Guarino M, Norton T, Berckmans D, Vranken E, Berckmans D. A blueprint for developing and applying precision livestock farming tools: a key output of the EU-PLF project. *Anim Front* 7(1):12-17, 2017.

Hastie T, Tibshirani R, Friedman J. *The Elements of Statistical Learning*. Springer: New York, NY, 2003.

Hensley DW, Mark AE, Abella JR, Netscher GM, Wissler EH, Diller KR. 50 years of computer simulation of the human thermoregulatory system. *J Biomech Eng* 290

135:021006, 2013.

Hunter MC, Smith RG, Schipanski ME, Atwood LW, Mortense DA. Agriculture in 2050: recalibrating targets for sustainable intensification. *BioScience* 67(4):386-391, 2017.

Kamilaris A, Prenafeta-Boldú FX. Deep learning in agriculture: a survey. *Comput Electron Agric* 147:70-90, 2018.

Kashiha M, Bahr C, Ott S, Moons CPH, Niewold TA, Ödberg FO, Berckmans D. Automatic weight estimation of individual pigs using image analysis. *Comput Electron Agric* 107:38-44, 2014.

Korthals RL, Eigenberg RA, Hahn GL, Nienaber JA. Measurements and spectral analysis of tympanic temperature regulation in swine. *Trans ASAE* 33(3):905-909, 1995.

Lao F, Brown-Brandl T, Stinn JP, Liu K, Teng G, Xin H. Automatic recognition of lactating sow behaviors through depth image processing. *Comput Electron Agric* 125:56-62, 2016.

Loughmiller JA, Spire MF, Dritz SS, Fenwick BW, Hosni MH, Hogge SB. Relationship between mean body surface temperature measured by use of infrared thermography and ambient temperature in clinically normal pigs and pigs inoculated with *Actinobacillus pleuropneumoniae*. *Am J Vet Res* 62(5):676-681, 2001.

McArthur AJ. Thermal resistance and sensible heat loss from animals. *J Therm Biol* 6:43-47, 1981.

McCafferty DJ, Gallon S, Nord A. Challenges of measuring body temperatures of free-ranging birds and mammals. *Anim Biotelemetry* 3:33, 2015.

Milan HFM, Gebremedhin KG. Triangular node for Transmission-Line Modeling (TLM) applied to bio-heat transfer. *J Therm Biol* 62:116-122, 2016a.

Milan HFM, Gebremedhin KG. Tetrahedral node for Transmission-Line Modeling (TLM) applied to Bio-heat Transfer. *Comp Biol Med* 79:243-249, 2016b.

Monteith J, and Unsworth M. Principles of environmental physics: plants, animals, and the atmosphere. Academic Press: Cambridge, MA, 2013.

Mostaço GM, Miranda KOS, Condotta ICF, Salgado DDA. Determination of piglets' rectal temperature and respiratory rate through skin surface temperature under climatic chamber conditions. *J Braz Assoc Agric Eng* 35(6):979-989, 2015.

Nasirahmadi A, Edwards SA, Sturm B. Implementation of machine vision for detecting behaviour of cattle and pigs. *Livest Science* 202:25-38, 2017.

Natekin A, Knoll A. Gradient boosting machines, a tutorial. *Front Neurobot* 7, 2013.

Nienaber JA, Hahn GL, Eigenberg RA. Quantifying livestock responses for heat stress management: a review. *Int J Biometeorol* 42:183-188, 1999.

Pathak M, Parkhurst AM, Arias RA, Mader TL. *Comparative study of time series and multiple regression for modeling dependence of cattle body temperature on environmental variables during heat stress*. Annual 21st Conference on Applied Statistics in Agriculture, pp. 1-20, 2009.

R Core Team. *R: A language and environment for statistical computing*. R Foundation for Statistical Computing: Vienna, Austria, 2017.

Ramirez BC. *A novel approach to measure, understand, and assess the thermal environment in grow-finish swine facilities*. Iowa State University. Graduate Theses and Dissertations. 16201, 2017.

Robertshaw D. Mechanisms for the control of respiratory evaporative heat loss in panting animals. *J App Physiol* 101:664-668, 2006.

Shao B, Xin H. A real-time computer vision assessment and control of thermal comfort for group-housed pigs. *Comput Electron Agric* 62:15-21, 2008.

Shi C, Teng G, Li Z. An approach of pig weight estimation using binocular stereo system based on LabVIEW. *Comput Electron Agric* 129:37-43, 2016.

Soerensen DD, Pedersen J. Infrared skin temperature measurements for monitoring health in pigs: a review. *Acta Vet Scand* 57:5, 2015.

Srivastava N, Hinton G, Krizhevsky A, Sutskever I, Salakhutdinov RR. Dropout: A simple way to prevent neural networks from overfitting. *J Mach Learn Res* 15:1929-

1958, 2014.

St-Pierre NR, Cobanov B, Schnitkey G. Economic losses from heat stress by US livestock industries. *J Dairy Sci* 86:E52-E77, 2003.

Silanikove N. Effects of heat stress on the welfare of extensively managed domestic ruminants. *Livest Prod Sci* 67:1-18, 2000.

The H2O.ai team. *h2o: R Interface for H2O, version 3.16.0.2*, 2017.

Turnpenny JR, McArthur AJ, Clark JA, Wathes CM. Thermal balance of livestock 1. A parsimonious model. *Agr Forest Meteorol* 101:15-27, 2000a.

Turnpenny JR, Wathes CM, Clark JA, McArthur AJ. Thermal balance of livestock 2. Application of a parsimonious model. *Agr Forest Meteorol* 101:29-52, 2000b.

Van Hertem T, Rooijackers L, Berckmans D, Peña Fernández A, Norton T, Berckmans D, Vranken E. Appropriate data visualization is key to precision livestock farming acceptance. *Comput Electron Agric* 138:1-10, 2017.

Vasdal G, Wheeler EF, Boe KE. Effect of infrared temperature on thermoregulatory behaviour in usckling piglets. *Animal* 3(10):1449-1454, 2009.

Wathes CM, Kristensen HH, Aerts J-M, Berckmans D. Is precision livestock farming an engineer's daydream or nightmare, an animal's friend or foe, and a farmer's panacea or pitfall? *Comput Electron Agric* 64:2-10, 2008.

Wolfenson D, Roth Z, Meidan R. Impaired reproduction in heat-stressed cattle: basic and applied aspects. *Anim Reprod Sci* 60:535-547, 2000.

Wongsriworaphon A, Arnonkijpanich B, Pathumnakul S. An approach based on digital image analysis to estimate the live weight of pigs in farm environments. *Comput Electron Agric* 115:26-33, 2015.

Zeiler MD. Adadelta: An adaptive learning rate method. *arXiv:1212.5701*, 2012.

Zou H, Hastie T. Regularization and variable selection via the elastic net. *J Royal Stat Soc Ser B* 67(2): 301–320, 2005.

## CHAPTER 8: PHOTOVOLTAIC PANELS AS SHADING RESOURCES FOR LIVESTOCK

Alex Sandro Campos Maia, Eric de Andrade Culhari, Vinícius de França Carvalho  
Fonsêca, Hugo Fernando Maia Milan, Kifle G. Gebremedhin

*Under Review.*

### ***Abstract***

Photovoltaic panels can provide artificial shades to protect livestock against intense solar radiation while serving as a clean energy source, reducing CO<sub>2</sub> emission, and providing an additional source of income to farmers. These benefits foster sustainable livestock farming practices. In this study, we (1) determined livestock shade preference for photovoltaic panels and the classical 80%-blockage cloth material, and (2) quantified the reduction in radiant heat load provided by these shade structures. To determine the shade preference, the behavior of five Corriedale lambs and six Corriedale ewes were observed in a paddock with two shade structures (one with photovoltaic panels and another with an 80%-blockage cloth). The following behavioral activities were determined using the instantaneous scan sampling method each 10-min from 07:00h to 17:00h: grazing, ruminating, idling, lying, standing, under the sun, under the shade from photovoltaic panels, and under the shade from cloth. To correlate animal behavior with environmental conditions and to quantify the reduction in radiant heat load provided by these shade structures, the following meteorological

variables were recorded: solar radiation (total and short-wave), air temperature, relative humidity, wind speed, and black-globe temperature (in the shades and in the sun). We observed that the animals spent less than 1% of their time under the shade from cloth compared to 38% under the shade from photovoltaic panels and 61% exposed to the sun. Sheep preference for shade projected by photovoltaic panels might be explained by the reduced radiant heat load (approximately lower  $40 \text{ W m}^{-2}$ ) compared to that from the cloth. When the intensity of solar radiation increased from 250 to  $850 \text{ W m}^{-2}$ , the time the animals spent outside the shades decreased from  $96.7 \pm 3.6 \%$  to  $30.2 \pm 6.3 \%$ , which was coupled with a similar increase in the time spent in the shade from photovoltaic panels (from  $13.0 \pm 3.3 \%$  to  $69.3 \pm 6.2 \%$ ). For the same increase in solar radiation, the energy generated (integrated over 5-min) by the photovoltaic panels increased from  $38.8 \pm 5.9$  to  $197.9 \pm 3.8$  kWh. Over a period of one year, an electric energy of 5.19 MWh (monthly average of 432.33 kWh) was generated and 2.77 tons of  $\text{CO}_2$  were not emitted to the atmosphere. In economic terms, the electric energy generated in one year was equivalent to a saving of \$740.

**Keywords:** Livestock; photovoltaic panel; shade; solar irradiance; tropical conditions.

### **Highlights**

- High levels of solar radiance in tropical countries heat-stresses livestock;
- Sheep unconditionally preferred shade from solar panels over 80%-blockage cloth;

- Lambs graze for longer times than ewes;
- Photovoltaic panels are a novel alternative to shading to Animals;

## ***1. INTRODUCTION***

The expected increase in the population of the world to 9.7 billion in 2050 (Umer et al., 2018) and the simultaneous increase in wealth, which drives up the per-capita consumption of animal products (Alexandratos and Bruinsma, 2012; Herrero et al., 2009; McAlpine et al., 2009; Popp et al., 2010), call for a dramatic increase in food production (25%-70% by 2050; Hunter et al., 2017). This food production increase must be followed by sustainable farming practices that improve animal comfort and welfare (Milan et al., 2018). One sustainable livestock farming practice that can improve comfort and welfare of livestock managed in open pasture or feedlots is to provide shades using photovoltaic panels.

Consumers are increasingly concerned about livestock comfort and welfare. Research showed that 69% of consumers believe that animal welfare is important and is perceived to result in safer, healthier, and higher quality food products (Grimshaw et al., 2014; Verbeke et al., 2010). To encourage animal comfort and welfare practices by companies and farmers, the Humane Farm Animal Care organization (certificating more than 160 companies and 5,500 farms in the USA, Canada, Chile, Peru, and Brazil) developed the Certified Humane Raised & Handled certification. Among the requirements for this certification (HFAC 2012, 2013, 2014, 2017) is access to shade areas that can accommodate all animals simultaneously. Similarly, the Animal Welfare Committee of Australia recommends the provision of shades for livestock exposed to heat stressful conditions (PISC, 2004).

One of the major issues for comfort and welfare of livestock managed in open pasture or feedlots is the intense heat load from solar radiation. In tropical regions, solar radiation may exceed  $800 \text{ W m}^{-2}$  (Maia et al., 2015; Da Silva et al., 2015), negatively impacting animal comfort, welfare, and production (e.g., weight gain or milk yield; DaSilva et al., 2010; Domingos et al., 2013; Maia et al., 2015; Polsky and von Keyserlingk, 2017; Tucker et al., 2015; von Keyserlingk et al., 2009). For instance, in the USA, livestock heat stress is responsible for an estimated \$3 billion annual loss (Ferreira et al., 2016; Polsky and von Keyserlingk, 2017; St-Pierre et al., 2003). To cope with heat stress, animals use physiological and behavioral responses. Physiological responses include panting and sweating (Domingos et al., 2013; Maia et al. 2005, 2015). Behavioral responses include standing up to increase the surface area for convective heat loss (Gebremedhin et al., 2011) and shade-seeking (Oliveira et al., 2014, 2019).

The benefits of shade have been widely studied for beef cattle (Averós et al., 2014; Brown-Brandt et al. 2005, 2013, 2016; Eigenberg et al., 2010; Gaughan, et al., 2010; Gaughan e Mader, 2014; Mitlöhner et al., 2001, 2002), and for dairy cows (Kamal et al., 2018; Oliveira et al., 2014, 2019; Schütz et al., 2009, 2008, 2014; Tucker et al., 2008) but little is known about shade preference by sheep (Cloete et al. 2000). For example, lactating Holstein cows in Brazil can spend approximately 80% of their time under the shade from 100%-blockage cloth structures (Oliveira et al., 2019). Similar results were reported for Holstein cows in the USA (Schütz et al. (2009; Tucker et al.,

2008) and for lactating Holstein-Friesian cows in Australia (Gaughan et al., 1998). In addition, Gebremedhin et al. (2011) reported a direct correlation ( $R^2 \sim 0.90$ ) between the solar absorbing capacity of hair coat and percent of time heifers (Black Angus, white Charolais, tan-colored MARC I, and dark-red colored MARC III) spent in shade.

While high levels of solar radiation compromise animal comfort and welfare, they can generate clean and renewable electrical energy through photovoltaic cells (Hinrichs et al., 2015), reducing CO<sub>2</sub> emission from power generation plants. In addition, photovoltaic panels could be used to provide artificial shade for humans (Middel et al., 2016) or animals. Using photovoltaic panels to provide artificial shade for animals can lead to a “co-generation” of electrical energy and agricultural products. The possibility of such integrated systems has elicited the interest of policy makers and governmental agencies, such as the Brazilian Governmental Company for Research on Energy (EPE; responsible for future planning of energy consumption, demand, and generation). The EPE recently manifested an expectation in the innovation of “sustainable co-generation systems,” combining power generation plants (e.g., photovoltaic panels) and agricultural systems (EPE, 2018).

Sustainable co-generation systems using photovoltaic panels are suitable in several parts of the world (Hinrichs et al., 2015). For instance, the American Solar Grazing Association (recently created) encourages scientists to quantify the benefits of integrating grazing livestock and solar farms, which can reduce land competition for

renewable energy and agricultural production, increase crop biomass production, grasses for livestock, and offer cooler microclimates for animals (lower air temperature and thermal radiation, Adeh et al., 2018; Mitchell et al., 2018; Sobrosa Neto et al., 2018). Recently, American farmers (Dickrell, 2018) reported behavioral and productive benefits for animals under the shade from solar panels. Another strong motivation for the implementation of sustainable co-generation systems using photovoltaic panels is the continuous decrease of the price of photovoltaic panels (from US\$ 3.90 per Wp in 2006 to US\$ 0.39 per Wp in 2016; 5% expected annual price drop; Ferreira et al., 2018; IRENA, 2017; Pereira et al., 2017) as well as the development of new technologies expected to increase the efficiency of energy conversion (from 18% to 45% using Single-Junction GaAs, Thin-Film Crystal; IRENA, 2017). This study investigated the potential of a co-generation system using photovoltaic panels to generate electrical energy and to provide shade for sheep managed in paddock. Specifically, we determined the shade preference of sheep (lambs or ewes) for artificial shade structures with photovoltaic panels over conventional (80%-blockage cloth) shade structures and quantified the reduction of radiant heat load provided by these shade structures. This is the first study to present scientific data on photovoltaic panels as a shading resource for livestock.

## **2. MATERIALS AND METHODS**

### **2.1. Animals and experimental design**

Animal use and research protocol (Proc. 006062/19) was approved by the Institutional Animal Care and Use Committee of São Paulo State University. This experiment was conducted in the Animal Biometeorology Laboratory of the São Paulo State University (Latitude 21°15' S Longitude 48°19' W). Five Corriedale lambs ( $36.46 \pm 1.17$  kg BW, mean  $\pm$  SD) and six Corriedale ewes ( $64.62 \pm 5.46$  kg BW, mean  $\pm$  SD) were monitored in April, 2018, for five days (08:00h to 17:00h). The animals were kept in a paddock (area  $\pm 650$  m<sup>2</sup>), fed *Cinodon* grass, and water was provided ad libitum. Two types of shade structures were used in the study. The first one (Figure 63; lower height: 3.0 m; inclination angle: 15°; width: 4.0 m; length: 5.0 m; area: 20 m<sup>2</sup>; projected shade area: 19.3 m<sup>2</sup>; share area per animal: 1.76 m<sup>2</sup> animal<sup>-1</sup>) consisted of ten photovoltaic panels (1.0 m  $\times$  2.0 m; 335 Wp, peak efficiency of 16.72%, Canadian Solar model CS6U-335P, Guelph, ON; installed by Blue Sol, Blue Sol Energia Solar, Ribeirão Preto, SP). The second shade structure (height: 1.6 m; width: 3.05 m; length: 5.1 m; area: 15.56 m<sup>2</sup>; projected shade area: 15.56 m<sup>2</sup>; share area per animal: 1.3 m<sup>2</sup> animal<sup>-1</sup>) consisted of shade cloth (80% of solar radiation blockage). Between 17:00h and 06:00h, animals were housed in a barn and fed a concentrated diet (corn meal, soybean meal, and mineral mixture).



Figure 63. Photo showing sheep under the shade from photovoltaic panels.

## 2.2. Behavioral observations

Animal behavior was monitored by direct observation using the instantaneous scan sampling method at 10-min intervals (Martin and Bateson, 2007) from 08:00h to 17:00h by two observers. The inter-observer agreement was above 90% (Fonsêca et al., 2014). Animals were identified using black painted numbers on their left and right rumps. Animal behavior was recorded as L.P.A., where, L represents location (S: under the sun; P: under the shade from photovoltaic panels; C: under the shade from cloths), P represents posture (L: lying; S: standing), and A represents activity (G: grazing; R: ruminating; I: idling) (Figure 64). Grazing was defined when the head of the sheep was pointing towards the ground and the sheep was searching for or

ingesting grass; ruminating was defined as chewing movements without feed in the mouth, feed regurgitation, or both (Schutz et al., 2014); otherwise, idling was recorded. Lying was defined when the flank of the sheep was in direct contact with the ground; otherwise, standing was recorded. Under a shade was recorded when at least the head or one of the hooves of the sheep were within the shade projected by the artificial structure; otherwise, sun was recorded.

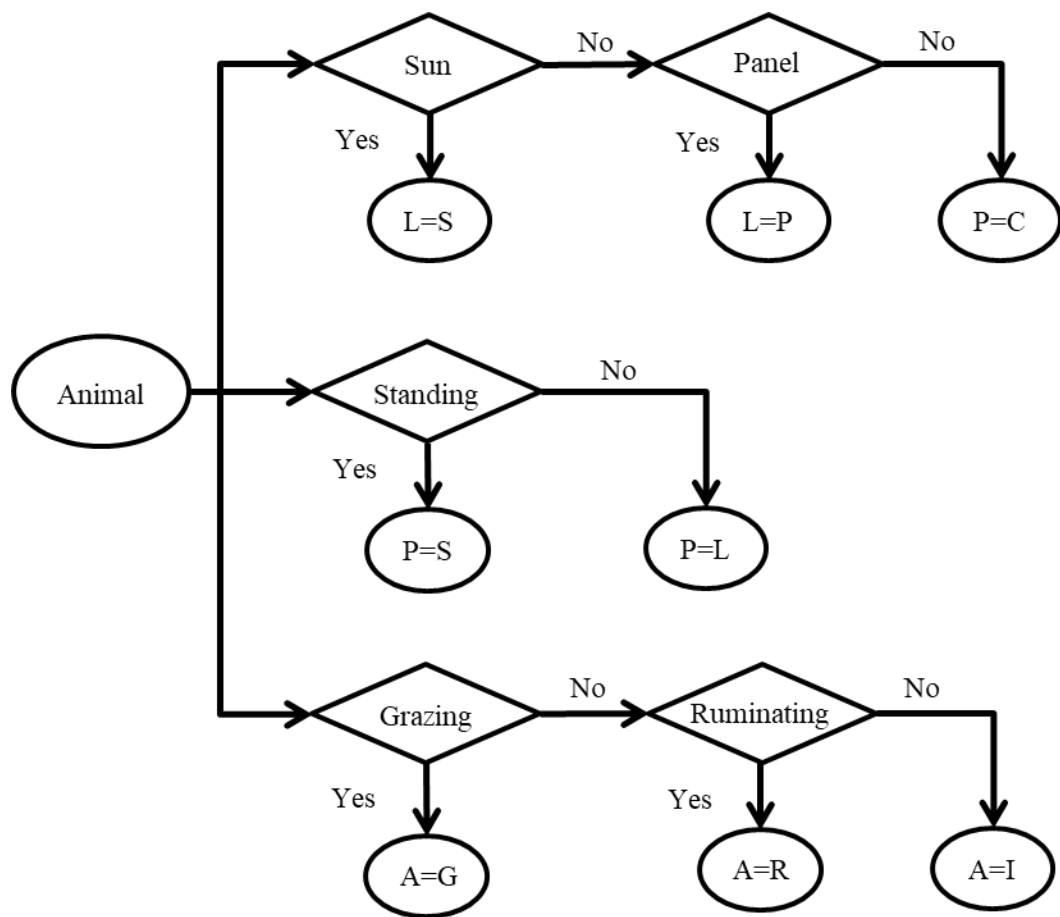


Figure 64. Flowchart of animal behavior recording.

### **2.3. Meteorological data**

Meteorological data were recorded every minute using a portable weather station (WS-18 model 110, Nova Lynk, Auburn, CA, USA) placed within ~1 m of the paddock. The recorded meteorological data were solar radiation ( $R_s$ ,  $W\ m^{-2}$ ; CMP-22, Kipp and Zonen, Delft, Netherlands; spectral range = 0.3 – 3.6  $\mu m$ ), ultraviolet solar radiation ( $U_v$ ,  $W\ m^{-2}$ ; spectral range = 0.28 – 0.4  $\mu m$ ), air temperature ( $T_A$ ,  $^{\circ}C$ ; accuracy  $\pm 0.1\ ^{\circ}C$ ), black-globe temperature ( $T_G$ ,  $^{\circ}C$ ; accuracy  $\pm 0.1\ ^{\circ}C$ ), relative humidity (RH, %; accuracy  $\pm 3\ %$ ), and wind speed ( $W_s$ ,  $m\ s^{-1}$ ; accuracy  $\pm 0.44\ m\ s^{-1}$ ). To avoid animal interference with the recording instruments, after the behavioral experiment, black-globe temperatures under the shades projected by the structures, underneath and outside the structure, were recorded every minute for six days from 07:00h to 17:00h (Hobo Data Logger, Onset Computer Corporation, Bourne, MA; accuracy  $\pm 0.1\ ^{\circ}C$ ). The thermal comfort provided by the shading structures was estimated using the Radiant Heat Load (RHL,  $W\ m^{-2}$ ; DaSilva and Maia, 2013).

### **2.4. Electricity generation and CO<sub>2</sub> savings estimation**

Electricity generated by the photovoltaic panels for the period between April/2018 and March/2019 was recorded every 5 min by the frequency inverter (Fronius 3 kWp). The amount of CO<sub>2</sub> not emitted to the atmosphere because of electricity generated by the photovoltaic panels was calculated using the 2018 daily Brazilian CO<sub>2</sub> emission factor for electric energy generation (hydroelectric, wind, photovoltaic, and thermal;

MCTIC, 2018).

## 2.5. Statistical analyses

The experimental data were analyzed using generalized least squares with the general linear model procedure (PROC GLM) of the Statistical Analysis System (SAS Institute, Version 8), according to Littell et al. (2006). The behavioral classes used in the statistical analysis were SSG, SSI, PSR, PLR, PSI and PLI (represented >98% of the observations). The generalized linear model used to describe the behavioral observations (expressed in percentage, with a logarithmic transformation) is expressed as

$$Y_{ijkLm} = \mu + C_i + A_j(C_i) + D_k + D_k A_j(C_i) + R_L + (CR)_{iL} + e_{ijkLm} \quad (225)$$

where,  $Y_{ijkLm}$  is the  $m^{\text{th}}$  observation of the behavioral activity;  $C_i$  is the fixed effect of the  $i^{\text{th}}$  age group ( $i = \text{lamb}$ s or  $\text{ewe}$ s);  $A_j(C_i)$  is the random effect of the  $j^{\text{th}}$  animal within the  $i^{\text{th}}$  age group (if  $i = \text{lamb}$ s, then  $j = 1, \dots, 5$ ; if  $i = \text{ewe}$ s, then  $j = 6, \dots, 11$ );  $D_k$  is the random effect of the  $k^{\text{th}}$  day of observation ( $k = 1, \dots, 5$ );  $D_k A_j(C_i)$  is the interaction between the random effect of the  $k^{\text{th}}$  day of observation within the random effect of the  $j^{\text{th}}$  animal within the  $i^{\text{th}}$  age group;  $R_L =$  fixed effect of the  $L^{\text{th}}$  class of solar radiation ( $<200$ ;  $200 \leq R_S < 300$ ;  $300 \leq R_S < 400$ ;  $400 \leq R_S < 500$ ;  $500 \leq R_S < 600$ ;  $600 \leq R_S < 700$ ;  $700 \leq R_S < 800$  and  $R_S \geq 800 \text{ W m}^{-2}$ );  $e_{ijkLm}$  is the residual term, assumed to be independent and identically distributed (iid) over  $N(0, \sigma)$ ;  $\mu$  is the overall mean;  $N(a, b)$  represents a normal distribution with mean  $a$  and standard deviation  $b$ .

The probability of the choice of shade (cloth, panel, or exposed to the sun) was analyzed using a machine learning algorithm: multinomial logistic generalized additive model (GAM; Wood et al., 2016; Wood, 2017). GAM was used to model the equations defined below:

$$h_{panel} = \alpha + f_1(R_S)_{lamb} + f_2(R_S)_{ewe} + \alpha_{lamb} + N(0, \sigma_{lamb}) + N(0, \sigma_{ewe}) \quad (226)$$

$$h_{sun} = \beta + f_3(R_S)_{lamb} + f_4(R_S)_{ewe} + \beta_{lamb} + N(0, \gamma_{lamb}) + N(0, \gamma_{ewe}) \quad (227)$$

$$p_{cloth} = \frac{1}{1 + \exp(h_{panel}) + \exp(h_{sun})} \quad (228)$$

$$p_{panel} = \frac{\exp(h_{panel})}{1 + \exp(h_{panel}) + \exp(h_{sun})} \quad (229)$$

$$p_{sun} = \frac{\exp(h_{sun})}{1 + \exp(h_{panel}) + \exp(h_{sun})} \quad (230)$$

where,  $h_{panel}$  and  $h_{sun}$  represent link functions;  $\alpha$  and  $\beta$  represent intercepts;  $f_1(R_S)_{lamb}$  and  $f_3(R_S)_{lamb}$  represent smooth functions for lambs;  $f_2(R_S)_{ewe}$  and  $f_4(R_S)_{ewe}$  represent smooth functions for ewes;  $\alpha_{lamb}$  and  $\beta_{lamb}$  represent additive effects for lambs;  $\sigma_{lamb}$  and  $\gamma_{lamb}$  represent the standard deviation of the random effect of the lambs;  $\sigma_{ewe}$  and  $\gamma_{ewe}$  represent the standard deviation of the random effect of the ewes;  $p_{cloth}$ ,  $p_{panel}$ , and  $p_{sun}$  represent the probability of animals at the shade from cloth, solar panels, or exposed to the sun, respectively. Input solar radiation in the model was averaged over a 10-min window.

The shade preference prediction (cloth, solar panel, or sun) from this model can be determined as the shade preference with the maximum predicted probability. The accuracy of the model in predicting shade preference was assessed using sensitivity, specificity, precision, and accuracy. Sensitivity was calculated as the number of shade preference correctly predicted divided by the total number of observations of the same shade preference. Specificity was calculated as the number of other shade preferences correctly predicted divided by the total number of observations of these shade preferences. Precision was calculated as the number of shade preference correctly predicted divided by the total number of predictions for the same shade preference. Accuracy was calculated as the number of correctly predicted shade preferences divided by the number of observations.

The power output by the photovoltaic panels was analyzed using the following model:

$$P = \alpha + f(R_S) + N(0, \sigma_{day}) + N(0, \sigma) \quad (231)$$

where,  $P$  represents the power output (W);  $\alpha$  represents the intercept;  $f(R_S)$  represents a smooth function;  $\sigma_{day}$  is the standard deviation of the random effect of the day;  $\sigma$  is the standard deviation of the residues.

The effect of the shades in the RHL was analyzed using the following model:

$$RHL = \alpha_{i,j} + f_{i,j}(time) + N(0, \sigma_d) + N(0, \sigma_{j,d}) + N(0, \sigma_{i,j,d}) + N(0, \sigma) \quad (232)$$

$$cor(\varepsilon_m, \varepsilon_n) = \varphi^s \quad (233)$$

where,  $\alpha_{i,j}$  represents the intercept for location  $i$  (underneath or outside the structure) and structure  $j$  (panel or cloth);  $f_{i,j}(time)$  represents a smooth function for location  $i$  and structure  $j$ ;  $\sigma_d$  is the standard deviation of the random effect of the day  $d$ ;  $\sigma_{j,d}$  is the standard deviation of the random effect of the structure  $j$  within the day  $d$ ;  $\sigma_{i,j,d}$  is the standard deviation of the random effect of the location  $i$  within the structure  $j$  within the day  $d$ ;  $\sigma$  is the standard deviation of the residues;  $cor(\varepsilon_m, \varepsilon_n)$  represents the correlation between residues of the observations  $m$  and  $n$  within the location  $i$  within the structure  $j$  within the day  $d$ ;  $s$  is the time interval between observations  $m$  and  $n$  ( $\geq 0$ );  $\varphi$  is the correlation coefficient ( $\geq 0$ ). Equation (233) represents the continuous time autoregressive model of order 1 (Pinheiro and Bates, 2000). Statistical difference between the smooth functions was determined using the method from Rose et al. (2012) with the inclusion of fixed effects.

Equations (226) to (233) were modelled in R (R Core Team, 2018) using the mgcv package (Wood, 2011) and adding a penalty in the null space of the smooth functions (Marra and Wood, 2011). Statistical significance of the terms was analyzed using the chi-square test and terms not statistically significant were removed from the model. Expected values and the simultaneous 95% Bayesian credible intervals (similar to a 95% confidence intervals) were obtained through simulating 10,000 draws from the

Bayesian posterior probability density of the model, as described by Simpson (2016). The expected value was obtained through averaging the draws and the 95% Bayesian credible intervals were obtained from the quantiles of the draws.

### ***3. RESULTS AND DISCUSSION***

The mean measured values for solar radiance ( $R_S$ ), ultraviolet solar irradiance ( $U_V$ ), air temperature ( $T_A$ ), relative humidity ( $R_H$ ), and wind speed ( $W_S$ ) were  $501.9 \pm 47.4 \text{ W m}^{-2}$ ,  $23.7 \pm 1.8 \text{ W m}^{-2}$ ,  $28.1 \pm 0.54 \text{ }^\circ\text{C}$ ,  $39.2 \pm 2.9 \%$  and  $0.33 \pm 0.15 \text{ m s}^{-1}$ , respectively. Figure 65 shows that  $R_S$  and  $U_V$  have similar trends, with values above  $700 \text{ W m}^{-2}$  for  $R_S$  and  $30 \text{ W m}^{-2}$  for  $U_V$  between 10:00h to 14:00h, respectively. The peak values were  $>800 \text{ W m}^{-2}$  for  $R_S$  and  $35 \text{ W m}^{-2}$  for  $U_V$  and occurred at around 12:00h.  $R_S$  and  $U_V$  were generally higher in the morning than in the afternoon, likely because of the existence of larger number of clouds in the afternoon. From 11:00h to 17:00h,  $T_A$  was above  $29^\circ\text{C}$  and  $R_H$  was below 40%.  $W_S$  was very low throughout the day ( $<0.5 \text{ m s}^{-1}$ ), with moderate increase of  $W_S$  to  $0.7 \text{ m s}^{-1}$  between 09:00h and 12:00h (convection heat loss was calculated to be approximately  $10 \text{ W m}^{-2}$ ; Silva and Maia, 2013). High values of  $R_S$  and  $T_A$  and low values of  $W_S$  are typical in tropical areas. This environmental condition cause heat stress livestock (Costa et al., 2018ab; Maia et al., 2015) and compromise animal comfort and welfare (Kamal et al. 2018). For these environmental conditions, the Humane Farm Animal Care organization requires shades for the animals (HFAC 2012, 2013, 2014, 2017).

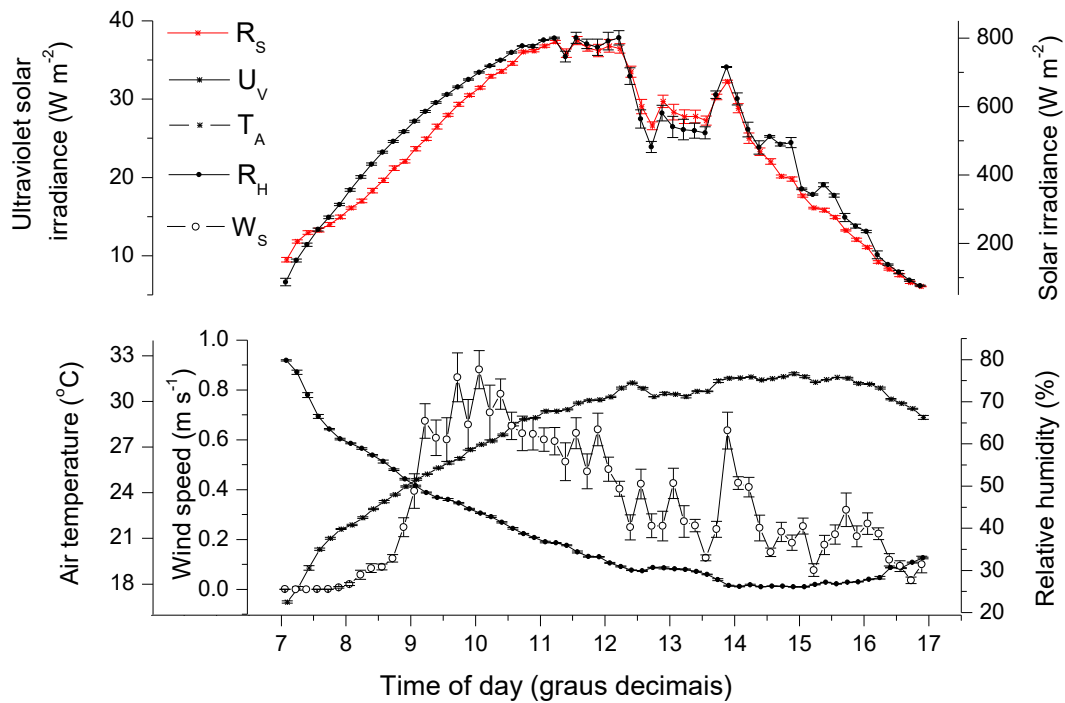


Figure 65. Means ( $\pm$ SEM) of air temperature ( $T_A$ , °C), relative air humidity ( $R_H$ , %), solar radiation ( $R_S$ ,  $W m^{-2}$ , spectral range = 0.3-3.6  $\mu m$ ), ultraviolet solar irradiance ( $U_V$ ,  $W m^{-2}$ , spectral range = 0.28-0.4  $\mu m$ ), and wind speed ( $W_S$ ,  $m s^{-1}$ ).

The results from ANOVA showed that the animals spent less than 1% of their time under the shade projected from cloth (independently of level of solar irradiance), 38% to that from photovoltaic panels, and 61.2% exposed to the sun (Figure 66). Oliveira et al. (2019) reported that, for a similar intensity of solar radiation, Holstein cows stayed ~50% of the time in a shade from 100%-blockage cloth. The intensity of solar radiance (not air temperature, which increased continually throughout the day; Figure 65 and Figure 67) seemed to be the major factor leading to the shade-seeking behavior

of the sheep (Figure 66; a similar observation was reported for Holstein cows; Oliveira et al., 2019). However, the guidelines by the Humane Farm Animal Care (HFAC, 2014, 2012) accounted for air temperature alone (“If daytime summer temperatures are consistently above 29.4°C, shade, fans, misting/fogging systems or other cooling equipment must be provided to animals (dairy cow and young dairy beef)”). Our observations, together with previous observations (Gebremedhin et al., 2011; Oliveira et al., 2019), indicate that level of solar radiance should be considered in conjunction with air temperature. Future research should consider the effects of solar radiation as a thermal environmental trigger for shade-seeking behavior (DaSilva et al., 2010; DaSilva et al., 2015; Mitchell et al., 2018; Oliveira et al., 2014) as well as other factors such as social hierarchy and interaction, phenotype adaptation, and maturity.

Sheep were thermally comfortable under the shade from photovoltaic panels because they were majority lying down, a behavior known to indicate thermal comfort (Gebremedhin et al., 2011). Sheep spent ~90% of the observed time doing the following activities: (1) exposed to the sun, standing and grazing (SSG), (2) under the shade from photovoltaic panels, lying and ruminating (PLR), and (3) under the shade from photovoltaic panels, lying and idling (PLI). SSG decreased ( $p < 0.05$ ) from  $83.61 \pm 3.62$  % to  $26.91 \pm 6.29$  % when  $R_s$  increased from 250 to  $850 \text{ W m}^{-2}$  (Figure 67) whereas PLR and PLI increased from  $0.61 \pm 2.36$  % to  $22.5 \pm 3.88$  % and  $0.27 \pm 2.94$  to  $40.73 \pm 3.42$  %, respectively. PLR was not significantly different ( $p > 0.05$ ) between lambs and ewes but ewes had higher PLI than lambs ( $p < 0.05$ ). The time

spent in the shade projected from cloth was negligible.

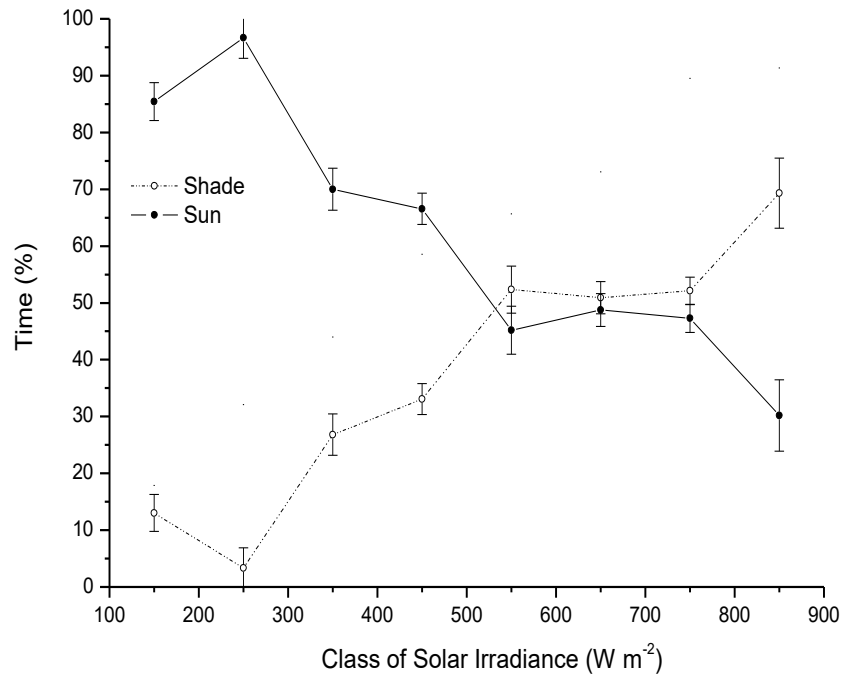


Figure 66. Least square means ( $\pm$ SEM) of the time animals spent in the shade or under the sun (%) for different levels of solar radiation.

Lambs spend more time in the sun than ewes (Figure 68), which can be explained by the lower grazing efficiency of lambs. Lambs have lower bite strength and compensate by grazing for longer periods of time ( $p < 0.05$ ; Figure 67; Vallentine, 2001). Lambs spent 69.3% of their time exposed to the sun vs. 28.7% for ewes. For high levels of  $R_s$  (between 09:00 to 14:00 hours, which peaked at  $800 W m^{-2}$ ), lambs spent  $\sim 40\%$  of their time in the shade while ewes spent  $\sim 60\%$  (Figure 68).

The statistical model developed to predict shade preference explained 15% of the

deviance. Table 37 shows the confusion matrix, sensitivity, specificity, precision, and accuracy of the model. Except for predicting shade preference for cloth, which had a low number of observations, performance metrics were satisfactory. For example, shade preference predictions were ~70% accurate.

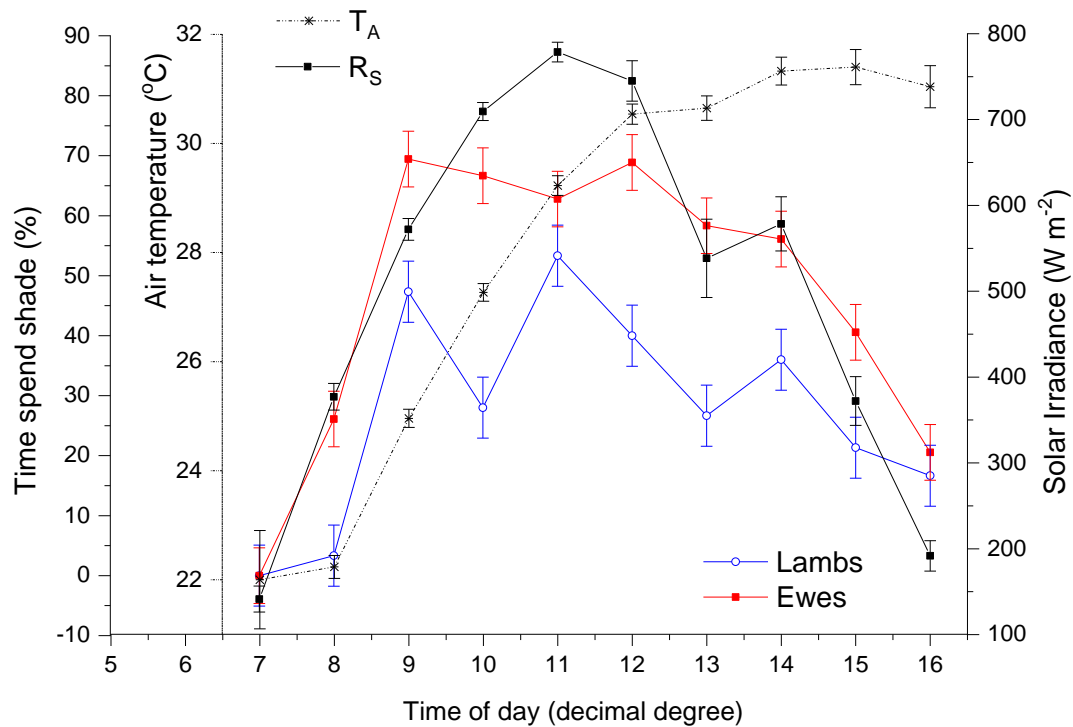


Figure 67. Least square mean ( $\pm$ SEM) of air temperature ( $T_A$ , °C), solar radiation ( $R_S$ ,  $W m^{-2}$ ; spectral range = 0.3-3.6  $\mu m$ ) and time lambs and ewes spent in the photovoltaic panel shade (%) by lambs and ewe.

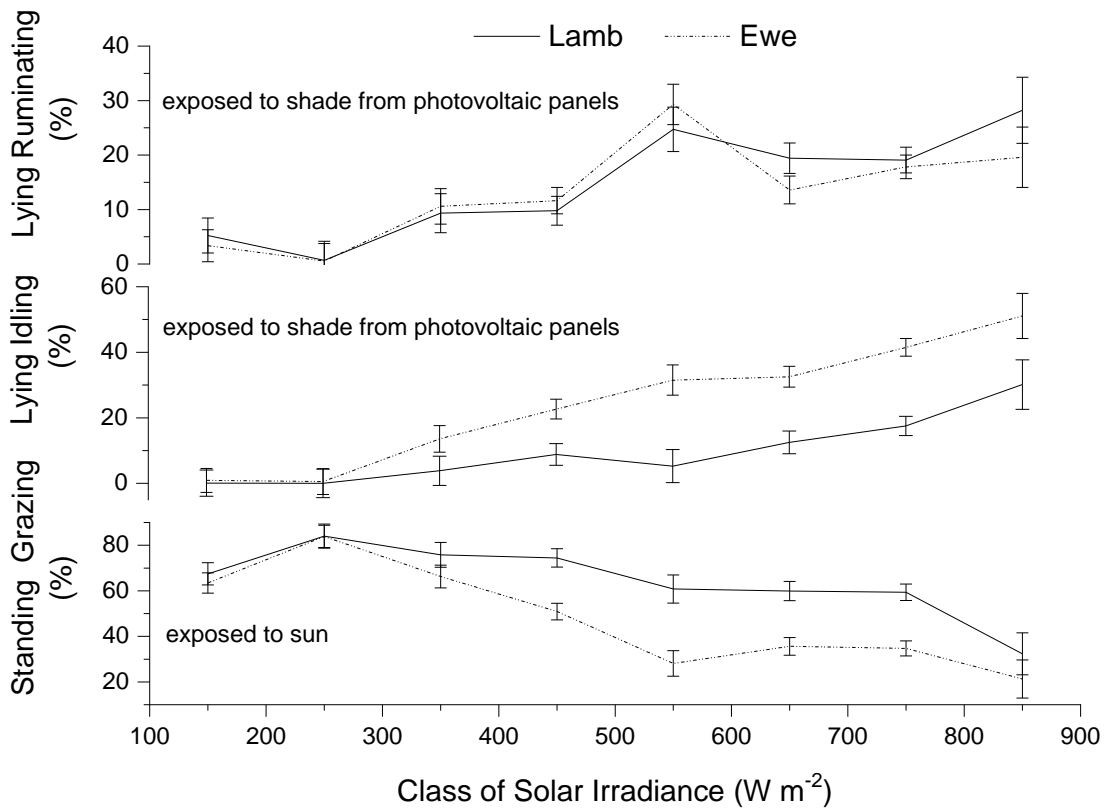


Figure 68. Least square means ( $\pm$ SEM) of time of animal activities (%).

Figure 69 and Figure 70 show the estimated and observed probabilities, respectively, of shade preference. Both Figures show similar trends, which validates the statistical model. The preference for shade from photovoltaic panels increased with increasing solar radiation while no practical preference was observed for the shade from cloth. In addition, the lower bound of the confidence interval for the probability of preferring shade from solar panels was consistently higher than that of the upper bound of the confidence interval for the probability of preferring shade from cloth (Figure 69). This shows that animals preferred shade from solar panels over cloth unconditionally on the intensity of the solar irradiance. The advantage of making inference using machine

learning models (Figure 69) over ranges of observed data (Figure 70) is twofold. First, inference is based on continuous values of  $R_S$  (rather than on discrete ranges), thus allowing for precise inference over values of  $R_S$ . Second, inference includes measures of uncertainty (credible intervals), which cannot be obtained from observed data alone. This shows the advantage of using modern machine learning techniques, such as multinomial GAM models, to precisely analyze large datasets (Milan et al., 2018, 2019).

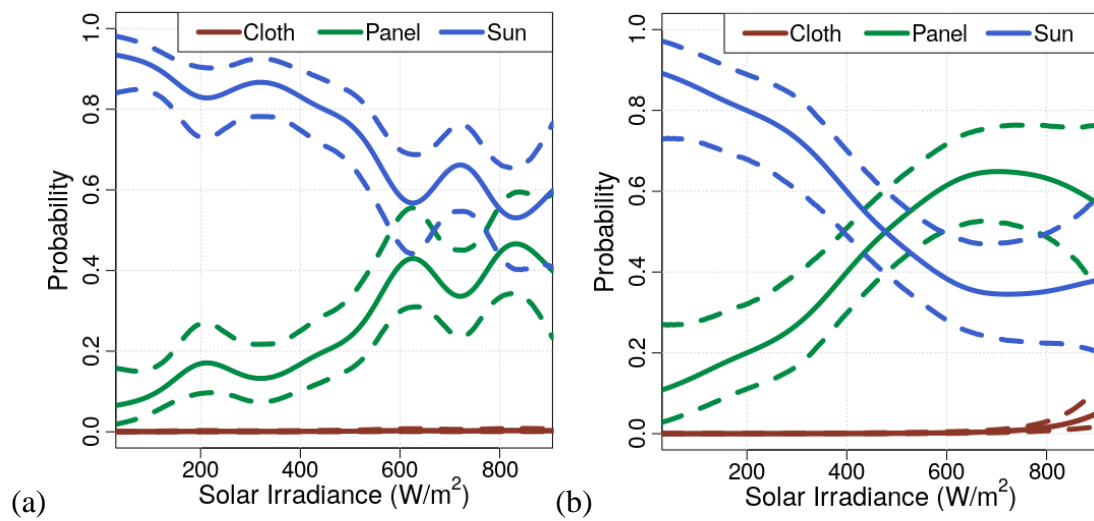


Figure 69. Estimated probabilities for lambs (a) and ewes (b) under the shade from cloth (Cloth) or solar panels (Panel) or exposed to the sun (Sun). Continuous lines represent expected values. Broken lines represent simultaneous 95% Bayesian credible intervals.

Table 37. Confusion matrices and performance metrics (sensitivity, specificity, precision, and accuracy) of the statistical model developed to predict shade preference. Results shown for lambs, ewes, and both animals.

|                 |       | Observed |       |       |       |       |       |       |       |       |       |       |       |
|-----------------|-------|----------|-------|-------|-------|-------|-------|-------|-------|-------|-------|-------|-------|
|                 |       | Lambs    |       |       |       | Ewes  |       |       |       | Both  |       |       |       |
|                 |       | Cloth    | Panel | Sun   | Total | Cloth | Panel | Sun   | Total | Cloth | Panel | Sun   | Total |
| Predicted       | Cloth | 0        | 0     | 0     | 0     | 0     | 0     | 0     | 0     | 0     | 0     | 0     | 0     |
|                 | Panel | 0        | 56    | 37    | 93    | 3     | 616   | 344   | 963   | 3     | 672   | 381   | 1,056 |
|                 | Sun   | 2        | 351   | 1,025 | 1,378 | 6     | 220   | 611   | 840   | 8     | 571   | 1,636 | 2,215 |
| Total           |       | 2        | 407   | 1,062 | 1,471 | 9     | 836   | 955   | 1,800 | 11    | 1,243 | 2,017 | 3,271 |
| Sensitivity (%) |       | 0        | 13.76 | 96.52 | -     | 0     | 73.68 | 63.98 | -     | 0     | 54.06 | 81.11 | -     |
| Specificity (%) |       | 73.59    | 96.33 | 15.86 | -     | 68.51 | 63.38 | 72.90 | -     | 70.80 | 80.67 | 53.59 | -     |
| Precision (%)   |       | 0        | 60.22 | 74.38 | -     | 0     | 63.97 | 72.74 | -     | 0     | 63.64 | 73.86 | -     |
| Accuracy (%)    |       | -        | -     | -     | 73.49 | -     | -     | -     | 68.17 | -     | -     | -     | 70.56 |

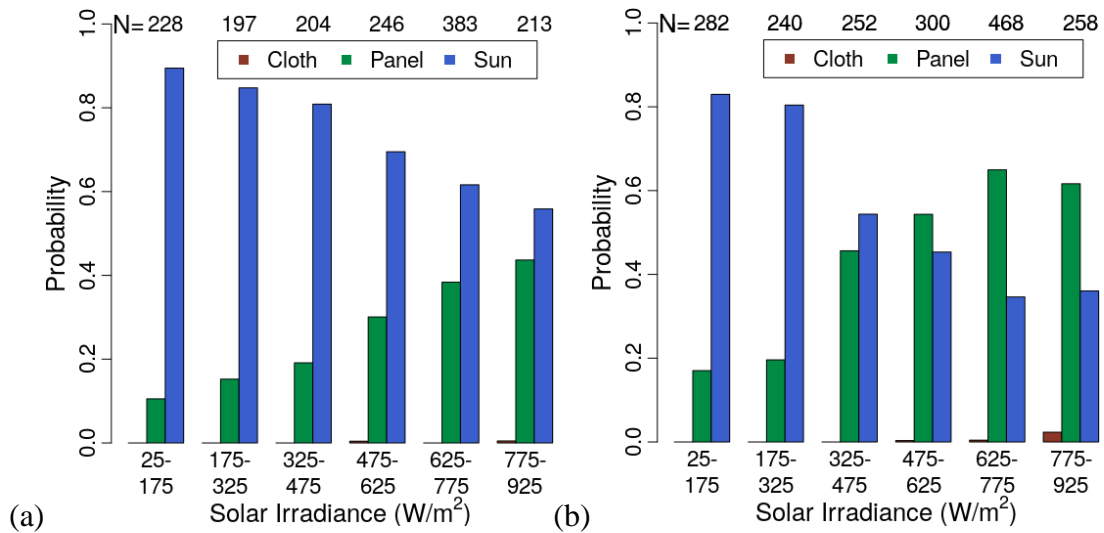


Figure 70. Observed probabilities for lambs (a) and ewes (b) under the shade from cloth (Cloth) or solar panels (Panel) or exposed to the sun (Sun). N represents number of samples for each range of solar radiation. The ranges for solar radiation were inclusive for the lower bound and exclusive for the upper bound.

The shade preference reflected the differences in the thermal comfort provided by the shade structures (Figure 71). The thermal comfort was assessed using the radiant heat load (RHL), which was  $\sim 40 \text{ W m}^{-2}$  lower in the shade underneath the photovoltaic panels than in the shade underneath the cloth. Previous studies reported a similar conclusion on shade-preference of dairy cows (Schütz et al., 2009; Tucker et al., 2008).

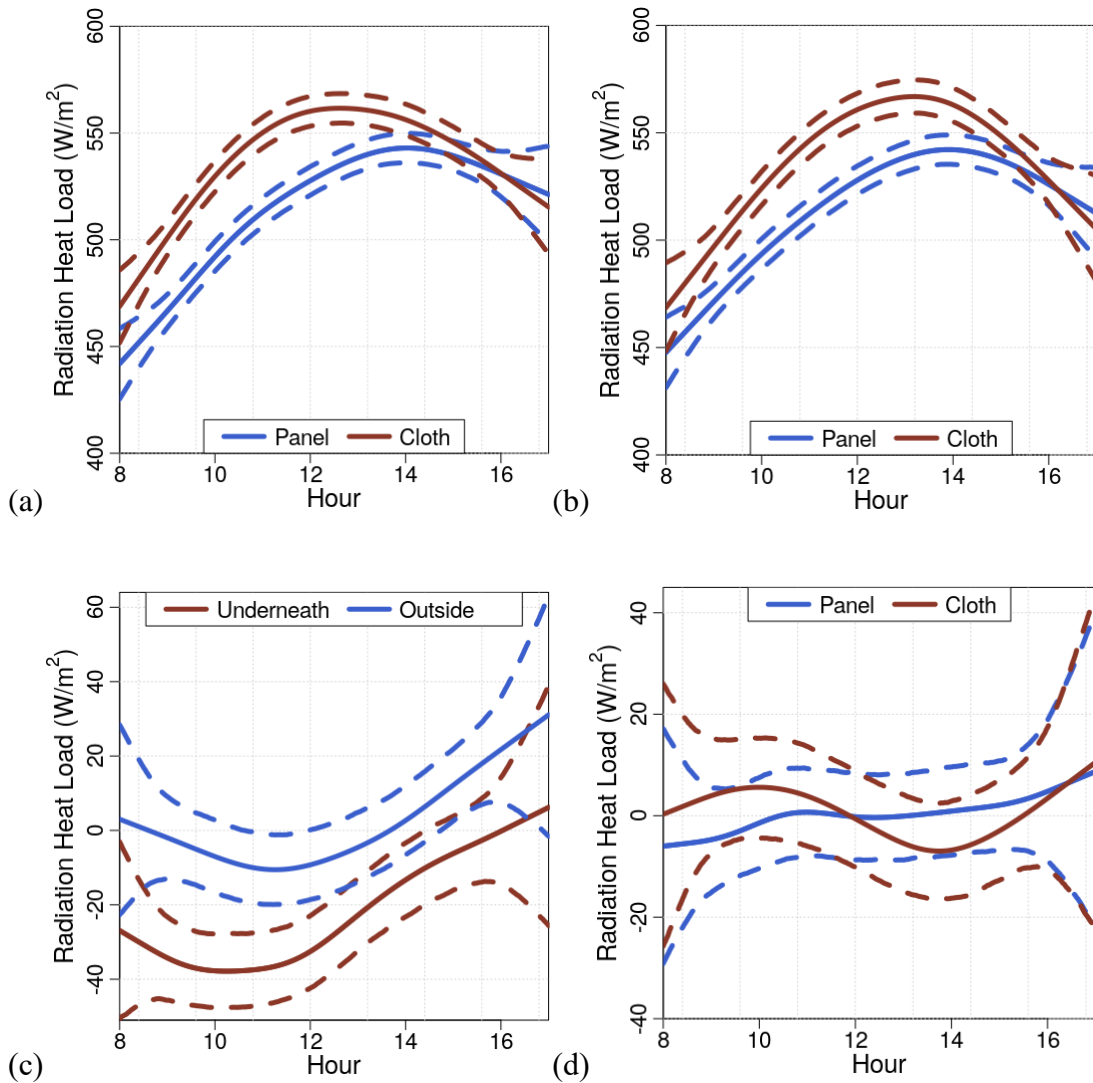


Figure 71. Radiant heat load measured in the shade projected underneath the shade structure (a) or outside (b). Difference between radiant heat load in the shade projected by photovoltaic panels and cloth (c), and between underneath and outside (d). Broken lines represent simultaneous 95% Bayesian credible intervals.

As expected, Figure 72a shows that when RS increased the power output from the photovoltaic panels also increased. The GAM model for power output explains 67.2%  
320

of the deviance. The estimated efficiency of the photovoltaic panels was  $17.96 \pm 0.19$  % (mean  $\pm$  SEM), close to the designed peak efficiency of 16.72%. Figure 72b shows the electrical energy generated by the photovoltaic panels and the amount of CO<sub>2</sub> not emitted to the atmosphere. During one year, the artificial shading structure using photovoltaic panels generated 5.19 MWh and reduced the emission of 2.77 ton-CO<sub>2</sub> to the atmosphere. Assuming that the price of the electricity is 0.1424 US\$/kWh, this shade structure saved US\$ 740 per year. The total cost was US\$ 6400.00.

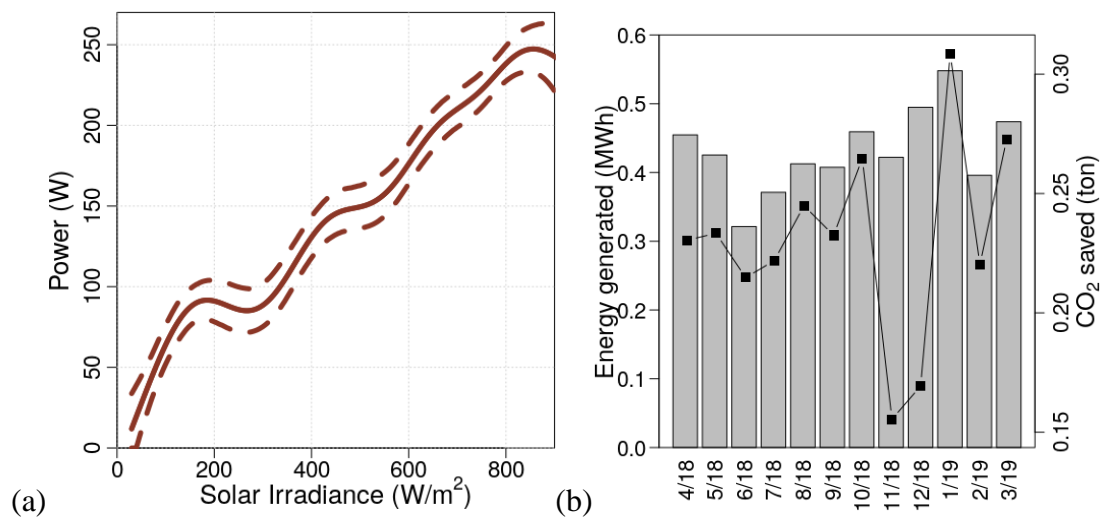


Figure 72. Power output vs. intensity of solar radiation (a). Monthly energy generated by the photovoltaic panels (bars) and amount of CO<sub>2</sub> (points) not emitted to the atmosphere (b). Broken lines represent simultaneous 95% Bayesian credible intervals.

Our results favor the development of sustainable co-generation systems using photovoltaic panels, which co-generate electrical energy and agricultural products. We specifically studied co-generation with agricultural products from sheep and we

encourage future research to explore the possibility of sustainable co-generation systems with other livestock species. These studies could also determine the number of shade structures and the area for each shade structure for different livestock species. Each livestock specie has an unique social hierarchy and social interaction (e.g., even though a shade structure might have enough shade area for all cattle in a farm, they might not use it simultaneously because of social conflicts between the animals), which requires specific studies to determine the number and the area of the shade structures. Future research could also evaluate the reduction in heat-stress by photovoltaic panels based on measuring physiological data (we inferred heat-stress based on the RHL index, Figure 71). Such data could demonstrate the correlation between heat-stress physiological responses and the shade-seeking behavior.

#### ***4. CONCLUSION***

The following conclusions can be drawn from this study:

- (1) Sheep (lambs and ewes) prefer shade from photovoltaic panels over shade from cloth with 80% blockage of solar radiation, regardless of the intensity of solar radiation.
- (2) Sheep (lambs and ewes) spend more than 70% of the time under the shade from photovoltaic panels when solar radiation was  $\geq 800 \text{ W m}^{-2}$ .
- (3) Lambs spent more time grazing in the sun than ewes (69.3% vs. 28.7%).

(4) In one year, the photovoltaic panels produced 5.19 MWh, reduced the emission of 2.77 ton-CO<sub>2</sub> to the atmosphere, and saved US\$ 740.

### ***Acknowledgment***

The authors acknowledge the technical support provided by Prof. Dr. Pedro da Costa Aguiar Alves, Mr. Cláudio Roberto Pires (Blue Sol Energia Solar), Mrs. Animal Scientist Maria Elivânia Vieira Almeida. Funding provided by the São Paulo State University “Júlio de Mesquita Filho,” São Paulo Research Foundation (FAPESP, grant numbers: 2014/09639-7, 2011/17388-6, 2016/12278-1, 2018/112218-4), Universities Federation of Animal Welfare (UFAW), Brazilian National Council of Technological and Scientific Development (CNPq, Proc. 203312/2014-7), and United States Department of Agriculture (USDA/HATCH funds as part of the W-3173 Regional Project through Cornell University).

## REFERENCES

- Adeh EH, Selker JS, Higgins CH. Remarkable agrivoltaic influence on soil moisture, micrometeorology and water-use efficiency. *PLoS ONE* 13(11):e0203256, 2018.
- Alexandratos N, Bruinsma J. *World Agriculture Towards 2030/2050: The 2012 Revision*. Food and Agriculture Organization of the United Nations. ESA Working Paper no. 12-03, 2012.
- Averós X, Lorea A, Beltrán de Heredia I, Arranz J, Ruiz R, Estevez I. Space availability in confined sheep during pregnancy, effects in movement patterns and use of space. *PLoS ONE* 9(4):e94767, 2014.
- Brown-Brandl TM, Eigenberg RA, Nienaber JA, Hahn GL. Dynamic response indicators of heat stress in shaded and non-shaded feedlot cattle, part 1: analyses of indicators. *Biosystems Eng* 90:451–462, 2005.
- Brown-Brandl TM, Eigenberg RA, Nienaber JA. Benefits of providing shade to feedlot cattle of different breeds. *Trans ASABE* 6(4):1563–1570, 2009.
- Brown-Brandl TM, Chitko-McKown CG, Eigenberg RA, Mayer JJ, Welsh TH, Davis JD, Purswell JL. Physiological responses of feedlot heifers provided access to different levels of shade. *Animal* 11:1344–1353, 2017.
- Cloete SWP, Muller CJC, Durand A. The effects of shade and shearing date on the production of Merino sheep in the Swartland region of South Africa. *S Afr J Anim Sci* 324

30(3):164–171, 2000.

da Silva RG, Guilhermino MM, de Moraes DAEF. Thermal radiation absorbed by dairy cows in pasture. *Int J Biometeorol* 54(1):5–11, 2010.

da Silva RG, Maia ASC. *Principles of Animal Biometeorology*. Springer: Berlin, Germany, 2013

da Silva RG, Maia ASC, de Macedo Costa LL. Index of thermal stress for cows (ITSC) under high solar radiation in tropical environments. *Int J Biometeorol* 59(5):551–559, 2015.

Costa CCM, Maia ASC, Brown-Brandl TM, Chiquitelli Neto M, Fonsêca VFC. Thermal equilibrium of Nellore cattle in tropical conditions: an investigation of circadian pattern. *J Therm Biol* 74:317–324, 2018a.

Costa CCM, Maia ASC, Nascimento ST, Nascimento CCN, Chiquitelli Neto MC, Fonsêca VFC. Thermal balance of Nellore cattle. *Int J Biometeorol* 62(5):723–731, 2018b.

Dickrell J. Solar Panels Double as Summer Cow Shades. Dairy Herd Management. Available at <https://www.dairyherd.com/article/solar-panels-double-summer-cow-shades> (Published in 10 September 2018 and accessed on 08 October 2019).

Domingos HGT, Maia ASC, Souza JBF, Silva RB, Vieira FMC, da Silva RG. Effect of shade and water sprinkling on physiological responses and milk yields of Holstein  
325

cows in a semi-arid region. *Livest Sci* 154:169–174, 2013.

Eigenberg RA, Brown-Brandl TM, Nienaber JA. Shade material evaluation using a cattle response model and meteorological instrumentation. *Int J Biometeorol* 54(6):509–515, 2010.

EPE. *Technical Note PR 04/18: Potential Energetic Resources for the 2050 Horizon [Portuguese]*. Brazilian Energy Research Enterprise, Ministry of Mines Energy, 2018.

Ferreira FD, Gennari RS, Dahl GE, De Vries A. Economic feasibility of cooling dry cows across the United States. *J Dairy Sci* 99:9931-9941, 2016.

Ferreira A, Kunh SS, Fagnani KC, De Souza TA, Tonezer C, Dos Santos GR, Coimbra-Araújo CH. Economic overview of the use and production of photovoltaic solar energy in Brazil. *Renew Sust Energ Rev* 81:181–191, 2018.

Fonsêca VFC, Saraiva EP, Pimenta Filho EC, Furtado DA, Mariz TMA, Silva AL, Almeida MEV, Pinheiro AC. Influence of the climatic environment and duration of labor on the mother-offspring interaction in Morada Nova sheep. *J Anim Sci* 92(9):4123–4129, 2014.

Gaughan JB, Goodwin PJ, Schoorl TA, Young BA, Imbeah M, Mader TL, Hall A. Shade preferences of lactating Holstein - Friesian cows. *Aust J Exp Agric* 38(1):17-21, 1998.

Gaughan JB, Mader TL. Body temperature and respiratory dynamics in un-shaded  
326

beef cattle. *Int J Biometeorol* 58(7):1443–1450, 2014.

Gaughan JB, Mader TL, Holt SM, Sullivan ML, Hahn GL. Assessing the heat tolerance of 17 beef cattle genotypes. *Int J Biometeorol* 54(6):617–627, 2010.

Gebremedhin KG, Lee CN, Hillman PE, Brown-Brandl TM. Body temperature and behavioral activities of four breeds of heifers in shade and full sun. *Appl Eng Agric.* 27(6):999-1006, 2011.

Grimshaw K, Miller RK, Palma MA, Kerth CR. Consumer perception of beef, pork, lamb, chicken, and fish. *Meat Sci* 96(1):443–444, 2014.

Herrero M, Thornton PK, Gerber P, Reid RS. Livestock, livelihoods and the environment: understanding the trade-offs. *Curr Opin Env Sust* 1(2), 111–120, 2009.

HFAC. *Animal Care Standards – Young Dairy Beef*. Humane Farm Animal Care, 2012.

HFAC. *Animal Care Standards - Sheep*. Humane Farm Animal Care, 2013.

HFAC. *Animal Care Standards - Cows*. Humane Farm Animal Care, 2014.

HFAC. *Animal Care Standards - Beef Cattle*. Humane Farm Animal Care, 2017.

Hinrich RA, Kleinbach M, dos Reis LB. *Energy and the Environment [Portuguese]* (2<sup>nd</sup> ed.). Cengage Learning: São Paulo, Brazil, 2015

Hunter MC, Smith RG, Schipanski ME, Atwood LW, Mortensen DA. Agriculture in 2050: Recalibrating Targets for Sustainable Intensification. *BioScience* 67(4):386–391, 2017.

Kamal R, Dutt T, Patel M, Dey A, Bharti PK, Chandran PC. Heat stress and effect of shade materials on hormonal and behavior response of dairy cattle: a review. *Trop Anim Health Prod* 50(4):701–706, 2018.

Littell RC, Milliken GA, Stroup WW, Wolfinger RD, Schabenberger O. *SAS® for Mixed Models* (2<sup>nd</sup> ed.). Cary, North Carolina, 2006.

Maia, ASC, da Silva RG, Loureiro CMB. Sensible and latent heat loss from the body surface of Holstein cows in a tropical environment. *Int J Biometeorol* 50(1):17–22, 2005.

Maia ASC, da Silva RG, Nascimento ST, Nascimento CCN, Pedroza HP, Domingos HGT. Thermoregulatory responses of goats in hot environments. *Int J Biometeorol* 59(8):1025–1033, 2015.

Marra G, Wood SN. Practical variable selection for generalized additive models. *Comput Stat Data Anal* 55:2372–2387, 2011.

Martin P, Bateson P. *Measuring Behaviour: An Introductory Guide*. Cambridge University Press: Cambridge, USA, 2007

McAlpine CA, Etter A, Fearnside PM, Seabrook L, Laurance WF. Increasing world  
328

consumption of beef as a driver of regional and global change: A call for policy action based on evidence from Queensland (Australia), Colombia and Brazil. *Global Environ Chang* 19(1):21–33, 2009

MCTIC. *CO<sub>2</sub> Emission Factors for the Generation of Electrical Energy in the Brazilian National Interconnected System 2018* [Portuguese]. Brazilian Ministry of Science, Technology, Innovation and Communication, 2018.

Middel A, Selover N, Hagen B, Chhetri N. Impact of shade on outdoor thermal comfort—a seasonal field study in Tempe, Arizona. *Int J Biometeorol* 60(12):1849–1861, 2016

Milan HFM, Maia ASC, Costa CCM, Gorczyca MT, Perano KM, Moura GAB, Castro PA, Fonsêca VFC, Hariharan B, Neto MC, Gebremedhin KG. Precision Livestock Farming Big Data (PLFBD): Physiological and Environmental Data. *In Preparation*, 2019.

Milan HFM, Perano KM, Gebremedhin KG. *Survey and Future Prospects in Precision Dairy Farming*. In: 10th International Livestock Environment Symposium (ILES X). Omaha, NE: ASABE, 2018.

Mitchell D, Snelling EP, Hetem RS, Maloney SK, Strauss WM, Fuller A. Revisiting concepts of thermal physiology: Predicting responses of mammals to climate change. *J Anim Ecol* 87:956–973, 2018.

Mitlöhner FM, Morrow JL, Dailey JW, Wilson SC, Galyean ML, Miller MF, McGlone JJ. Shade and water misting effects on behavior, physiology, performance, and carcass traits of heat-stressed feedlot cattle. *J Anim Sci* 79:2327-2335, 2001.

Mitlohner FM, Galyean ML, McGlone JJ. Shade effects on performance, carcass traits, physiology, and behavior of heat-stressed feedlot heifers. *J Anim Sci* 80(8):2043-2050, 2002.

Oliveira SEO, Costa CCM, de Souza JBF, de Queiroz JPAF, Maia ASC, Costa LLM. Short-wave solar radiation level willingly tolerated by lactating Holstein cows in an equatorial semi-arid environment. *Trop Anim Health Prod* 46:1413–1417, 2014.

Oliveira SEO, Costa CCM, Chiquitelli Neto M, Dalla Costa FA, Maia ASC. Effects of shade location and protection from direct solar radiation on the behavior of Holstein cows. *Int J Biometeorol* accepted, 2019.

Pereira EB, Martins FR, Gonçalves AR, Costa RS, Lima FJL, Ruther R, Abreu SL, Tiepolo GM, Pereira SV, Souza JG. *Atlas of Brazilian Potential Solar Energy [Portuguese]* (2<sup>nd</sup> ed). INPE São José dos Campos: INPE, 2017.

Pinheiro J, Bates D. *Mixed-effects models in S and S-PLUS*. Springer Science & Business Media, 2000.

Polsky L, von Keyserlingk MAG. Invited review: Effects of heat stress on dairy cattle welfare. *J Dairy Sci* 100:8645–8657, 2017.

Popp A, Lotze-Campen H, Bodirsky B. Food consumption, diet shifts and associated non-CO<sub>2</sub> greenhouse gases from agricultural production. *Global Environ Chang* 20:451–462, 2010.

R Core Team. *R: A Language and Environment for Statistical Computing*. R Foundation for Statistical Computing. Vienna, Austria, <https://www.R-project.org/>, 2018.

Rose NL, Yang H, Turner SD, Simpson GL. An assessment of the mechanisms for the transfer of lead and mercury from atmospherically contaminated organic soils to lake sediments with particular reference to Scotland, UK. *Geochimica et Cosmochimica Acta* 82:113–135, 2012.

SAS Institute. *SAS/STAT user's Guide, Version 8 (Vol. 2)*. SAS Institute. Carry, North Carolina, 1999.

Schütz KE, Cox NR, Matthews LR. How important is shade to dairy cattle? Choice between shade or lying following different levels of lying deprivation. *Appl Anim Behav Sci* 114:307–318, 2008.

Schütz KE, Rogers AR, Cox NR, Tucker CB. Dairy cows prefer shade that offers greater protection against solar radiation in summer: Shade use, behaviour, and body temperature. *Appl Anim Behav Sci* 116:28–34, 2009.

Schütz KE, Cox NR, Tucker CB. A field study of the behavioral and physiological

effects of varying amounts of shade for lactating cows at pasture. *J Dairy Sci* 97:3599–3605, 2014.

Simpson G. *Simultaneous Intervals for Smooths Revisited*. <https://www.fromthebottomoftheheap.net/2016/12/15/simultaneous-interval-revisited/> (Accessed on April 26 2019), 2016.

Sobrosa Neto RC, Berchin II, Magtoto M, Berchin S, Xavier WG, de Andrade Guerra JBSO. An integrative approach for the water-energy-food nexus in beef cattle production: A simulation of the proposed model in Brazil. *J Clean Prod* 204:1108-1123, 2018.

St-Pierre NR, Cobanov B, Schmitkey G. Economic Losses from Heat Stress by US Livestock Industries. *J Dairy Sci* 86:E52–E77, 2003.

Tucker CB, Rogers AR, Schütz KE. Effect of solar radiation on dairy cattle behaviour, use of shade and body temperature in a pasture-based system. *Appl Anim Behav Sci* 109:141–154, 2008.

Tucker CB, Coetzee JF, Stookey JM, Thomson DU, Grandin T, Schwartzkopf-Genswein KS. Beef cattle welfare in the USA: identification of priorities for future research. *Anim Health Res Rev* 16:107–124, 2015

Umer F, Aslam MS, Rabbani MS, Hanif MJ, Naeem N, Abbas MT. Design and Optimization of Solar Carport Canopies for Maximum Power Generation and

Efficiency at Bahawalpur. *Int J Photoene* 2019(6372503):1–8, 2019

Vallentine JF. *Grazing Management* (2<sup>nd</sup> ed). Elsevier, 2001.

Verbeke W, Pérez-Cueto FJA, Barcellos MD, Krystallis A, Grunert KG. European citizen and consumer attitudes and preferences regarding beef and pork. *Meat Sci* 84:284–292, 2010.

von Keyserlingk MAG, Martin NP, Kebreab E, Knowlton KF, Grant RJ, Stephenson M, Sniffen CJ, Harner JP, Wright AD, Smith SI. Invited review: Sustainability of the US dairy industry. *J Dairy Sci* 96:5405–5425, 2013.

Wood SN. Fast stable restricted maximum likelihood and marginal likelihood estimation of semiparametric generalized linear models: Estimation of Semiparametric Generalized Linear Models. *J R Statist Soc B* 73:3–36, 2011.

Wood SN, Pya N, Säfken B. Smoothing Parameter and Model Selection for General Smooth Models. *J Am Stat Assoc* 111(516):1548-1575, 2016.

Wood SN. *Generalized Additive Models: An Introduction in R* (2<sup>nd</sup> ed). Boca Raton: CRC Press, 2017.

## CHAPTER 9: PRECISION LIVESTOCK FARMING BIG DATA: PLFBD

Hugo F. M. Milan, Alex Sandro Campos Maia, Cintia C. M. Costa, Kristen M. Perano, Michael T. Gorczyca, Gustavo A. B. Moura, Patric A. Castro, Vinícius F. C. Fonsêca, Bharath Hariharan, Marcos Chiquitelli Neto, Kifle G. Gebremedhin

*In Preparation.*

### ***Abstract***

Machine learning and computer vision have great potential in precision livestock farming applications. The success of these applications depends on big data that is publicly available to researchers for developing and validating algorithmic procedures. This paper describes the first publicly available precision livestock farming big data for computer vision and machine learning (PLFBD). PLFBD contains extensive data on 3D meshes, photos, thermo-images, surface temperatures, internal-body temperatures, respiration rates, evaporation rates, physical measurements (e.g., length and body weight), thickness of tissues (e.g., muscle and fat), feed consumption, and environmental conditions (e.g., air temperature) from experiments performed with dairy cows and piglets. In this study, two benchmark tasks using PLFBD are demonstrated: (1) registration of 3D dairy cow meshes (computer vision application), and (2) development of supervised learning models to predict respiration rate of piglets (machine learning application). For registration of 3D dairy cow meshes, all 8 registration algorithms produced unsatisfactory results. This indicates that registration

of featureless, non-rigid, articulated objects such as animals needs to be improved. For predicting respiration rate of piglets, models from 7 of the 8 machine learning algorithms produced similar performance metrics. The relationships learned by these machine learning models were assessed through generalization and interpretability tests. These tests indicated that some machine learning models learned counterintuitive relationships, such as predicting that respiration rate increases while air temperature decreases. This indicates that precautions should be taken to ensure that machine learning model predictions agree with predictions obtained from first principles.

**Keywords:** big data; computer vision; machine learning; mesh registration; precision livestock farming; respiration rate.

### ***Highlights***

- Big data for computer vision and machine learning applications is made available.
- Applications of machine learning and computer vision algorithms are demonstrated.
- Algorithms for aligning non-rigid, featureless livestock meshes need improvement.
- Machine learning models accurately predicted respiration rate of piglets.
- Machine learning models can potentially produce counterintuitive predictions.

## ***1. INTRODUCTION***

Precision livestock farming focuses on monitoring and managing animals based on individual animal information, which accounts for variations in how each animal responds to environmental conditions (Wathes et al., 2008; Guarino et al., 2017; Milan et al., 2018). This approach offers promise in reducing feed waste, improving animal management, detecting and treating diseases earlier, and increasing animal comfort and welfare (Wathes et al., 2008; Guarino et al., 2017; Milan et al., 2018), which are necessary for sustainably increasing food production for the growing global population (Hunter et al., 2017). A major reason why precision livestock farming may deliver on these promises is because of recent developments in machine learning and computer vision techniques (data-driven techniques for intensive analysis; Milan et al., 2018), which can provide information for individual animal management and decision making.

One issue with applying machine learning and computer vision algorithms to problems in digital agriculture is that they can produce counterintuitive predictions (which might violate conservation laws and established research findings) when the dataset is small or has few predictor variables (Gorczyca et al., 2018; Milan et al., 2019). This issue may be resolved by using big data (defined by NASA as data with high computational and memory requirements; Cox and Ellsworth, 1997). In precision livestock farming, researchers have demonstrated the capability to collect big data (e.g., EU-PLF, Guarino et al., 2017), but this process is challenging, time-consuming, expensive, and

labor intensive. Sharing big data for precision livestock farming can reduce the need for many researchers to collect data as well as facilitate data aggregation from diverse sources. For example, data sharing has driven advances in other fields (Huffman et al., 1997) and data sharing supports the development of sophisticated models with strong predictive performance (Hastie et al., 2008).

The objective of this study is to collect and make publicly available Precision Livestock Farming Big Data (PLFBD; Milan et al., 2019). PLFBD contains physiological responses (skin-surface temperature, hair-coat surface temperature, core temperature, respiration rate, cutaneous evaporation rate), environmental conditions (e.g., air temperature, relative humidity, wind speed), physical measurements (e.g., length and body weight), thickness of tissues (hair-coat, skin, fat, and muscle) and feed consumption from experiments performed with dairy cows and piglets. This dataset provides the necessary information for developing machine learning models for animal bioenergetics.

This paper demonstrates two benchmark tasks using PLFBD: (1) alignment of incomplete 3D images (partial meshes) of dairy cows using computer vision registration algorithms and (2) prediction of respiration rate of piglets from environmental conditions using machine learning algorithms. This paper also discusses challenges and future directions for applying machine learning and computer vision algorithms in precision livestock farming.

## **2. MATERIALS AND METHODS**

PLFBD was developed from two separate experiments—one with dairy cows (Sec. 2.1) and another with piglets (Sec. 2.2). The procedure for aligning partial dairy cow meshes using computer vision algorithms is presented in Sec. 2.3. The procedure for developing machine learning models to predict respiration rate of piglets is presented in Sec. 2.4.

### **2.1. Experimental procedure using dairy cows**

Animal use and care protocol #2017-0029 was approved by the Institutional Animal Care and Use Committee of Cornell University. Table 38 shows the measured variables, the sampling rates, and the number of samples. Dairy cows (multiparous dry Holstein cows) housed in the free-stall Cornell Teaching Dairy Barn (42°26'46.0"N, 76°27'16.2"W) were moved to a tie-stall barn during the experimental period (Table 39). Animals were given access to water and feed ad libitum. During the first six days, the tie-stall barn was equipped with waterbeds (Perano et al., 2015), which were covered with ~1 cm of shavings. The dairy cows were allowed at least one hour to exercise every morning, which involved moving them to the free-stall barn without access to feed.

Table 38. Measured variables, sampling rates, and number of samples for the dataset obtained from the experiment performed with dairy-cows.

| Variables                                  | Sampling rate | #Samples |
|--|---------------|----------|
| Physiological data                         |               |          |
| Animals                                    | -             | 4        |
| 3D Meshes                                  | -             | 141      |
| Thermal images <sup>1</sup>                | -             | 5,063    |
| Photos                                     | -             | 10,463   |
| Skin-surface temperature                   | 30 sec        | *        |
| Hair-coat surface temperature              | 30 sec        | *        |
| Vaginal temperature                        | 1 min         | *        |
| Rectal temperature                         | Twice daily   | 133      |
| Respiration rate                           | Twice daily   | 152      |
| Evaporation rate                           | Twice daily   | 402      |
| Physical measurements <sup>2</sup>         | Once          | 4        |
| Hair-coat thickness                        | Once          | 96       |
| Thickness of internal tissues <sup>3</sup> | Once          | 52       |
| Feed data                                  |               |          |
| Consumption                                | Daily         | 16       |
| Composition                                | Once          | 1        |
| Dry weight                                 | Daily         | 81       |

| Environmental data         |        |        |
|----------------------------|--------|--------|
| Krestel data <sup>4</sup>  | 10 min | 1,996  |
| Campbell data <sup>5</sup> | 30 s   | 32,450 |

<sup>1</sup>Thermal image together with color image. <sup>2</sup>Weight, chest diameter, wither height, and body condition score. <sup>3</sup>Skin, fat, and muscle layers thickness. <sup>4</sup>Air temperature, wet bulb temperature, black-globe temperature, relative humidity, wind speed and direction, and others. <sup>5</sup>Air temperature, black-globe temperature, water flow to waterbeds, and water temperature to/from waterbeds. \*Under preparation.

Table 39. Experimental times that dairy cows were moved to the tie-stall barn and the time the pumps were turned on to circulate water through the waterbeds. Waterbeds were removed from the tie-stall barn after Day 6.

| Day | Cows  |      | Waterbeds      |         |
|-----|-------|------|----------------|---------|
|     | In    | Out  | On             | Off     |
| 1   | 12 pm | 9 pm | -              | -       |
| 2   | 8 am  | 6 pm | 4 pm           | 6 pm    |
| 3   | 8 am  | -    | 8:30 am        | 6 pm    |
| 4   | -     | -    | 11 am          | 8 pm    |
| 5   | -     | -    | 10:30 am       | 8 pm    |
| 6   | -     | 9 pm | 9:30 am        | 8:30 pm |
| 7   | -     | -    | R <sup>1</sup> | R       |

|    |       |       |   |   |
|----|-------|-------|---|---|
| 8  | -     | -     | R | R |
| 9  | 10 am | -     | R | R |
| 10 | -     | -     | R | R |
| 11 | -     | -     | R | R |
| 12 | -     | 12 pm | R | R |

---

<sup>1</sup>R: removed from the free-stall barn.

Three-dimensional scanning was performed, as previously described (Milan et al., 2017), using Kinect V1 (Microsoft, Redmond, WA; software ReconstructMe 2.5.1034, PROFACTOR, Steyr-Gleink, Austria), RealSense (Sense with RealSense SR300, 3D Systems, Rock Hill, SC; or R200, Intel, Santa Clara, CA; software Sense, 3D Systems, Rock Hill, SC), and photogrammetry (camera 3264 x 2448 pixels, BLU R1 HD, Miami, FL; software VisualSFM v0.5.26, Wu, 2011, 2013; or software Autodesk ReMake, Autodesk, Mill Valley, CA). Infrared images were recorded using FLIR E8 (resolution of 320 x 240 pixels, thermal sensitivity < 0.06°C, accuracy of ± 2°C, FLIR Systems, Wilsonville, OR). Skin and hair-coat surface temperatures were measured using iButtons (DS1922L or DS1923, accuracy ± 0.5 °C, OnSolution, Baulkham Hills, Australia) attached to cows through applying CraftBond (Ultra Stix All Clear, ELMER'S, High Point, NC) at the lateral side of the sensors and covering the sensors with thermal tape (thermally conductive adhesive transfer tape 8805, 125 µm thick, 3M Company, St. Paul, MN). Vaginal temperature was measured with a vaginal temperature probe (Hillman et al., 2009; accuracy ± 0.21 °C, Hobo Water Temp Pro,

Onset Computer Corporation, Bourne, MA). Rectal temperature was measured using a veterinarian digital thermometer (Ideal thermometer TA804-PROBE, accuracy  $\pm 1$  °C, Neogen Animal Safety, Lexington, KY) inserted ~5 cm into the rectum. Respiration rate was measured by counting the flank movement of the animals for 30 seconds. Evaporation rate was measured at the left and right back leg and chest of the cows using a VapoMeter (accuracy  $\pm 4\%$ , Delfin Technologies, Finland).

The weight of the cows was measured using load cells (FSK scale kit B for 9,000 kg total, accuracy  $\pm 0.5$  kg, A and A Scales LLC, Prospect Park, NJ) mounted on painted diamond plate steel platform (1.5 m x 0.76 m, VS-2200, A and A Scales LLC, Prospect Park, NJ). Chest diameter and wither height were measured using a tape. Body-condition scores were evaluated by an experienced veterinarian. Hair-coat thickness was measured using a caliper rule. Thickness of skin, fat, and muscle layers were measured using ultrasound (EVO with 8.5 MHz linear array, EI.Medical Imaging, Loveland, CO) by veterinarians from the Cornell ambulatory service, clipping the hair-coat in the scanned region and using 70% ethanol as a coupling agent.

Feed provided and leftovers were weighed using a scale (FSK scale kit B). The percentage of dry-matter content in the feed was measured by weighing feed samples, drying these samples (VWR High-Performance Horizontal Air Flow Oven Model 1680, VWR Scientific Products, Randor, PA), and weighing the resulting dried feed sample. Feed composition was analyzed in a laboratory (Dairy One, Ithaca, NY).

Two sets of environmental data are provided. The first set of environmental data, measured with Krestel (Krestel 5400AG Cattle Heat Stress Tracker, Krestel Instruments, Boothwyn, PA), included air temperature (accuracy  $\pm 0.5^{\circ}\text{C}$ ), relative humidity (accuracy  $\pm 2\%$ ), black-globe temperature (accuracy  $\pm 1.4^{\circ}\text{C}$ ), and wind speed (accuracy  $\pm 0.1$  m/s) and direction (accuracy  $\pm 5^{\circ}$ ). The second set of environmental data, measured with a Campbell data logger (CR1000, Campbell Scientific, Logan, UT), included air temperature, black-globe temperature (10-cm diameter hallow copper), and temperature of the water at the inlet and outlet of the waterbeds (thermocouples type T, PVC insulated), and water flow rate to each waterbed (turbine flow rate sensor FT-110, accuracy  $\pm 3\%$ , Gems Sensors, Plainville, CT).

## **2.2. Experimental procedure using piglets**

Animal use and care protocol #9726/17 was approved by the Ethical Committee in Animal Use of the College of Veterinary and Agricultural Science of São Paulo State University. Table 40 shows measured variables, sampling rates, and number of samples. Five male piglets (40-50 days old, lineage Agrocerces CAM x 337), housed in community suspended floor pens (1.4 m x 1.8 m x 0.8 m) and heated by 250 W infrared lamp (1.2 m from the floor) at the Swine Research Center of São Paulo State University (21°14'07.9"S, 48°17'26.8"W), were randomly selected and individually housed for five consecutive days. The lamps were turned off and the curtains of the barn were opened during afternoons to maintain animal comfort. Feed and water were

given ad libitum. Feed provided and leftovers were weighed. Data collection was performed from 8 am to 8 pm.

Table 40. Measured variables, sampling rates, and number of samples for the dataset obtained using piglets.

| Variables                                  | Sampling rate | #Samples |
|--|---------------|----------|
| Animals                                    | -             | 5        |
| 3D Meshes                                  | Hourly        | 344      |
| Thermal images                             | Hourly        | *        |
| Photos                                     | -             | 1,534    |
| Skin-surface temperature                   | 1 min         | 31,752   |
| Rectal temperature                         | Hourly        | 245      |
| Respiration rate                           | Hourly        | 243      |
| Evaporation rate                           | Daily         | 45       |
| Physical measurements <sup>1</sup>         | Once          | 5        |
| Hair-coat thickness                        | Once          | 40       |
| Thickness of internal tissues <sup>2</sup> | Once          | 15       |
| Environmental data <sup>3</sup>            | 1 min         | 6,195    |
| Feed consumption                           | Daily         | 15       |

<sup>1</sup>Weight, head length, torso length, total length, circumference of the front belly, circumference at the center belly, and circumference at the back belly. <sup>2</sup>Skin, fat, and

muscle layers thickness. <sup>3</sup>Air temperature, relative humidity, black-globe temperature in a pen with and another without infrared lamp, wind speed, short-wave radiation, and ultraviolet radiation. \*Under preparation.

3D surface area of animals was recorded using 3D scanners (ZED 2K stereo camera, Stereolabs, San Francisco, CA; or Kinect V1, software ReconstructMe 2.5.1034; or BLU R1 HD camera, software VisualSFM and Autodesk ReMake). Skin-surface temperature was measured using an infrared camera (640 x 480, FLIR SC660, accuracy  $\pm 0.5$  °C, FLIR Systems, Wilsonville, OR) and iButtons (DS1921G or DS1921H, accuracy  $\pm 0.5$  °C, OnSolution, Baulkham Hills, Australia) attached to the loin skin surface by applying CraftBond (Ultra Stix All Clear, ELMER'S, High Point, NC) at the lateral side of the sensors and covering the sensors with a thermal tape (thermally conductive adhesive transfer tape 8805, 125  $\mu\text{m}$  thick, 3M Company, St. Paul, MN). Rectal temperature was measured with a rectal temperature probe (MLT1403 or MLT415/A connected to ML309 temperature pod, connected to PowerLab 16/30, connected to LabChart, accuracy  $\pm 0.2$  °C, ADInstruments, Sydney, Australia). Respiration rate was measured by counting flank movements for 15 seconds. Cutaneous evaporation rate was measured for three days using the colorimetric method (Schleger and Turner, 1965).

On the last day of the experiment, weight, head length, torso length, total length, and circumferences at the front, center, and back belly were measured. Hair-coat thickness was measured using a caliper rule at the left and right loin, belly, upper back, and front

leg. Thickness of skin, fat, and muscle layers were measured using ultrasound (500v, linear probe with 3.5 MHz, 13.5cm, Aloka Ultrasound Company, Wallingford, CT) by scanning between the thoracic and lower back (point P2) vertebrae, 6 cm below the mean line (ABCS, 1973).

Air temperature (accuracy  $\pm 0.56^{\circ}\text{C}$ ), relative humidity (accuracy  $\pm 3\%$ ), wind speed (accuracy  $\pm 0.45 \text{ m/s}$ ), short-wave radiation (CMP22, spectral range of 0.2-3.6  $\mu\text{m}$ , accuracy  $\pm 5 \text{ W/m}^2$ , NovaLynx, Grass Valley, CA), ultraviolet radiation (240-CUV5, spectral range of 0.28-0.4  $\mu\text{m}$ , accuracy  $\pm 5\%$ , NovaLynx, Grass Valley, CA), and black-globe temperature in pens with and without infrared lamp, were measured with a portable weather station (110-WS-18, NovaLynx, Grass Valley, CA).

### **2.3. Computer vision benchmark task: mesh registration**

Scanning software for developing 3D meshes searches for matching feature points (same points in different meshes) between the already registered geometry and the recently scanned geometry of an object. When matching feature points are found, the software combines the already registered geometry with the recently scanned geometry at the matching feature points locations. This procedure makes scanning of live animals challenging because animal movement hinders the ability of scanning software to find matching feature points (these software programs were designed for rigid and motion-less objects). Hence, when 3D scanning livestock, partial meshes are obtained and they need to be aligned (registered) to create a complete mesh.

In this study, 8 mesh registration algorithms were assessed for their ability to align 12 different pairs of partial meshes from 4 dairy cows. The pairs were qualitatively grouped based on overlap (little, moderate, or considerable; Figure 73). The mesh registration algorithms considered for this study were (1) iterative closest point algorithm (ICP; Rusinkiewicz and Levoy, 2001; software MeshLab; Cignoni et al., 2008), (2) non-rigid ICP (NICP; Amberg et al., 2007; authors' code), (3) non-rigid depth scans (NDS; Li et al., 2008; code from Manu, 2017), (4) as-rigid-as-possible (ARAP; Sorkine and Alex, 2007; software cilantro; Zampogiannis et al., 2018), (5) embedded deformation for shape manipulation (EDSM; Sumner et al., 2007; software cilantro; Zampogiannis et al., 2018), (6) Markov random fields (MRF; Chen and Koltun, 2015; authors' code), (7) isometric deformations (ID; Huang et al., 2008; in-house code), and (8) isometric deformations with SHOT descriptors (SHOT; Salti et al., 2014; in-house code).

Mesh pairs were pre-processed in MeshLab, which involved (a) removing points in each pair of meshes that may distort alignment (noise), and (b) aligning each pair of meshes with ICP. These pre-processed meshes were inputs for 6 of the 7 remaining mesh registration algorithms except for the Markov Random Field algorithm, which required further pre-processing. Additional pre-processing for the Markov Random Field algorithm involved (c) reconstructing the input meshes using the Screened Poisson surface reconstruction algorithm (Kazhdan and Hoppe, 2013) to fill holes in the meshes and (d) subsampling the reconstructed meshes to reduce computational

cost.

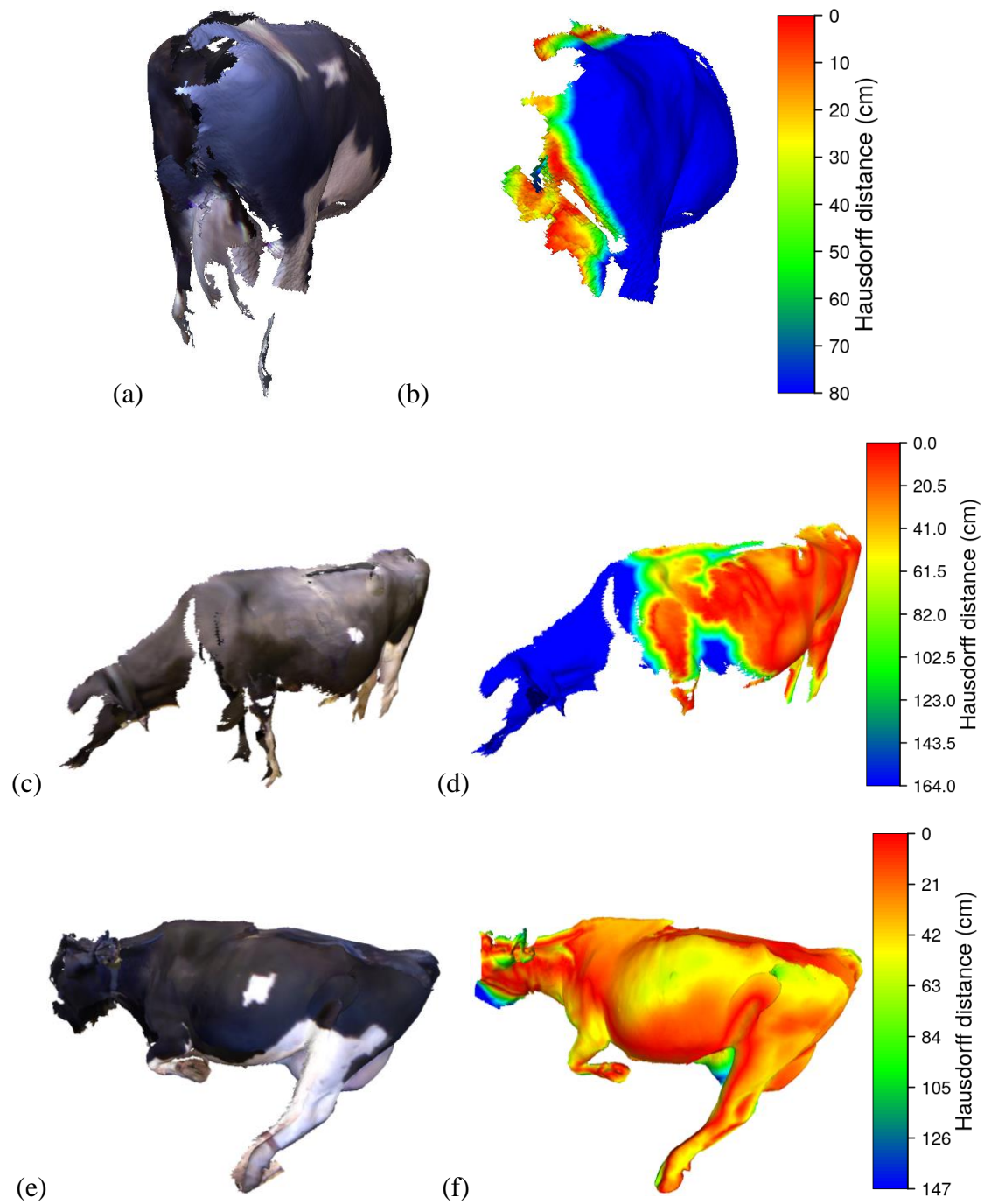


Figure 73. Examples of pairs of meshes (target and source) with little (a), moderate

(c), and considerable overlap (e). Pseudo-colors (b, d, f) represent the Hausdorff distance between the meshes pairs (Cignoni, Rocchini, Scopigno, 1998), from near (red) to far (blue). Color bars show the color scale for the Hausdorff distance.

All algorithms were evaluated using Euclidean distances on two sets of manually selected pairs of points, except for EDSM and MRF (these algorithms include sampling procedures that prevented manually tracking the position of correspondence points from pre-processed to registered meshes). The first set contains 10 ground truth corresponding pairs of points from each mesh (120 pairs of points in total), where the points in each pair would be in the same position if the meshes were perfectly aligned (a low performance metric indicates good alignment). The second set contains 5 pairs of points from each mesh (60 pairs of points in total), where the points in each pair would be far if the meshes were perfectly aligned (a high performance metric indicates good alignment).

#### **2.4. Machine learning benchmark task: supervised learning**

This study assessed 8 machine learning algorithms for their ability to develop models that predict respiration rate of piglets from environmental conditions (time of the measurement, air temperature, black-globe temperature exposed to the infrared lamp, black-globe temperature not exposed to the infrared lamp, relative humidity). The machine learning algorithms considered for this study were (1) ordinary least squares regression (OLS; Moser, 1996; Fox, 2016), (2) generalized additive models (GAM;

Hastie and Tibshirani, 1990; Wood, 2017), (3) Gaussian processes (GP; Rasmussen and Williams, 2006), (4) support vector machines (SVM; also known as support vector regression when applied to regression tasks; Cortes and Vapnik, 1995), (5) generalized linear regression with elastic net penalty (GLM; Zou and Hastie, 2005), (6) random forests (RF; Breiman, 2001), (7) gradient boosted machine (GBM; Friedman, 2001; Natekin and Knoll, 2013), and (8) deep learning (feedforward neural networks) with ReLU activation function (DL; Goodfellow et al., 2016).

Previous studies demonstrated that respiration rate of livestock is affected by time of measurement, temperature, relative humidity, and radiation (e.g., Collier and Gebremedhin 2015; Gebremedhin et al., 2010) and that changes in respiration rate may be affected by past environmental conditions (up to 3 hours before; e.g., Gaughan et al., 2000). To consider previous environmental conditions, the machine learning algorithms included a sequence of environmental measurements (from the previous 3 hours to the current time, with increments of 10 minutes; each environmental variable provided 19 predictor variables). Respiration rates sampled within the first 3 hours of the experiment were discarded due to lack of previous environmental data. If any of the remaining samples of data were missing environmental variables, the values were interpolated using a 30 min window spline interpolation method (Forsythe et al., 1977) in the R statistical software (R Core Team, 2018). After data pre-processing, the dataset consisted of 234 data points with 77 main predictors. The dataset was randomly divided into a training dataset for model development (80% of the entire

dataset; 187 observations) and a testing dataset for out-of-sample model assessment (20% of the entire dataset; 47 observations).

Many machine learning algorithms have hyper-parameters, which influence how a machine learning model learns relationships from data. For the machine learning algorithms with hyper-parameters, model development involved training several different models with randomly selected hyper-parameters (Bergstra and Bengio, 2012). Selection of the best model was performed based on which model minimized a random 5-fold cross-validation error metric on the training dataset (Kohavi, 1995). Performance of the best models from each algorithm was assessed using mean squared error (MSE) on the testing dataset.

For OLS and GAM, because of the high number of possible predictor variables (up to  $2^{77}$ , including interactions), predictor variables were selected using forward selection methods (Efron and Hastie, 2016) in R, while respecting the principle of marginality (Fox, 2016). For OLS, predictor variable selection was based on minimizing cross-validation Akaike Information Criterion (AIC; Fox, 2016). For GAM, predictor variable selection was based on minimizing cross-validation p-values  $< 0.01$  obtained from F-tests (Wood, 2017). GAM was developed with the mgcv R package (Wood, 2011).

For GP, the mean function was set to 0 and the kernel as well as its hyper-parameters were selected by iteratively optimizing the marginal log likelihood until cross-

validation MSE increased (using GPyTorch; Gardner et al., 2018). The kernels considered were (a) radial basis function, (b) Matérn, (c) linear, (d) cosine, and (e) periodic. The best kernel was selected based on cross-validation MSE.

SVM regression models were developed using the liquidSVM R package with a radial basis function kernel (Steinwart and Thomann, 2017). A random search (Bergstra and Bengio, 2012) for hyper-parameter optimization was performed, where 1,000 models were developed. The two hyper-parameters considered were  $\gamma \sim U(0.01, 100)$  and  $\lambda \sim 10^{U(-10, 0)}$  ( $a \sim f(.)$  stands for the random variable  $a$  follows the probability density function defined by  $f(.)$ ;  $U(a, b)$  represents an uniform distribution from  $a$  to  $b$ ). The best model was selected based on cross-validation MSE.

For GLM, RF, GBM, and DL, a random search for hyper-parameter optimization was performed using the h2o R package (The H2O.ai team, 2017). The sampling space for hyper-parameters was modified from a previous work (Gorczyca et al., 2018) to increase penalties for large regression weights for GLM, which reduces collinearity between predictor variables (Hastie et al., 2008). Specifically, during GLM development, the hyper-parameter  $\lambda \sim 10^{U(-10,4)}$ . The best model from each algorithm was selected based on cross-validation MSE.

The best performing machine learning models from each algorithm were evaluated for interpretability and generalization using partial dependence plots (Friedman, 2001). To produce partial dependence plots that correspond to reasonable environmental

conditions, partial dependence plot construction was based on the following procedure. First, 76 different GAM models were developed to predict environmental variables from time of measurement and air temperature using the environmental dataset (6,195 data points). These GAM models explained  $96.31 \pm 2.64\%$  of the deviance (mean  $\pm$  standard deviation). Then, these GAM models were used to construct an artificial dataset. This dataset consisted of (a) changing time of measurement from 8 am to 8 pm, (b) changing air temperature from 15°C to 30°C, and on (c) predicting the remaining 76 environmental variables using the 76 GAM models.

### ***3. RESULTS AND DISCUSSION***

#### **3.1. Mesh registration performance**

Figure 74 shows the performance of the mesh registration algorithms. When these algorithms were assessed on the set of close points (ground truth pairs of corresponding points where each point in a pair would be in the same position if two partial meshes were perfectly aligned), ARAP was the only algorithm that performed similarly to ICP. The other algorithms performed worse than ARAP and ICP (Figure 74ab. When these algorithms were assessed with the set of far points (pairs of points where each point in a pair would be far apart if two partial meshes were perfectly aligned), all algorithms attained similar performance metrics.

Figure 75-Figure 78 show results from the mesh registration algorithms. In Figure 75, the SHOT algorithm (similar results were observed with ID) could not find matching

characteristic feature points between two partial meshes, resulting in one mesh collapsing into a sphere-like geometry (Figure 75c). NICP (Figure 76) and NDS (Figure 77) were only able to correctly register partial mesh pairs with considerable overlap (Figure 76cd and Fig. Figure 77cd). The procedure for using MRF (Figure 78) resulted in deformed meshes. Meshes registered with EDSM and ARAP were similar to meshes registered with ICP.

### **3.2. Challenges and future directions in mesh registration**

Partial mesh registration has the potential to capture realistic, complete geometrical representations of dairy cows. These complete geometries can improve computational fluid dynamics and bioenergetic modeling by reducing errors associated with geometric approximations. Current models simplify the geometry of animals or their body parts to spheres (Norton et al., 2010), ellipses (Turner et al., 1987ab), semi-circles (Gebremedhin and Wu, 2016), semi-cylinders (Gebremedhin et al., 2016), or manikins (Gebremedhin and Wu, 2003, 2005; Mondaca and Choi, 2016; Wu and Gebremedhin, 2001ab). These geometrical approximations can introduce modeling errors as high as 33% (Dudley et al., 2013; Mondaca and Choi, 2016).

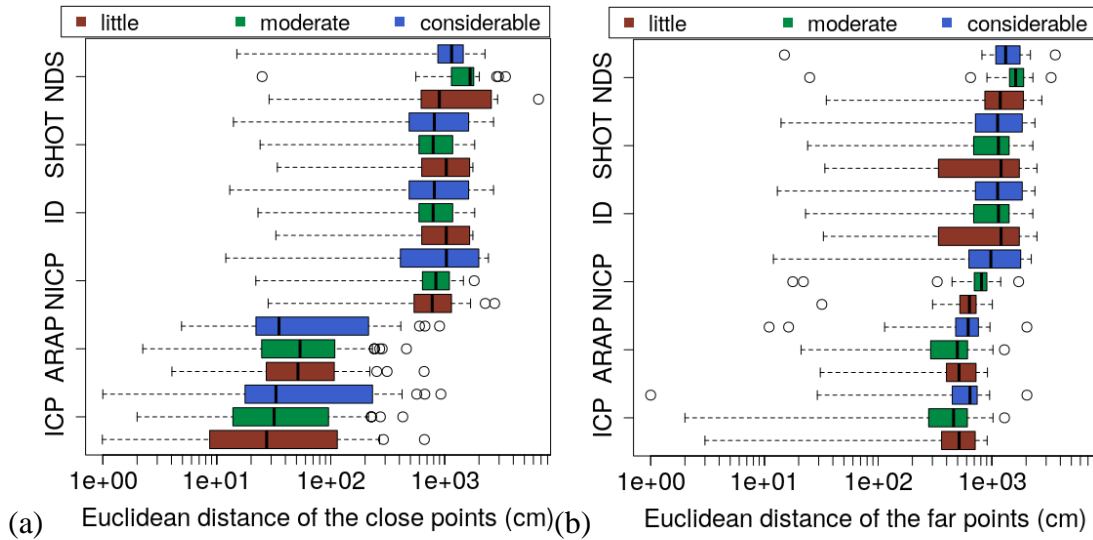


Figure 74. Euclidean distances evaluated on the sets of close points (ground truth corresponding points that should be in the same position if the meshes were perfectly aligned; a) and far points (pair of points that should be distant if the meshes were perfectly aligned; b). Boxplots sorted from high-to-low mean Euclidean distance (top-to-bottom). Performance metrics for EDSM and MRF are not shown because they involved sampling procedures, which prevented manually tracking the position of correspondence points in pre-processed and registered meshes. ICP: iterative closest point algorithm; ARAP: as-rigid-as-possible; NICP: non-rigid ICP; ID: isometric deformations; SHOT: isometric deformations with SHOT descriptors; NDS: non-rigid depth scans. EDSM: embedded deformation for shape manipulation; MRF: Markov random fields.

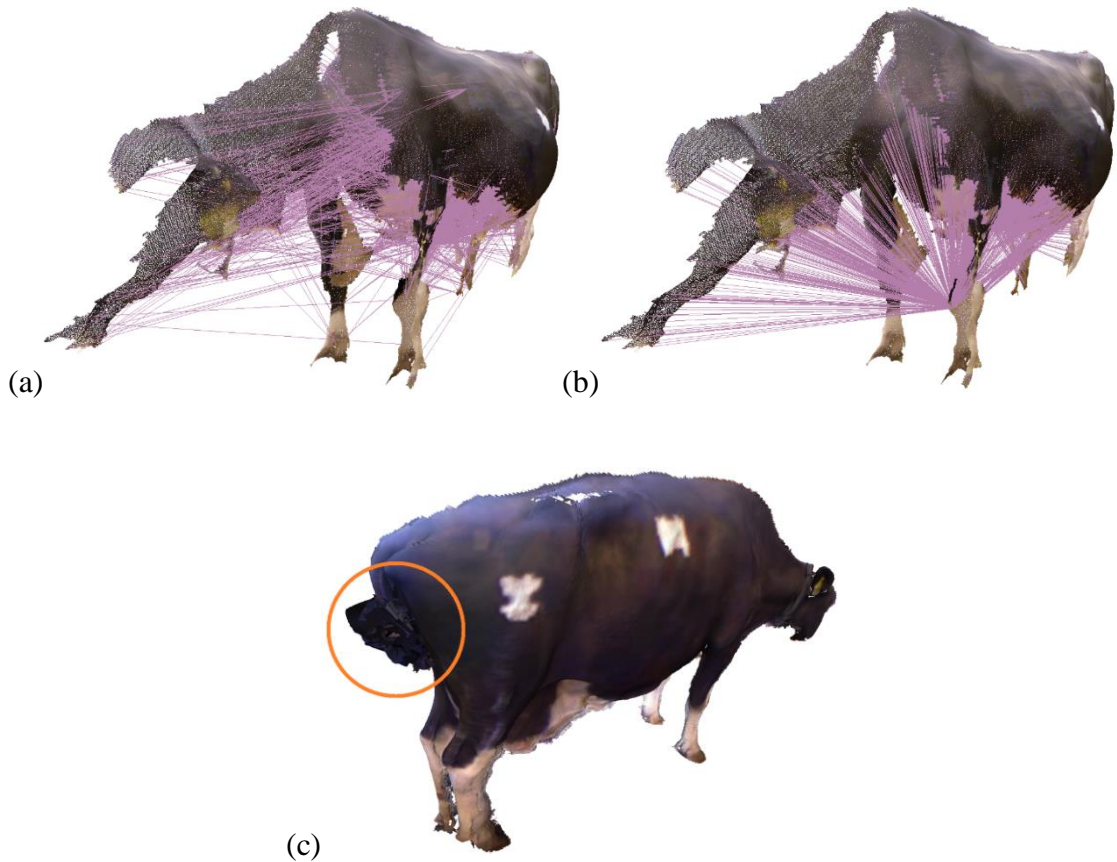


Figure 75. Initial (a) and final (b) correspondences obtained with SHOT on two partial meshes with moderate overlap (pair of meshes shown in Figure 73cd). Alignment performed with SHOT distorted one of these partial meshes to a spherical-like geometry (c; inside the orange circle). Overlap between these two meshes occurs on the left side of the cow. Initial correspondences were found between parts of the partial meshes that did not relate to ground truth, such as correspondences between the thorax and head. Final correspondences were mostly found between legs in one mesh and other body parts in the other mesh. Correspondences are indicated as purple lines connecting point clouds of the two meshes.

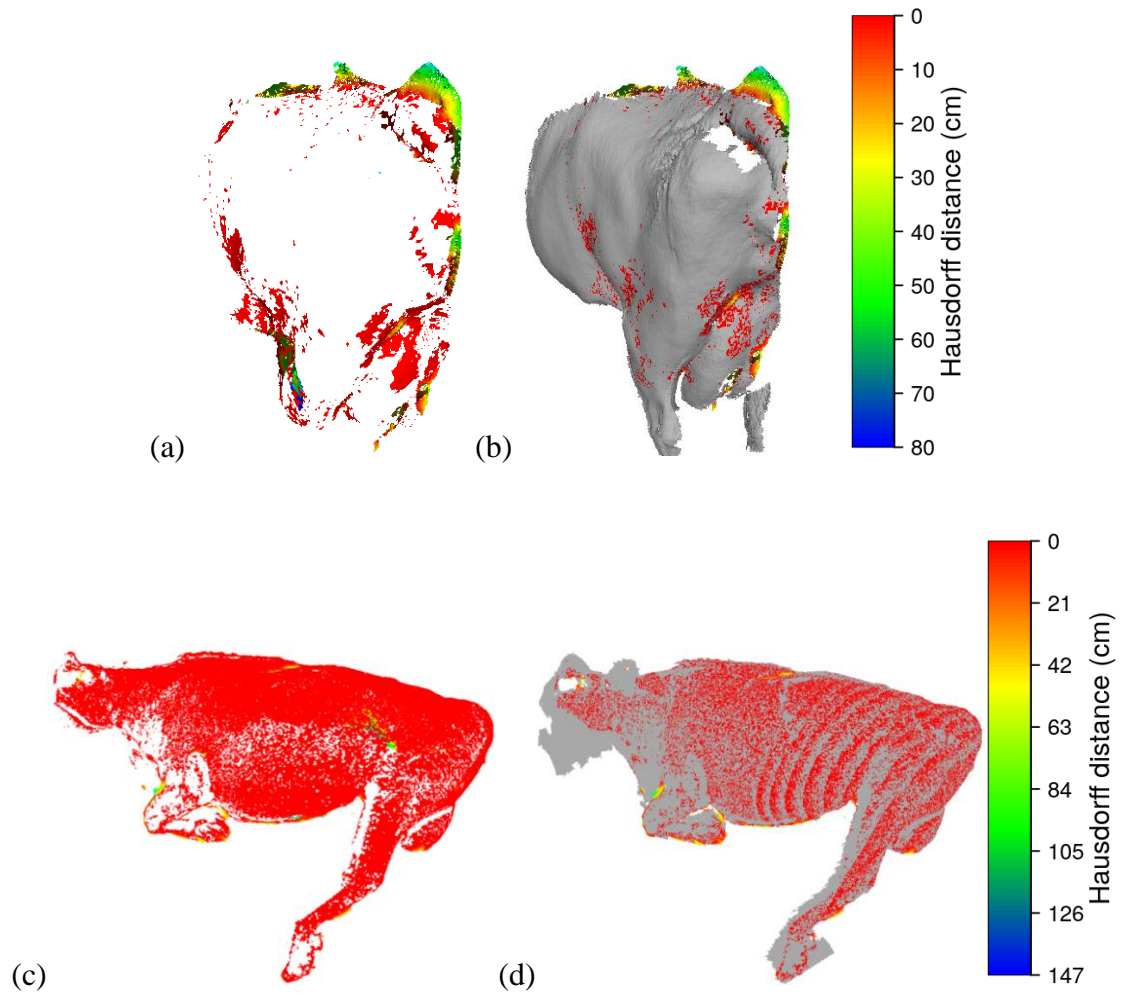


Figure 76. Hausdorff distance between mesh pairs with little (a, b; Figure 73ab) and considerable (c, d; Fig. Figure 73ef) overlap when registered with non-rigid iterative closest point algorithm (NICP). Pseudo-colors represent near (red) to far (blue) Hausdorff distances. Gray color (b, d) represents the target mesh. Color bars show the color scale for the Hausdorff distance.

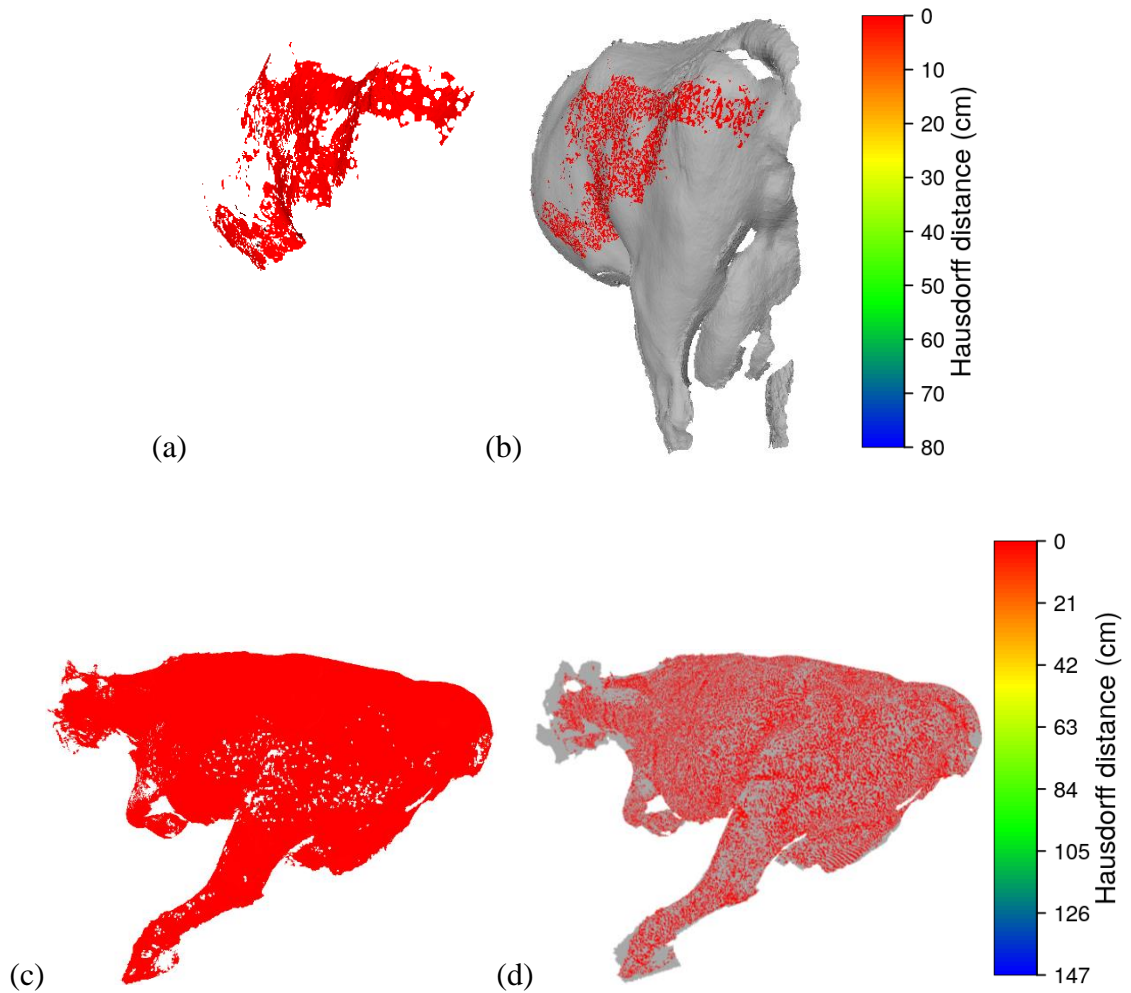


Figure 77. Hausdorff distance between mesh pairs with little (a, b; Figure 73ab) and considerable (c, d; Figure 73ef) overlap when registered with non-rigid depth scans (NDS). Pseudo-colors represent near (red) to far (blue) Hausdorff distances. Gray color (b, d) represents the target mesh. Color bars show the color scale for the Hausdorff distance.

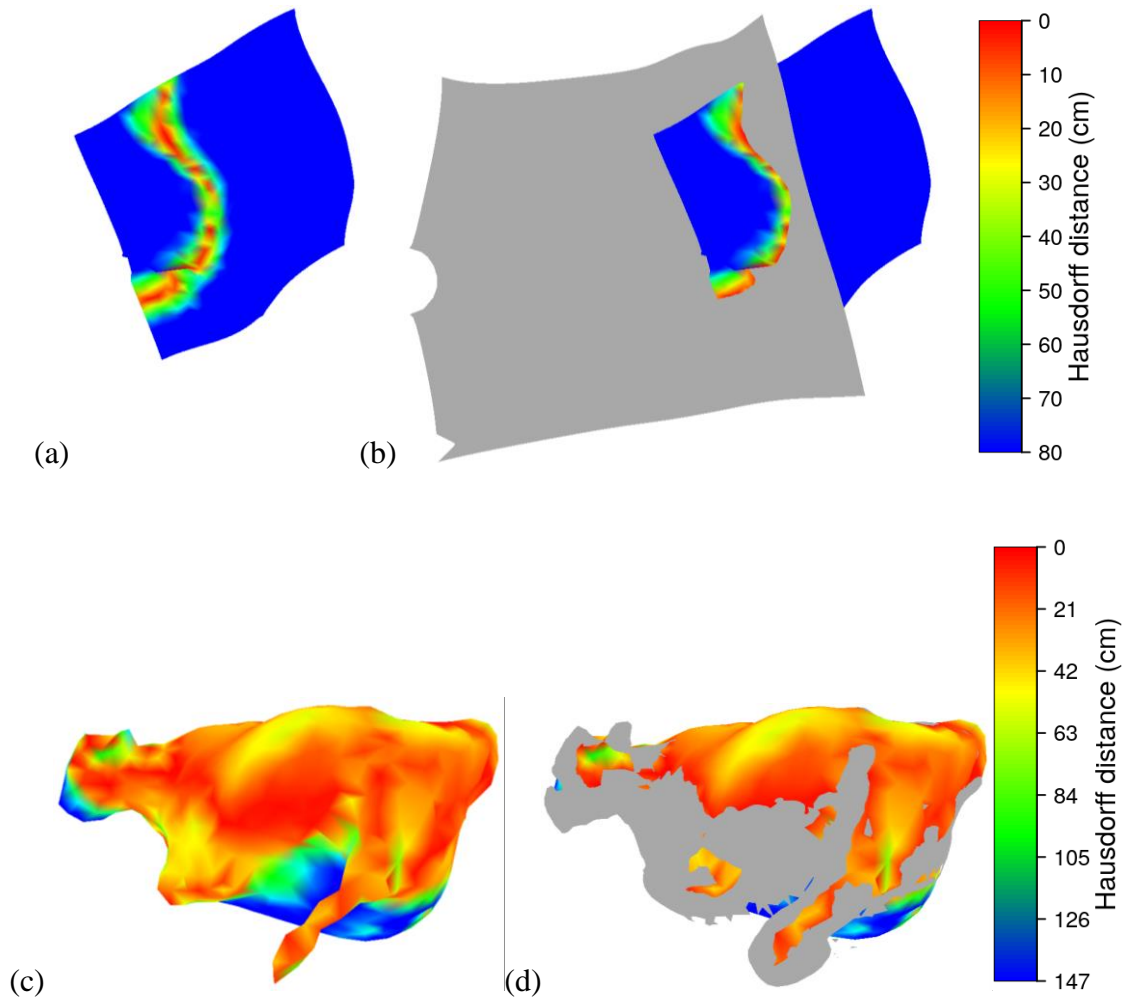


Figure 78. Hausdorff distance between mesh pairs with little (a, b; Figure 73ab) and considerable (c, d; Figure 73ef) overlap when registered with the Markov random fields algorithm (MRF). Pseudo-colors represent near (red) to far (blue) Hausdorff distances. Gray color (b, d) represents the target mesh. Color bars show the color scale for the Hausdorff distance.

One explanation for poor alignment performance (Figure 74-Figure 78) is that animals are featureless, non-rigid, articulated objects (van Kaick et al., 2011), and evaluation of registration algorithms in this setting has been predominantly performed on synthetic datasets (Bogo et al., 2014). Registration of featureless meshes (meshes with similar colors and curvatures at their surface) is a challenging problem in computer vision research because of the difficulty in finding matching characteristic points between them. This challenge is demonstrated in Figure 75, which shows that a small region in one mesh may have correspondences with multiple regions in another mesh. Another challenge is registration of non-rigid and articulated meshes (meshes consisting of functionally independent components, e.g., limbs of a cow can move independently). While this study used algorithms for registering non-rigid, articulated meshes, empirically these algorithms were only able to deal with minor changes in shape.

Similar results were attained with meshes created from photogrammetry techniques (not shown). Photogrammetry involves reconstructing the geometry of a 3D object with multiple 2D photos of that object (Milan et al., 2017). The reason that photogrammetry failed is likely due to animals being featureless, non-rigid, articulated objects. For instance, few feature points were detected and matched across different images, which resulted in incomplete and noisy meshes.

To overcome the challenges involved in mesh registration for livestock, we have previously proposed manual reconstruction of complete meshes from partial meshes

(Milan et al., 2018). We reported that physical measurements on manually reconstructed complete meshes are not statistically different from physical measurements gathered from the animal, which validates this technique. The two main limitations of this approach, however, are that manual reconstruction is time consuming and requires the assistance of an expert on 3D geometric modeling.

Others have proposed giving preanesthetic medication to animals to reduce their movement before 3D scanning them (Simão et al., 2017). This approach, to the best of our knowledge, is the only reported procedure capable of acquiring complete 3D meshes of real livestock. The limitations of this procedure, however, are that it is time consuming, requires a certified professional to administer the preanesthetic, and the use of preanesthetics may have long-term effects on the animal as well as on the data collected afterwards.

Future work in this area may involve the development of improved techniques for acquisition and registration of livestock meshes. One alternative could involve developing prior geometric representations of livestock (Zuffi et al., 2017), which could be used as templates to fit partial meshes. Another alternative could involve the development of new algorithms for featureless, non-rigid, articulated objects (e.g., Chan et al., 2017). These algorithms still have to be tested with livestock meshes.

### **3.3. Machine learning performance**

Figure 79 shows training, cross-validation, and testing MSE for the 8 supervised

learning algorithms tested in this paper. For all best models, training MSE was lower than cross-validation MSE, which was lower than testing MSE. All machine learning models showed similar MSE values on the testing dataset, except for GLM (highest MSE). Testing MSE was lowest for GAM. Previous studies reported similar errors when predicting respiration rate of feedlot heifers (Brown-Brandl et al., 2005) and lower errors when predicting respiration rate of dairy cows (Gorczyca and Gebremedhin, 2019).

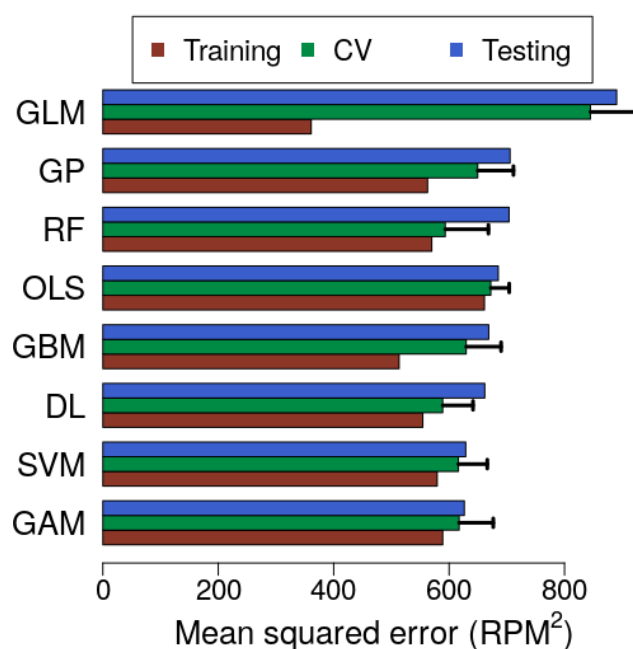


Figure 79. Performance of the best machine learning models developed to predict respiration rate of piglets from environmental variables. Data shown in order from high-to-low (top-to-bottom) testing mean squared error (MSE). Error bars represent standard error of the mean (SEM) for CV (5-folds) MSE. RPM: number of respirations per minute; CV: cross-validation; GAM: generalized additive model; 362

SVM: support vector machine with radial basis function kernel; DL: deep learning with ReLU activation function; GBM: gradient boosted machine; OLS: ordinary least squares regression; RF: random forests; GP: Gaussian processes with radial basis function kernel; GLM: generalized linear regression model with elastic net regularization.

### **3.4. Machine learning interpretability and generalization assessment**

Because Machine learning models may overfit to the data and violate first principles or established research findings (Gorczyca et al., 2018; Molnar, 2018; Milan et al., 2019), machine learning models for precision livestock farming applications should be tested for generalization and interpretability. Interpretability and generalization tests for machine learning algorithms include model-agnostic methods (Molnar, 2018) such as partial dependence plots (Friedman, 2001).

Figure 80 shows dependence plots for the functions learned by GAM (Figure 80a) and OLS (Figure 80b). The interpretation of the function learned by GAM is straightforward: respiration rates have a basal level of  $\sim 45$  respirations per minute up to  $\sim 23$  °C. After this threshold, respiration rate increases almost linearly with increased temperature. Note, however, that the function learned by GAM did not predict a plateau in respiration rate for high temperatures values (Eigenberg et al., 2005). This may be because animals in this dataset were not exposed to high heat-stress conditions, which would saturate their capability to increase respiration rate and

show the expected plateau (Eigenberg et al., 2005; Robertshaw, 2006). On the other hand, the function learned by OLS was more restrictive (more bias introduced by the functional form of the linear model) and could only predict that respiration rate increases as temperature increases.

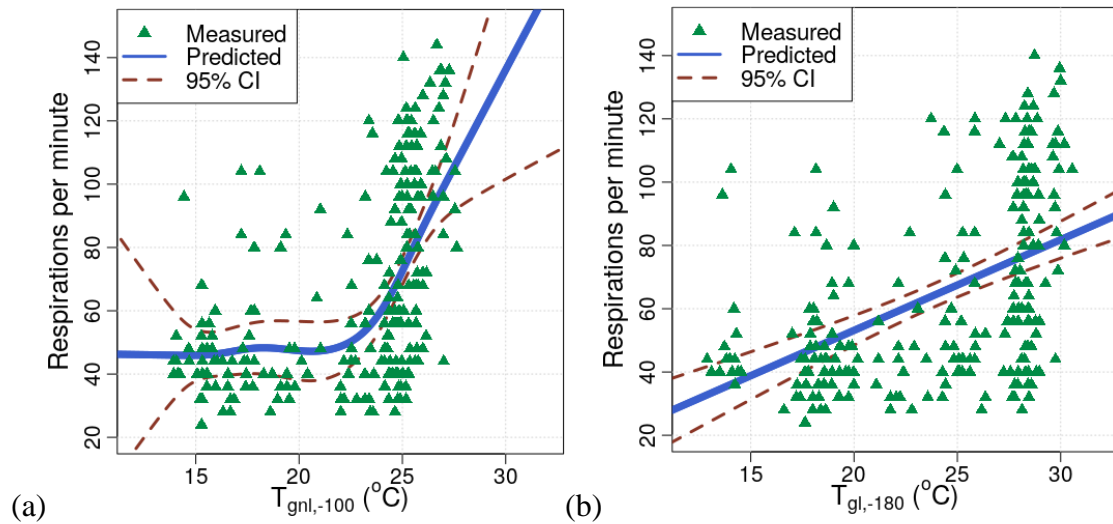


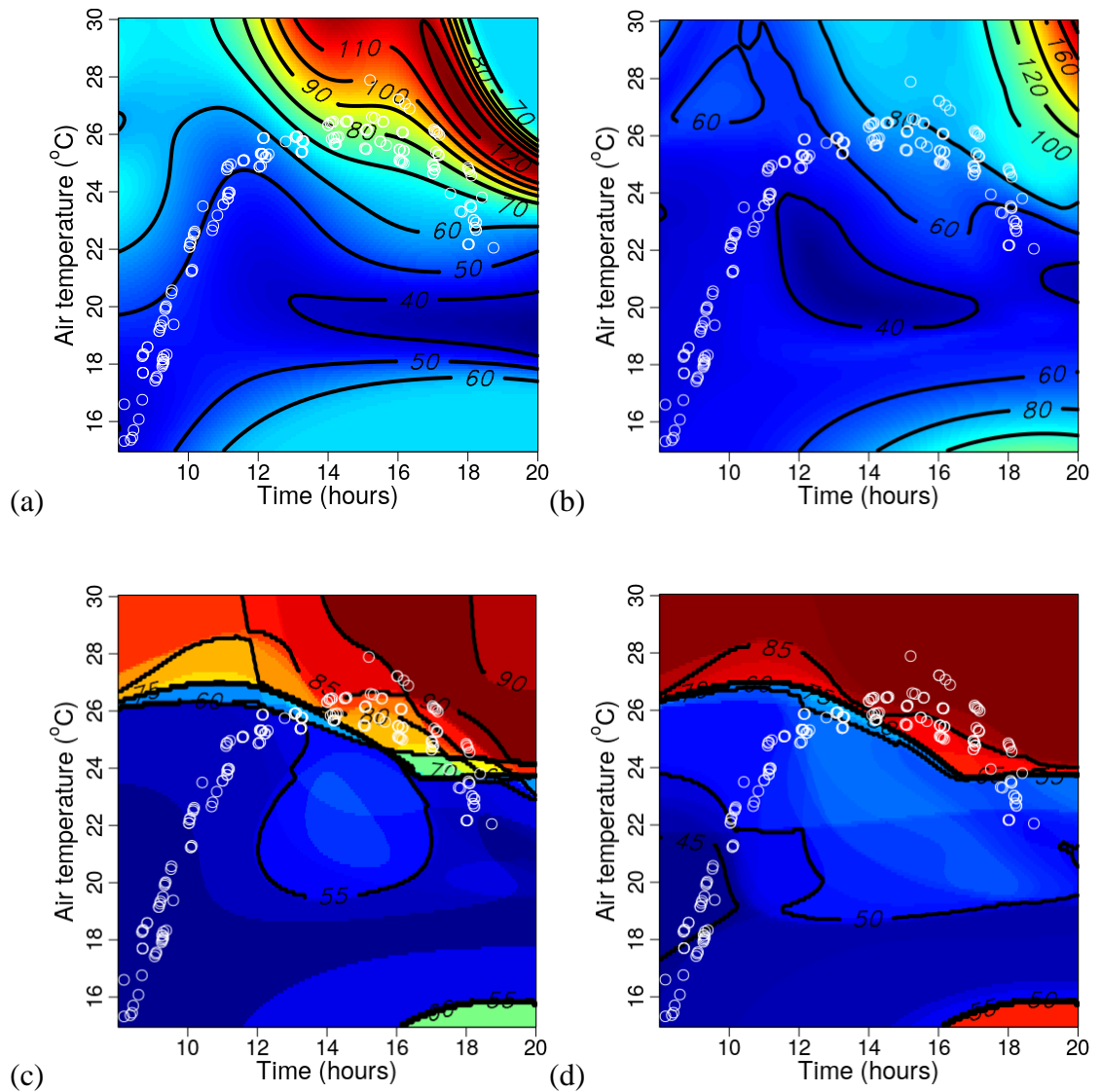
Figure 80. Measured and predicted respiration rate using generalized additive model (a) and ordinary least squares regression (b).  $T_{\text{gnl},-100}$ : black-globe temperature, not exposed to the infrared lamp, measured 100 min. before recording respiration rate;  $T_{\text{gl},-180}$ : black-globe temperature, exposed to the infrared lamp, measured 180 min. before recording respiration rate. 95% CI: predicted 95% confidence interval for the mean.

Previous studies reported similar observations on how environmental conditions affect respiration rate of animals (Stevens, 1981; Eigenberg et al., 2005; Maia et al., 2005; Camerero et al., 2016; Costa et al., 2017; Atkins et al., 2018). What makes this study unique is the use of GAM, which learned the functional form of the relationships

between environmental conditions and respiration rate given data, which removed biases in manually choosing data relationships and functional forms (Hastie et al., 2008). Examples of these biases include (1) grouping responses based on air temperature ranges (Eigenberg et al., 2005; Camerero et al., 2016; Costa et al., 2017), (2) fitting piecewise linear functions to the data (Atkins et al., 2018), (3) fitting quadratic functions to the data (Maia et al., 2005), or (4) fitting exponential functions to the data (Stevens, 1981).

Figure 81 shows the results from assessing generalization and interpretability for SVM (Figure 81a), DL (Figure 81b), GBM (Figure 81c), RF (Figure 81d), GP (Figure 81e), and GLM (Figure 81f). Unlike the functions learned by GAM (Figure 81a) and OLS (Figure 81b), the functions learned by these models are more difficult to interpret. For example, SVM, DL, GP, and GLM predict that respiration rate increases with decreasing temperature (see, e.g., the region near 18:00 and 25 °C in Figure 81a). This contradicts previous reports that established that respiration rate increases monotonically with temperature (Stevens, 1981; Eigenberg et al., 2005; Maia et al., 2005; Camerero et al., 2016; Costa et al., 2018ab; Atkins et al., 2018). The relationships learned by RF and GBM were complex and, as expected, consisted of segmenting the prediction space. This shows that predictions from RF and GBM are very sensitive to small changes in the predictor variables. Predictions using GP quickly returned to the mean function value (0) for regions without data points, indicating that a mean function could be developed to improve predictions from GP. In this situation, GP

would learn deviations from the mean function given data. Predictions from GLM were unbounded and included regions with negative respiration rate values (e.g., see the region near 10:00 and 26 °C in Figure 81f).



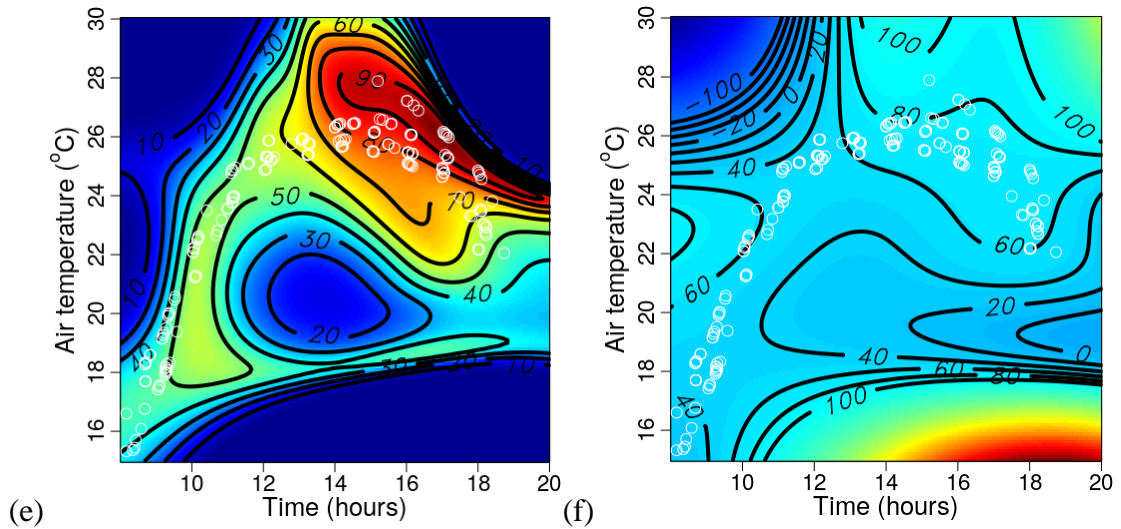


Figure 81. Partial dependence plots for respiration rate predicted using support vector machines (SVM; a), deep learning (DL; b), gradient boosted machine (GBM; c), random forests (RF; d), Gaussian processes (GP; e), and generalized linear regression (GLM; f). These figures show a surface plot for the effects of changing time of measurement (x axis) and air temperature (y axis) in respiration rate (shown with color gradients and contours). The other predictors were changed accordingly to values predicted from time of measurement and air temperature using generalized additive models as described in Sec. 2.4. Numbers and lines in the surface plots indicate contour plots. Number and lines in (f) were constrained to the range [-100, 100] for clarity. White circles represent the location of measured training data points.

### 3.5. Challenges and future directions in machine learning

The use of machine learning algorithms for digital agricultural application is significant because they can automatically select predictor variables and find non-

linear relationships in the data, removing subjectivity from researcher selecting predictor variables and assuming data relationships (Hastie et al., 2008). Furthermore, machine learning models have demonstrated greater predictive accuracy than carefully hand-crafted models (including fundamentally-based models; Hastie et al., 2008; Gorczyca et al., 2018; Milan et al., 2019).

To advance the applicability of machine learning algorithms in precision livestock farming, two limitations must be addressed. (1) Predictions from machine learning models are not transferable between different settings (Pan and Yang, 2010). Specifically, model predictions are limited to the population represented when training a model, which highlights the significance of data sharing to support the development of models and systems that can generalize to larger populations. (2) The predictions may not comply with first principles, even when big data is used (Caruana et al., 2015; Gorczyca et al., 2018; Milan et al., 2019). This limitation is because of the intrinsic bias in precision livestock farming datasets (predictor variables cannot be randomly changed to explore the whole predictor space). For example, it would be unethical to induce life-threatening levels of heat-stress in livestock without providing cooling. Consequently, machine learning algorithms are constrained to the information available in real-world datasets (Caruana et al., 2015).

One possible solution to develop models that comply with first principles and established research findings would involve combining fundamentally-based models with machine learning models, which have led to the development of strong

performing integrated models that obey first principles (Milan et al., 2019). Another possible solution to this problem would involve artificially increasing the training dataset using adversarial examples (Biggio and Roli, 2018). For example, when a machine learning model under training produces counterintuitive predictions (such as respiration rate decreasing while temperatures increases), the adversarial machine learning model should be able to artificially increase the training dataset to improve model robustness. This approach is computationally expensive and may not guarantee compliance with first principles and established research findings for all possible inputs.

One practical disadvantage of developing systems with machine learning algorithms without probing them for generalization and interpretability is as follows. Suppose a control environment system is developed based on artificial intelligence. This system would work as expected in most conditions. However, this system might fail during rare conditions, such as heat-waves. In a rare, intense heat-wave, the system might predict that less cooling is required with increasing heat-stress levels (similar to what was observed in Figure 81). Then, this system will provide less cooling and animals or plants in the environment controlled by this system will suffer severe heat-stress and might even die.

### **3.6. Algorithm selection**

While this study indicated that the iterative closest point (ICP) algorithm worked well

for aligning 3D dairy cow meshes (computer vision) and generalized additive models (GAM) worked well for predicting the respiration rate of piglets (machine learning), this does not imply that ICP and GAM will work well in all settings. In fact, the algorithm that will produce the best predictive performance model cannot be determined before model development, as these algorithms are data-driven procedures and the underlying relationships in real-world datasets are complex and unknown (Wolpert and Macready, 1997). This differs from the development of fundamentally-based models where, given boundary conditions and assumptions about the problem, the exact equation needed to be solved is known (see, e.g., Datta, 2016).

When developing computer vision and machine learning algorithms, the current framework for systematic model selection is empirically based on selecting the algorithm that produces the best performance metrics. Following a systematic procedure for selecting an algorithm and its hyper-parameters is critical because models developed using the same algorithm and hyper-parameters can learn noise instead of the true non-linear relationships in the data. This paper provides an example of a framework for machine learning model development and selection. This framework consisted of (a) developing models from 8 different machine learning algorithms, (b) optimizing hyper-parameters for each algorithm based on a cross-validation performance metric on the training dataset, and (c) selecting the best performing model based on a performance metric on out-of-sample data (test dataset).

The model development framework for GAM and OLS resulted in the selection of a

single predictor (GAM: black-globe temperature, not exposed to infrared lamp, measured 100 min. before recording respiration rate; OLS: black-globe temperature, exposed to infrared lamp, measured 180 min. before recording respiration rate) out of the possible set of  $2^{77} - 1$  predictors (main factors plus all interactions minus the intercept term). A possible explanation for this selection may be high concurrency (non-linear correlation) of the predictors. Although research has established that machine learning algorithms can handle correlated predictors well (Hastie et al., 2008), proofs to this argument are usually based on the limiting case of an infinite number of data points. For example, GLM consists of OLS with penalties in the objective function for large-valued coefficients, resulting in automatic predictor selection (Zou and Zhang, 2009). The best GLM model (which had the highest testing MSE) only shrunk to zero weights of 11 out of 77 predictor variables while OLS only selected 1 predictor variable. Hence, one possibility to improve performance of machine learning algorithms in data limited settings could be to include predictor selection as a hyper-parameter when training the models. This is particularly valuable for precision livestock farming because datasets in this area usually have a limited number of data points (mainly because collecting each data point is expensive, time-consuming, and labor intensive).

### **3.7. Other applications of PLFBD**

PLFBD could have several other applications in precision livestock farming. For example, (1) researchers could study the coding scripts from this study to incorporate

computer vision and machine learning algorithms in their research programs, (2) coding scripts and the dataset could be used to teach computer vision and machine learning concepts to undergraduate and graduate students, (3) the livestock meshes could be used to facilitate the development of improved mesh registration algorithms for featureless, non-rigid, articulated objects, (4) the physiological data from dairy-cows and piglets could be combined to develop prediction models for different livestock species, (5) the physiological data could be used to validate mechanistic models, (6) thermal images in the dataset could be used to determine the surface area of cows in contact with waterbeds used in conductive cooling, (7) thermal images and 3D meshes could be combined to develop 3D surface-temperature models (Milan et al., 2017), and (8) the dataset could be mined to discover new patterns in the data (Williams et al., 2016).

#### ***4. CONCLUSION***

- PLFBD: Precision Livestock Farming Big Data for computer vision and machine learning applications is made available for public use.
- Computer vision algorithms used to register 3D dairy-cow meshes produced unsatisfactory results for some meshes, likely because animals are featureless, non-rigid, articulated objects.
- Machine learning models developed to predict respiration rate of piglets produced accurate results. Predictions from machine learning models need to be probed for generalization and interpretability.

- Generalization and interpretability tests performed with partial dependence plots (Figure 80 and Figure 81) showed that 6 out of the 8 developed machine learning models produced counterintuitive predictions.

### *Acknowledgment*

Funding: Brazilian National Council of Technological and Scientific Development (CNPq, Proc. 203312/2014-7), São Paulo Research Foundation (FAPESP, Proc. 2014/11170-7 and 2014/09639-7), the National Institute of Food and Agriculture, U.S. Department of Agriculture, Multi-state/Hatch under W-3173 through Cornell University, and The Graduate School of Cornell University (research travel grant to HFMM). Technical support: Dr. Blake Nguyen from Cornell Teaching Dairy Barn, Dr. David P. Orr from Cornell University Local Roads Program for support with drying feed samples, and Prof. Luciano Hauschild and M.S. Student Raphael Perini Caetano from Swine Research Center of São Paulo State University.

## REFERENCES

- ABCS. *Brazilian Association of Swine Producers: Brazilian Method to Classify Carcasses [Portuguese]*. Technical note n. 2, Estrela, Rio Grande do Sul, 1973.
- Amberg B, Romdhani S, Vetter T. *Optimal Step Nonrigid Icp Algorithms for Surface Registration*. In *Computer Vision and Pattern Recognition* (pp. 1-8). Minneapolis, USA: Computer Vision Foundation, 2007.
- Atkins IK, Cook NB, Mondaca MR, Choi CY. Continuous respiration rate measurements of heat-stressed dairy cows and relation to environment, body temperature, and lying time. *Trans ASABE* 61(5):1475-1485, 2018.
- Bergstra J, Bengio Y. Random search for hyper-parameter optimization. *J Mach Learn Res* 13:281-305, 2012.
- Biggio B, Roli F. Wild patterns: ten years after the rise of adversarial machine learning. *Pattern Recogn*, 84, 317-331, 2018.
- Bogo F, Romero J, Loper M, Black MJ. Faust: *Dataset and Evaluation for 3D Mesh Registration*. In *Computer Vision and Pattern Recognition* (pp. 3794-3801). Columbus, USA: Computer Vision Foundation, 2014.
- Breiman L. *Random forests*. *Mach Learn* 45:5-32, 2001
- Brown-Brandl TM, Jones DD, Woldt WE. Evaluating modeling techniques for cattle

heat stress prediction. *Biosystems Eng* 91(4):513-524, 2005.

Camerro LZ, Maia ASC, Neto MC, Costa CCM, Castro PA. Thermal equilibrium responses in Guzerat cattle raised under tropical conditions. *J Therm Biol* 60:213-221, 2016.

Caruana R, Lou Y, Gehrke J, Koch P, Sturm M, Elhadad N. *Intelligible Models for Healthcare: Predicting Pneumonia Risk and Hospital 30-Day Readmission*. In Proceedings of the 21th ACM SIGKDD International Conference on Knowledge Discovery and Data Mining (pp. 1721-1730). Sidney, Australia: KDD, 2015.

Chan J, Lee JA, Kemao Q. *BIND: Binary Integrated Net Descriptors for Texture-Less Object Recognition*. In Computer Vision and Pattern Recognition (pp. 2068-2076). Honolulu, USA: Computer Vision Foundation, 2017.

Chen Q, Koltun V. *Robust Nonrigid Registration by Convex Optimization*. In Computer Vision and Pattern Recognition (pp. 2039-2047). Boston, USA: Computer Vision Foundation, 2015.

Cignoni P, Callieri M, Corsini M, Dellepiane M, Ganovelli F, Ranzuglia G. *MehsLab: an Open-Source Mesh Processing Tool*. In Sixth Eurographics Italian Chapter Conference (pp. 129-136). Salerno, Italy: Eurographics Association, 2008.

Cignoni P, Rocchini C, Scopigno R. Metro: measuring error on simplified surfaces. *Comput Graph Forum* 17(2):167-174, 1998.

Collier RJ, Gebremedhin KG. Thermal biology of domestic animals. *Annu Rev Anim Biosci* 3:513-532, 2015.

Cortes C, Vapnik VN. Support-vector networks. *Mach Learn* 20(3):273–297, 1995.

Costa CCM, Maia ASC, Brown-Brandl TM, Chiquitelli Neto M, Fonsêca VFC. Thermal equilibrium of Nellore cattle in tropical conditions: an investigation of circadian pattern. *J Therm Biol* 74:317–324, 2018a.

Costa CCM, Maia ASC, Nascimento ST, Nascimento CCN, Chiquitelli Neto MC, Fonsêca VFC. Thermal balance of Nellore cattle. *Int J Biometeorol* 62(5):723–731, 2018b.

Cox M, Ellsworth D. *Application-Controlled Demand Paging for Out-of-Core Visualization*. In IEEE Proceedings of Visualization (pp. 235-244). Phoenix, AZ: IEEE, 1997.

Datta AK. Toward computer-aided food engineering: mechanistic frameworks for evolution of product, quality and safety during processing. *J Food Eng* 176:9-27, 2016.

Dudley PN, Bonazza R, Porter WP. Consider a non-spherical elephant: computational fluid dynamics simulations of heat transfer coefficients and drag verified using wind tunnel experiments. *J Exp Zool* 319A:319-327, 2013.

Efron B, Hastie T. *Computer Age Statistical Inference: Algorithms, Evidence, and* 376

*Data Science*. New York: Cambridge University Press, 2016.

Eigenberg RA, Brown-Brandl TM, Nienaber JA, Hahn GL. Dynamic response indicators of heat stress in shaded and non-shaded feedlot cattle, part 2: predictive relationships. *Biosystems Eng* 91(1):111-118, 2005.

Forsythe GE, Malcolm MA, Moler CB. *Computer Methods for Mathematical Computations*. Hoboken: Wiley, 1977.

Fox J. *Applied Regression Analysis and Generalized Linear Models* (3rd ed.) Los Angeles: Sage, 2016.

Friedman JH. Greedy function approximation: a gradient boosting machine. *Ann Statist* 29(5):1189-1232, 2001.

Gardner JR, Pleiss G, Bindel D, Weinberger KQ, Wilson AG. *GPyTorch: Blackbox Matrix-Matrix Gaussian Process Inference with GPU Acceleration*. In *Neural Information Processing Systems* (pp. 1-21). Montréal, Canada: NIPS Foundation, 2018.

Gaughan JB, Holt SM, Hahn GL, Mader TL, Eigenberg R. Respiration rate – is it a good measure of heat stress in cattle? *Asian-Aus J Anim Sci* 13(C):329-332, 2000.

Gebremedhin KG, Lee CN, Hillman PE, Collier RJ. Physiological responses of dairy cows during extended solar exposure. *Trans ASABE* 53(1):239-247, 2010.

Gebremedhin KG, Wu BX. Characterization of flow field in a ventilated space and simulation of heat exchange between cows and their environment. *J Therm Biol* 28:301-319, 2003

Gebremedhin KG, Wu B. Simulation of flow field of a ventilated and occupied animal space with different inlet and outlet conditions. *J Therm Biol* 30:343-353, 2005.

Gebremedhin KG, Wu B. Modeling heat loss from the udder of a dairy cow. *J Therm Biol* 59:34-38, 2016.

Gebremedhin KG, Wu B, Perano K. Modeling conductive cooling of thermally stressed dairy cow. *J Therm Biol* 56:91-99, 2016.

Goodfellow I, Bengio Y, Courville A. *Deep Learning*. Cambridge: The MIT Press, 2016.

Gorczyca MT, Milan HFM, Maia ASC, Gebremedhin KG. Machine learning algorithms to predict core, skin, and hair-coat temperatures of piglets. *Comput Electron Agric* 151:286-294, 2018.

Gorczyca MT, Gebremedhin KG. Ranking of environmental heat stressors for Dairy cows. *In preparation*, 2019.

Guarino M, Norton T, Berckmans D, Vranken E, Berckmans D. A blueprint for developing and applying precision livestock farming tools: a key output of the EU-PLF project. *Anim Front* 7(1):12-17, 2017.

Hastie TJ, Tibshirani RJ. *Generalized Additive Models*. New York: Chapman & Hall/CRC, 1990.

Hastie T, Tibshirani R, Friedman J. *The Elements of Statistical Learning: Data Mining, Inference, and Prediction* (2<sup>nd</sup> ed.). New York: Springer, 2008.

Hillman PE, Gebremedhin KG, Willard ST, Lee CN, Kennedy AD. Continuous measurements of vaginal temperature of female cattle using a data logger encased in a plastic anchor. *Appl Eng Agric* 25(2):291-296, 2009.

Huang QX, Adams B, Wicke M, Guibas LJ. *Non-Rigid Registration under Isometric Deformations*. In Eurographics Symposium Geometry Processing (pp. 1449-1457). Copenhagen, Denmark: Eurographics Association, 2008.

Huffman GJ, Adler RF, Arkin P, Chang A, Ferraro R, Gruber A, Janowiak J, McNab A, Rudolf B, Schneider U. The Global Precipitation Climatology Project (GPCP) Combined Precipitation Dataset. *Bull Amer Meteor Soc* 78(1):5-20, 1997.

Hunter MC, Smith RG, Schipanski ME, Atwood LW, Mortense DA. Agriculture in 2050: recalibrating targets for sustainable intensification. *BioScience* 67(4):386-391, 2017.

Hutson M. Artificial intelligence faces reproducibility crisis. *PNAS* 115(11):2628-2631, 2018.

Kazhdan M, Hoppe H. Screened Poisson surface reconstruction. *ACM Trans Graphics* 379

32(3):29:1-13, 2013.

Kohavi R. *A Study of Cross-Validation and Bootstrap for Accuracy Estimation and Model Selection*. In Proceedings of the 14th International Joint Conference on Artificial Intelligence (pp. 1137-1143). San Mateo, CA: Morgan Kaufmann, 1995.

Li H, Sumner RW, Pauly M. Global correspondence optimization for non-rigid registration of depth scans. *Comput Graph Forum* 27(5):1421-1430, 2008.

Maia, A. S. C., da Silva, R. G., & Loureiro, C. M. B. (2005). Respiratory heat loss of Holstein cows in a tropical environment. *International Journal of Biometeorology*, 49, 332-336.

Manu. nonrigidICP (v1.15.0.0). Accessed on March 18, 2017. Retrieved from <https://uk.mathworks.com/matlabcentral/fileexchange/41396-nonrigidicp>

Milan HFM, Maia ASC, Gebremedhin KG. Data for mechanistic modeling of bio-heat transfer of piglets. <https://doi.org/10.17605/OSF.IO/FSQXJ>, 2018.

Milan HFM, Maia ASC, Gebremedhin KG. Prediction of optimum supplemental heat for piglets. *Trans ASABE* 62(2):321-342, 2019.

Milan HFM, Moura GAB, Castro PA, Maia ASC, Gebremedhin KG. Measurement of 3-D Surface Area of Piglets. In 10th International Livestock Environment Symposium (pp. 1-6). Omaha, USA: ASABE, 2018.

Milan HFM, Perano KM, Gebremedhin KG. *Procedures for Measuring 3-D Surface Area and Surface Temperature of Livestock*. In VII Brazilian Congress of Biometeorology, Ambience, Behaviour and Animal Welfare “Environmental Responsibility and Innovation” (pp. 1-5). Jaboticabal, Brazil: Figshare, 2017.

Milan HFM, Perano KM, Gebremedhin KG. *Survey and Future Prospects in Precision Dairy Farming*. In 10th International Livestock Environment Symposium (pp. 1-8). Omaha, USA: ASABE, 2018.

Molnar C. *Interpretable Machine Learning: A Guide for Making Black Box Models Explainable*. Leanpub, 2018.

Mondaca M, Choi CY. An evaluation of simplifying assumptions in dairy cow computational fluid dynamic models. *Trans ASABE* 59(6):1575-1584, 2016.

Moser WR. *Linear models: a mean model approach*. New York: Elsevier, 1996.

Natekin A, Knoll A. Gradient boosting machines, a tutorial. *Front Neurobot* 7:21:1-21, 2013.

Norton T, Grant J, Fallon R, Sun DW. Improving the representation of thermal boundary conditions of livestock during CFD modelling of the indoor environment. *Comput Electron Agric*, 73:17-36, 2010.

Pan SJ, Yang Q. A survey on transfer learning. *IEEE Trans Knowl Data Eng* 22(10):1345-1359, 2010.

Perano KM, Usack JG, Angenent LT, Gebremedhin KG. Production and physiological responses of heat-stressed lactating dairy cattle to conductive cooling. *J Dairy Sci* 98:5252-5261, 2015.

R Core Team. *R: A Language and Environment for Statistical Computing*. R Foundation for Statistical Computing. Vienna, Austria, <https://www.R-project.org/>, 2018.

Rasmussen CE, Williams CKI. *Gaussian Processes for Machine Learning*. Cambridge: the MIT Press, 2006.

Robertshaw D. Mechanisms for the control of respiratory evaporative heat loss in panting animals. *J Appl Physiol* 101:664-668, 2006.

Rusinkiewicz S, Levoy M. *Efficient Variants of the ICP Algorithm*. In IEEE Third International Conference on 3D digital imaging and modeling (pp. 145-152). Quebec City, Canada: IEEE, 2001.

Schleger AV, Turner HG. Sweating rates of cattle in the field and their reaction to diurnal and seasonal changes. *Aust J Agric Res* 16:92-106, 1965.

Simão BR, Maia ASC, Castro PA, Moura GAB, Fonsêca VFC. *Estimation of the Body Surface Area and Its Impact on the Heat Transfer by Convection in Sheep: a Computational Way*. In VII Brazilian Congress of Biometeorology, Ambience, Behaviour and Animal Welfare “Environmental Responsibility and Innovation” (pp.

1-5). Jaboticabal, Brazil: Figshare, 2017.

Sorkine O, Alex M. *As-Rigid-As-Possible Surface Modeling*. Symposium on Geometry processing (pp. 109-116). Barcelona, Spain: Eurographics Association, 2007.

Steinwart I, Thomann P. liquidSVM: a fast and versatile SVM package. *arXiv* 1702.06899, 2017.

Stevens DG. A model of respiratory vapor loss in Holstein dairy cattle. *Trans ASAE* 24:151-158, 1981.

Sumner RW, Schmid J, Pauly M. Embedded deformation for shape manipulation. *ACM Trans Graphics* 26(3):80:1-8, 2007.

Salti S, Tombari F, Di Stefano L. SHOT: Unique signatures of histograms for surface and texture description. *Comput Vis Image Und* 125:251-264, 2014.

The H2O.ai team. h2o: R interface for H2O: R package version 3.16.0.2. <https://CRAN.R-project.org/package=h2o>, 2017.

van Kaick O, Zhang H, Hamarneh G, Cohen-Or D. A survey on shape correspondence. *Comput Graph Forum* 30(6):1681-1707, 2011.

Wathes CM, Kristensen HH, Aerts J-M, Berckmans D. Is precision livestock farming an engineer's daydream or nightmare, an animal's friend or foe, and a farmer's panacea

or pitfall? *Comput Electron Agric* 64:2-10, 2008.

Williams ML, Mac Parthaláin N, Brewer P, James WPJ, Rose MT. A novel behavioral model of the pasture-based dairy cow from GPS data using data mining and machine learning techniques. *J Dairy Sci* 99:2063-2075, 2016.

Wolpert DH, Macready WG. No free lunch theorems for optimization. *IEEE Trans Evolut Comput* 1(1):67-82, 1997.

Wood SN. Fast stable restricted maximum likelihood and marginal likelihood estimation of semiparametric generalized linear models. *J R Statist Soc B* 73(1):3-36, 2011.

Wood SN. *Generalized Additive Models: An Introduction in R* (2nd 3d). Boca Raton: CRC Press, 2017.

Wu B, Gebremedhin KG. CFD development and simulation of flow fields in ventilated spaces with multiple occupants. *Trans ASAE* 44(6):1839-1850, 2001a.

Wu B, Gebremedhin KG. Numerical simulation of flow field around a cow using 3-D body-fitted coordinate system. *J Therm Biol* 26:563-573, 2001b.

Wu C. VisualSFM: A visual structure from motion system. Retrieved from <http://ccwu.me/vsfm/>, 2011.

Wu C. *Towards Linear-Time Incremental Structure From Motion*. In IEEE

International Conference on 3D Vision (pp. 127-134). Seattle, USA: IEEE, 2013.

Zampogiannis K, Fermüller C, Aloimonos Y. cilantro: a lean, versatile, and efficient library for point cloud data processing. *arXiv*, 1807.00399, 2018.

Zou H, Hastie T. Regularization and variable selection via the elastic net. *J R Statist Soc B* 67(2):301–320, 2005.

Zou H, Zhang HH. On the adaptive elastic-net with a diverging number of parameters. *Ann Stat* 37:1733-1751, 2009.

Zuffi S, Kanazawa A, Jacobs D, Black MJ. *3D menagerie: Modeling the 3D Shape and Pose of Animals*. In Computer Vision and Pattern Recognition (pp. 5524-5532). Honolulu, USA: Computer Vision Foundation, 2017.